

Investigation of Electromagnetic Band-Gap Structures
Using Metallic Open Square Rings For Microwave
Applications

by

Hassna Ouassal

A thesis submitted to the Faculty of Graduate and Postdoctoral
Affairs in partial fulfillment of the requirements for the degree of

Doctor in Philosophy

in

Electrical Engineering

Carleton University
Ottawa, Ontario

© 2016, Hassna Ouassal

My Lord increase me in knowledge
Quran, 20:114

رَبِّ زِدْنِي عِلْمًا

To The Memory of My Beloved Father

ABSTRACT

Electromagnetic band-gap (EBG) materials, also known as photonic band-gap (PBG) materials or electromagnetic crystals (ECs), exhibit a forbidden range of frequencies, i.e., band gap across which electromagnetic wave cannot propagate. This thesis investigates an EBG structure, composed of multi-layer metallic open square rings (OSRs) structure and its application to novel microwave designs. The structure is studied in air and dielectric media.

First, the operating principles (eigenmodes, dispersion diagrams and confined modes) are elucidated for an infinite layered structure in air media. The effects of OSR geometrical parameters on the band gap are investigated. A maximum width of band gap is obtained by judicious selection of the structural parameters of the EBG. Then, studies of finite layered structures such as EBG slabs and EBG slab line-defect waveguides are performed. It is shown that the number of guided modes at different frequencies are specified by the number of layers with defects. On the other hand, in absence of defects within the layers, guided modes cease to exist. Following these findings, detailed studies are conducted on EBG slabs and EBG slab line-defect waveguides in dielectric media. Similar modal behaviour has been observed for the EBG OSR structure in both media.

In a first application, line defect EBG waveguides that are fed with integrated conventional microwave circuits are designed, fabricated and experimentally tested. Designs are developed to operate at Ku band (12-18 GHz) and acceptable agreement was found between simulations and measurements of the foam (air)-supported guide. Then, dielectric-supported guides are developed. Good agreement was also observed between theoretical and experimental results in X-band (8-12 GHz). In both EBG channel types, the insertion loss per unit length does not change significantly by increasing the length of the periodic channel.

In a second application, novel layered OSR line-defect waveguide directional couplers capable of producing arbitrary coupling are designed. Quasi-0-dB couplers and 3-dB couplers are numerically demonstrated, with good phase balance, and isolation. Unique features of these couplers are wave propagation in the forward- and/or backward-directions that can be reconfigured by simply rotating coupling elements.

ACKNOWLEDGEMENTS

First and foremost, I would like to express my deepest and sincere gratitude to my supervisors, Dr. Langis Roy and Dr. Jafar Shaker who gave me the great opportunity to do my research in a topic well suited for my interest. I am profoundly indebted to them for their precious guidance, care, encouragement, patience and financial support throughout this research. Indeed, my gratitude cannot be expressed in few words. I also express my gratitude to Dr. Reza Chaharmir for his contribution to this thesis. Special thanks also to Dr. Khelifa Hettak for the help with the measurements and insightful ideas. The fruitful discussions during conference and face-to-face meetings were very valuable to my research. I feel very grateful and lucky to have been able to have discussion with all of them about my research.

I would like to thank all my thesis committee members for their time and effort in serving on my committee.

I would like to thank Prof. Mustapha Yagoub and Prof. Derek McNarama. The undergraduate courses that I had taken with them had directed me to pursue Graduate Studies in the field of Electromagnetic. Thank you Professors!

I spent all my research time in the Dipak and Tara Roy lab. I am extremely grateful for this workspace. Without it, my stay would have been much more difficult and stressful.

This work would not have been possible without the help and support from many people in the department of Electronics. I am extremely grateful to Mr. Nagui Mikhail for giving me privileged access to many servers to perform my research during all the Ph. D years. The help and assistance offered by Dr. Leonard MacEachern is gratefully acknowledged. I enjoyed my research and teaching time at Carleton University.

I received special help to advance and finish my research after my supervisor left the university. I sincerely thank Dr. Niall Tait, chair of the department, Ms Blazenka Power and Mr Scott Bruce.

I would like to thank Mr Rob Vandusen, Mr Stephen Maclaurin, Ms Anna Lee and Ms Sylvie Beekmans for their friendly and helpful service.

I would like to aknowledge Rogers corporation for providing me with free samples to fabricate my circuits.

I would like to express my deepest respects and gratitude to my mother and my brother Abdelhadi. Special gratitude and thanks to my brothers Omar, Noureddine, Abdelaziz and Abdelghani. Thank you my sisters..

Thank you my mother, my brothers and my sisters for your contribution to my education. This thesis is dedicated to you.

TABLE OF CONTENTS

ABSTRACT	V
ACKNOWLEDGEMENTS	VI
TABLE OF CONTENTS.....	VIII
LIST OF TABLES.....	XI
LIST OF FIGURES	XII
LIST OF ABBREVIATIONS.....	XXI
LIST OF SYMBOLS	XXIV
CHAPTER 1. INTRODUCTION	1
1.1 Introduction to Electromagnetic Band Gap	1
1.2 Motivation of The Thesis	2
1.3 Thesis Objectives	5
1.4 Thesis Organization	5
CHAPTER 2. STATE OF THE ART OF EBG STRUCTURES	7
2.1 Introduction	7
2.2 General EBG Structures.....	8
2.3 Defects For EBG Structures.....	17
2.3.1 Special Structures Such as Couplers, Switches, Waveguides And Antennas	17
2.4 A Brief Discussion of EBG Structure Used in Thesis	22
2.5 Chapter Summary	22
CHAPTER 3. STUDY OF ELECTROMAGNETIC BANDGAP COMPOSED OF METALLIC OPEN SQUARE RINGS	24
3.1 Introduction	24
3.2 Infinite Open Square Rings in Free Space	25
3.2.1 Computational Method	25
3.2.2 Parametric Study	27
3.3 EBG Slab of OSRs in Free Space	38
3.3.1 Method of Computation.....	38
3.3.2 Band Structure	39
3.3.3 Effect of Slab Thickness	41
3.4 EBG Slab Waveguide in Free Space	41

3.4.1	Channel Waveguide Structure	41
3.4.2	Modes in The EBG Slab Waveguide	42
3.5	Infinite Open Square Rings in Dielectric.....	49
3.6	EBG Slab of OSRs in Dielectric	51
3.6.1	Structure.....	51
3.6.2	Relationship Between the Slab Thickness and the Size of the Bandgap	51
3.6.3	Band Structure	53
3.7	EBG Slab Waveguide in Dielectric	54
3.8	Design For Different Frequency Bands	58
3.9	Conclusion	63
CHAPTER 4.	IMPLEMENTATION AND CHARACTERIZATION.....	64
4.1	Introduction.....	64
4.2	EBG Waveguide Foam Supported.....	64
4.2.1	Channel Field Distributions and Feed Transition Concept.....	65
4.2.2	Fabricated Prototypes.....	66
4.2.3	Simulated and Measured Results	70
4.2.4	Sensitivity Analysis and Vertical Misalignment.....	76
4.3	EBG Waveguide Dielectric Supported	80
4.3.1	Feed Transition	80
4.3.2	Excitation of the EBG Waveguide.....	82
4.3.3	Simulated and Measured Results	84
4.3.4	Detailed Waveguide Characterization Through De-embedding	90
4.3.5	Performance Comparison With Other Transmission lines	100
4.4	Conclusion	101
CHAPTER 5.	EBG COUPLED LINE-DEFECT WAVEGUIDE DIRECTIONAL COUPLER	103
5.1	Introduction.....	103
5.2	Architecture and Design of the EBG Line-defect Waveguide Directional Coupler	104
5.3	Implementation	109
5.4	Results and Discussion	110

5.4.1	Quasi-0-dB Forward-Wave Coupler.....	110
5.4.2	Quadrature Forward-wave Coupler	111
5.4.3	Through Coupling.....	115
5.4.4	Quasi-0-dB Forward/Backward Wave Coupler.....	116
5.4.5	3-dB Forward-/Backward-Wave Coupler.....	118
5.5	Conclusion	121
CHAPTER 6. CONCLUSIONS, CONTRIBUTIONS AND RECOMMENDATION FOR FUTURE WORK		122
6.1	Summary	122
6.2	Contributions.....	123
6.3	Future Work	123
BIBLIOGRAPHY		125

LIST OF TABLES

Table 3.1: Computed bandgap for different OSRs structures. Bolded values refer to nominal case.....	37
Table 3.2: Bandgaps of the U-rings structure in different mediums.	50
Table 3.3: Bandgaps of the reduced 1 U-OSR structure in different mediums. Geometrical parameters are : L = 1.5 mm, W = 0.5 mm, G = 0.5 mm, H = 0.5 mm and T = 2 mm.	59
Table 3.4: Bandgaps of the reduced 2 U-OSR structure in different mediums. Geometrical parameters are : L = 1.5 mm, W = 0.5 mm, G = 0.5 mm, H = 0.5 mm and T = 1.7 mm.	61
Table 3.5: Bandgaps of the conventional and reduced U-OSR structure in different mediums. Geometrical parameters are :.....	61
Table 4.1: Performances of the fabricated de-embedded EBG waveguides in dielectric.	93
Table 4.2: Performances of the EBG waveguide and other transmission lines.	100

LIST OF FIGURES

Figure 1.1 Naturally abundant periodic structures. (a) Opal stone. (b) Bee hives.....	2
Figure 1.2 Conventional EBG structures. (a) Hole structure [2]. (b) Rod structure [2]. (c) Metallic pads with vias [9]. (d) Metallic pads without vias [10].....	3
Figure 1.3 Metallic open square rings (OSRs) EBG structure [21].....	4
Figure 2.1 (a) First EBG structure fabricated by drilling holes at 35.26° to normal and 120° to each other. (b) Cross section [2, 33].....	8
Figure 2.2 The layer-by-layer structure [34].....	9
Figure 2.3 Proposed planar dipole antenna lying over the photonic-crystal region of a semi-insulating GaAs substrate [24].....	10
Figure 2.4 First layer-by-layer metallic EBG structure [41].....	11
Figure 2.5 Several EBG structures for microstrip circuits : (a) Honeycomb-lattice square-hole. (b) Square-lattice square hole. (c) Honeycomb-lattice circular-hole. (d) triangular-lattice square-hole [7].....	11
Figure 2.6 Three-dimensional view of a proposed EBG structure. The square lattice circles are etched in the ground plane of a microstrip line [30].....	12
Figure 2.7 (a) Cross section of a high-impedance surface, fabricated as a printed circuit board: The structure consists of a lattice of metal plates, connected to a solid metal sheet by vertical conducting vias. (b) Top view of the high-impedance surface, showing a triangular lattice of hexagonal metal plates [8].....	13
Figure 2.8 (a) Schematic of UC-PBG metallic pattern on a dielectric substrate. (b) Unit cell of the UC-PBG structure [4].....	13
Figure 2.9 The structure of a conventional CB-CPW [4].....	14
Figure 2.10 Two-dimensional photonic crystal. This structure is a square lattice of dielectric rods with radius r and dielectric constant ϵ_r . It is periodic along x and y directions with lattice constant a , and homogeneous along z . The left inset is a top view of the square lattice, with unit cell shown in red [2].....	15
Figure 2.11 Band structure for a square array of dielectric rods with $r = 0.2a$ and $\epsilon_r = 8.9$ embedded in air. The left inset is the brillouin zone, with the irreducible zone shaded blue. The frequency is expressed as dimensionless ratio $\omega a/2\pi c$ [2].....	16

Figure 2.12 Displacement fields of TM states inside a square array of dielectric rods in air of Fig. 2.10. Modes are shown at the Γ point [2].....	16
Figure 2.13 (a) Optical microscope image. (b) SEM image for a fabricated directional Coupler structure combined with the bent waveguide. Each waveguide contains four 60° bends (total is eight). (c) The cleaved end of the single-line-defect waveguide. L_c is the coupling length and a is the lattice constant [50].	18
Figure 2.14 (a) SEM of the fabricated coupler with a straight-coupled channel (type I). The fabricated coupler has a larger separation between the two output channels compared with the modeled coupler. (b) Modeled coupler with a straight-direct channel (type II) [52].....	19
Figure 2.15 Schematic of PC directional coupler used as switching structure [53].	20
Figure 2.16 Electric field distribution inside the coupler. (a) Cross state. (b) Bar state. (c) Control signal used to tune the switch [53].	20
Figure 2.17 EBG waveguide for TM mode [55].....	21
Figure 2.18 TEBG antenna geometry and (inset) triangular lattice of circular dielectric rods [56].....	22
Figure 3.1 The first Brillouin zone for a 2D square lattice. Parameters k_x , k_y are the x and y components of the wave vector k' , respectively, and T is the lattice period in X and Y directions.....	26
Figure 3.2 (a) Schematic of the stacked OSRs arrays. (b) Unit cell setup and applied boundary conditions.....	27
Figure 3.3 Unit cell of the stacked OSRs with geometrical parameters as follows: $H = 0.5$ mm, $T_x = T_y = 5$ mm, $G = 0.5$ mm, $W = 0.5$ mm and $L = 4.5$ mm [21].....	28
Figure 3.4 Effect of modifying the gap G on the band gap. Frequencies 5.28 GHz, 6.8 GHz, 8.87 GHz, and 9.2 GHz are the band gap between modes 1 and 2 for $G = 0.1$ mm, 0.5 mm, 2 mm and 3.5 mm respectively. Other parameters are as in Fig. 3.3.	29
Figure 3.5 The electric fields (top), magnetic fields H_z (center) and surface currents (bottom) at the X-point for $G = 0.1$ mm (a) and 3.5 mm (b) (i.e., other parameters are as in Fig. 3.3). Modes 1 and 2 are the left and right panels, respectively.....	29

Figure 3.6 Effect of modifying lattice period T on the band gap. Frequencies 10.38 GHz, 6.8 GHz, 1.74 GHz correspond to band gap between modes 1 and 2 for T = 4.6 mm, 5 mm, and 8 mm respectively. Other parameters are as in Fig. 3.3.....	32
Figure 3.7 The electric fields (top), magnetic fields Hz (center) and surface currents (bottom) at the X-point for T = 4.6 mm (a) and T = 8 mm (b) (i.e., other parameters are as in Fig. 3.3). Modes 1 and 2 are the left and right panels, respectively.....	32
Figure 3.8 Effect of modifying metal width on the band gap. Frequencies 7.1 GHz, 6.8 GHz, and 5.4 GHz correspond to band gap between modes 1 and 2 for W = 0.1 mm, 0.5 mm and 1 mm respectively, but no band gap for W = 2 mm. Other parameters are as in Fig. 3.3.....	33
Figure 3.9 The magnetic fields H _z (top) and surface currents (bottom) at the X-point for W = 0.1 mm (a) and W = 2 mm (b) (i.e., other parameters are as in Fig. 3.3). Modes 1 and 2 are the left and right panels, respectively.....	34
Figure 3.10 Effect of modifying separation H. Frequencies 6.8 GHz, and 1.3 GHz correspond to band gap between modes 1 and 2 for H = 0.5 mm and 10 mm respectively. No band gap for H = 20 mm. Other parameters are as in Fig. 3.3.	35
Figure 3.11 The magnetic fields H _z (top) and surface currents (bottom) at the X-point for H = 0.5 mm (a) and H = 20 mm (b) (i.e., other parameters are as in Fig. 3.3). Modes 1 and 2 are the left and right panels, respectively.....	35
Figure 3.12 Effect of modifying outer-ring size L on the band gap. 3 GHz, 6.8 GHz, correspond to band gap for L= 3 mm and 4.5 mm respectively. Other parameters are as in Fig. 3.3.....	36
Figure 3.13 The magnetic fields Hz (top) and surface currents (bottom) at the X-point for L = 4.5 mm (a) and L = 3 mm (b) (i.e., other parameters are as in Fig. 3.3). Modes 1 and 2 are the left and right panels, respectively.....	36
Figure 3.14 (a) Slab structure. (b) Super-cell model. The slab thickness d is 1.2 T (i.e. stack of 7 rings, spaced by 1 mm and in air), where T is the period in the x and y directions. The medium above and below the slab is air.....	39
Figure 3.15 Projected band structure for the structure shown in Fig. 3.14 with 7 rings in the Z direction separated by 1 mm in air.	40

Figure 3.16 E-field of the slab structure in Fig. 3.15 depicted in the unit cell at X for modes 7 and 8 at the lower and upper edges of the band gap respectively. Horizontal (xy) cross section (bottom). Vertical (yz) cross section (top). Modes at the lower and upper edges of the band gap are at (a) and (b) respectively.....	40
Figure 3.17 (a) Structure of EBG slab waveguide composed of seven layers suspended in air. (b) Ring dimensions.....	42
Figure 3.18 Super-cell for band calculation of the waveguide. The wave propagation direction is in the x direction.....	43
Figure 3.19 Band diagram of the waveguide modes. Cross section of the guide is shown in the inset, which shows seven stacked defects (in all layers) in the channel of the guide.	
.....	44
Figure 3.20 E-field cross sections at (a) $f = 16.37$ GHz (a), 18.47 GHz (b), 19.12 GHz (c) and 19.39 GHz (d) for modes 1-4 respectively in line-defect waveguide of seven defects. Horizontal (xy) cross section (top).Vertical (yz) cross section orthogonal to the guided direction (bottom).....	45
Figure 3.21 E-field cross sections at $f = 19.49$ GHz (a), 19.57 GHz (b) and 19.58 GHz (c) for modes 5-7 respectively in line-defect waveguide of seven defects. Horizontal (xy) cross section (top).Vertical (yz) cross section orthogonal to the guided direction (bottom).....	46
Figure 3.22 E-field cross sections at $f = 16.56$ GHz (in the gap) (a) and $f = 22.85$ GHz (outside the gap) (b) for modes 1 and 2 respectively in line-defect waveguide of one layer (vertically centered) defects. Horizontal (xy) cross section (top). Vertical (yz) cross section orthogonal to the guided direction (bottom).....	47
Figure 3.23 Band diagram of the waveguide modes with defect in single layer. Cross section of the guide is shown in the inset, which shows defect in the fourth layer only.....	48
Figure 3.24 Band diagram of line-defect waveguide for various number of layers having defects. Only confined modes in the channel are shown in the graph (Seven layers with defects : only three confined modes are shown).....	49
Figure 3.25 Dispersion diagrams of the infinite U-rings in dielectric mediums of ϵ_r of 2, 2.94, 4 and 9. Air medium case is shown for comparison.....	50

Figure 3.26 (a) Schematic of an EBG Slab: 2D square array of stacked U rings is a dielectric medium. (b) The super-cell for the EBG Slab.....	51
Figure 3.27 Variation of the band gap frequencies with slab thickness in different mediums : vertical spacing between rings is $H = 0.25$ mm.....	52
Figure 3.28 Variation of the band gap frequencies with slab thickness in different mediums : vertical spacing between rings is $H = 1$ mm.....	53
Figure 3.29 Band structure of the EBG slab of seven layered OSRs in dielectric medium of $\epsilon_r = 2.94$ and thickness $d = 3$ mm. Vertical spacing between rings is $H = 0.25$ mm. Black solid lines are the light lines.....	54
Figure 3.30 Line-defects slab waveguides embedded in a dielectric medium. (a) Line-defect in single layer. (b) Line-defect in all layers.....	55
Figure 3.31 Band structure for channel waveguide having defects in single layer.	56
Figure 3.32 Band structure for channel waveguide having defects in all layers.	57
Figure 3.33 Band diagram of mode 1 of EBG waveguide of single layer defects with various rows on the sides of the channel.	57
Figure 3.34 Dispersion diagram of the infinite reduced 1 U-OSR in air and dielectric mediums. Geometrical parameters are : $L = 1.5$ mm, $W = 0.5$ mm, $G = 0.5$ mm, $H = 0.5$ mm and $T = 2$ mm.....	59
Figure 3.35 Dispersion diagram of the infinite reduced 2 U-OSR in air and dielectric mediums. Geometrical parameters are : $L = 1.5$ mm, $W = 0.5$ mm, $G = 0.5$ mm, $H = 0.5$ mm and $T = 1.7$ mm.....	60
Figure 3.36 Band gap frequencies of the UOSR in different mediums. (a) Conventional UOSR, (b) Reduced 1 UOSR and (c) Reduced 2 UOSR. Narrow and wide lines represent first and second band gaps respectively.....	62
Figure 4.1 Field distributions of mode 1 of the EBG channel based-foam. (a) E-field in horizontal (xy) cross section. (b) H-field in vertical (yz) cross section.....	65
Figure 4.2 Geometry of the CPW-to-Slot line transition.....	66
Figure 4.3 Simulated and measured S-parameters of the back-to-back CPW-to-slot line transition of lengths $L = 43.8$ mm and 63.8 mm. (a) S11 and (b) S21. Transition is shown in the inset of (b).....	67

Figure 4.4 CPW-to-Slot line fed EBG waveguide based-foam. The guide has seven layers with defects and six rows on each side of the channel. The channel length is 19.8 mm (4 periods). Total dimensions of the guide are L (43.8 mm) x W (65 mm) x H _r (6.18 mm).....	68
Figure 4.5 Photo of the fabricated EBG waveguide prototypes with transitions. The enlarged view shows the connection between the slot line of the transition on Duroid and the existing slot line on the Kapton sheet. Conducting tapes are used to make the connection.....	69
Figure 4.6 Simulated and measured: (a) S11, (b) S22 and (c) S21 of EBG guide in Fig. 4.4 of lengths L = 43.8 mm, 63.8 mm and 103.8 mm. Cross section of the guide is shown in the inset of (a)	71
Figure 4.7 Simulated and measured: (a) S11, (b) S22 and (c) S21 of EBG RDR guide of lengths L = 43.8 mm and 63.8 mm. Cross section of the guide is shown in the inset of (a)	73
Figure 4.8 Simulated and measured: (a) S11, (b) S22 and (c) S21 of EBG RRR guide of lengths L = 43.8 mm and 63.8 mm. Cross section of the guide is shown in the inset of (a)	74
Figure 4.9 Electric field distribution at f = 15.8 GHz in the EBG waveguide channel of length: (a) Four periods (a). (b) Eight periods.	76
Figure 4.10 Simulated results of the RDR waveguide of length L = 43.8 mm: (a) S11, (b) S22 and (c) S21. Layers above and below the fourth layer are positioned 0.5 mm and 1 mm offset horizontally (along positive x-axis). Cross section of the guide is shown in the inset of (a)	78
Figure 4.11 Simulated Offset 1 mm and measured results of the RDR waveguide: (a) S11 (a), (b) S22 and (c) S21.....	79
Figure 4.12 Simulated and measured S-parameters of the back-to-back CPW-to-slot line transition of lengths L = 49 mm and 69 mm. (a) S11. (b) S21	81
Figure 4.13 EBG waveguide in dielectric fed by CPW-to-slot line transitions. The waveguide has 3 rows on the sides of the channel. The size of the waveguide is L x W x H _r = 49 mm x 35 mm x 3 mm.	82
Figure 4.14 EBG waveguide configurations.....	83

Figure 4.15 Photo of the fabricated EBG waveguides embedded in a dielectric.	84
Figure 4.16 Simulated and measured: (a) S11, (b) S22 and (c) S21 of EBG guide with three rows and lengths L of 49 mm, 69 mm and 109 mm. Cross section of the guide is shown in the inset of (a).	86
Figure 4.17 Simulated and measured: (a) S11, (b) S22 and (c) S21 of EBG guide with one row and lengths of 69 mm and 109 mm. Cross section of the guide is shown in the inset of (b).	87
Figure 4.18 Simulated and measured: (a) S11, (b) S22 and (c) S21 of EBG guide with six rows and length of 49 mm. Cross section of the guide is shown in the inset of (a).	88
Figure 4.19 Electric field distribution at $f = 10.5$ GHz in the EBG waveguide. (a) Channel length of eight periods with one row and (b) with three rows. (c) Channel length of four periods with three rows and (d) and six rows.....	89
Figure 4.20 De-embedding technique using transmission matrix bisect de-embedding. (a) Measured structure having the DUT. (b) THRU structure.	90
Figure 4.21 S-parameters of the calculated, simulated THRU structure of length $L = 29.2$ mm and measured back-to-back transition of length $L = 49$ mm.	92
Figure 4.22 Characteristic S-parameters before and after de-embedding of EBG guide with three rows and length L of 49 mm. Raw is simulated result of DUT. (a) S11, (b) S22 and (c) S21.	94
Figure 4.23 Characteristic S-parameters before and after de-embedding of EBG guide with three rows and length L of 69 mm. Raw is simulated result of DUT. (a) S11, (b) S22 and (c) S21.	95
Figure 4.24 Characteristic S-parameters before and after de-embedding of EBG guide with three rows and length L of 109 mm. Raw is simulated result of DUT. (a) S11, (b) S22 and (c) S21.	96
Figure 4.25 Characteristic S-parameters before and after de-embedding of EBG guide with one row and length L of 69 mm. Raw is simulated result of DUT. (a) S11, (b) S22 and (c) S21.	97
Figure 4.26 Characteristic S-parameters before and after de-embedding of EBG guide with one row and length L of 109 mm. Raw is simulated result of DUT. (a) S11, (b) S22 and (c) S21.	98

Figure 4.27 Characteristic S-parameters before and after de-embedding of EBG guide with six rows and length L of 49 mm. Raw is simulated result of DUT. (a) S11, (b) S22 and (c) S21	99
Figure 4.28 Simulated group delay of the EBG guide in the V-band. (a) 54GHz-63 GHz band and (b) 58GHz-60GHz band.	101
Figure 5.1 Schematic diagram of the proposed line-defect EBG slab waveguide coupler. (a) xyz plane: d is the thickness of the slab. (b) xy plane: the sizes of the lattice ring, waveguide ring and coupling ring are d_l , d_w and d_c respectively. The highlighted rectangle is the supercell used to calculate the dispersion relation.....	105
Figure 5.2 Dispersion of modes of single EBG line-defect waveguide.....	106
Figure 5.3 Dispersion of supermodes of the proposed EBG waveguide coupler.	106
Figure 5.4 (a) Electric and (b) magnetic field profiles for the super-modes.....	108
Figure 5.5 Dispersion relation of the proposed EBG coupler for different d_c values....	108
Figure 5.6 (a) Structure of the proposed EBG coupler. (b) Coupling region, where layered rings are spaced by $s = 2$ mm along y-direction.	109
Figure 5.7 S-parameters of the quasi-0-dB EBG forward-wave coupler.....	110
Figure 5.8 E-field distribution at 10.7 GHz for the quasi-0-dB EBG forward-wave coupler.	111
Figure 5.9 S-parameters of the quadrature forward-wave EBG coupler.	112
Figure 5.10 S21 and S41 of the quadrature EBG coupler.....	112
Figure 5.11 Amplitude difference between S21 and S41.	113
Figure 5.12 Phase difference between S21 and S41.	113
Figure 5.13 Phase difference between S21 and S41 in the coupling bandwidth 10.55-10.8 GHz.	114
Figure 5.14 E-field distribution at 10.7 GHz for the quadrature EBG coupler.	114
Figure 5.15 S-parameters of the through propagation.	115
Figure 5.16 E-field distribution at 10.7 GHz of the through propagation.	116
Figure 5.17 Structure of the quasi-0-dB EBG coupler with rotated channel rings'. (a) Rings are rotated by 90°. (b) Rings are rotated by 180°.	117
Figure 5.18 S-parameters of the quasi-0-dB coupler, with channel rings' rotated 90°... 117	117
Figure 5.19 S-parameters of the quasi-0-dB coupler, with channel rings' rotated 180°. 118	118

Figure 5.20 Structure of 3-dB forward-/backward- wave EBG coupler.....	119
Figure 5.21 S-parameters of the 3-dB forward-/backward- wave EBG coupler.	119
Figure 5.22 Amplitude difference between S31 and S41.	120
Figure 5.23 Phase difference between S31 and S41.	120
Figure 5.24 E-field distribution at 10.65 GHz of the 3-dB forward-/backward- wave EBG coupler.....	121
Figure 6.1 Reconfigurable coupler, to be implemented using the ON-OFF green and black segments.....	124

LIST OF ABBREVIATIONS

A _{DUT}	ABCD parameters of Device Under Test
A _{HALF}	ABCD parameters of half THRU CPW-slot line transition
$[A_{HALF}]^{-1}$	Inverse of A _{HALF}
$\overline{A_{HALF}}$	Symmetric conjugation of A _{HALF}
A _{MEAS}	ABCD parameters of Measured EBG waveguide
A _{THRU}	ABCD parameters of THRU CPW-slot-line transition
C-band	Frequency range from 4 to 8 GHz
CB-CPW	Conductor Backed Coplanar Waveguide
CPU	Central Processing Unit
CPW	Coplanar waveguide
1D	One-dimensional
2D	Two-dimensional
3D	Three-dimensional
dB	Decibel
dBi	Decibel relative to Isotropic
DBR	Distributed Bragg Reflection
DRIE	Deep Reactive Ion Etching
DUT	Device Under Test
EBG	Electromagnetic Band Gap
EC	Electromagnetic Crystal
E-field	Electric field
EM	ElectroMagnetic
E-plane	Electric plane
Eps-r:	Epsilon r

e.g	For example
etc	Etcetera
et.al	And others
FDTD	Finite Difference Time Domain
FEM	Finite Element Method
FTBR	Front to Back Ration
GaAs	Gallium Arsenide
GHz	Gigahertz
HFSS	High Frequency Structure Simulator
H-Field	Magnetic Field
H-plane	Magnetic plane
i.e	That is
In	Entrance
Ku-band	Frequency range from 12 to 18 GHz
LC	Inductor-Capacitor
MIS	Microstrip
MCM	Multi-Chip Modules
μm	Micrometer
mm	Millimeter
nm	Nanometer
ns	Nanosecond
Ω	Ohm
OSR	Open Square Ring
Out	Exit
Oz	Ounce
PBG	Photonic Band Gap

PC	Photonic Crystal
PC-DC	Photonic Crystal Directional Coupler
PCW	Photonic Crystal Waveguide
PEC	Perfect Electric Conductor
PMC	Perfect Magnetic Conductor
RDR	Reduced Defect Rings
RF	Radio Frequency
RGW	Ridge Gap Waveguide
RRR	Reduced Rows of Rings
RW	Rectangular Waveguide
$S_{i,j}$	Scattering parameter between the i^{th} port ($i = 1, 2, \dots$) and j^{th} port ($j = 1, 2, \dots$)
SEM	Scanning Electron Microscope
S_{DUT}	Scattering parameters of Device Under Test
SIW	Substrate Integrated Waveguide
SMA	SubMiniature version A
SOI	Silicon-on-Insulator
TE	Transverse Electric
TEBG	Triangular EBG
TEM	Transverse Electromagnetic
THz	Terahertz
TM	Transverse Magnetic
UC-PBG	Uniplanar Compact- Photonic Band Gap
V-band	Frequency range from 40 to 75 GHz
W-band	Frequency range from 75 to 110 GHz
X-band	Frequency range from 8 to 12 GHz

LIST OF SYMBOLS.

ϵ_r	Relative permittivity
a, A	Lattice constant of photonic crystal
r	Rod/hole radius
ω	Angular frequency
c	Speed of light in free space
Γ, X, M	Square lattice symmetry points
L_c	Coupling length
n_H	High refractive index
n_L	Low refractive index
r_c	Reduced rod radius
h	Rod Length
p	Probe length
H''	Magnetic field
r'	Position vector
k'	Wave vector
ξ	Periodic function
T'_i	Translation vector in i direction ($i = x, y$)
x'	Vector x
y'	Vector y
T	Lattice constant of ring structure in x and y directions
k	Wavenumber
D'	Reciprocal lattice vector
W	Metal width of ring
G	Gap size of ring
L	Outer ring size
H	Vertical spacing between stacked rings
T_i	Lattice constant of the ring structure in i direction ($i = x, y$)

λ	Wavelength
Ω_{LC}	Resonance frequency of OSR structure
C_{self}	Self capacitance
ϵ_0	Permitivity of free space
C_{mut}	Mutual capacitance
L_{mut}	Mutual inductance
L_{self}	Self inductance
μ_0	Permitivity of free space
A	Area enclosed by ring
d	Thickness of OSR slab
$\tan \delta$	Loss tangent
kT	Phase constant
f	Frequency
t	Thickness of dielectric slab above and below stack of rings
W_g	Coplanar slot width W_g
W_c	Coplanar central conductor width
W_s	Slot line width
$L \times W \times H$	Dimension of EBG-OSR waveguide
Z_0	Characteristic impedance
d_l	Size of lattice U-ring
d_w	Size of defect U-ring in channel
n_r	Number of rows in coupling region
d_c	Size of defect U-ring in coupling region

k_e	Wavenumber of even mode
k_o	Wavenumber of odd mode
Δk	Difference between k_e and k_o
κ	Coupling coefficient
s	Spacing between U-rings in coupling region

CHAPTER 1. INTRODUCTION

This chapter gives an introduction to electromagnetic band gap (EBG) structures, presents the motivation and objectives of the study of EBG comprised of open square rings (OSRs). Finally, it concludes with an outline of the thesis.

1.1 Introduction to Electromagnetic Band Gap

The rapidly growing field of radio communication is driving the development of novel structures that will enhance and advance the present microwave components (e.g., in terms of linearity, bandwidth, implementation, etc.). A significant amount of research has been recently undertaken in the area of artificial materials that entail periodicity as a key feature. Periodic structures are present in nature in the form of opal gemstones, bee hives (see Fig. 1.1), butterfly wings, etc. For example, opals consist of spheres of amorphous silica spheres of diameter ranging from 100 nm to over 1000 nm, arranged in a regular lattice with a periodicity that is in the range of visible light wavelength in all three dimensions. Scattering of visible light (reflection, diffraction, transmission) from the opals results in the colorful opals. In fact, the materials reflect certain wavelengths of light, because the structure presents a band gap. i.e., a spectral range that has high reflectivity and arises from the periodicity of the spatial spheres distribution in the crystal. These colors or wavelengths cannot pass through the material, and hence are reflected back, as a result of constructive reflections from the periodic arrangement of the cell elements. These properties have been the subject of intense research and investigation in the context of artificial periodic structures throughout a wide spectrum of electromagnetic waves (from optics to microwave and millimeter wave). The main motivation is the possibility of interesting applications of periodic structures. For instance, John Maddox comment's about artificial periodic structures is [1] : “If only it were possible to make dielectric materials in which electromagnetic waves cannot propagate at certain frequencies, all kinds of almost-magical things would be possible”. The following terminologies have often been used interchangeably to refer to the same type of structure : photonic crystal (PC) [2], photonic band gap (PBG), electromagnetic band gap (EBG), electromagnetic crystal (EC).

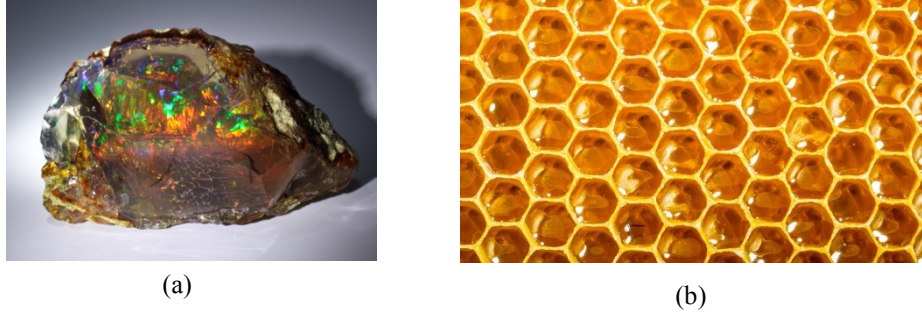


Figure 1.1 Naturally abundant periodic structures. (a) Opal stone. (b) Bee hives.

Electromagnetic bandgap (EBG) materials, primarily known as photonic crystals (PCs) or photonic bandgap (PBG) materials, exhibit stop-bands or band gap of frequencies for which electromagnetic waves are not allowed to propagate (evanescent waves), irrespective of the propagation direction in space [3]. These band gaps are separated by frequency pass bands where the wave propagates freely along the material. This characteristic is used in many applications for the suppression of spurious passbands at higher order harmonics and undesirable frequency bands [4]. The lattice size of EBGs is on the order of half wavelength of the propagating wave [5]. Furthermore, they can be designed for different frequency range simply by scaling their dimensions [2].

1.2 Motivation of The Thesis

In modern RF systems, high-performance microwave circuits with low fabrication complexity, steep rejection of interferers (i.e., spurious bands), and multi-functionality are widely needed. To meet these requirements, EBG structures have been recently proposed. Overall, two types of EBG are widely used to date (Fig. 1.2). The first conventional type consists of dielectric rods or cylindrical holes within a dielectric substrate [2,6-7] and the second is metallic pads (with/without grounding vias) [4,8-10] within a substrate. A high dielectric constant material must be used in all these designs. The via-based EBGs suffer from electric loss and fabrication complexity (i.e., non-planar fabrication process), while the dielectric rods and holes are structurally complicated and heavy. The main shortcoming of the latter operating at sub-mm and THz range [11-12] is that they are difficult to fabricate because of the high dielectric constant material required. The use of material of high

dielectric constant (ϵ_r of 12, 40, 90 etc.) yields an improved electromagnetic performance (wider fractional stopbands) and smaller physical dimensions.

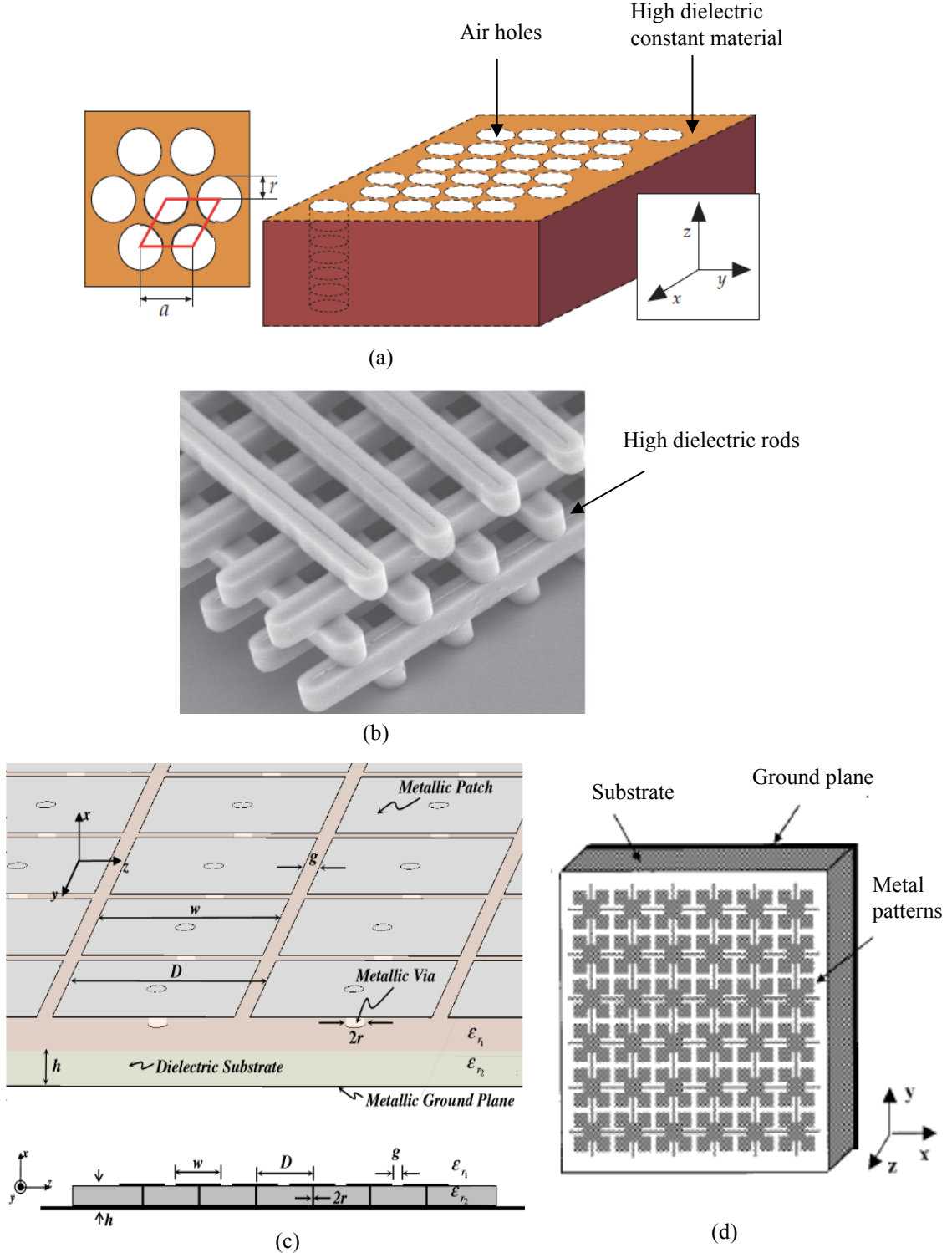


Figure 1.2 Conventional EBG structures. (a) Hole structure [2]. (b) Rod structure [2]. (c) Metallic pads with vias [9]. (d) Metallic pads without vias [10].

But the microfabrication process is more challenging because characteristic dimension decreases and manufacturing tolerances become tighter, while the dielectric materials tend to be more brittle [11]. A variety of fabrication techniques, such as dicing saw machining [13-14], wet etching [15], deep reactive ion etching (DRIE) [16-17], deep X-ray lithography [18-19] and laser micromachining [20], have been explored for fabrication of EBG components. Some of these methods are expensive, and require significant care. In addition, for certain dielectric materials, the range of these machining techniques is limited due to material characteristics, structure sizes and tight dimensional tolerances.

A novel EBG concept consisting of a multi-layer square lattice of metallic open square rings (OSRs) has been proposed recently [21] (Fig 1.3). This EBG structure does not suffer from the aforementioned fabrication process drawbacks. Moreover, it is of great interest due to its ease of fabrication, lighter weight, absence of via holes, less dependence on a given dielectric material (i.e., dual-band gap in dielectric material with low permittivity), adjustment of operation through judicious selection of structural parameters, and compatibility with planar circuits.

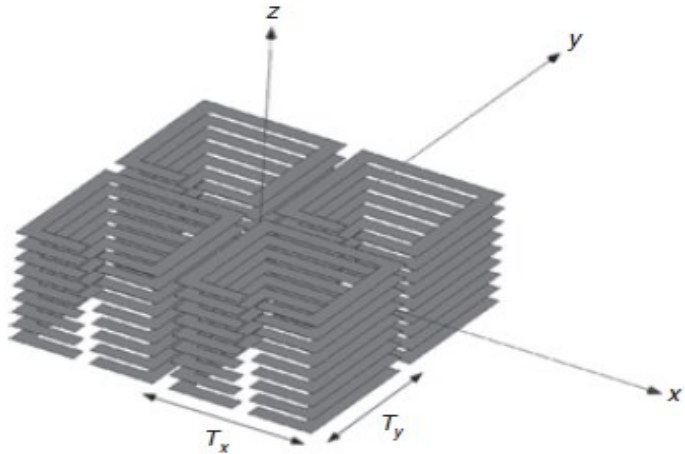


Figure 1.3 Metallic open square rings (OSRs) EBG structure [21].

The behavior of periodic stacked rings bears close resemblance to those of the two-dimensional periodic dielectric rods [2] (i.e., a stack of rings represents a rod). The lattice of open square rings can be viewed as a lattice of rods comprised of high permeability (associated with high confinement of magnetic field). In a 2D periodic structure, modes

can be either TM or TE polarizations. TE modes have the magnetic field normal to the plane of the periodicity and the electric field in the plane. TM modes, have the reverse: the electric field is normal to the plane of the periodicity while the magnetic field is in the plane. In the case of OSR structure, the modes are TE.

1.3 Thesis Objectives

The aim of this thesis is to demonstrate the various possibilities of the application of EBG-OSRs in the microwave band. This frequency band allows for convenient feature sizes and ease of fabrication, while still enabling relatively simple measurement techniques with available equipment. In that regard, a novel approach to the implementation of EBG structures is pursued. Specifically, the thesis objectives are as follows:

- 1) Study the EBG dispersion characteristics as a function of designable parameters.
Dispersion characteristic of EBG with infinite and finite thickness will be calculated.
- 2) Develop novel line defect-based EBG-OSR waveguides and verify experimentally the simulated results.
- 3) Apply the new EBG-OSR waveguides to microwave circuits such as couplers and power splitters and multifunctional variants of these.

1.4 Thesis Organization

This thesis is organized into six chapters. Chapter two is devoted to the state of the art of the work previously reported in the EBG field. A historical background of EBG is provided. Then, some previous related research contributions are reviewed.

Chapter three covers in detail the proposed novel OSR EBG structure. EBGs with air and dielectric host material are considered. Parametric studies are performed to demonstrate dependence of dispersion characteristics on the structural parameters. Then, a study of OSR EBG slabs is presented. The thorough study of guiding mechanisms by embedding a 1D defect in the regular OSR lattice is undertaken subsequently. Various techniques are presented for the design of OSR-based EBG slab waveguides. The performance of the U-ring structure at microwave frequencies is considered next.

Chapter four focuses on the implementation and experimental characterization of slab waveguides in air (foam) and dielectric material, based on the design of the slab structures presented in chapter three. A set of waveguides are designed for operation in the 13.5-16.5 GHz bands. Specifically, compact and simple CPW feeding structures are designed and integrated into the waveguides. Challenges of physical realization are identified and methods to overcome them are proposed and verified experimentally by new waveguides that operate in the 8-12 GHz band.

Chapter five presents the design of novel directional couplers based on EBG waveguide by setting linear defects in close proximity and introducing an isolated coupling region.

Finally, Chapter six presents a summary of the work and the research contributions, and discusses avenues for future open ring EBG structure research.

CHAPTER 2. STATE OF THE ART OF EBG STRUCTURES

2.1 Introduction

Electromagnetic bandgap (EBG) materials are periodic structures in which electromagnetic (EM) waves are forbidden in certain frequency bands. The similarity of EM wave propagation in periodic lattice structures to electron wave propagation in crystals is a strong motivation to explore novel EBG structures inspired by their electronic bandgap counterparts. In the latter, there are allowed energy bands that electrons can occupy, and forbidden bands that cannot be occupied. In EBGs, the forbidden bands pertain to energy levels that photons are not permitted to occupy. EBGs were reported for the first time in 1987 by E. Yablonovitch [22]. Such structures have been built to operate at microwave and the far-infrared frequency bands. However, there have been challenges to fabricate PBG structures with bandgaps in the optical frequency band. Unique features of a frequency band gap can be used to control propagation of EM waves. For instance, a defect (i.e., which is a perturbation in the periodicity of the structure) can be created to cause localization of energy inside the defect region [2, 23] to allow propagation of EM waves within that same region. The energy is confined to the defect region if the operating frequency happens to be in the band gap of the crystal. The introduction of line defects into the structure creates a channel waveguide and the introduction of a point defect generates a resonant cavity. The ability to confine and guide EM energy can be used in applications at microwave and millimeter-wave frequencies for antennas [24-26], waveguides [27-28], and filters [29].

EBGs can be realized using metallic or dielectric elements arranged in one-dimensional (1D), two-dimensional (2D) (Fig. 1.2 (a,c,d)) or three-dimensional (3D) (Fig. 1.2 (b)) periodic lattices; which may be implemented in two common configurations, namely, the perforated and metallo-dielectric. The former consists of drilling periodic holes in the dielectric [2,7] (Fig. 1.2 (a)), while the latter consists of etching gaps in the metal of the

dielectric slab [8-10, 30-31] (Fig.1.2 (c-d)), or the signal line [32]. Various examples of EBGs are presented below.

2.2 General EBG Structures

The first three-dimensional electromagnetic band gap (EBG) structure that was manufactured in 1991 by Yablonovitch *et al.* [33] consisted of three sets of holes that are drilled into a dielectric slab at angles of 35.26° from the z-axis and 120° , relative to each other as shown in Fig. 2.1. It exhibited a full 3D bandgap, preventing incident microwave from propagating in any direction. However, the structure has proved to be too difficult to manufacture (to drill uniform holes with appreciable depth with micron diameters) for operation at optical frequencies and innovative design that are more amenable to simple fabrication methods had to be devised.

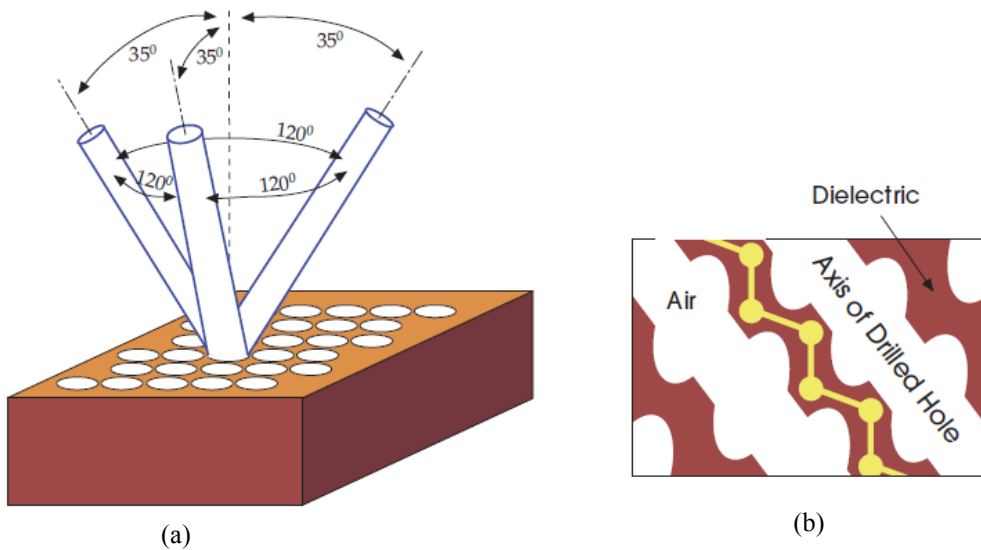


Figure 2.1 (a) First EBG structure fabricated by drilling holes at 35.26° to normal and 120° to each other. (b) Cross section [2, 33].

A successful 3D structure that offered a complete band gap is the layer-by-layer woodpile photonic crystal [34] (Fig. 2.2). It was constructed by stacking one-dimensional (1D) rods with a center to center separation of a . The rods are turned by 90° in each consecutive layer. At any reference layer, the rods of every second nearby layer are parallel to the reference layer but moved by a distance of $0.5a$ perpendicular to the rod axes. This results in stacking order along the z axis that repeats every four layers. The layered structure was fabricated

using alumina rods with dielectric constant $\epsilon_r = 9.6$. Silicon micromachining techniques have been used to scale down the size of the structure and make it operational up to 500 GHz. Laser rapid prototyping has been used to fabricate woodpile structures that can operate as high as 2 THz [35]. The work in [36-40] has demonstrated the layer-by-layer woodpile structure at 30 and 200 THz frequency ranges.

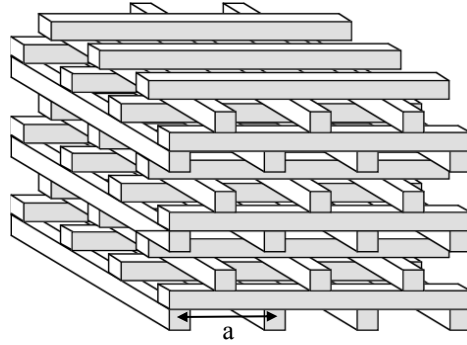


Figure 2.2 The layer-by-layer structure [34].

As discussed above, 3D EBG structures are technologically challenging. A photonic crystal that can be fabricated using simpler fabrication techniques is desirable, not only for cost reasons but also for compatibility to conventional microwave technologies. For instance, planar EBGs are built similar to microwave integrated circuits on flat substrate. Planar EBG structures consist of uniformly distributed periodic metallic patterns on one side of a dielectric slab. They exhibit interesting features such as distinctive passbands and stopbands, low attenuation in the passbands and suppression of surface waves when serving as the ground of planar microstrip circuit.

In 1993, Brown *et al.* addressed building a planar antenna on photonic crystal substrate [24]. The paper presented for the first time the idea of using PBG structures in the microwave and millimeter wave bands. The interest was stated in three applications which are (1) planar antennas, (2) delay lines, and (3) nonreciprocal devices. Signal propagation and control are the common feature of these applications. The photonic crystal is appropriate for these applications because of its capability to guide and control electromagnetic wave propagation within the band gap frequency range. Fabrication of

microwave and mm-wave photonic crystal is simpler as a result of larger lattice constant as compared to similar structures that operate in optical frequency band.

The structure shown in Fig. 2.3 has been suggested in [24] as an example of the use of EBG technology in the field of planar antennas. It consists of a dipole antenna, fed by coplanar stripline that was fabricated on the top surface of a photonic crystal composed of holes at different orientations in semi-insulating GaAs substrate. When operated at a frequency within the band gap, the antenna radiates mainly into the air rather than the substrate. This is in contrast to the case when the antenna is etched on a solid non-perforated semiconductor substrate for which bulk of the power is trapped into the substrate and only a small portion (2%) of power contributes to radiation into the air region.

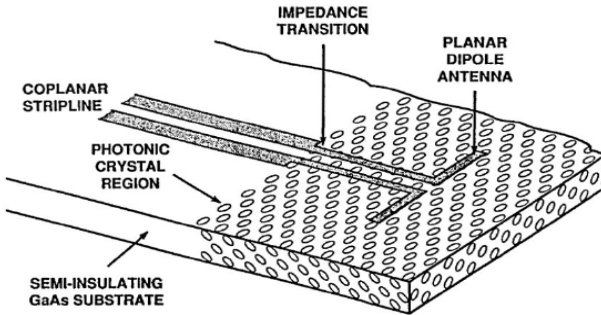


Figure 2.3 Proposed planar dipole antenna lying over the photonic-crystal region of a semi-insulating GaAs substrate [24].

A layer-by-layer structure for metallic photonic crystal was developed in [41]. The structure was built by stacking three layers of square metallic grids aligned to each other and separated by a dielectric as shown in Fig. 2.4. The transmission characteristic of this structure exhibited a band gap extending from zero frequency up to a cutoff frequency, showing a high-pass response. A change in the periodicity of the center grid layer created a defect mode in the band gap, forming a bandpass characteristic. The size of the defect determined the location of the defect mode frequency in the band gap. Structures were designed to operate in the W-band millimeter-wave region [41]. A structure with a cutoff near 160 GHz had a lattice constant a of 0.544 mm with metal lines 0.1 mm wide, using 20 mil Duroid with 1 oz copper (36 μ m thick). A defect in the second layer with radius of $0.4a$ results in a peak in the transmission at 111 GHz, while a defect radius of $0.2a$ gives a peak at 92 GHz. As the defect radius decreases, the defect mode shifts to lower frequency.

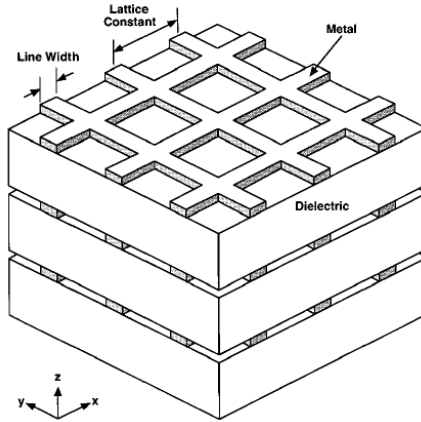


Figure 2.4 First layer-by-layer metallic EBG structure [41].

In 1997, Qian *et al.* reported the first comprehensive investigation of synthesized dielectric materials which possess distinctive stopbands for microstrip lines [7]. They performed the first full-wave, comprehensive study of a category of EBG structures which are suitable for microstrip-based circuits and antennas. Four types of these EBG structures had been simulated using FDTD. Fig. 2.5 shows the four types of EBG structures. The EBG holes were drilled through the dielectric substrate.

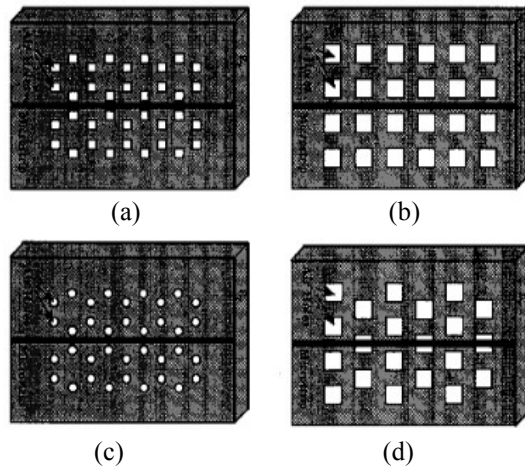


Figure 2.5 Several EBG structures for microstrip circuits : (a) Honeycomb-lattice square-hole. (b) Square-lattice square hole. (c) Honeycomb-lattice circular-hole. (d) triangular-lattice square-hole [7].

In 1998, Radisic *et al.* proposed a two-dimensional (2D) EBG structure for microstrip lines [30], in which a periodic 2D pattern consisting of circles was etched in the ground plane of microstrip line. No drilling through the substrate was required. Three circuits were

fabricated with different circle radii, and measurement showed wider stopbands. Fig. 2.6 shows the proposed (2D) EBG structure.

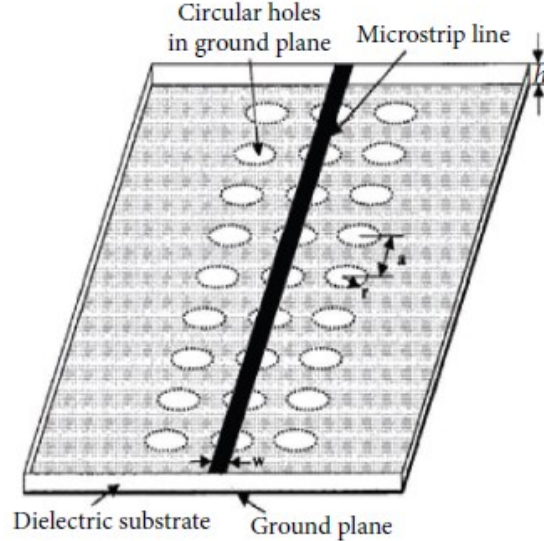


Figure 2.6 Three-dimensional view of a proposed EBG structure. The square lattice circles are etched in the ground plane of a microstrip line [30].

In 1999, two different well-known EBG structures were presented: The grounded metallic plates (mushroom) structure published by Yablonovitch *et al.* [8], and the Uniplanar Compact- Photonic Bandgap (UC-PBG) structure published by Itoh *et al.* [4]. The first structure is the high impedance electromagnetic surface [8], known by the mushroom structure, shown in Fig. 2.7. It consists of an array of metal plates connected to ground with vias, that prevents wave propagation within a forbidden frequency bandgap while allowing efficient radiation into the surrounding space. The structure also reflects electromagnetic waves with no phase reversal within a given frequency band, henceforth the resemblance to an artificial magnetic conductor within that same band. Using high-impedance ground plane, antennas have been demonstrated that take advantage of both the suppression of surface waves, and the unusual reflection phase. An antenna on a high-impedance ground plane produces a smoother radiation profile than a similar antenna on a conventional metal ground plane, with less power wasted in the backward direction. Furthermore, radiating elements can lie directly adjacent to the high-impedance surface without being shorted out.

This EBG, although is very effective, it is associated with fabrication complexity due to the vertical via placement.

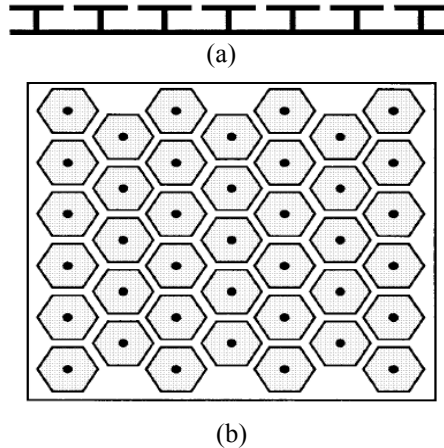


Figure 2.7 (a) Cross section of a high-impedance surface, fabricated as a printed circuit board: The structure consists of a lattice of metal plates, connected to a solid metal sheet by vertical conducting vias. (b) Top view of the high-impedance surface, showing a triangular lattice of hexagonal metal plates [8].

The UC-PBG structure (Fig. 2.8) is a 2D photonic band gap (PBG) structure for microwave integrated circuits. It consists of a 2D periodic square lattice with each element comprising a metal pad etched in the ground plane connected by narrow lines to form a distributed LC network. Via holes or multilayer substrates are not required in this novel PBG structure. However, the structure is limited to TEM mode applications.

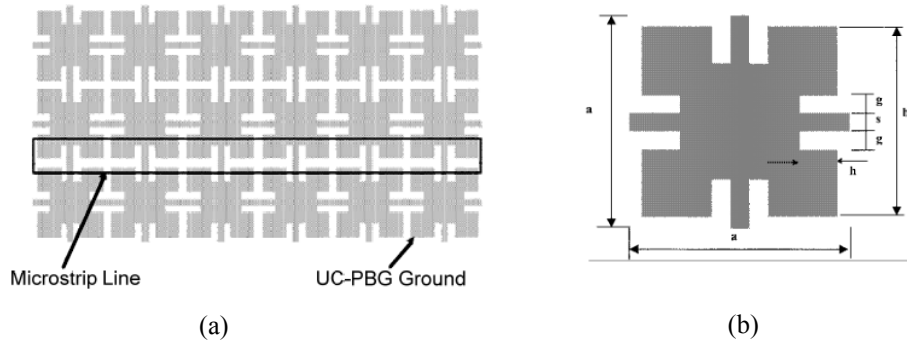


Figure 2.8 (a) Schematic of UC-PBG metallic pattern on a dielectric substrate. (b) Unit cell of the UC-PBG structure [4].

Several application examples had been demonstrated, including a non-leaky conductor-backed coplanar waveguide (CB-CPW), a compact spurious-free bandpass filter and TEM waveguide.

The conventional CPW is usually backed with another ground plane to improve mechanical strength, permit implementation of mixed CPW-microstrip circuits, or provide a heat sink [42]. Nonetheless, the conductor-backed CPW (CB-CPW) will excite the parallel-plate mode, that degrade CPW performance. Fig. 2.9 shows the schematic of a conventional CB-CPW. A parallel-plate waveguide will be formed between top and bottom ground planes. The power will leak at an angle from the slot axis once the wave is launched. This leakage is significant even at low frequencies, which will cause serious problems, such as crosstalk and undesirable coupling to neighboring lines. The wide stopband of a UC-PBG structure can be used to suppress the propagation of this parallel-plate mode. The UC-PBG can be easily etched in the top ground plane of a CB-CPW circuit.

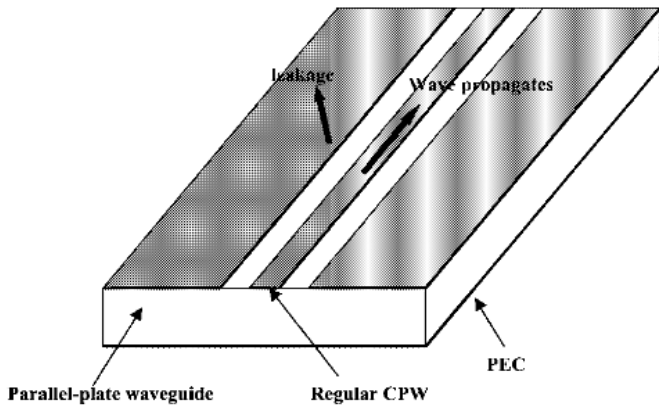


Figure 2.9 The structure of a conventional CB-CPW [4].

Another application of EBG structure is in the field of radiating elements and antennas. It is well known that best performance patch antennas are built on low permittivity substrates, to avoid surface waves that are usually excited on high dielectric constant. The stopband provided by the UC-PBG structure can be employed to reduce surface-wave losses of patch antennas on high permittivity substrates. It was shown [10] that excitation of surface waves was strongly reduced in the E-plane.

Rectangular waveguides with uniform field distributions are of great interest for applications in quasi-optical power combining. A TEM-waveguide can be realized by placing PMC on the two sidewalls of a waveguide, creating a magnetic boundary condition to suppress the parallel-plate mode. The UC-PBG structure has already been demonstrated to behave like a perfect magnetic conductor (PMC) within its stopband [43], and therefore can be applied to build a TEM waveguide [44].

Fig. 2.10 shows a two-dimensional (2D) photonic crystal composed of a square array of periodic dielectric rods in air, with lattice constant a . As is well known [2], this type of crystal can possess a photonic band gap for TM-modes, where the magnetic field is in the plane (xy) and electric field is parallel to the rods ($E//z$). The frequency band structure for a crystal of rods with $\epsilon_r = 8.9$ and radius $r = 0.2a$ is plotted in Fig. 2.11. Both TE and TM band structures are shown. The horizontal axis is the value of the in-plane wave vector along the triangular edge of the irreducible Brillouin zone, from Γ to X to M, as shown in the inset of the figure.

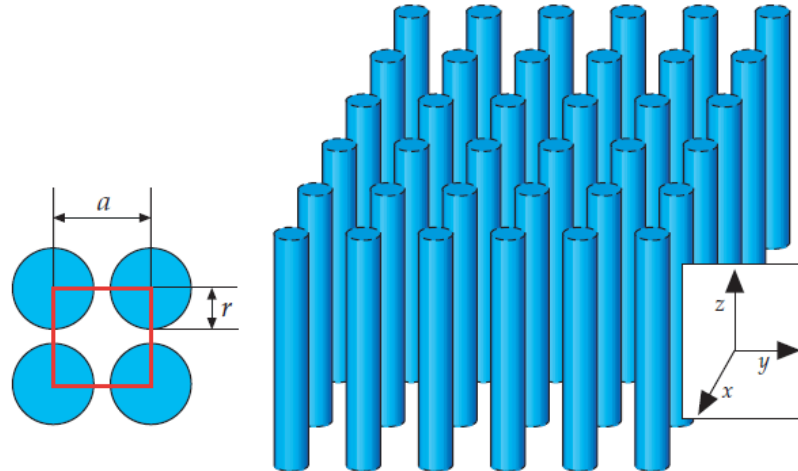


Figure 2.10 Two-dimensional photonic crystal. This structure is a square lattice of dielectric rods with radius r and dielectric constant ϵ_r . It is periodic along x and y directions with lattice constant a , and homogeneous along z. The left inset is a top view of the square lattice, with unit cell shown in red [2].

There is a large complete band gap between the first and second TM modes. However, there is no complete band gap for TE modes. The field profiles of the TM modes of the first and second bands at X point are shown in Fig. 2.12.

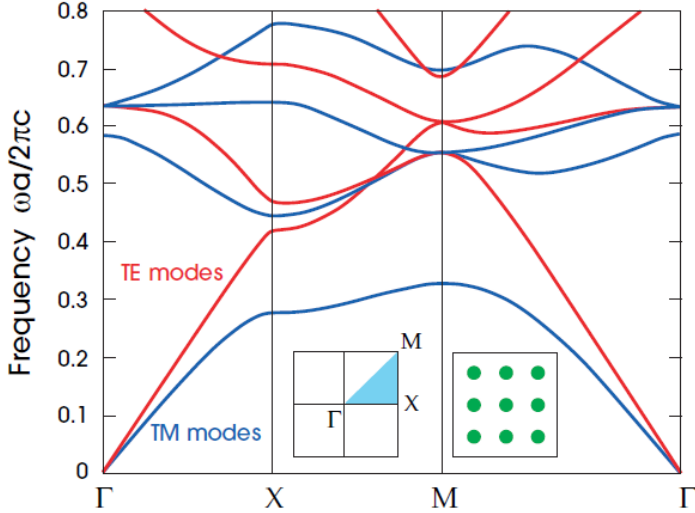


Figure 2.11 Band structure for a square array of dielectric rods with $r = 0.2a$ and $\epsilon_r = 8.9$ embedded in air. The left inset is the Brillouin zone, with the irreducible zone shaded blue. The frequency is expressed as dimensionless ratio $\omega a/2\pi c$ [2].

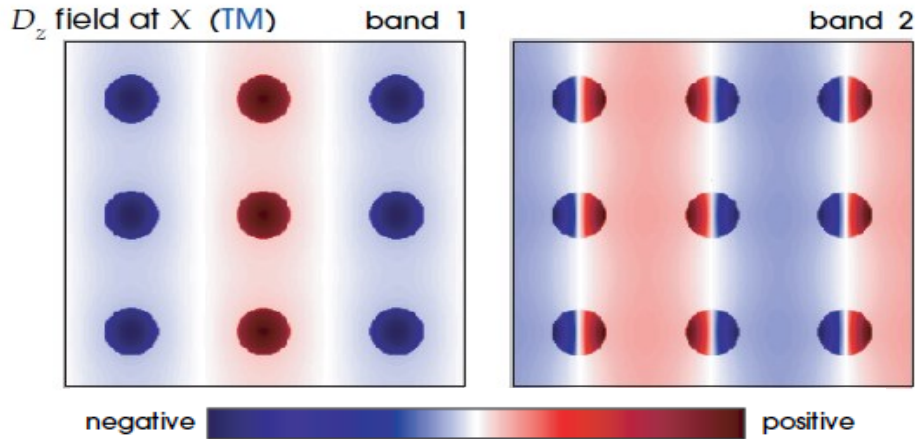


Figure 2.12 Displacement fields of TM states inside a square array of dielectric rods in air of Fig. 2.10. Modes are shown at the Γ point [2].

The field related to the lowest TM mode (the dielectric band) is strongly concentrated in the dielectric region. This is in contrast to the field pattern of the air band. There is a nodal plane cuts through the dielectric rods, displacing some of the field from the high- ϵ region. A mode concentrates most of its electric- field energy in the high ϵ_r regions in order to lower its frequency and upper bands must be orthogonal to lower bands [2]. This statement explains the splitting between the two bands. The first band has most of its energy confined in the dielectric region to maintain a low frequency while the second band shows a nodal

plane in order to be orthogonal to the first band, and has most of its energy in the air region (low ϵ_r region) that corresponds to a higher operating frequency.

EBGs composed of dielectric rods demonstrate better electromagnetic performance with higher permittivity ϵ_r dielectric but micro-manufacturing requirements tend to be more demanding, as the characteristic dimension is small and fabrication tolerances decrease with increasing ϵ_r .

It should also be noted that metamaterials [45] and substrate integrated waveguide (SIW) [46] have been used in conjunction with EBG concepts.

2.3 Defects For EBG Structures

As mentioned above, a defect in an electromagnetic band-gap (EBG) material can support a localized mode when the mode frequency falls inside the bandgap. An EBG waveguide can be created by introducing a linear defect in the periodic lattice of the EBG crystal structure [27]. A linear defect in an EBG crystal can be created for example by changing the geometry or removing one row of the structure. Based on these approaches, different components such as bends [47], power splitters [48-49], directional couplers [50-52], switches [53-54] and waveguides [50-55] have been designed. Defects in the EBG can also be used to achieve directive patterns of an antenna [56].

2.3.1 Special Structures Such as Couplers, Switches, Waveguides And Antennas

Fig. 2.13 shows a photonic crystal directional coupler (PC-DC) constituted of straight and 60° bend waveguides [50]. Fig. 2.13(a) shows an optical microscope image and Fig. 2.13(b) shows a scanning electron microscope (SEM) image for the PC-DC waveguide. The SEM image corresponds to the center part of the upper image. The two adjacent straight waveguides are separated by three rows of air holes, which form a coupling region of length L_c . The cleaved end of the single-line-defect waveguide is given in Fig. 2.13(c). The PC-DC had a triangular lattice pattern of air holes formed in a 2D dielectric slab (e.g., GaAs). Each waveguide was formed simply by removing a single row of air holes. The lattice constant and hole diameter were set at 345 nm and 220 nm , respectively. The entire length ($\sim 1\text{ mm}$) of the PC waveguides was determined by cleaving both ends of the waveguides.

The experimental transmission of the coupler was affected by imperfect fabrication in hole shapes or positions and bending efficiency.

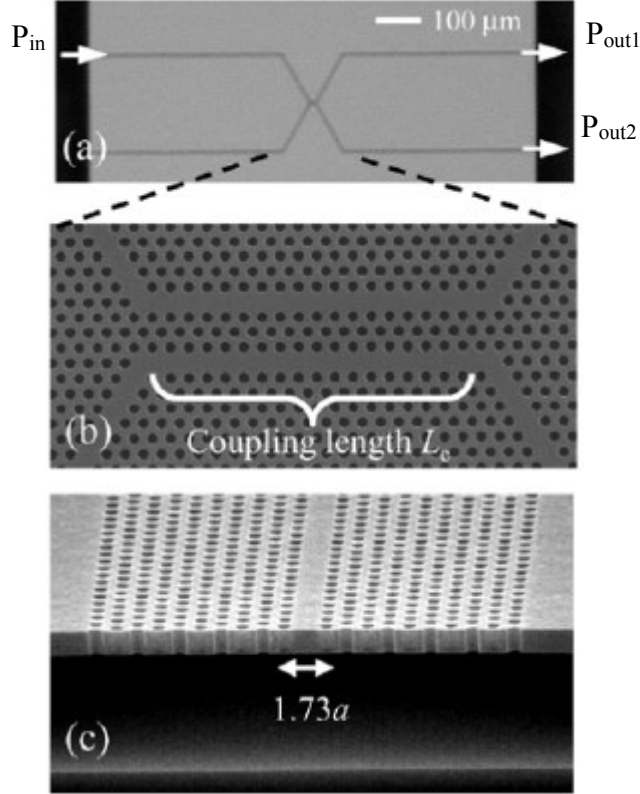


Figure 2.13 (a) Optical microscope image. (b) SEM image for a fabricated directional Coupler structure combined with the bent waveguide. Each waveguide contains four 60° bends (total is eight). (c) The cleaved end of the single-line-defect waveguide. L_c is the coupling length and a is the lattice constant [50].

Thorhauge *et al.* [52] demonstrated highly efficient and broadband coupling in photonic crystal directional couplers for TE polarized light. The PC structures were designed as a triangular pattern of holes with radius of 0.365Λ in a silicon-on-insulator (SOI) material, where Λ being the lattice constant. The PC waveguides (PCWs) were created as line defects by removing rows of holes. The fabricated structures have coupling regions that consist of two PCWs placed next to each other, separated by a single row of coupling holes, as shown in Fig. 2.14. The length of the coupling region is 27Λ , and the radius of the coupling holes is 0.23Λ . Coupling of light takes place from the direct channel to the coupled channel and is the result of beating between an even and an odd super-mode for the two channels. The energy in any one channel is given as a superposition of the two super-modes. When

complete destructive interference arises, a positive and a negative lobe coincide and no energy is present. However, energy is present whenever the superposition does not lead to complete destructive interference. Two versions of the coupler were realized: a type I, with the direct channel bent away from the coupled channel by use of two consecutive 60° bends that are separated by a 30Λ intermediate PCW section, as shown in Fig. 2.14 (a), and a type II, with the coupled channel bent away as shown in Fig. 2.14(b). Each 60° bend was optimized by displacing one hole in the bend. The fabricated photonic crystal waveguide couplers exhibit very high, broadband, and spectrally flat coupling, which lies at approximately -1.3 ± 0.3 dB from 1450 to 1490 nm for TE polarized light.

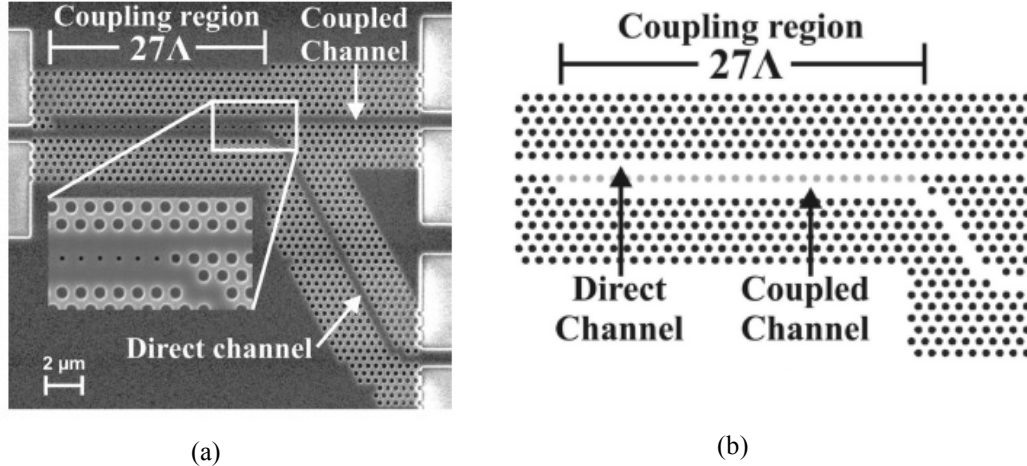


Figure 2.14 (a) SEM of the fabricated coupler with a straight-coupled channel (type I). The fabricated coupler has a larger separation between the two output channels compared with the modeled coupler. (b) Modeled coupler with a straight-direct channel (type II) [52].

Fig. 2.15 shows a photonic crystal (PC) directional coupler used as a switching structure [53]. It consists of a two-dimensional (2D) hexagonal pattern of high refractive-index rods ($n_H = 3.46$) with radius $r = 0.2a$, a being the lattice constant, embedded in a low refractive index material ($n_L = 1.45$). The directional coupler is created by removing two parallel rows of rods in the ΓK direction that act as waveguides and are separated by a single row of defects with a reduced radius $r_c = 0.7r$. Optical switching is achieved by modifying the refractive index of row of rods between both waveguides by means of an optical control signal (Fig. 2.16 (c)) that is confined in the central region. Thus the state of the directional coupler may be inverted from the cross to the bar state or vice versa (Fig. 16 (a-b)).

Therefore, the central row of rods that separates the waveguides in the coupling region behaves as another waveguide and it is used to direct the control signal of the switch. Small length (around *1.1 mm*) and low optical power consumption (over *1.5 Watts*) were the main features estimated for this switching structure.

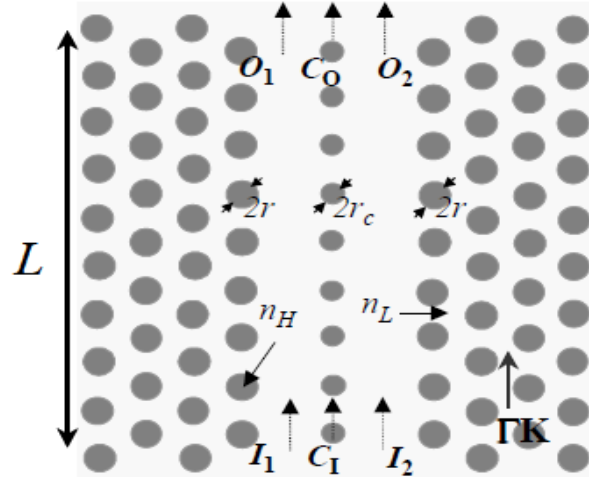


Figure 2.15 Schematic of PC directional coupler used as switching structure [53].

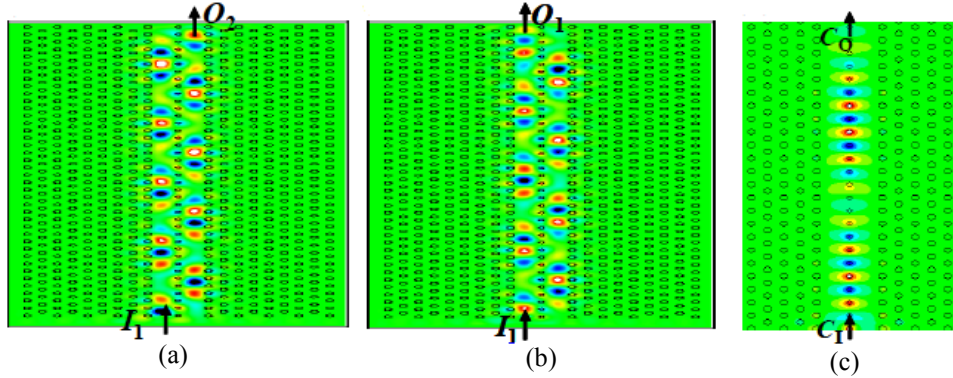


Figure 2.16 Electric field distribution inside the coupler. (a) Cross state. (b) Bar state. (c) Control signal used to tune the switch [53].

A square lattice of holes has been used to design the EBG waveguide [55] for TM mode (magnetic field parallel to the substrate surface and perpendicular to the holes), and the perturbation to realize linear defect has been implemented by removing one row of air holes in the EBG substrate (Fig. 2.17). A microstrip-to-waveguide tapered transition was employed in order to excite the EBG waveguide. An EBG waveguide of *49.1 mm* (equivalent to 19 EBG cells) was designed and fabricated. The simulation results showed

better than 10 dB return loss performance from 27 GHz to 31.5 GHz with insertion loss of better than 2.5 dB over the same bandwidth, and also high isolation in the range of 20 dB with an adjacent EBG waveguide.

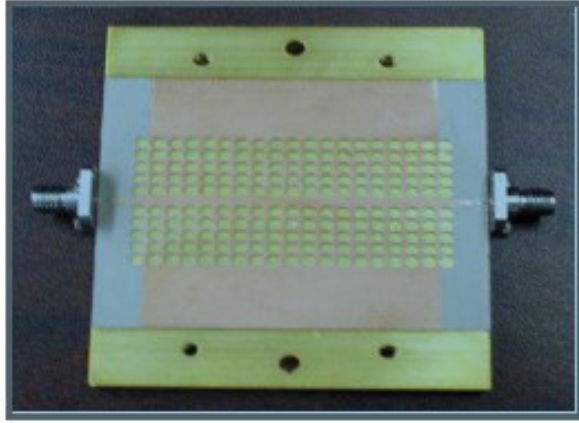


Figure 2.17 EBG waveguide for TM mode [55].

In [56], a two-dimensional triangular lattice EBG (TEBG) antenna (Fig. 2.18) was realized with dielectric rods of length $h = 20 \text{ mm}$, radius $r = 1.5 \text{ mm}$, and $\epsilon_r = 37$ arranged in a triangular lattice with $a = 13 \text{ mm}$. Excitation was done through a quarter-wavelength probe of length $p = 7.2 \text{ mm}$, which excite TM modes. The triangular lattice geometry (Fig. 2.18 (inset)) composed of infinite long dielectric rods presented a complete band-gap for TM polarized waves. An angular defect window was created in the TEBG structure by removing two rods from the first layer, three rods from second layer, and so on, as shown in the figure. Measurement results showed that the antenna was very directive in the H-plane, in frequencies within the band gap, reaching a peak gain of 12 dBi in the same angular direction as the defect and front back-to-back ration (FTBR) of 34 dB. Outside the band-gap, the antenna lost directivity; the radiation pattern was very uniform in all directions.

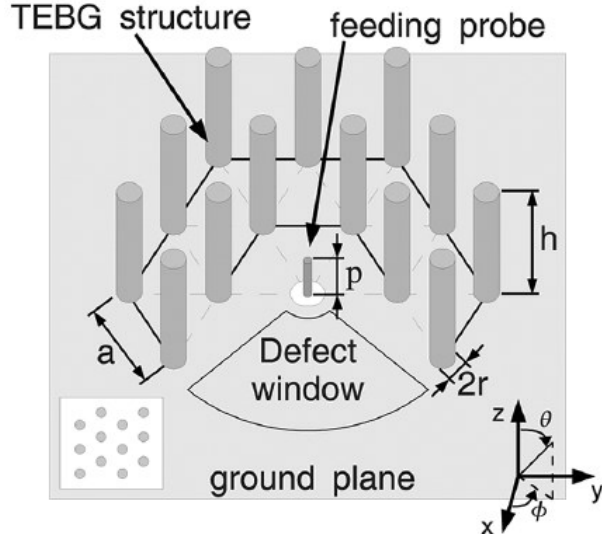


Figure 2.18 TEBG antenna geometry and (inset) triangular lattice of circular dielectric rods [56].

The conventional EBG structures presented above are capable in efficient guiding and controlling of the propagation of electromagnetic wave but they suffer from the requirement of high permittivity dielectric material in their construction, or presence of vias that are associated with fabrication complexities at high frequencies. This paves the way for the introduction of a novel EBG structure that is based on open square rings immersed in a dielectric material which is the subject of this thesis.

2.4 A Brief Discussion of EBG Structure Used in Thesis

As mentioned in Section 1.2, Shaker and Chaharmir [21] introduced a novel EBG structure composed of open square rings. The rings are placed in a regular lattice along the axis normal to the plane of rings to construct quasi-rods, which are then set in a regular 2D lattice to obtain the EBG structure as shown in Fig. 1.3. This structure presents a potential alternative as compared to the conventional PBG composed of dielectric rods. The structure had not been thoroughly investigated. It is the purpose of this thesis to study this structure.

2.5 Chapter Summary

This chapter reviewed several EBG based structures employed in microwave and optical applications. It was seen that all of the designs presented interesting, enhanced performance

characteristics at the expense of complicated fabrication techniques (use of rods, vertical vias, unrealizable permittivity contrasts, drilling through the substrate) and/or limited applications (TEM based only), etc. The OSR EBG structure, however, was seen to not suffer from these drawbacks and in fact has potentially very attractive performance warranting further investigation.

CHAPTER 3. STUDY OF ELECTROMAGNETIC BANDGAP COMPOSED OF METALLIC OPEN SQUARE RINGS

3.1 Introduction

In addition to the structures described in Chapter 2, there has been considerable interest in a defining feature of an EBG structure, i.e., the frequency band gap in which all propagating EM waves of a given polarization are prohibited. This phenomenon can be employed to enhance the efficiency of antennas or realize broadband and frequency selective components.

This chapter deals with the implementation of electromagnetic band gap (EBG) structures comprised of open square rings (OSRs). As mentioned earlier, the behavior of periodic stacked rings bears close resemblance to that of two-dimensional periodic dielectric rods [2], in that a stack of rings represents the magnetic dual of a dielectric rod. The lattice of open square rings can therefore be viewed as a lattice of rods comprised of high permeability, associated with strong confinement of magnetic field within the stack of OSR's. Advantageous features of this crystal structure are ease of fabrication (no vias), less dependence on dielectric material (i.e. wider band gap for dielectric material with low permittivity), low cost, flexible adjustment of operation through judicious selection of structural parameters, and compatibility with planar microwave circuits.

This chapter is organized as follows: Section 3.2 investigates the concept of infinite free standing OSR. Numerical modeling and analysis of the periodic ring lattice are presented. Then, the impact of geometrical parameters on the band gap and dispersion characteristics of the EBG are examined. Section 3.3 considers finite EBG slab structure composed of OSR where the computational method is discussed followed by the presentation of band structure for different slab thicknesses. Section 3.4 is devoted to the study of EBG line defect waveguide, formed within the EBG slab. Dispersion diagrams and eigen-field distributions are computed and analyzed. Section 3.5 presents infinite OSR structure immersed in dielectric medium. Section 3.6 is focused on the study of EBG slab supported

by dielectric material. Subsequently, section 3.7 addresses EBG waveguide in selected dielectric media while section 3.8 examines the operation of OSR at different frequency bands. Finally, conclusions are drawn in Section 3.9 of this chapter. Some material of this chapter can be found in [57-58]

3.2 Infinite Open Square Rings in Free Space

3.2.1 Computational Method

The analysis of EBGs is based on the Bloch-Floquet [59] theorem that describes the theory of wave propagation in infinite periodic structures. According to the theorem, the fields in a two-dimensional periodic structure can be expressed in Bloch state:

$$H''(r') = e^{jk' \cdot r'} \xi(r') \quad (3.1)$$

where $H''(r')$ is the magnetic field, k' is the wave vector, r' is the position vector and $\xi(r')$ is a periodic function.

$$\xi(r' + pT'_x + qT'_y) = \xi(r') \quad (3.2)$$

for all integers p and q .

$T'_x = Tx'$ and $T'_y = Ty'$ are translation vectors in X and Y directions, respectively and T is the lattice constant. This means that the components of electromagnetic waves for any translation $pT'_x + qT'_y$ differ only in phase.

$$H''(r' + pT'_x + qT'_y) = e^{jk'(pT'_x + qT'_y)} H''(r') \quad (3.3)$$

wavenumber, k , is dependent on frequency among other parameters. Dispersion characteristic is also periodic, as described by

$\omega(k') = \omega(k' + D')$ where $D' = \frac{2m\pi}{T}x' + \frac{2m\pi}{T}y'$ is known as the reciprocal lattice vector and m is an integer number. Therefore, one needs dispersion characteristic for k in the range $[-\pi/T, \pi/T]$, namely Brillouin zone in order to construct the full dispersion behavior of the EBG. The first Brillouin zone for a 2D periodic structure with square lattice is depicted in Fig. 3.1. Exploiting symmetries of a square lattice allows reduction of the Brillouin zone to an irreducible triangular area as outlined in red in Fig. 3.1. Computing the dispersion

diagram entails calculation of the eigen-frequencies of eigenmodes along the edges of this triangle.

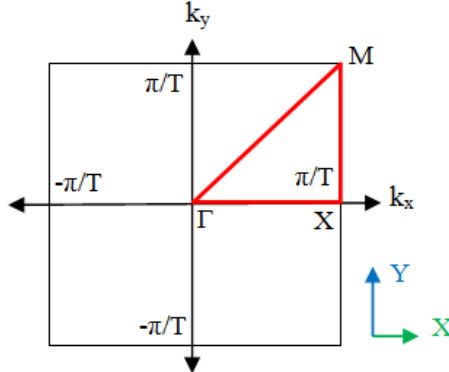


Figure 3.1 The first Brillouin zone for a 2D square lattice. Parameters k_x , k_y are the x and y components of the wave vector k' , respectively, and T is the lattice period in X and Y directions.

The numerical simulations have been performed using the eigenmode solver of the commercial full-wave software Ansys High Frequency Structure Simulator (HFSS™) [60], which is based on the finite element method (FEM). In order to simulate the stacked ring EBG structure, only one unit cell is modeled and the periodic nature of the structure was captured by imposing appropriate periodic boundary conditions. The schematic of the periodic stacked OSRs arrays and the geometry of the unit cell are shown in Fig. 3.2. The structure is infinite in all directions X, Y, and Z, and suspended in air. The unit cell consists of an open square ring, encapsulated by an air box. The former is assigned a perfect electric conductor (PEC) boundary condition, while the surrounding surfaces of the latter are assigned master/slave (i.e., to establish periodicity in the X, Y directions) boundaries at the sidewalls and perfect magnetic conductor (PMC) at the top and bottom wall to establish periodicity in the Z direction and restrict the modes to TE modes (E-field parallel to the plane of rings).

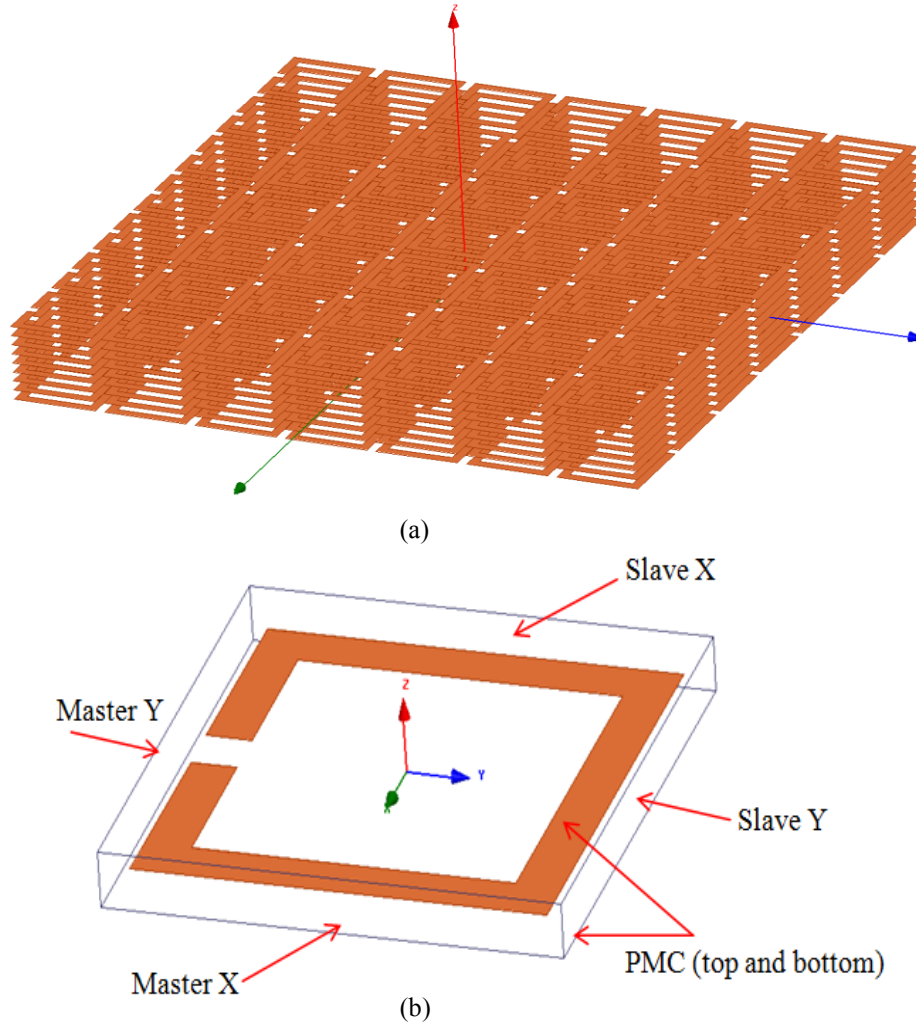


Figure 3.2 (a) Schematic of the stacked OSRs arrays. (b) Unit cell setup and applied boundary conditions.

3.2.2 Parametric Study

To gain a better understanding of the modal behavior of the periodic ring lattice, a parametric analysis is performed by changing one geometrical parameter at a time while keeping the other parameters constant. The impact of geometrical parameters such as gap size, lattice constant, ring outer size, metal width and vertical spacing and their effect on the band gap and dispersion characteristics of the EBG are investigated. A schematic drawing of the unit cell along with nominal values for geometrical parameters is given in Fig. 3.3. Nominal parameters [21] are as follows: metal width $W = 0.5 \text{ mm}$, gap size $G = 0.5 \text{ mm}$, outer ring size $L = 4.5 \text{ mm}$, vertical spacing between stacked rings (height of air box) $H = 0.5 \text{ mm}$, lattice period $T = T_x = T_y = 5 \text{ mm}$.

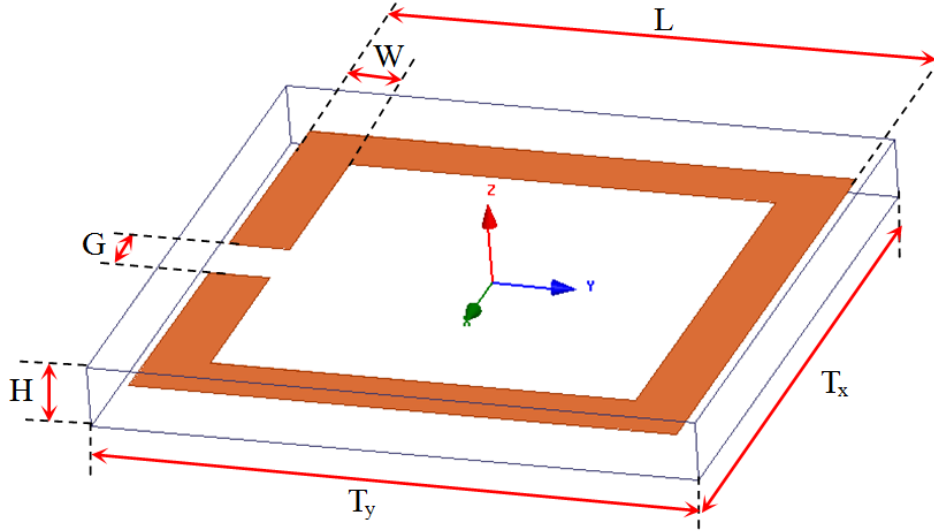


Figure 3.3 Unit cell of the stacked OSRs with geometrical parameters as follows: $H = 0.5$ mm, $T_x = T_y = 5$ mm, $G = 0.5$ mm, $W = 0.5$ mm and $L = 4.5$ mm [21].

3.2.2.1 Effect of Gap Size

Fig. 3.4 shows the calculated dispersion diagram for the above structure with different gap sizes (G). Along Γ -X, the phase $k_x T_x$ is changed from 0 to 180° along x-axis direction while $k_y T_y$ is fixed at zero. This produces the frequencies for the wave propagation in the Γ -X segment of the Brillouin zone. Then the $k_x T_x$ is fixed at 180° and the phase constant along the segment X-M, $k_y T_y$, is changed from 0 to 180° . Hence, the second range of eigen mode frequencies is found. Lastly, the phase constants of both $k_x T_x$ and $k_y T_y$ are changed in simultaneously from 180° to 0° . Thus, the last range of eigenmode frequencies is found for the M- Γ segment.

The width of the bandgap is determined by frequency separation of the extrema of consecutive eigen modes of the EBG; which in this case is the maximum frequency of the mode 1 and minimum frequency of the mode 2.

One can see that as G increases, the frequencies of the modes increase and the band gap frequency enlarges as well. To explain this trend, the electric and magnetic field (H_z component) distributions of the modes 1 and 2 and surface currents at the X point are examined. The fields are displayed for $G = 0.1$ mm and 3.5 mm in Figs. 3.5 (a) and (b), respectively. From the field and current plots in both figures, one can observe the following: circulating currents flow over the arc length around the OSR ring, lead to

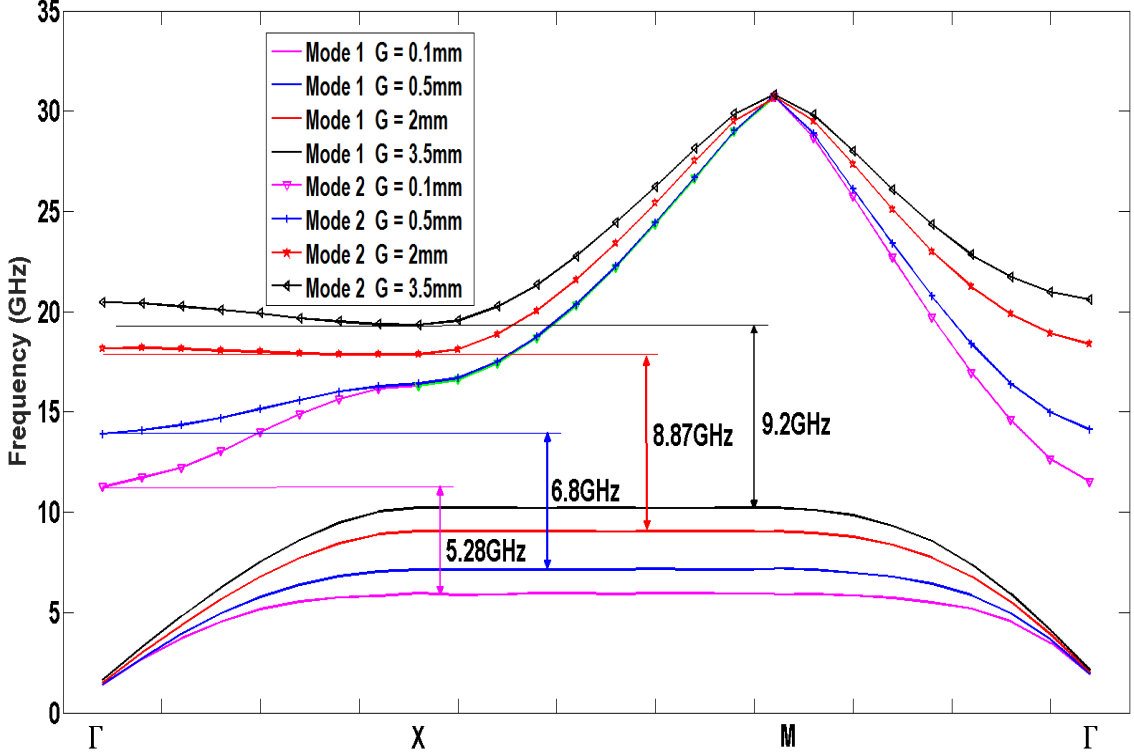


Figure 3.4 Effect of modifying the gap G on the band gap. Frequencies 5.28 GHz, 6.8 GHz, 8.87 GHz, and 9.2 GHz are the band gap between modes 1 and 2 for $G = 0.1$ mm, 0.5 mm, 2 mm and 3.5 mm respectively. Other parameters are as in Fig. 3.3.

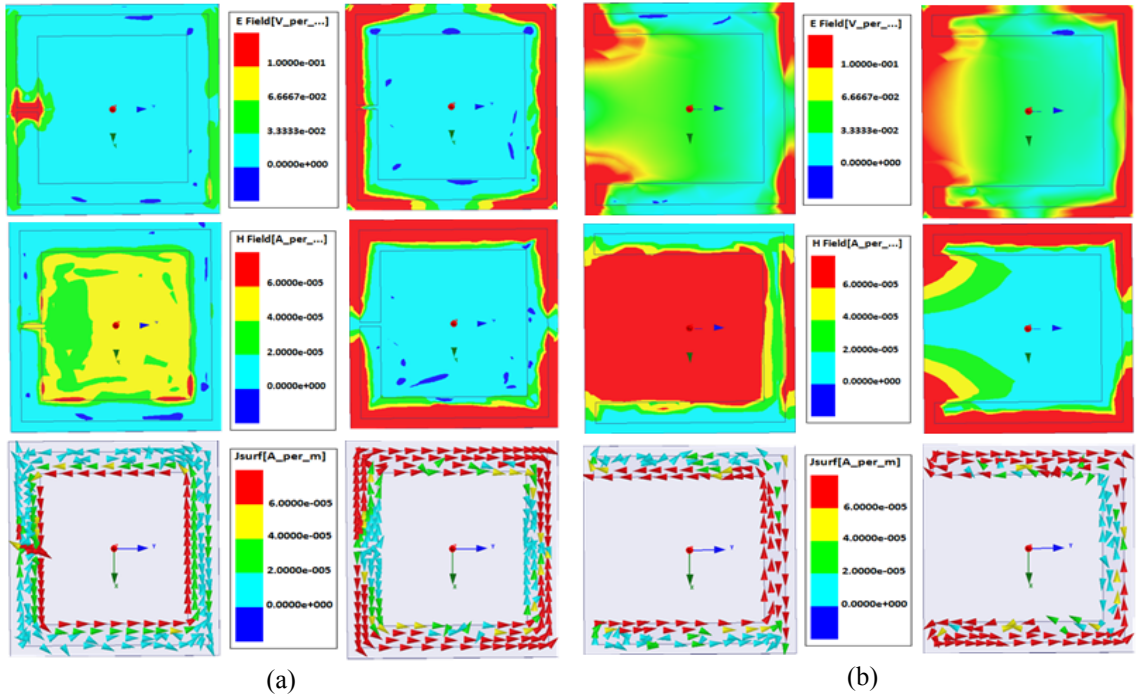


Figure 3.5 The electric fields (top), magnetic fields H_z (center) and surface currents (bottom) at the X-point for $G = 0.1$ mm (a) and 3.5 mm (b) (i.e., other parameters are as in Fig. 3.3). Modes 1 and 2 are the left and right panels, respectively.

magnetic fields inside and outside the OSR for modes 1 and 2, respectively. These currents give rise to a resonant magnetic dipole moment normal to the OSR plane [61]. The currents of modes 1 and 2 would correspond to half wavelength $\lambda/2$ (first-order) and wavelength λ (second-order) resonance modes of the OSR, respectively. This character is consistent with simulations reported in [61-64] that explain the resonances of the OSR by unfolding the ring into a rod that supports resonant eigenmodes.

Electric field is stronger in the region within the gap G . This is an expected result due to the charge accumulation around the gap region [65], induced by the circulating electric current. Therefore, an OSR structure can be viewed as a resonant LC structure [66] exhibiting a resonant response at a frequency Ω_{LC} . Total capacitance of the OSR system has mainly two contributions, one arising from self-capacitance C_{self} of the individual rings ($C_{self} = \epsilon_0 W/G$, normalize to plate thickness) and the other from mutual capacitance C_{mut} (capacitive coupling) between adjacent rings. Inductance originates from the mutual inductance L_{mut} (inductive coupling) between the rings and the self-inductance L_{self} of element rings, ($L_{self} = \mu_0 A$ where A is the area enclosed by the ring [67]).

As can be seen from Fig. 3.5(a), mode 1 exhibits intense electric field within the gaps (G), indicating strong capacitive coupling between the two sides of the gap. The downward resonance frequency of the mode indicates higher total capacitance (high self-capacitance due to smaller gap) as the OSR gap (G) is narrowed down. It is noteworthy that this resonance disappears when the ring is closed. Mode 2 exhibits strong magnetic field between the outer edges of the rings indicating inductive coupling between adjacent rings (currents on the neighboring edges of adjacent rings flow in the same direction). This inductive coupling is a result of strong surface currents along the outer edges of the rings as seen from Figs. 3.5 (a) and (b). The upward resonance frequency of the mode 2 implies low total inductance. This explanation of modes 1 and 2 is consistent with [63] and demonstrates that all resonances can be associated with the modes of the OSR structure.

Another way to describe the behavior of modes 1 and 2 is by noticing that mode 1 confines its (magnetic) energy inside the ring in order to lower its frequency [2]. Whereas mode 2 concentrates its energy outside the rings in order to raise its frequency, leading to the emergence of a bandgap between these two modes. This explanation demonstrates the resemblance of the EBG under study to the more conventional EBG composed of rods [2].

The lattice of open square rings can be understood as a lattice of rods comprised of high permeability. Therefore, the roles of electric and magnetic fields in the case of the current EBG should be interchanged as compared to dielectric rods. In other words, if the first mode is defined by the high confinement of E-field within the rod, the confinement of H-field within the ring is the salient feature of that same mode in the EBG comprised of OSRs. Given the above explanations, it is obvious that the band gap in the ring lattice is generated by the ring element resonance and periodicity.

For the case of $G = 3.5 \text{ mm}$ shown in Fig. 3.5(b), one can observe that mode 1 presents less electric field within the gap region (which leads to smaller self-capacitance), whereas mode 2 displays strong electric field (within the gaps) and magnetic field in the region between adjacent rings. The upward frequency of mode 2 and the emergence of band gap suggest the dominance of magnetic coupling between adjacent rings (the widening bandgap can be inferred by the change of field confinement factor of the EBG structure).

From both figures, one can see that as G increases, electric field of mode 1 becomes less confined (i.e., part of the energy leaves the gap) in the gap area, which results in reduced total capacitance (i.e., low self-capacitance) to cause upward shift of the mode. Mode 2 (i.e., magnetic field) dominates the area between the outer neighboring edges of adjacent rings as the current concentrates along those edges (i.e., removal of gap sides, that introduces low self-inductance) and flows in the same direction. This leads to decreased total inductance and hence the upward shift of mode 2.

3.2.2.2 Effect of Lattice Size

In this section, the impact of the square lattice size (T) is examined. As can be seen from Fig. 3.6, mode 1 frequency increases and mode 2 frequency decreases with increasing T and the band gap between these two modes shrinks. Again, we turn to the field distribution to understand the behavior of the modes. The fields for $T = 4.6 \text{ mm}$ and 8 mm are shown in Figs. 3.7 (a) and (b), respectively.

As T increases, the electric field of mode 1 becomes less confined in the area between the rings, indicating weak capacitive coupling which leads to a decrease in total capacitance (i.e., low mutual capacitance, because of reduced interaction between the OSRs). Therefore, mode 1 raises its frequency. The current distribution for the second mode along

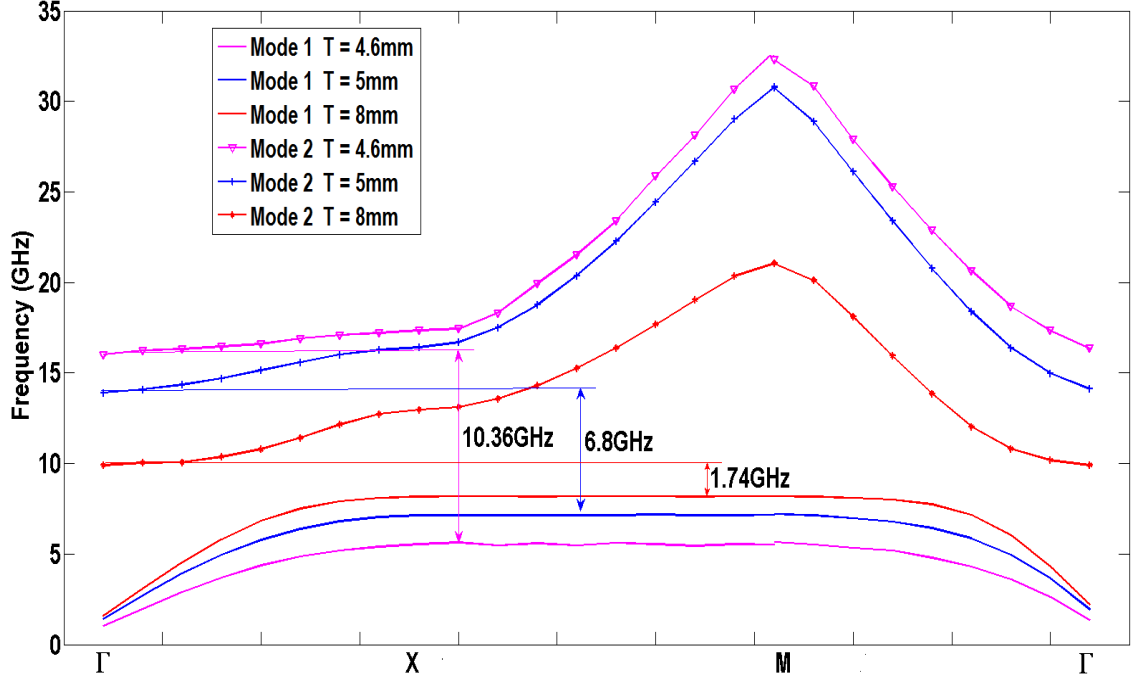


Figure 3.6 Effect of modifying lattice period T on the band gap. Frequencies 10.38 GHz, 6.8 GHz, 1.74 GHz correspond to band gap between modes 1 and 2 for $T = 4.6$ mm, 5 mm, and 8 mm respectively. Other parameters are as in Fig. 3.3.

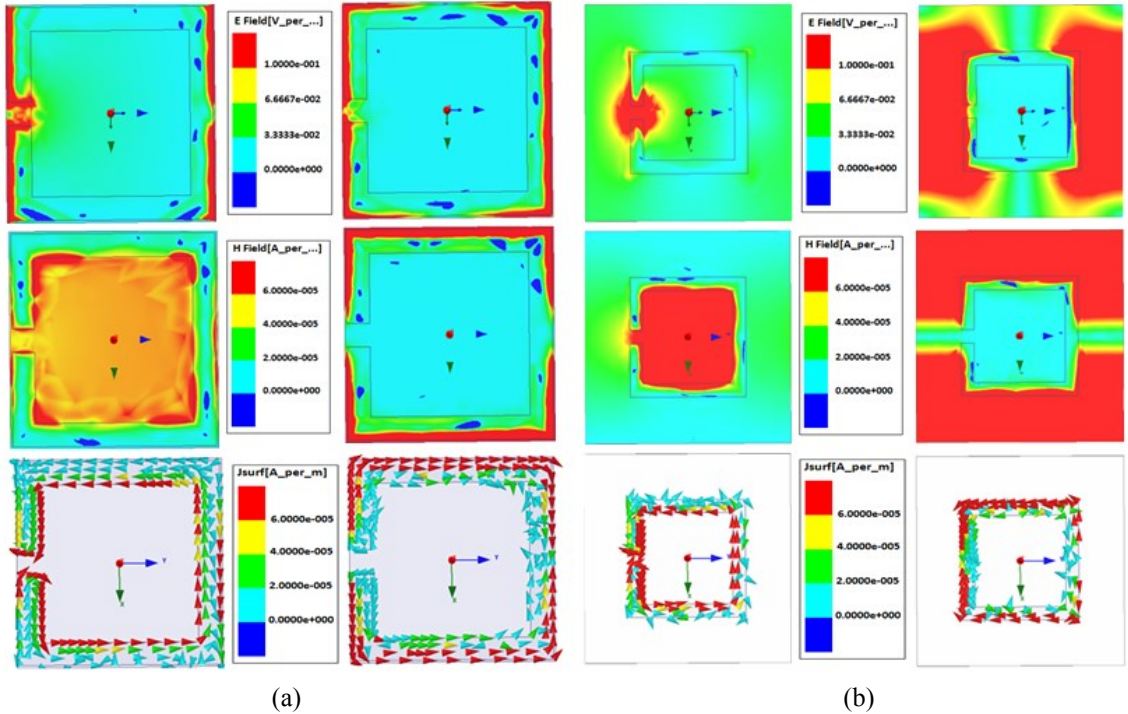


Figure 3.7 The electric fields (top), magnetic fields Hz (center) and surface currents (bottom) at the X-point for $T = 4.6$ mm (a) and $T = 8$ mm (b) (i.e., other parameters are as in Fig. 3.3). Modes 1 and 2 are the left and right panels, respectively.

the outer side edges induces magnetic field outside the ring that is comparable (i.e., same figure of confinement) to the field inside the ring for mode 1. In other words, the gap in the confinement factors of the two modes tends to narrow down for increased lattice size. Hence, the gap between modes 1 and 2 gets narrow down, which leads to narrower bandgap between these two modes. It is also worth noting that electric field of mode 2 presents strong field between the OSRs, indicating strong capacitive coupling which results to a significant decrease of the resonance frequency of the mode.

3.2.2.3 Effect of The Width of The Open Square Ring

Fig. 3.8 shows the dispersion characteristic of the ring structure with different metal line width ($W = 0.1, 0.5, 1 \text{ and } 2 \text{ mm}$). We notice from the graph that the bandgap narrows down for thicker OSR. i.e., mode 1 frequency increases, while mode 2 stays around the same frequency. The band gap disappears when $W = 2 \text{ mm}$.

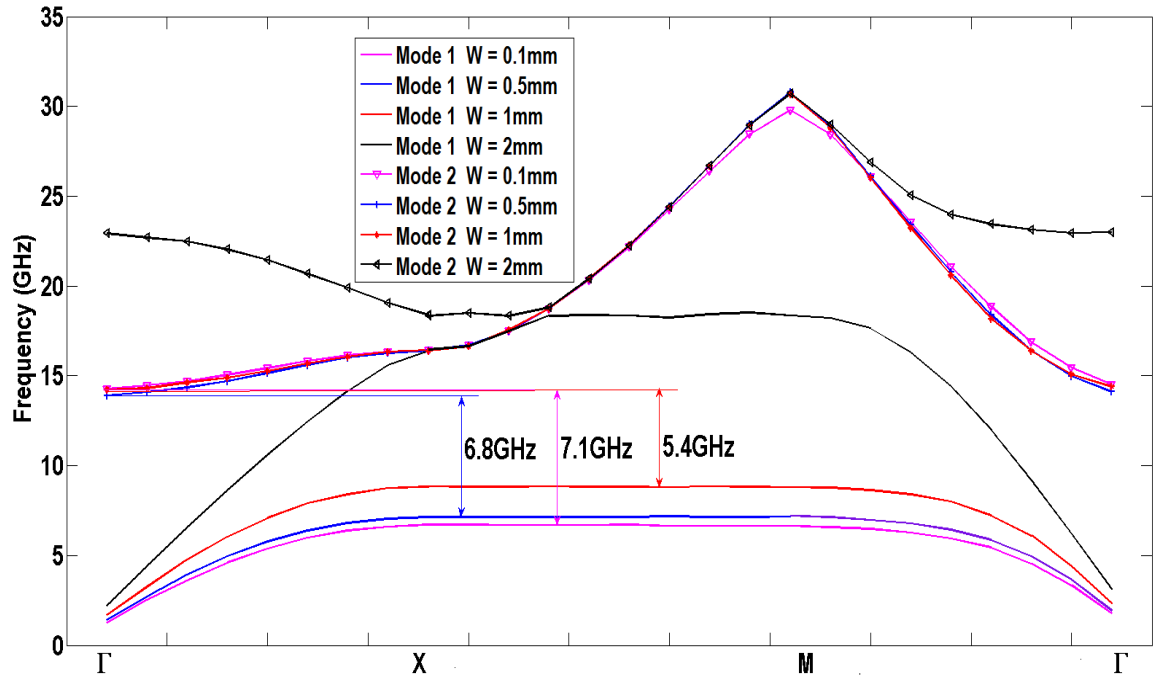


Figure 3.8 Effect of modifying metal width on the band gap. Frequencies 7.1 GHz, 6.8 GHz, and 5.4 GHz correspond to band gap between modes 1 and 2 for $W = 0.1 \text{ mm}, 0.5 \text{ mm}$ and 1 mm respectively, but no band gap for $W = 2 \text{ mm}$. Other parameters are as in Fig. 3.3.

Examination of the fields and currents for $W = 0.1 \text{ mm}$ and 2 mm are shown in Figs. 3.9 (a) and (b), respectively, shows that: $W = 0.1 \text{ mm}$, mode 1 (associated with low resonance

due to $\lambda/2$ current density wave) confines within the OSR and mode 2 (associated with high resonance due to λ current density wave) confines in the region between the loops leading to large band gap between the two modes. For $W = 2 \text{ mm}$, mode 1 is less localized to the interior of the ring (due to low current in the patch, and reduced self-inductance due to decreased A (area enclosed by the ring), raising mode frequency. Mode 2 is concentrated outside the ring (and in the gap, forcing magnetic energy to leave the ring) raising mode frequency. So, both modes show similar energy concentration outside the ring, resulting in the absence of band gap.

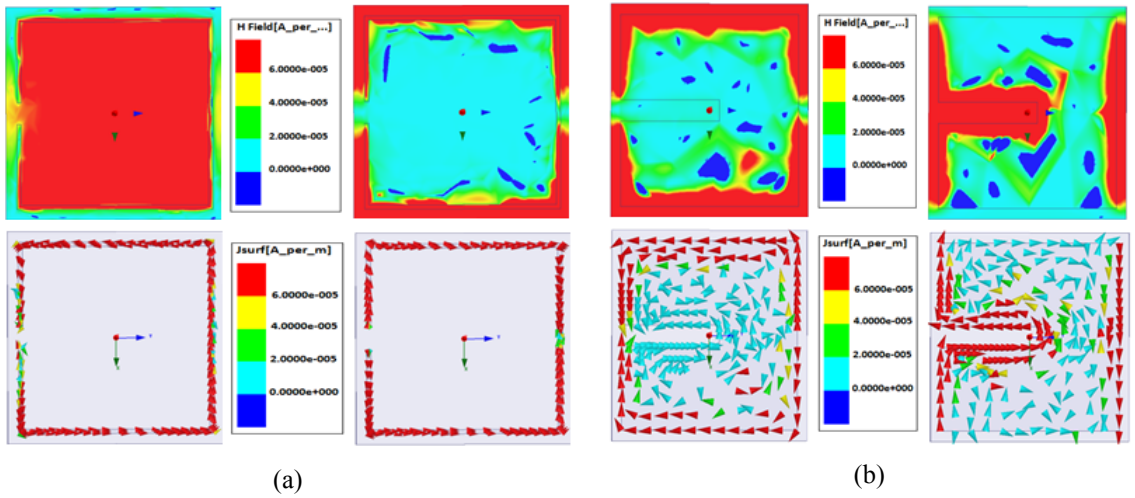


Figure 3.9 The magnetic fields H_z (top) and surface currents (J_{surf}) (bottom) at the X-point for $W = 0.1 \text{ mm}$ (a) and $W = 2 \text{ mm}$ (b) (i.e., other parameters are as in Fig. 3.3). Modes 1 and 2 are the left and right panels, respectively.

It should also be noted that as the width of the ring is increased, it approaches a square patch that has generally a higher resonance frequency as compared to a square ring of the same size [68].

3.2.2.4 Effect of Vertical Distance

To investigate the impact of vertical separation between OSRs on the band gap, Fig. 3.10 presents the band structures with different separation values (H) of 0.5 , 10 , and 20 mm . Examining the dispersion data, one can see that increasing H , results in reducing the band gap between modes 1 and 2. The fields for $H = 0.5 \text{ mm}$ and 20 mm are shown in Fig. 3.11 (a) and (b), respectively.

Increased separation between the OSRs is equivalent to reduced permeability of the equivalent magnetic rods which causes a reduction of the frequency gap width. As H increases, the magnetic field of mode 1 displays less confinement within the ring, which leads to increased frequency of the mode. Mode 2 exhibits same rate of confinement as mode 1 (the magnetic field spreads-out to the interior of the ring), which leads to narrower bandgaps between these two modes.

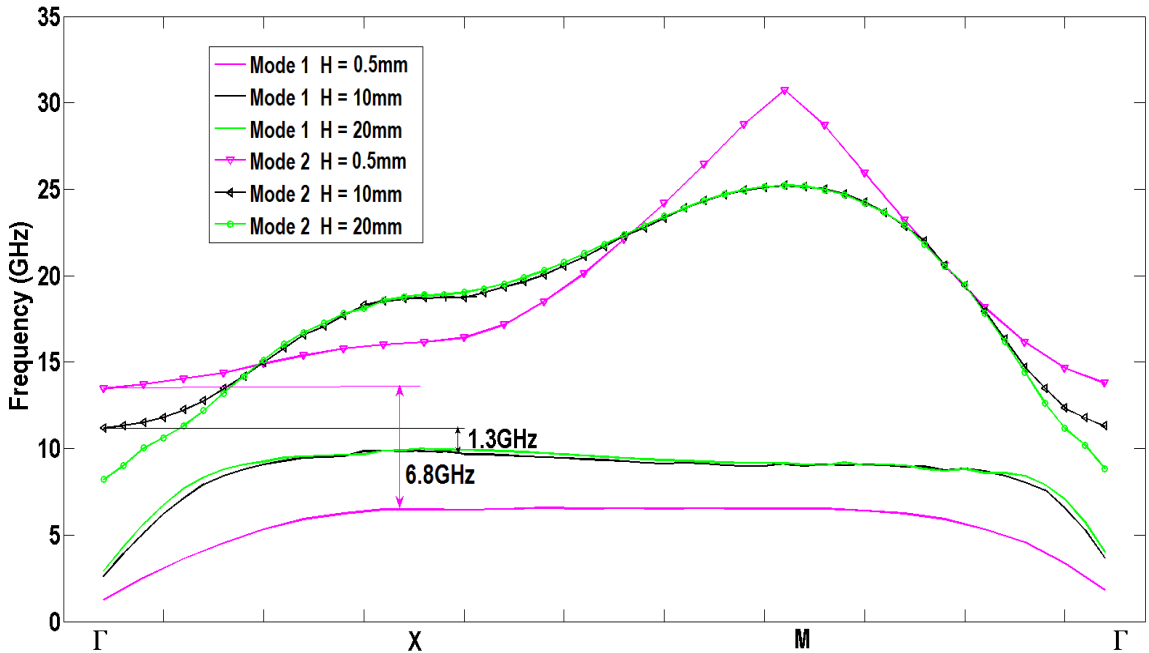


Figure 3.10 Effect of modifying separation H . Frequencies 6.8 GHz, and 1.3 GHz correspond to band gap between modes 1 and 2 for $H = 0.5$ mm and 10 mm respectively. No band gap for $H = 20$ mm. Other parameters are as in Fig. 3.3.

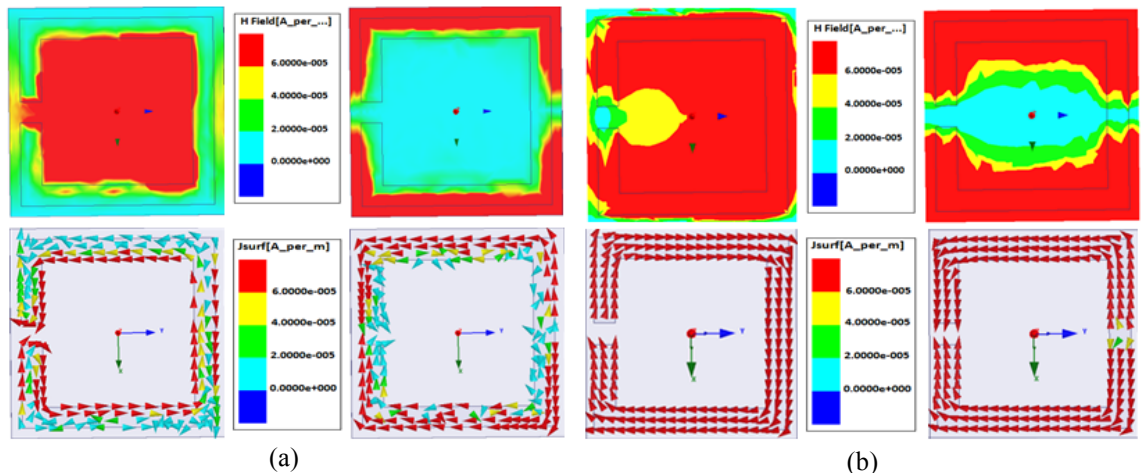


Figure 3.11 The magnetic fields H_z (top) and surface currents (bottom) at the X-point for $H = 0.5$ mm (a) and $H = 20$ mm (b) (i.e., other parameters are as in Fig. 3.3). Modes 1 and 2 are the left and right panels, respectively.

3.2.2.5 Effect of The Ring Size

In this section, we present the effect of the ring size (L) on the band gap. Since the lattice constant is fixed, decreasing the size of the rings will increase the separations between the rings. Fig. 3.12 displays the dispersion characteristics of EBG for $L = 4.5 \text{ mm}$ and 3 mm . The results show that decreasing the size of the ring, results in an increase of the frequency of modes 1 and 2.

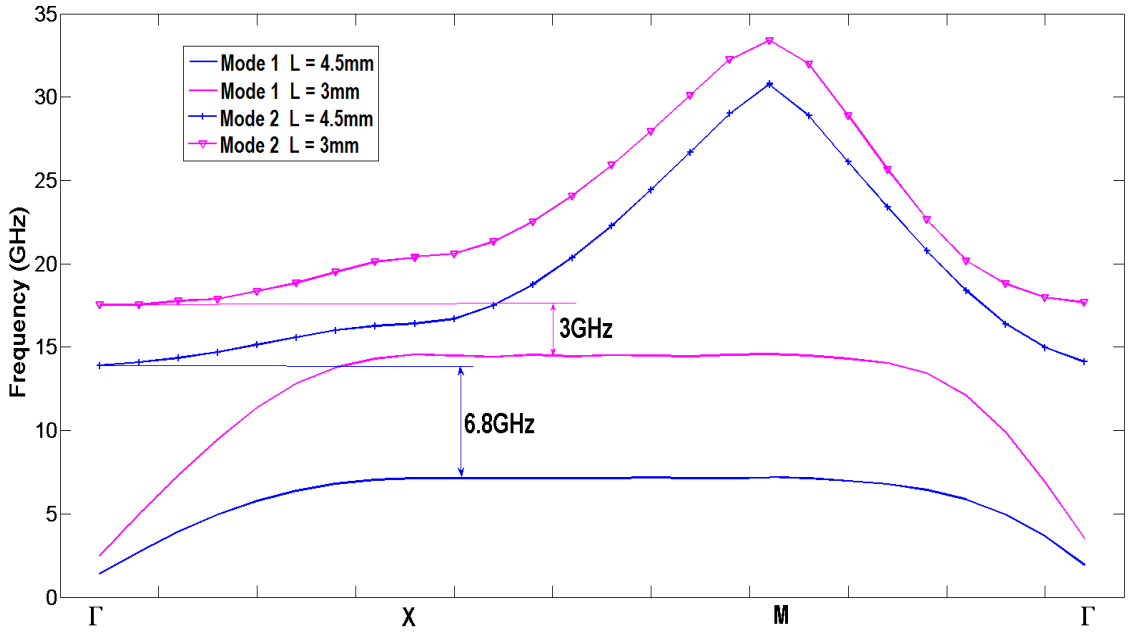


Figure 3.12 Effect of modifying outer-ring size L on the band gap. 3 GHz, 6.8 GHz, correspond to band gap for $L= 3 \text{ mm}$ and 4.5 mm respectively. Other parameters are as in Fig. 3.3.

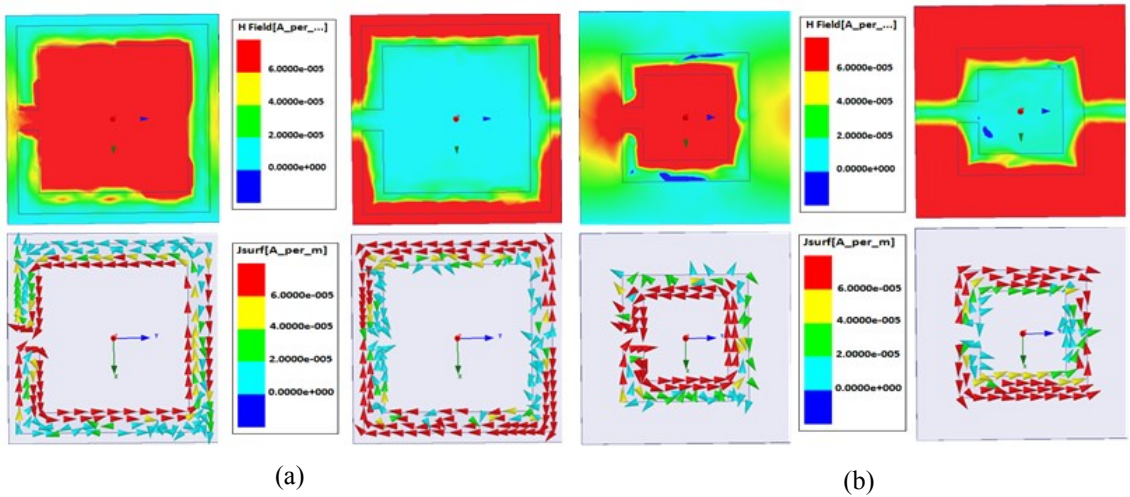


Figure 3.13 The magnetic fields Hz (top) and surface currents (bottom) at the X-point for $L = 4.5 \text{ mm}$ (a) and $L = 3 \text{ mm}$ (b) (i.e., other parameters are as in Fig. 3.3). Modes 1 and 2 are the left and right panels, respectively.

From the fields and currents distributions of Fig. 3.13 (a) and (b) for $L = 4.5 \text{ mm}$ and 3 mm , respectively, one can see that as the size L decreases: the magnetic field of mode 1 is less confined in the interior of the ring (due to decreased self-inductance i.e., decreased ring geometry) and mode 2 displays more field confinement in the exterior of the ring (similar to mode 2 of increased lattice size). This results in upward shifts for both modes 1 and 2.

A different explanation of this trend can be inferred by focusing on the modal behavior of the OSR EBG that is tightly linked to the resonance behavior of the OSR cell element. Upward shift of the resonance frequency of the OSR as the loop size decreases is compatible with higher modal frequencies of modes 1 and 2.

3.2.2.6 Summary

Using the results shown in sections 1-5, Table 3.1 gives the calculated band gap for different configurations of the EBG composed of OSRs. A key observation of the table is that the band gap depends strongly on the geometrical features of the structure. This is due to the change in the frequencies of OSR modes as its geometrical parameters are varied.

Table 3.1: Computed bandgap for different OSRs structures. Bolded values refer to nominal case.

	Parameter (mm)	Band gap (GHz)
G	0.1	5.28
	0.5	6.8
	2	8.87
	3.5	9.2
T	4.6	10.36
	5	6.8
	8	1.74
W	0.1	7.1
	0.5	6.8
	1	5.4
	2	0
H	0.5	6.8
	10	1.3
	20	0
L	4.5	6.8
	3	3

The reduced lattice constant T and increased gap separation G lead to a considerable variation of frequency band gap between modes 1 and 2. Section 3.3, focuses on the structure with gap separation $G = 3.5 \text{ mm}$ (i.e. band gap of 9.2 GHz); where the rings are completely open on one side, having a U-shaped form. This choice ensures the largest band gap and while maintaining a reasonable T (5 mm) for reliability of fabrication. Many other choices are of course possible according to the specific application requirements, showing the flexibility afforded by this new EBG structure.

3.3 EBG Slab of OSRs in Free Space

In section 3.2, the structure was of infinite extent in the direction perpendicular to the transverse plane where the elements are located. A realistic design of finite height, in the form of EBG slab structure, is addressed in this section. The finite height leads to modal confinement in the vertical direction, and the two-dimensional periodicity has the effect of in-plane confinement. The computational method, used for the calculation of dispersion characteristics, is briefly introduced in the next section along with the band structure for different slab thicknesses.

3.3.1 Method of Computation

The slab has periodicity in only two dimensions (in-plane) and is finite in the third dimension. In order to model the structure, The super-cell concept as outlined in [69-70] was used. This unit cell contains a large volume of air outside the slab to ensure electromagnetic isolation between adjacent super-cells. The height of the super-cell was increased until the eigen-mode frequencies become insensitive to the height of super-cell. The slab structure and super-cell are shown in Fig. 3.14.

The thickness of the slab is equal to d . Periodic boundary conditions are enforced on the sides and perfect magnetic boundary (PMCs) are imposed on top and bottom faces of the super-cell.

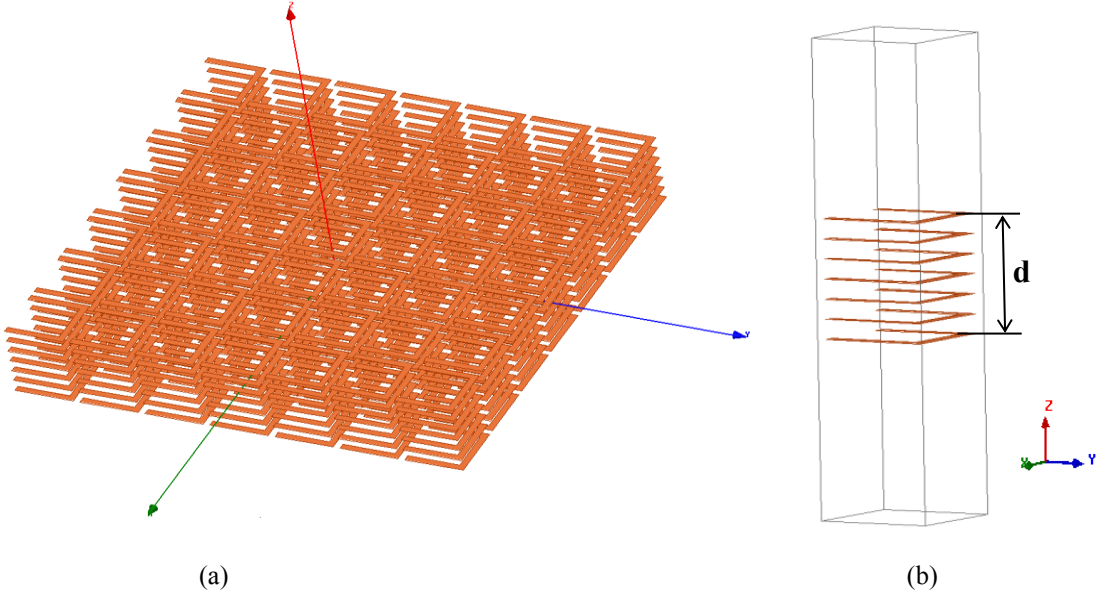


Figure 3.14 (a) Slab structure. (b) Super-cell model. The slab thickness d is 1.2 T (i.e. stack of 7 rings, spaced by 1 mm and in air), where T is the period in the x and y directions. The medium above and below the slab is air.

3.3.2 Band Structure

The resulting band (dispersion) diagram for a typical slab is given in Fig. 3.15. It includes the light cone (i.e., propagation in air) and guided modes (slow waves) along with radiation or leaky modes (fast waves) [70]. The latter lie above the light line of air ($\omega = ck$) and extends to infinity and have complex propagation wavenumbers. However, guided waves correspond to discrete modes, which exist below the light line, confined in the slab and have real wavenumbers. A band gap in this case is the range of frequencies under the light line where no guided modes exist. It is to be considered as a partial gap due to the presence of radiating modes at those frequencies. Therefore, a band gap exists between the X point of the highest-order mode (mode 7 of the first bundle of modes) and the crossing point [71] of the lowest-order modes (mode 8 in the second bundle of modes) with the light line. The E-field of these two modes is shown in Fig. 3.16. It is apparent from these figures that these guided modes are localized within the slab.

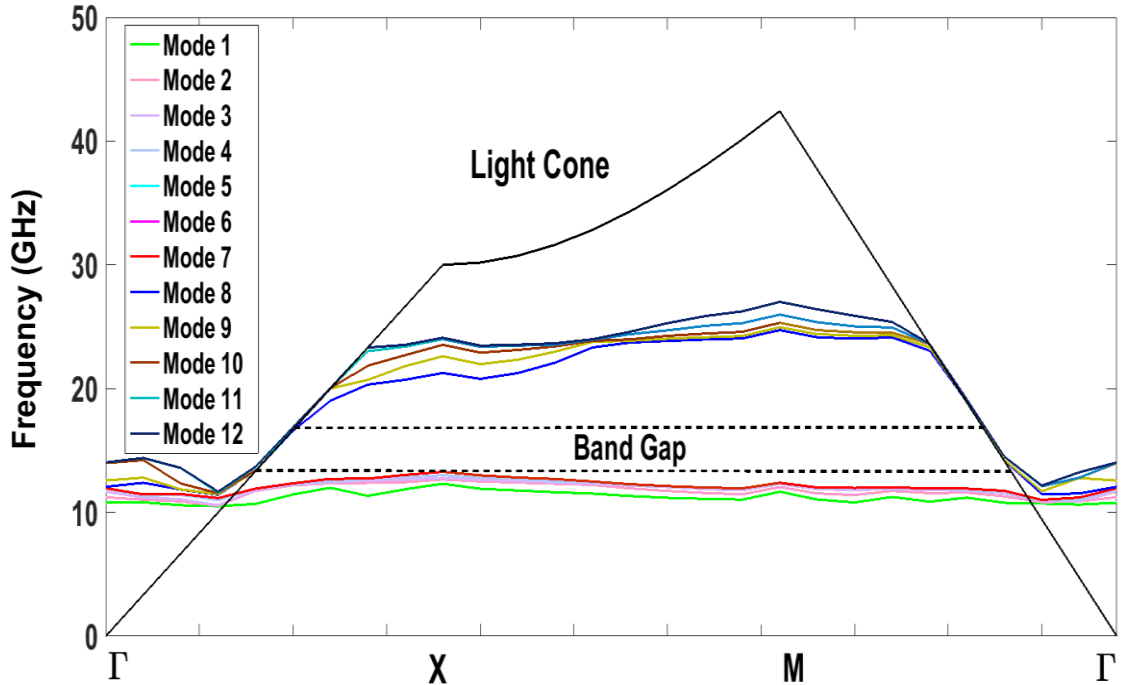


Figure 3.15 Projected band structure for the structure shown in Fig. 3.14 with 7 rings in the Z direction separated by 1 mm in air.

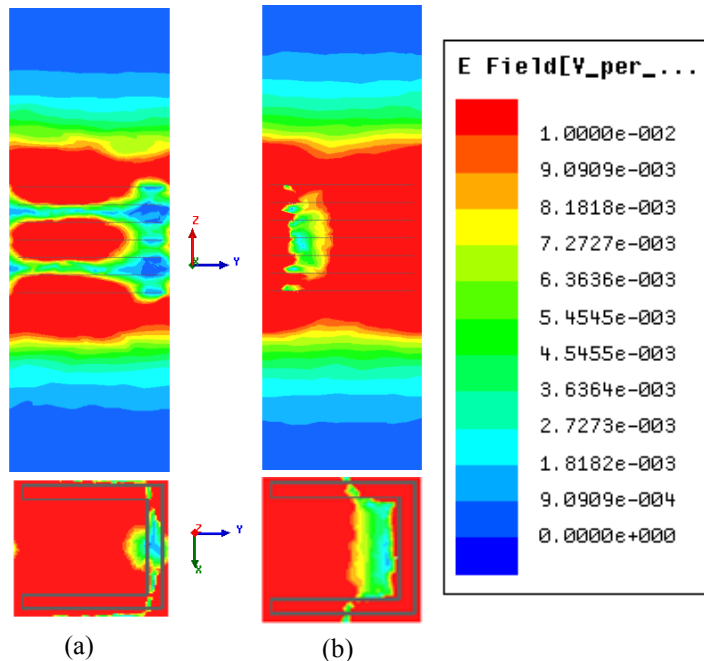


Figure 3.16 E-field of the slab structure in Fig. 3.15 depicted in the unit cell at X for modes 7 and 8 at the lower and upper edges of the band gap respectively. Horizontal (xy) cross section (bottom). Vertical (yz) cross section (top). Modes at the lower and upper edges of the band gap are at (a) and (b) respectively.

3.3.3 Effect of Slab Thickness

The effect of thickness d of the EBG slab for various separations between the elements (0.5 mm , 1 mm , and 2 mm) along the z-axis is studied for different numbers of rings along the slab height (3, 5, 7, 11 and 13). It was observed that as the number of stacked rings increases, (i.e. slab becomes thicker), the second bundle of modes (i.e. modes above the upper edge of band gap) shifts to lower frequencies (below the edge of the band gap). At the same time band gap size does not change significantly. Except for the slab with thickness of $0.2 T$ (1 mm height with 3 rings separated by 0.5 mm), which shows a narrow band gap of 0.7 GHz, the other fourteen slab structures mentioned above, offer a calculated band gap of 3.57 GHz (from 13.31 GHz to 16.88 GHz). Therefore, given the minimal difference between the various configurations, significant fabrication flexibility exists.

3.4 EBG Slab Waveguide in Free Space

Previous section shows that the EBG slab provides a bandgap over which no modes exist. By breaking the periodicity in one spatial direction, localized (defect or Bloch) mode(s) with frequency inside the full lattice bandgap can be excited that are confined to the line defect or waveguide channel area. The following subsections provide a detailed presentation of the waveguides in square lattice slabs embedded in air.

3.4.1 Channel Waveguide Structure

The structure under study is shown in Fig. 3.17 (a); a one-dimensional (1D) channel waveguide in an EBG slab suspended in air. The waveguide is created by reducing the size [2] of one row of seven stacked rings in the EBG slab. Ring geometry is shown in Fig. 3.17 (b) and further discussion of the choice of defect dimensions is given later. Rings are etched on a thin (1 mil) dielectric Kapton® membrane of $\epsilon_r = 3.5$, that altogether forms a single layer. The presence of this thin substrate was found to have negligible effect on the results of Fig. 3.15. The layers are separated by 1 mm foam (Rohacell® 31 HF, $\epsilon_r = 1.046$ and $\tan \delta = 0.0017$) spacers that emulate free space between layers. Finally, every layer has defect rings along defect line (or channel of the guide) that serves as the guiding medium along the x-axis (i.e., the waveguide must be periodic along the direction of wave propagation).

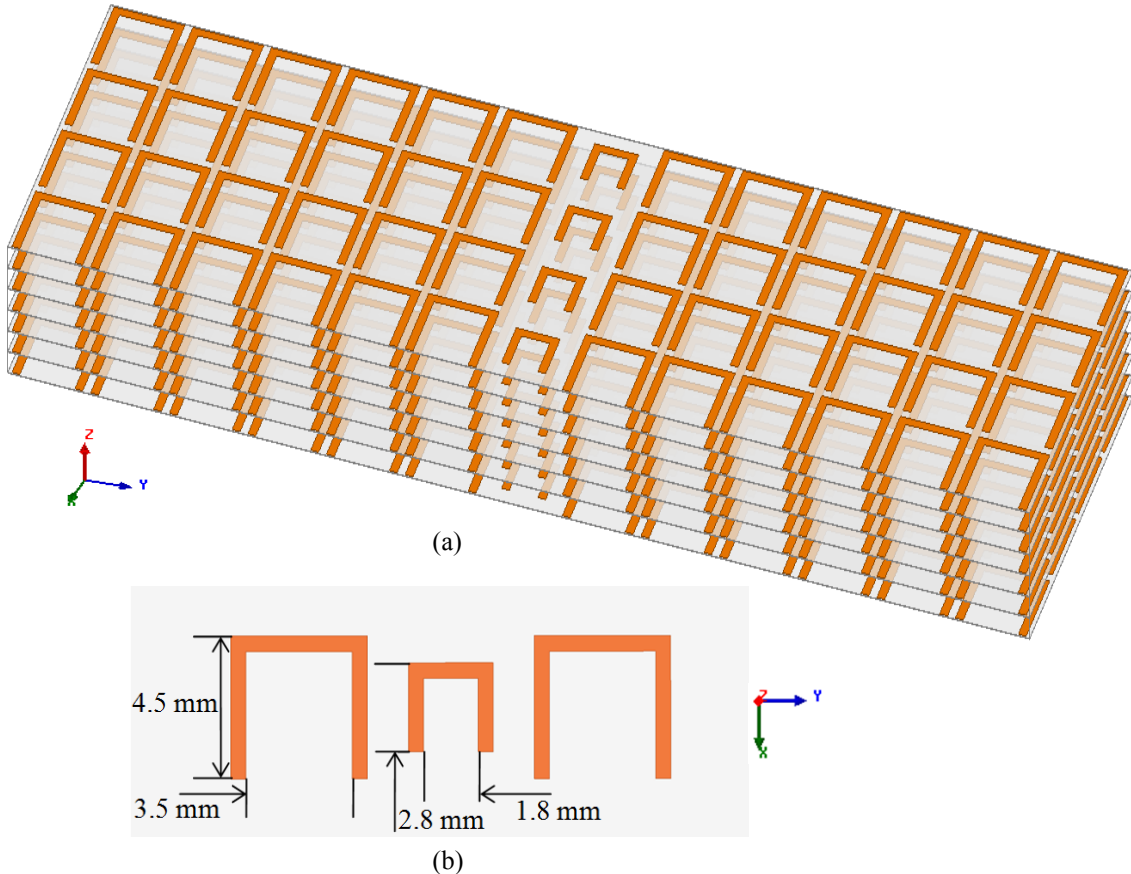


Figure 3.17 (a) Structure of EBG slab waveguide composed of seven layers suspended in air. (b) Ring dimensions.

3.4.2 Modes in The EBG Slab Waveguide

3.4.2.1 Band Structure and Field Distribution

To calculate the band structure of the waveguide, a super-cell with six rows on either side of the defect row was employed. Fig. 3.18 shows a schematic view of the super-cell. Perfect magnetic conductors (PMCs) were assigned on the top, bottom, and enclosing walls parallel to xoz plane, while periodic boundary conditions were used on the enclosing walls parallel to yoz plane. The length of the cell along x -axis corresponds to the periodicity of the stacked rings in that same direction, whereas the width represents various lattice constants for the super-cell along y -axis. The following widths were investigated: three, five, seven, thirteen and twenty-one lattice constants that represent one, two, three, six and ten row(s) on each side of the channel. It was noticed that by varying the super-cell width,

the eigenmode frequencies do not change significantly and waveguide modes remain highly localized to the channel area.

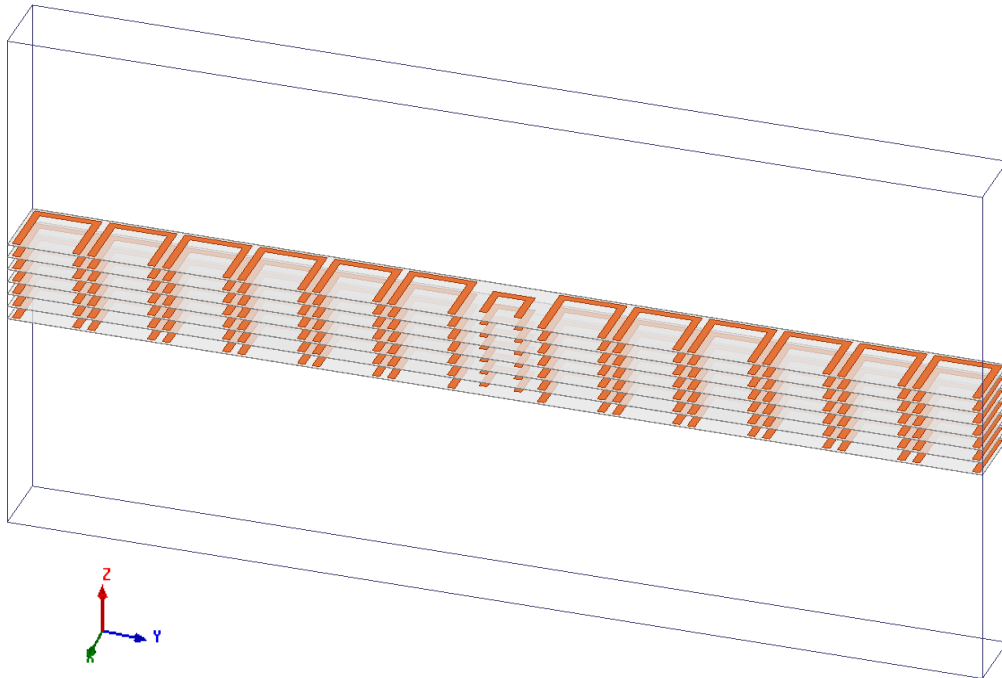


Figure 3.18 Super-cell for band calculation of the waveguide. The wave propagation direction is in the x direction.

Fig. 3.19 shows the band structure of the waveguide shown in the inset of that same figure. The horizontal axis corresponds to the propagation wave vector $k' = k_x x'$ in the direction of the channel, and so the dispersion relation is plotted in the reduced Brillouin zone Γ -X (i.e., phase constant $k_x T$ is varied along x-axis from 0 to 180°). Guided slab modes and radiating modes (leaky modes) appear below and above light line, respectively. Finally, waveguide (defect) modes are within the gap [2] and are confined to the defect line. As was shown in Fig. 3.15, the 2-D EBG slab composed of metallic rings exhibits a band gap from about 13.31 GHz to 16.88 GHz. It is observed in Fig. 3.19 that mode 1 is only partially within the band gap. The field profiles for the mode at frequency in the band gap $f = 16.37$ GHz, are shown in Fig. 3.20 (a). The mode is strongly confined in the channel both horizontally (xy plane) and vertically (yz plane).

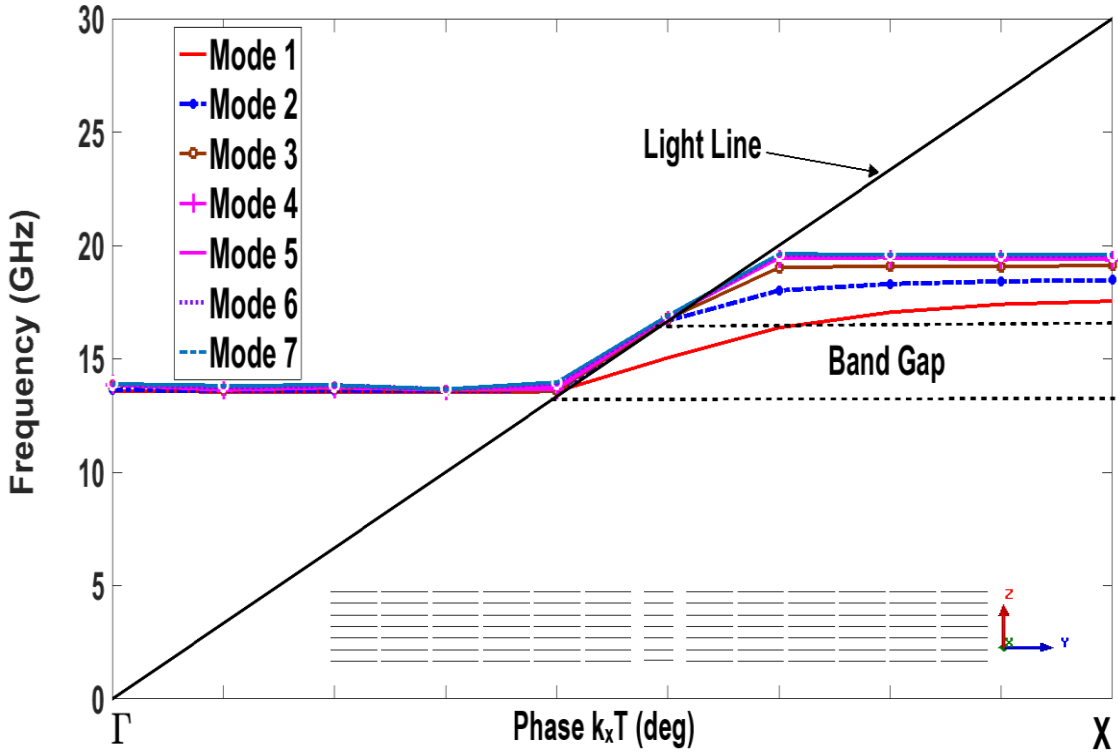


Figure 3.19 Band diagram of the waveguide modes. Cross section of the guide is shown in the inset, which shows seven stacked defects (in all layers) in the channel of the guide.

Surprisingly, there is a set of modes that are confined in the channel even though they fully lie outside the EBG lattice bandgap. Fig. 3.20 (b-d) and Fig. 3.21(a-c) show the field patterns of these modes. Note that these outside-gap guided modes (i.e., modes 1-7) will become lossy, if there are other modes of the EBG crystal that propagate outside the band gap at the same frequency and wave vector and can couple to the guided modes [72]. This will result in low confinement of the field in the channel region, thus low transmitted power. It is also important to note that these confined modes (modes 2-7) present a flat behavior and run very close to each other and very close to the light line. This indicates that these modes are likely to experience high power coupling. In addition, they have low group velocity [73] implying a narrow frequency bandwidth that poses a restriction for practical waveguide application using this type of modes. The flattening of the dispersion of mode 1 near the X point is due to the effect of distributed Bragg reflection, caused by the EBG crystal [72]. This effect is an outcome of coupling between a forward and backward Bloch mode [74].

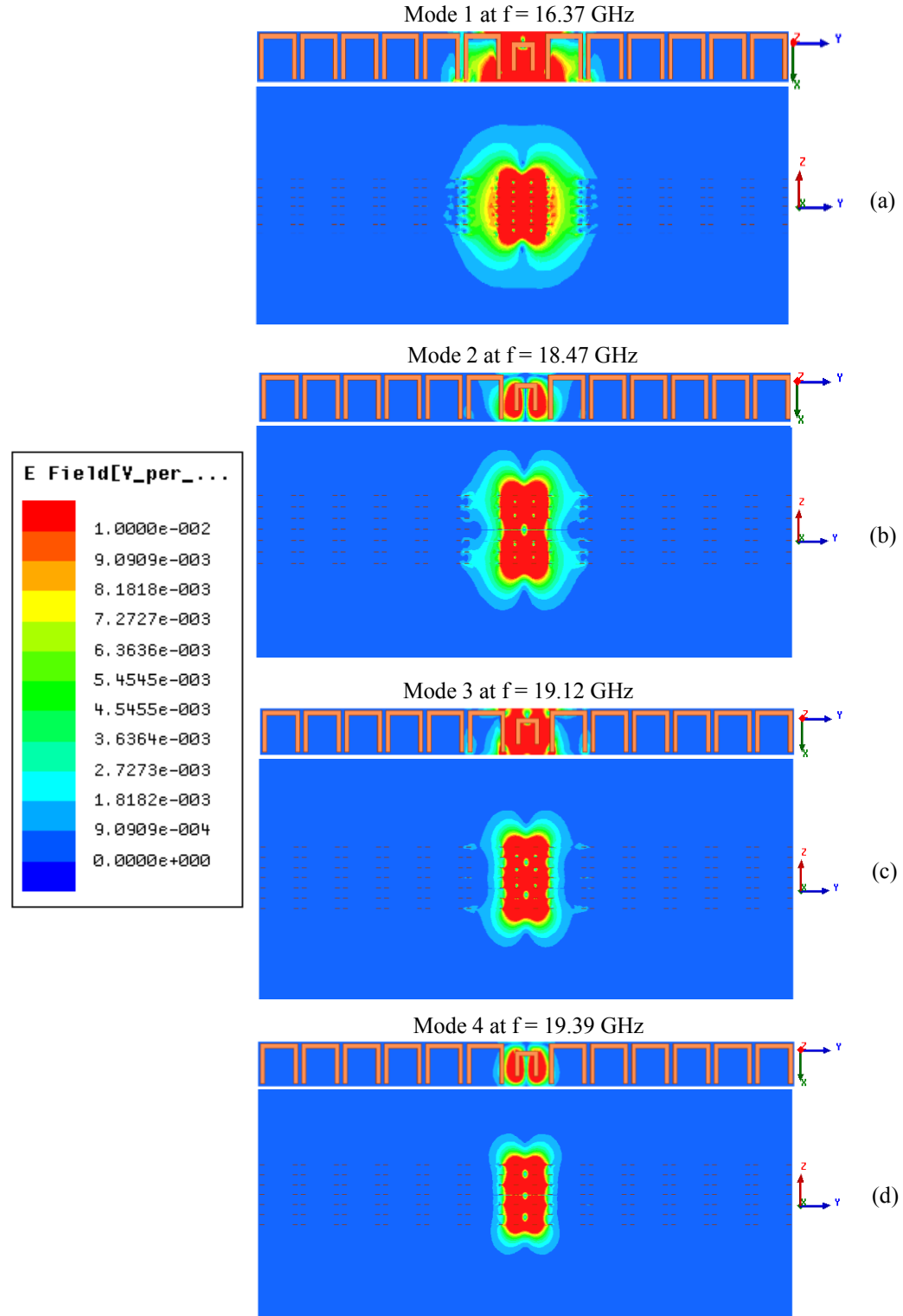


Figure 3.20 E-field cross sections at (a) $f = 16.37$ GHz (a), 18.47 GHz (b), 19.12 GHz (c) and 19.39 GHz (d) for modes 1-4 respectively in line-defect waveguide of seven defects. Horizontal (xy) cross section (top). Vertical (yz) cross section orthogonal to the guided direction (bottom).

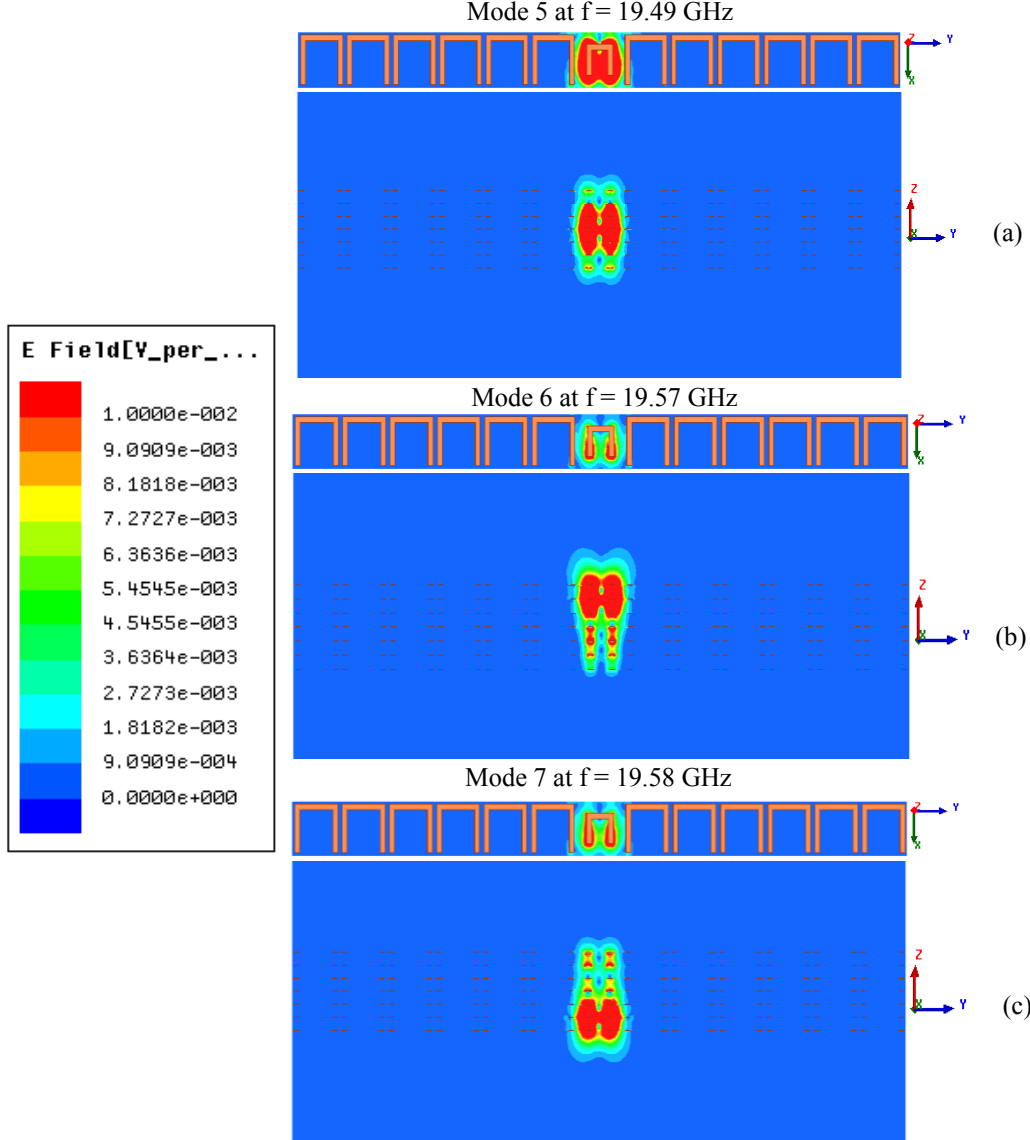


Figure 3.21 E-field cross sections at $f = 19.49$ GHz (a), 19.57 GHz (b) and 19.58 GHz (c) for modes 5-7 respectively in line-defect waveguide of seven defects. Horizontal (xy) cross section (top).Vertical (yz) cross section orthogonal to the guided direction (bottom).

The group velocity of the mode should be large enough to realize a long transmission length. If the group velocity of the mode is very small, the travel time per distance is long. This can result in large dissipation due to radiation losses [73]. According to [75], a low group velocity is associated with loss.

Seven confined modes exist in the channel which is equal to the number of defect layers. This point is illustrated in Fig. 3.22, which presents field profiles of the first two modes for the waveguide created by establishing defect only at the vertically centered layer (fourth

layer from the bottom). It can be seen that mode 1 is confined to the channel as opposed to mode 2 which is an extended slab mode in the surrounding of the channel (i.e., this modal behavior holds, for any position of the single layer defect along vertical direction). This is compatible with observations from Fig. 3.23 which shows dispersion characteristic of the guide. Mode 1 is partially inside the gap, but very close to the light line.

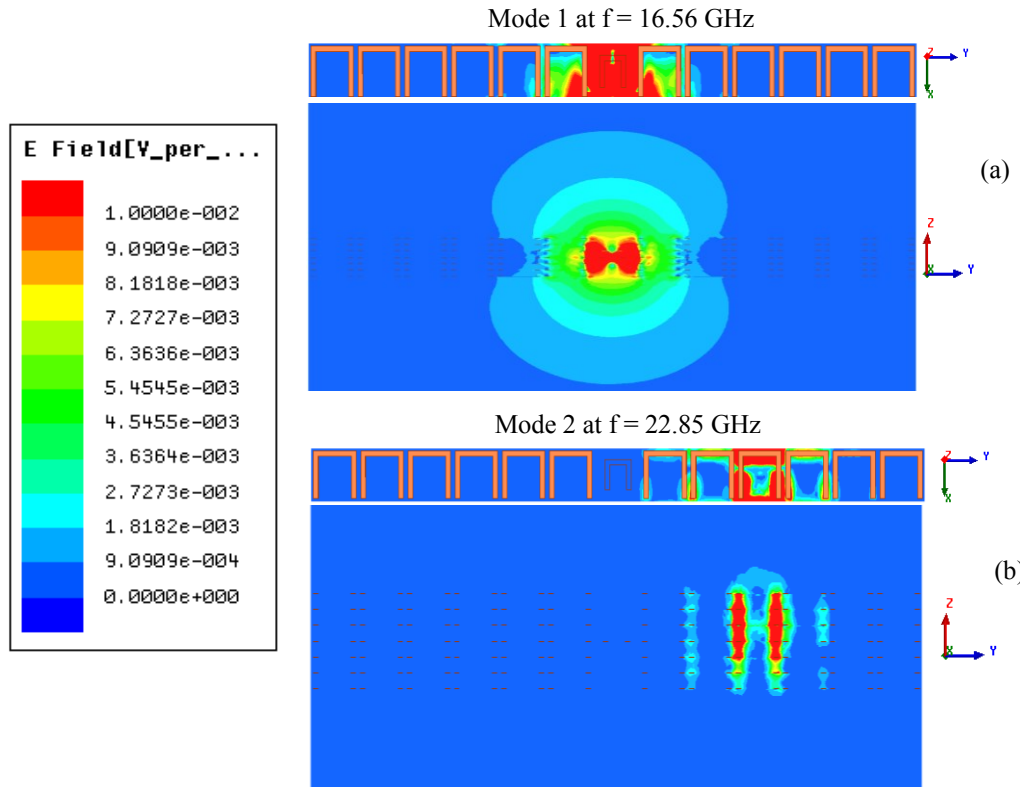


Figure 3.22 E-field cross sections at $f = 16.56$ GHz (in the gap) (a) and $f = 22.85$ GHz (outside the gap) (b) for modes 1 and 2 respectively in line-defect waveguide of one layer (vertically centered) defects. Horizontal (xy) cross section (top). Vertical (yz) cross section orthogonal to the guided direction (bottom).

The dispersion relations for defects composed of different number of rings are presented in Fig. 3.24. Only modes that are confined in the channel are shown in the graph (i.e., only three confined modes for the case of seven layers with defects, are presented to maintain the clarity of the plot). The figure and the field profiles of modes (not shown here) demonstrate that there is only one guided defect mode (mode 1) inside the band gap (mode 2 is inside the band gap but very close to light line and has different polarization as compared to mode 1) irrespective of the number of layers within the defect region. Therefore, the channel guided mode is a single mode in the frequency range of the lattice

bandgap. Interestingly, as the number of layers with defect increases, this single in-gap mode moves away from the light line into the bandgap. At the same time, it exhibits a broadband behavior.

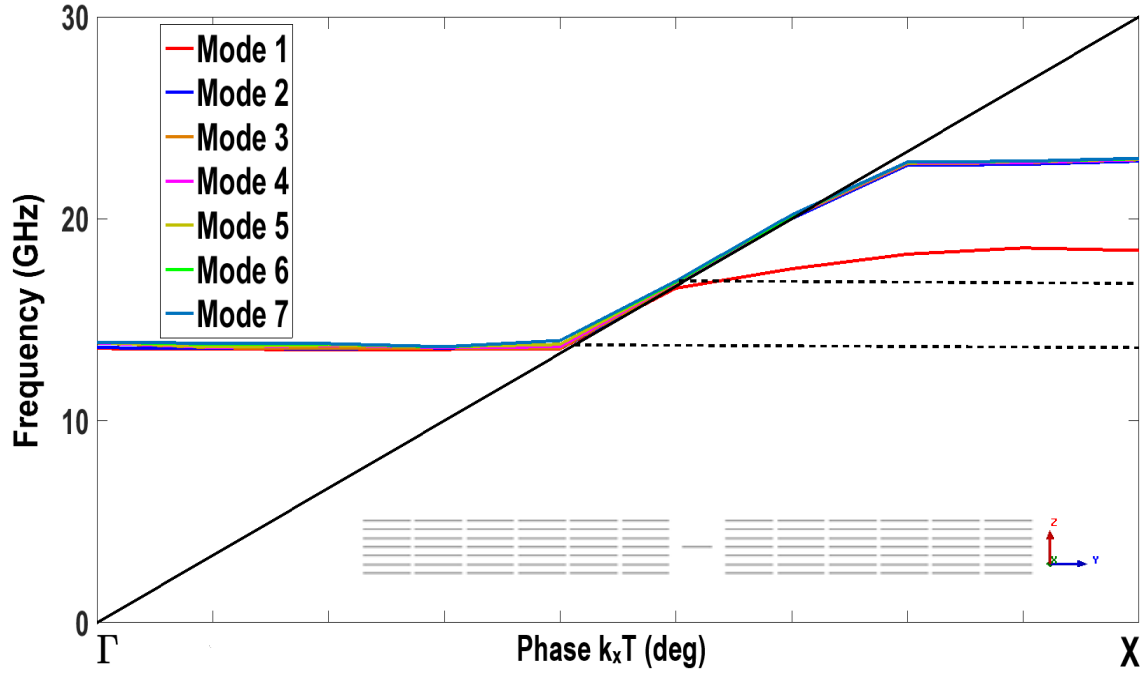


Figure 3.23 Band diagram of the waveguide modes with defect in single layer. Cross section of the guide is shown in the inset, which shows defect in the fourth layer only.

If the number of OSRs in the defected region is decreased below a certain size or removed, the waveguide will not support any guided mode as all modes lie entirely above the light line. This is solely due to the lack of confinement in the vertical direction. Because of this, waves cannot be guided in an empty defect channel surrounded by metallic rings. This was investigated through computer simulations and the dimensions in Fig. 3.17 were found to be optimal.

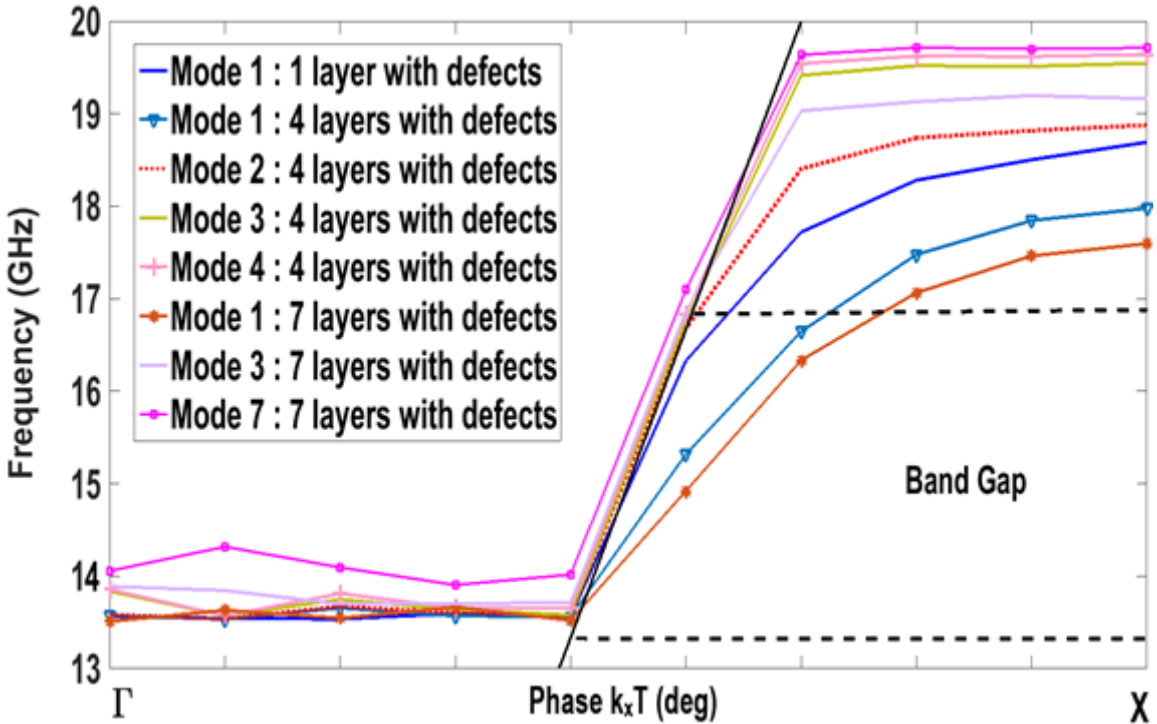


Figure 3.24 Band diagram of line-defect waveguide for various number of layers having defects. Only confined modes in the channel are shown in the graph (Seven layers with defects : only three confined modes are shown).

3.5 Infinite Open Square Rings in Dielectric

Up to now, the focus of the thesis has been OSRs-based EBG that are in the air. This section is devoted to the investigation of the case where the rings are immersed in a dielectric medium of ϵ_r of 2, 2.94, 4 and 9. The U- shape structure is the case study for the rest of this thesis. Fig. 3.25 shows the resulting dispersion characteristic for an OSRs-based EBG immersed in dielectric material. From the graphs, one clearly observes that the dielectric has the effect of lowering the frequencies of the modes (i.e., the case of U-rings in air is shown for comparison). On the other hand, as the value of the dielectric constant increases, the band gap shrinks and shifts to lower frequency band. Although the study is limited to the band gap between modes 1 and 2, the OSR design exhibits a second minor band gap between modes 2 and 3 (not displayed in the figure).

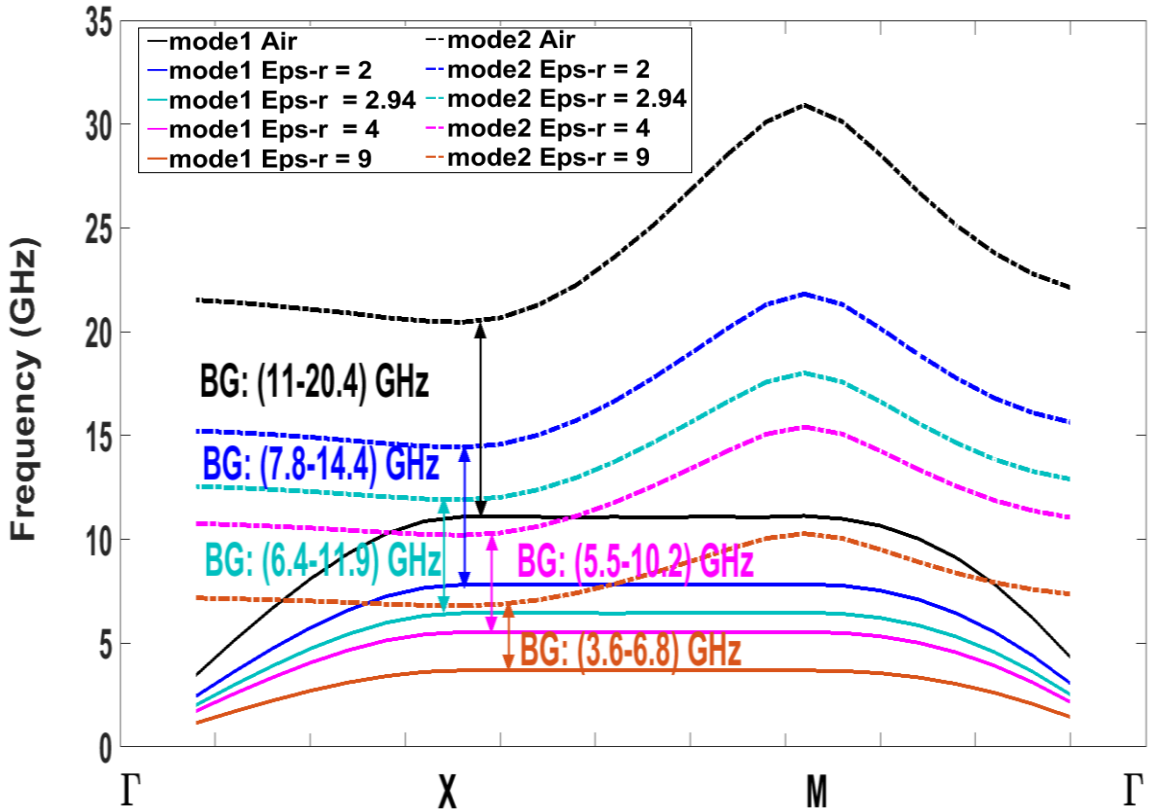


Figure 3.25 Dispersion diagrams of the infinite U-rings in dielectric mediums of ϵ_r of 2, 2.94, 4 and 9. Air medium case is shown for comparison.

Having more than one band gap allows, for instance, the suppression of undesired harmonics. Table 3.2 summarizes the different band gaps of the U-rings structure in air and dielectric.

Table 3.2: Bandgaps of the U-rings structure in different mediums.

Medium	First Major Band Gap	Second Minor Band Gap
Air	(11 - 20.4) GHz	(30.9 - 35.5) GHz
$\epsilon_r = 2$	(7.8 - 14.4) GHz	(21.8 - 25.1) GHz
$\epsilon_r = 2.94$	(6.4 - 11.9) GHz	(18.1 - 20.7) GHz
$\epsilon_r = 4$	(5.5 - 10.2) GHz	(15.4 - 17.8) GHz
$\epsilon_r = 9$	(3.6 - 6.8) GHz	(10.2 - 11.8) GHz

3.6 EBG Slab of OSRs in Dielectric

3.6.1 Structure

EBG slabs suspended in free space were presented in the previous sections. While EBG slabs in a dielectric medium are presented in this section. A typical slab structure is depicted in Fig. 3.26 (a). The slab is composed of a square array of layered OSRs immersed within a dielectric structure. The thickness of the dielectric slab above and below the stack of rings is t and the thickness of the slab is d . Layered rings are spaced by distance H and the regions above and below the slab continue to be filled by air.

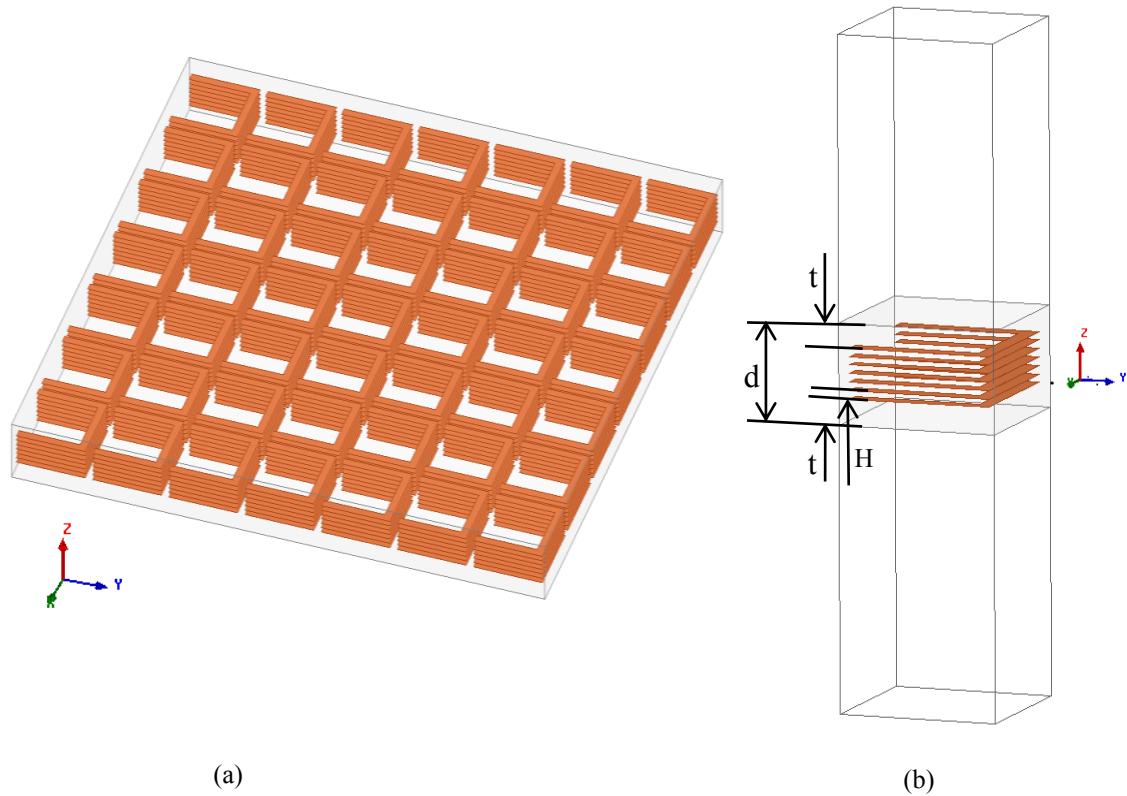


Figure 3.26 (a) Schematic of an EBG Slab: 2D square array of stacked U rings is a dielectric medium. (b) The super-cell for the EBG Slab.

3.6.2 Relationship Between the Slab Thickness and the Size of the Bandgap

The effect of slab thickness on the width of bandgap is investigated for different slab thicknesses in different media for the cases of 3, 5, and 7 rings spaced with $H = 0.25\text{mm}$ and 1mm . Four different materials are considered, with relative permittivity ϵ_r of 2, 2.94, 4

and 9.2, as the supporting background for the OSR-based EBG structures. Dispersion characteristics shown in Figs. 3.27 and 3.28 demonstrate the impact of H on the band structure. The width of the bandgap can be maximized by selection of optimal number of rings for given H , slab thickness d , and permittivity. The figures show complete disappearance of band gap for certain parameters. This is due to the effect of dielectric material; the dielectric constant has the effect of shifting up (down) the frequencies of first (second) bundle of guided modes, causing additional modes to the detriment of the bandgap.

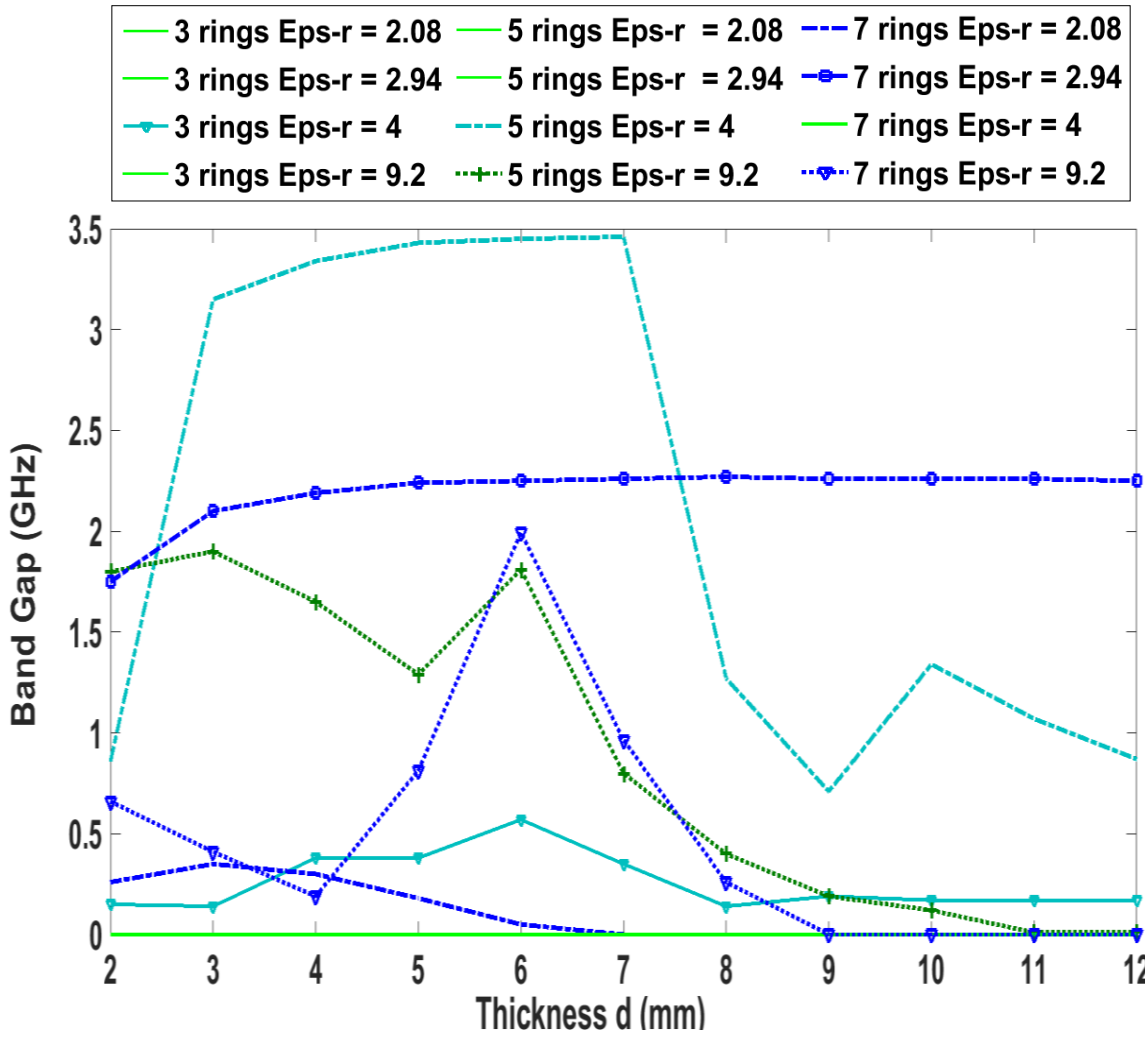


Figure 3.27 Variation of the band gap frequencies with slab thickness in different mediums : vertical spacing between rings is $H = 0.25$ mm.

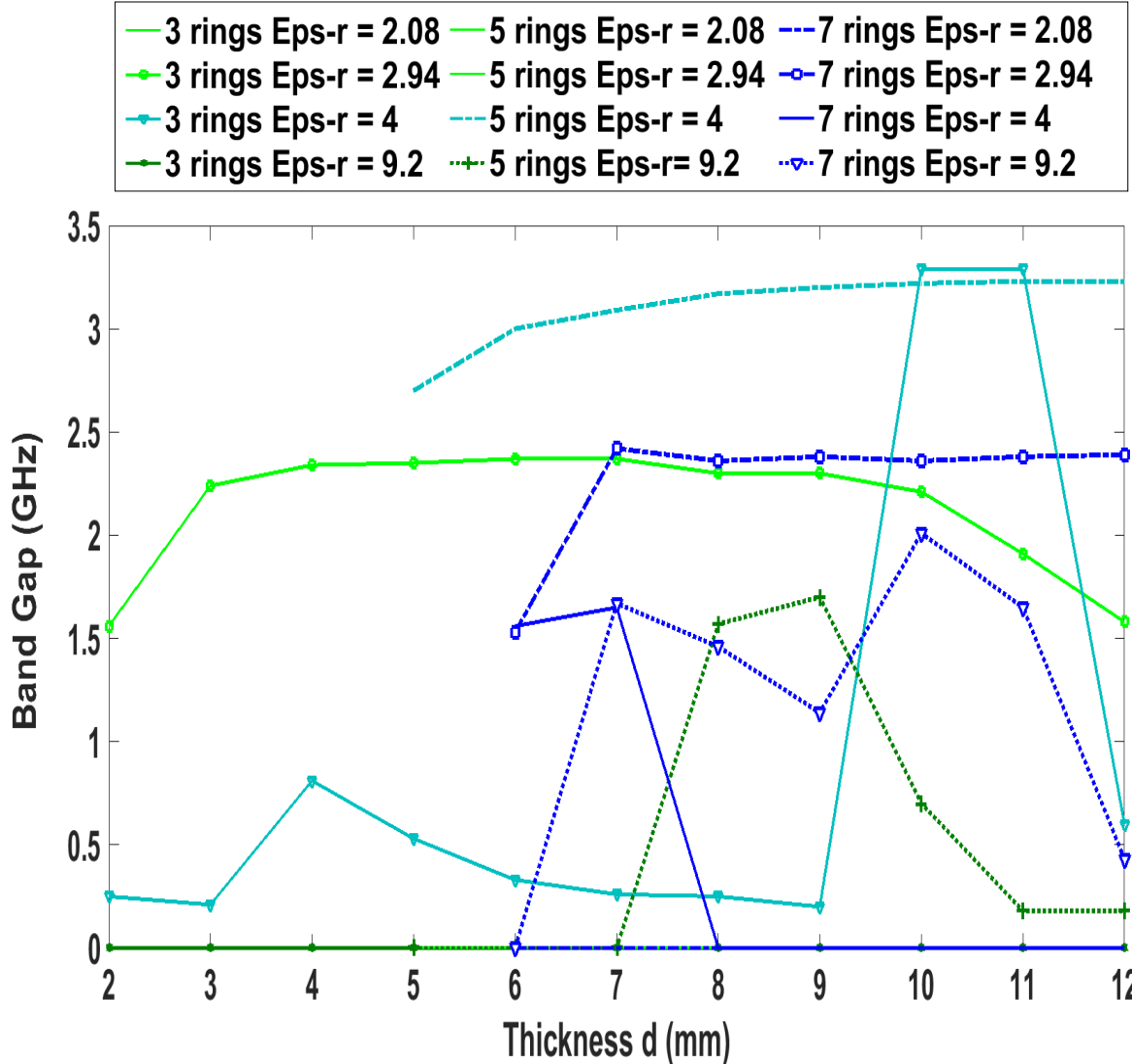


Figure 3.28 Variation of the band gap frequencies with slab thickness in different media : vertical spacing between rings is $H = 1 \text{ mm}$.

3.6.3 Band Structure

The OSR-based EBG slab structure was implemented with seven layered rings in Duroid dielectric medium RT 6002 with relative permittivity of 2.94 and loss tangent of 0.0012. The thickness of the substrate above and below the stacked rings is $t = 0.75 \text{ mm}$ and the thickness of the slab is $d = 3 \text{ mm}$. The vertical spacing between rings is $H = 0.25 \text{ mm}$. The band diagram for this slab is presented in Fig. 3.29, which shows a bandgap from frequency 8 GHz to 10.15 GHz. The solid black lines represent the light line, which determine the boundary between guided and radiation leaky modes. The former are modes localized within the slab while the latter are extended infinitely outside the slab.

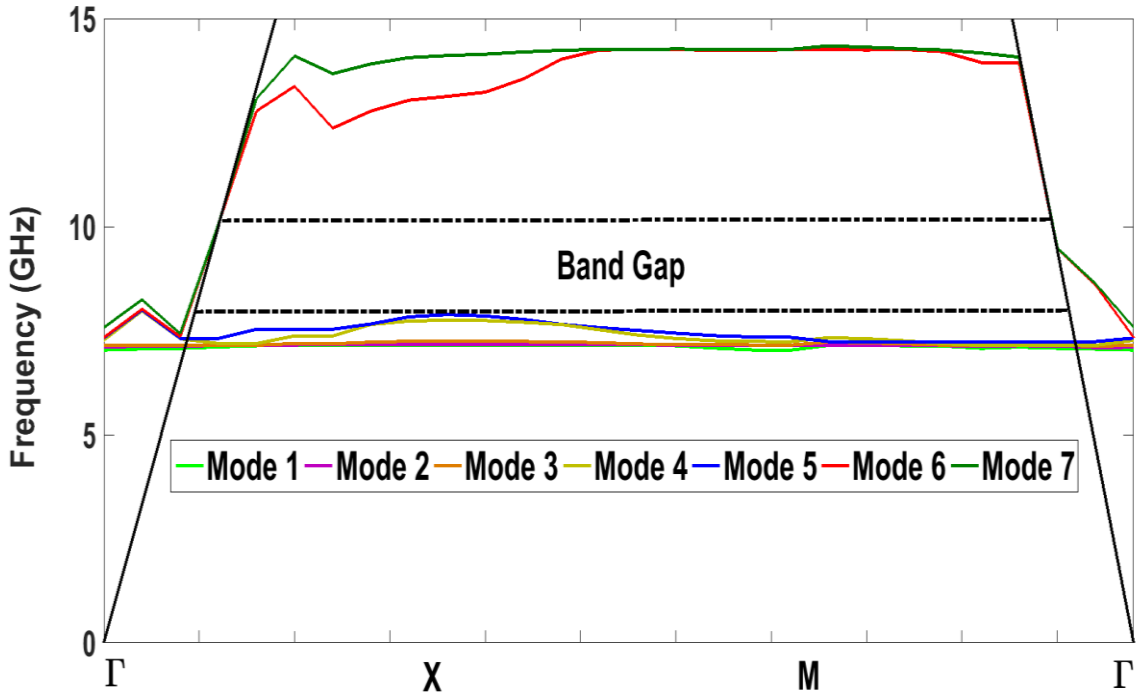


Figure 3.29 Band structure of the EBG slab of seven layered OSRs in dielectric medium of $\epsilon_r = 2.94$ and thickness $d = 3$ mm. Vertical spacing between rings is $H = 0.25$ mm. Black solid lines are the light lines.

3.7 EBG Slab Waveguide in Dielectric

As in section 3.4.1, a linear-defect waveguide can be formed by reducing the size of one row of rings (i.e., breaking the periodicity of the perfect crystal) in the layered EBG slab. Two types of waveguides were examined : line defect in single layer and line defect in all layers. Fig. 3.30 shows two waveguide configurations implemented in the slab structure presented in the previous section. Ring dimension was set the same as the one reported in Fig. 3.17.

To calculate the band structure of the waveguide, a super-cell with periodic boundary conditions was used. The cases of one, three, and six row(s) of stacked rings (i.e., which correspond to number of lattice constant(s)) on each side of the channel were investigated. Dispersion characteristic of the guide was not impacted significantly for different number of rows around the defect area and waveguide modes were confined to the channel area. It was observed that the line defect composed of n OSRs along z gives rise to n confined waveguide modes which established multi-mode guiding structure. These modes are

confined horizontally by the slab band gap and vertically by the slab itself. Single mode waveguide arises for single layer line of defects.

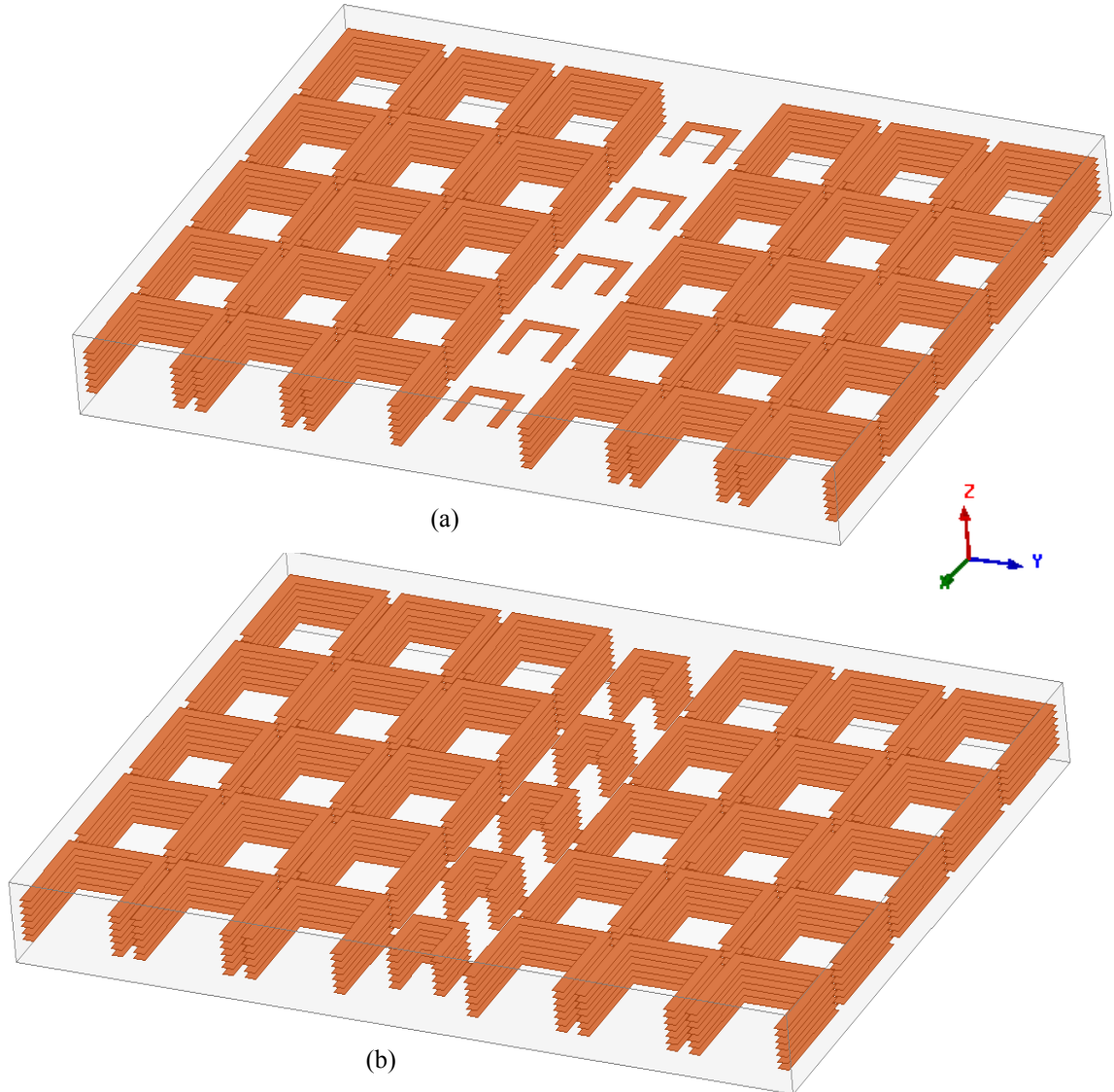


Figure 3.30 Line-defects slab waveguides embedded in a dielectric medium. (a) Line-defect in single layer. (b) Line-defect in all layers.

The dispersion diagram for waveguide having defects in single layer is shown in Fig. 3.31. Modes 1 and 2 lie within the band gap, but mode 2 is very close to the light line which reduces its chance to be confined within the channel guide. Fields and current profiles of these two modes show that only mode 1 is localized within the channel which qualifies the waveguide as single mode guiding structure.

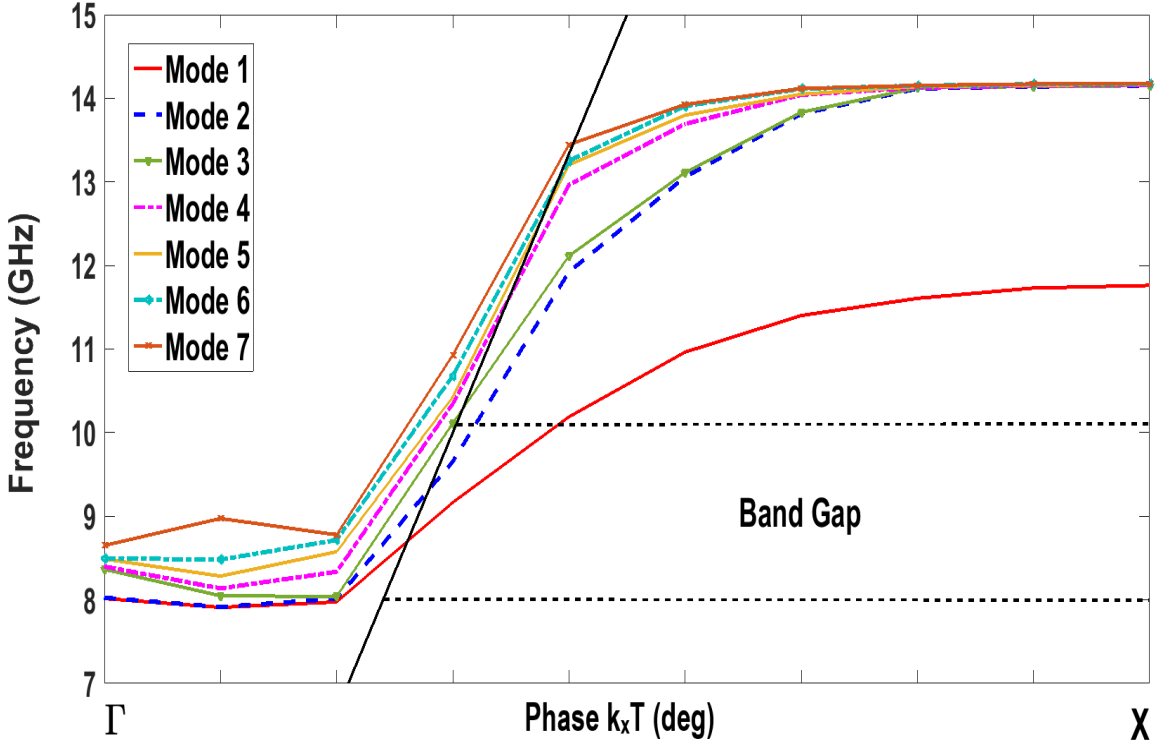


Figure 3.31 Band structure for channel waveguide having defects in single layer.

Having defects in all layers, results in typical band diagram shown in Fig. 3.32 which demonstrates downward shift of dispersion diagram to lower frequencies. This behavior is similar to the case with EBG within the air. Mode 1 is close to the lower edge of the band gap, thus, susceptible to coupling (i.e., for a shift of band gap edges toward upper frequencies, due to fabrication imperfection) to other slab modes. However, the other modes show some field confinement (at certain phase constants $k_x T$) in the defect region. Hence, the waveguide may present the possibility of having multi-modes. Note the flat behavior of the mode at increasing phase constant, which indicate that the mode presents low group velocity [75].

Despite the broadband characteristic offered by the two waveguides, the single-layered defects waveguide is superior as it offers single mode operation, which inhibits losses due to the coupling of energy to other confined modes outside the bandgap.

The impact of number of rows surrounding the channel on the dispersion diagram was investigated as well by considering waveguides with one, three and six row(s) of stacked rings on the sides of the channel and the result is shown in Fig. 3.33. It is observed that the

modes exhibit similar dispersion profiles, which proves that the number of rows of the perfect crystal adjacent to the channel has no significant impact on the guiding mode.

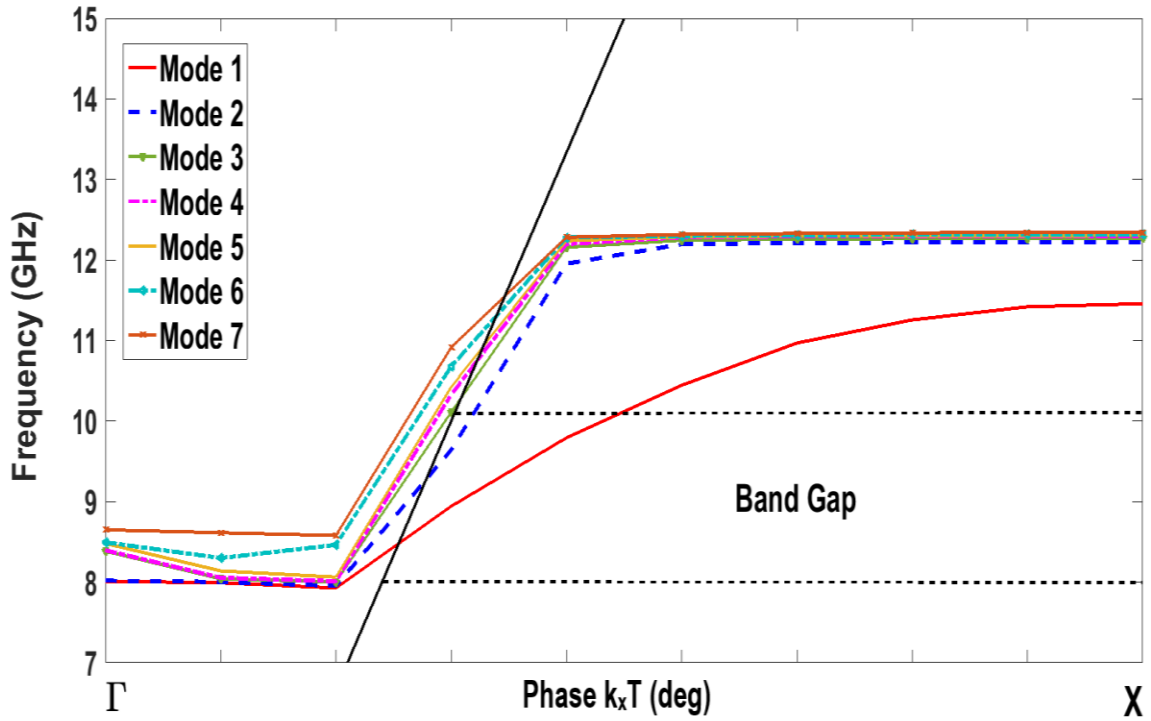


Figure 3.32 Band structure for channel waveguide having defects in all layers.

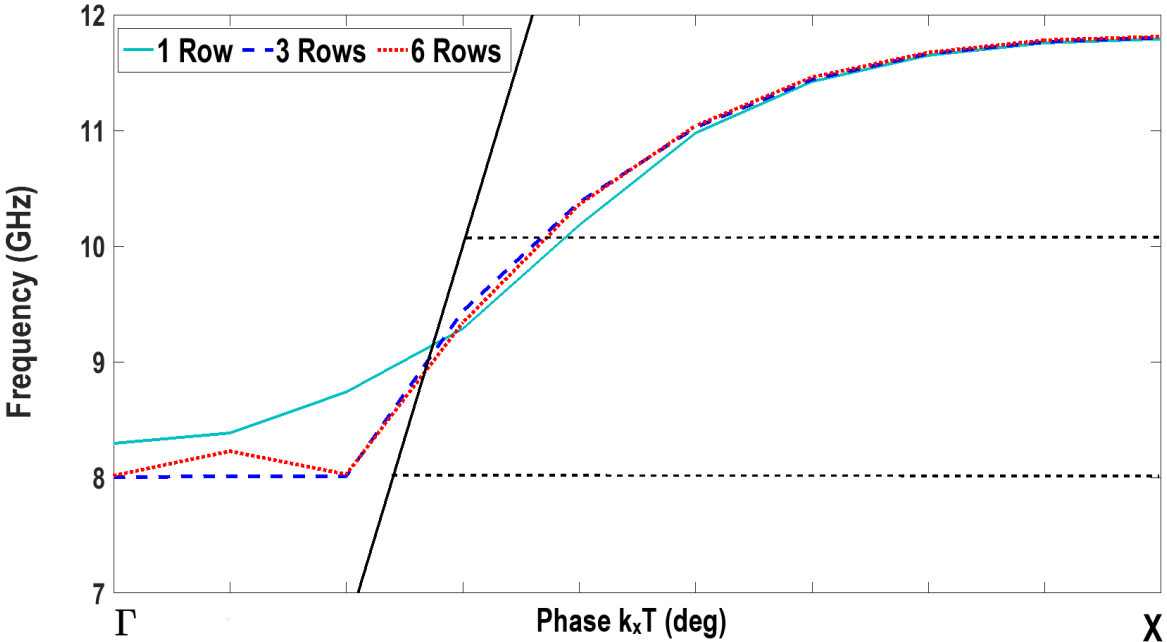


Figure 3.33 Band diagram of mode 1 of EBG waveguide of single layer defects with various rows on the sides of the channel.

3.8 Design For Different Frequency Bands

The analyses presented in this thesis were started by developing an EBG composed of OSRs that exhibits a band gap in the frequency range of 11-20.4 GHz. This design was validated at Ku-band by demonstrating an air-suspended line defect within an EBG slab. The operation of the structure was also verified in the frequency range 6.4 - 11.9 GHz by demonstrating a dielectric-supported line defect waveguide in the X-band. Therefore, The OSR structure can be designed to operate at a given frequency range by adjusting its embedded medium and/or structural parameters.

To operate the EBG at higher frequencies, the size of the geometrical features must be reduced. Keeping the above fact in mind, decreasing the size L element ring, gives rise to an upward shift of the frequency of modes 1 and 2. i.e., the OSR structure gives an LC effect and the bandgap positions can be determined by it. Therefore, the resonance is inversely proportional to the size of OSR.

$$\Omega_{LC} \propto \frac{1}{\text{size}}$$

The size of the OSR ring was reduced from 4.5 mm to 1.5 mm while other parameters kept unchanged. The parameters of the new U-shape design are as follows : $L = 1.5 \text{ mm}$, $W = 0.5 \text{ mm}$, $G = 0.5 \text{ mm}$, $H = 0.5 \text{ mm}$, and $T = T_x = T_y = 2 \text{ mm}$. Fig. 3.34 shows the dispersion diagram of the proposed structure in air and dielectric media.

The resulting band gap between modes 2 and 3 is quite wide. This design also offers a minor gap between 1 and 2. Table 3.3 illustrates these two band gaps.

The parametric analysis of the OSR ring, showed that reduced gap G and lattice constant T lead to decreased and increased frequency of the mode respectively. Hence, to locate the band gap in an upper (lower) frequency band, the lattice constant (the OSR gap) should be decreased. The lattice constant of the structure in Fig. 3.34 is reduced to 1.7 mm and the resulting dispersion characteristic is shown in Fig. 3.35. Table 3.4 presents the two band gaps of the adjusted design.

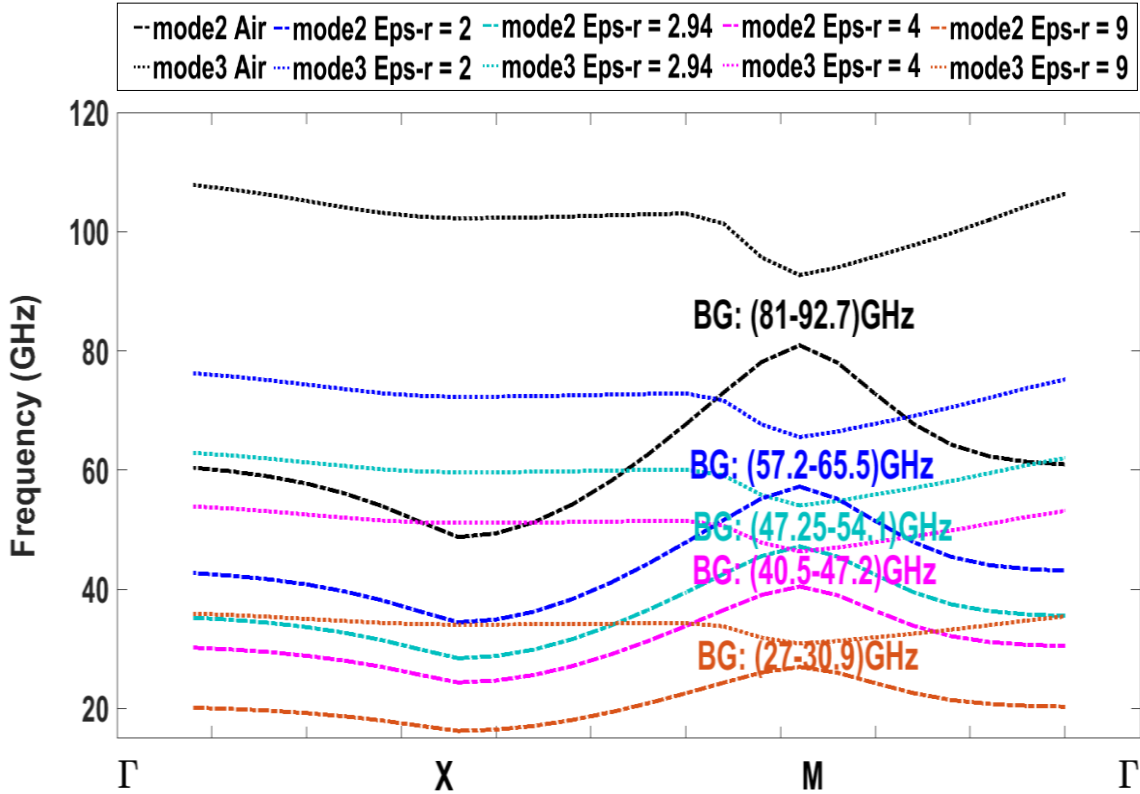


Figure 3.34 Dispersion diagram of the infinite reduced 1 U-OSR in air and dielectric media. Geometrical parameters are : L = 1.5 mm, W = 0.5 mm, G = 0.5 mm, H = 0.5 mm and T = 2 mm.

Table 3.3: Bandgaps of the reduced 1 U-OSR structure in different media. Geometrical parameters are : L = 1.5 mm, W = 0.5 mm, G = 0.5 mm, H = 0.5 mm and T = 2 mm.

Medium	First Minor Band Gap	Second Major Band Gap
Air	(47 - 48.7) GHz	(81 – 92.7) GHz
$\epsilon_r = 2$	(33.3 - 34.4) GHz	(57.2 – 65.5) GHz
$\epsilon_r = 2.94$	(27.4 - 28.4) GHz	(47.25 – 54.1) GHz
$\epsilon_r = 4$	(23.5 - 24.3) GHz	(40.5 – 47.2) GHz
$\epsilon_r = 9$	(15.6 -16.2) GHz	(27 – 30.9) GHz

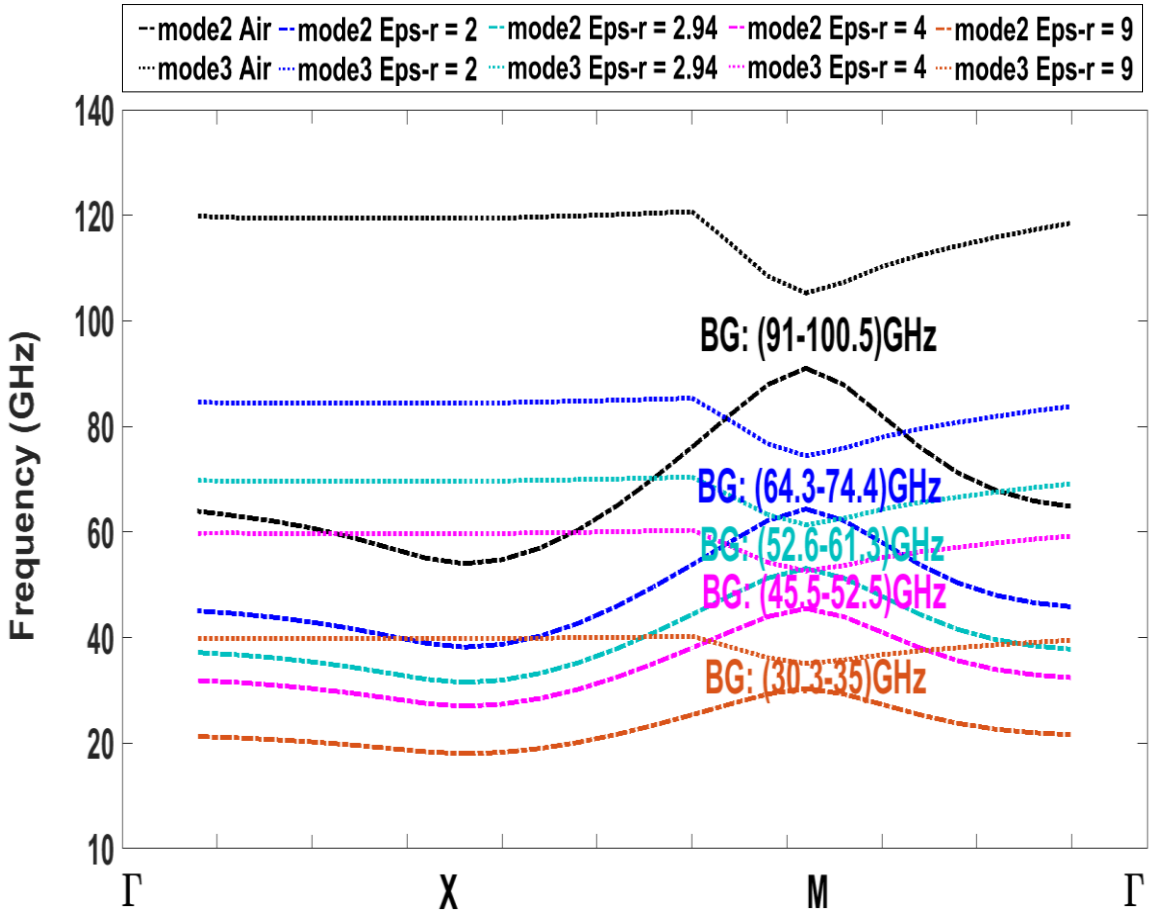


Figure 3.35 Dispersion diagram of the infinite reduced 2 U-OSR in air and dielectric media. Geometrical parameters are : $L = 1.5$ mm, $W = 0.5$ mm, $G = 0.5$ mm, $H = 0.5$ mm and $T = 1.7$ mm.

Table 3.5 and Fig. 3.36 results demonstrate dependence of the achievable resonance frequency on the geometric size of the OSR structure. An inverse proportionality relationship between the resonance frequency and dimensions of the OSRs causes translation of the operating band from C-band to W-band.

Table 3.4: Bandgaps of the reduced 2 U-OSR structure in different mediums. Geometrical parameters are : L = 1.5 mm, W = 0.5 mm, G = 0.5 mm, H = 0.5 mm and T = 1.7 mm.

Medium	First Minor Band Gap	Second Major Band Gap
Air	(45.2 – 54) GHz	(91 – 100.5) GHz
$\epsilon_r = 2$	(31.4 – 38.2) GHz	(64.3 – 74.4) GHz
$\epsilon_r = 2.94$	(26.3 – 31.4) GHz	(52.6 – 61.3) GHz
$\epsilon_r = 4$	(22.6 – 26.3) GHz	(45.5 – 52.5) GHz
$\epsilon_r = 9$	(15 – 18) GHz	(30.3 – 35) GHz

Table 3.5: Bandgaps of the conventional and reduced U-OSR structure in different mediums. Geometrical parameters are :

L = 4.5 mm, W = 0.5 mm, G = 3.5 mm, H = 0.5 mm and T = 5 mm (conventional U-OSR)

L = 1.5 mm, W = 0.5 mm, G = 0.5 mm, H = 0.5 mm and T = 2 mm (reduced 1 U-OSR)

L = 1.5 mm, W = 0.5 mm, G = 0.5 mm, H = 0.5 mm and T = 1.7 mm (reduced 2 U-OSR)

Medium	U-OSR	First Band Gap	Second Band Gap
Air	Conventional U-OSR	(11 - 20.4) GHz	(30.9 - 35.5) GHz
	Reduced 1 U-OSR	(47 – 48.7) GHz	(81 – 92.7) GHz
	Reduced 2 U-OSR	(45.2 – 54) GHz	(91 – 100.5) GHz
$\epsilon_r = 2$	Conventional U-OSR	(7.8 - 14.4) GHz	(21.8 - 25.1) GHz
	Reduced 1 U-OSR	(33.3 – 34.4) GHz	(57.2 – 65.5) GHz
	Reduced 2 U-OSR	(31.4 – 38.2) GHz	(64.3 – 74.4) GHz
$\epsilon_r = 2.94$	Conventional U-OSR	(6.4 – 11.9) GHz	(18.1 – 20.7) GHz
	Reduced 1 U-OSR	(27.4 – 28.4) GHz	(47.25 – 54.1) GHz
	Reduced 2 U-OSR	(26.3 – 31.4) GHz	(52.6 – 61.3) GHz
$\epsilon_r = 4$	Conventional U-OSR	(5.5 – 10.2) GHz	(15.4 – 17.8) GHz
	Reduced 1 U-OSR	(23.5 – 24.3) GHz	(40.5 – 47.2) GHz
	Reduced 2 U-OSR	(22.6 – 26.3) GHz	(45.5 – 52.5) GHz
$\epsilon_r = 9$	Conventional U-OSR	(3.6 – 6.8) GHz	(10.2 – 11.8) GHz
	Reduced 1 U-OSR	(15.1 – 16.2) GHz	(27 – 30.9) GHz
	Reduced 2 U-OSR	(15 – 18) GHz	(30.3 – 35) GHz

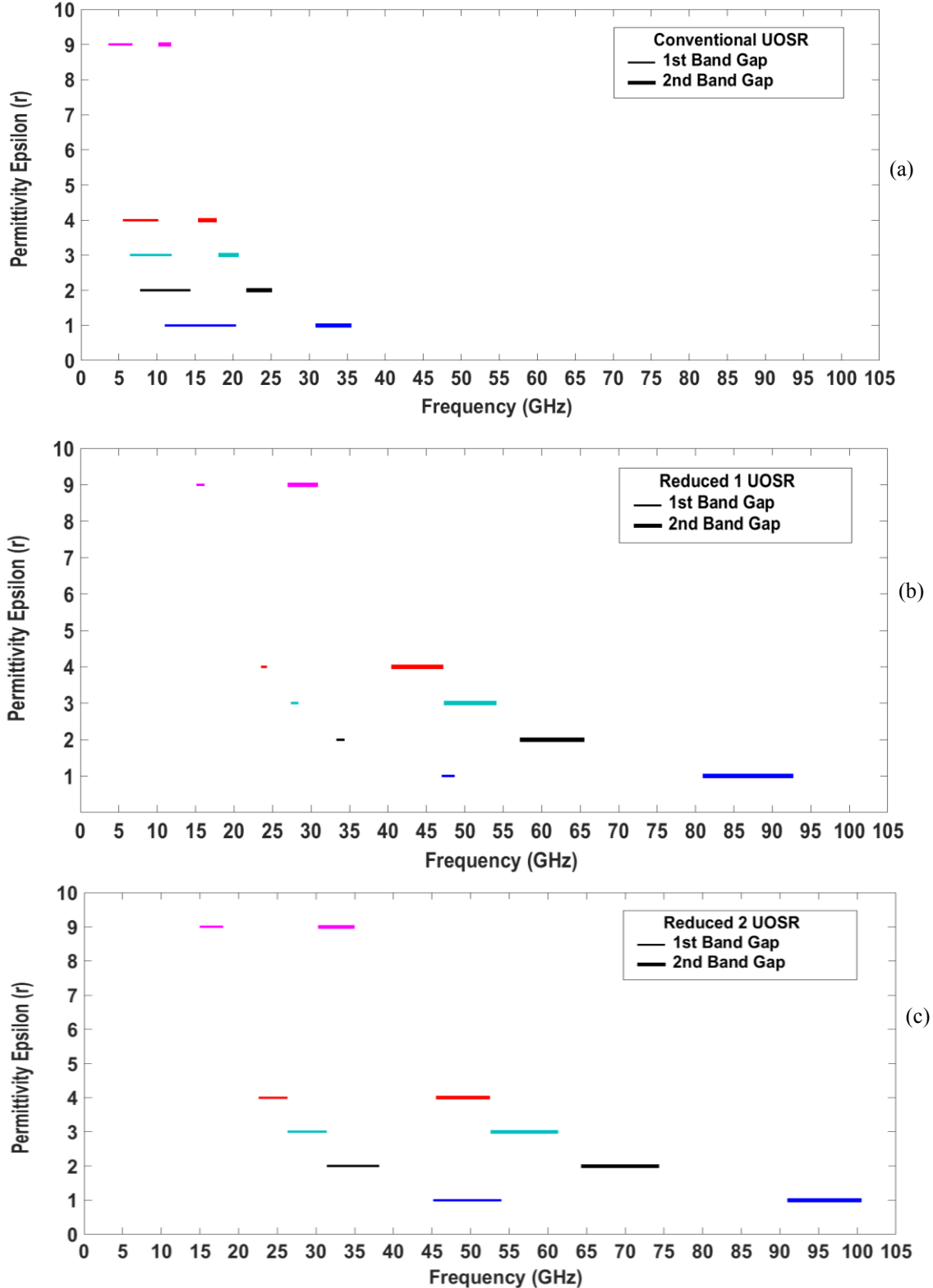


Figure 3.36 Band gap frequencies of the UOSR in different mediums. (a) Conventional UOSR, (b) Reduced 1 UOSR and (c) Reduced 2 UOSR. Narrow and wide lines represent first and second band gaps respectively.

3.9 Conclusion

A novel EBG based open square rings was presented in this chapter. The structure was first studied in air, then in dielectric using eigenmode solver of the full-wave Ansys HFSS. The effects of ring geometrical parameters on the band gap were investigated for the OSR-based EBG in the air medium. As one possible outcome, the optimum ring size for maximum width of the band gap was obtained. The band structure of arrays of finite thickness, i.e. slab EBG structure, was also analyzed. The effect of slab thickness on the band gap was studied. By changing the size of a row of rings in the slab structure, guiding structure was created operating within frequency band of the full lattice EBG bandgap. It was shown that the number of guided modes at different frequencies are specified by the number of layers within the defect region. On the other hand, in absence of defects within the layers, guided modes cease to exist. Having selected the U-OSR, a detailed study was performed of EBG slab and waveguide in dielectric medium. Similar modal behaviour has been observed for the EBG OSR structure in both media.

In order to operate the U-OSR at higher frequencies, one can reduce the size of the ring, and/or the lattice constant of the crystal. OSR structure provides major and minor band gaps.

The geometrical parameters of this EBG OSR can be designed to meet application requirements. To be more specific, such design requirements might correspond to matching the operational bandwidth of a device to the bandgap of the EBG.

CHAPTER 4. IMPLEMENTATION AND CHARACTERIZATION

4.1 Introduction

In the previous chapter, numerical characterization of OSR structures was presented in air or dielectric media using eigen-mode analysis. The dispersion diagrams and field patterns of infinite arrays of cells were computed and followed by a study of a two-dimensional (2-D) EBG slab waveguide. The present chapter focuses on design, fabrication and experimental verification of EBG linear-defect waveguides with integrated feeding circuits. The fabricated EBG guides were based on the models presented in sections 3.4.1 and 3.7 that operate at Ku- and X- bands, respectively. A unique feature of the proposed structures is the planar layered PCB fabrication. Specifically, the excitation circuit is single layer and the layers are supported by either foam or dielectric material.

This chapter is organized as follows. Section 4.2 is devoted to the implementation of foam-based EBG waveguide along with the presentation of field distributions inside the EBG channel and the conventional feed circuit, which is composed of a CPW to slot-line transition. Simulation and experimental results of three configurations of Ku-band prototypes are presented and sensitivity analysis is performed to investigate the impact of vertical misalignment. Section 4.3 addresses design, implementation, and experimental characterization of dielectric-based EBG waveguide. Finally, Section 4.4 is devoted to the concluding remarks.

4.2 EBG Waveguide Foam Supported

This section deals with the implementation of foam-based EBG waveguide through detailed presentation of the feeding scheme, as well as simulation and measurement results for a set of foam-based EBG guiding structures. To recall, the foam configuration most closely represents the original air-based OSR structure. Some material of this section is in [76].

4.2.1 Channel Field Distributions and Feed Transition Concept

In order to realize an appropriate transition from conventional waveguides to the EBG channel, we first examine the field distributions. The E- and H- field distributions of mode 1 of the EBG waveguide are shown in Fig. 4.1, which exhibit resemblance to the field distributions of the dominant mode TE₁₀ of a slot line [77]. This is not unexpected as the EBG structure supports TE modes. This implies the possibility of exciting the in-gap EBG guided mode with a conventional slot line. An effective way to feed the EBG channel with a slot line is to use CPW-to-slot line transition.

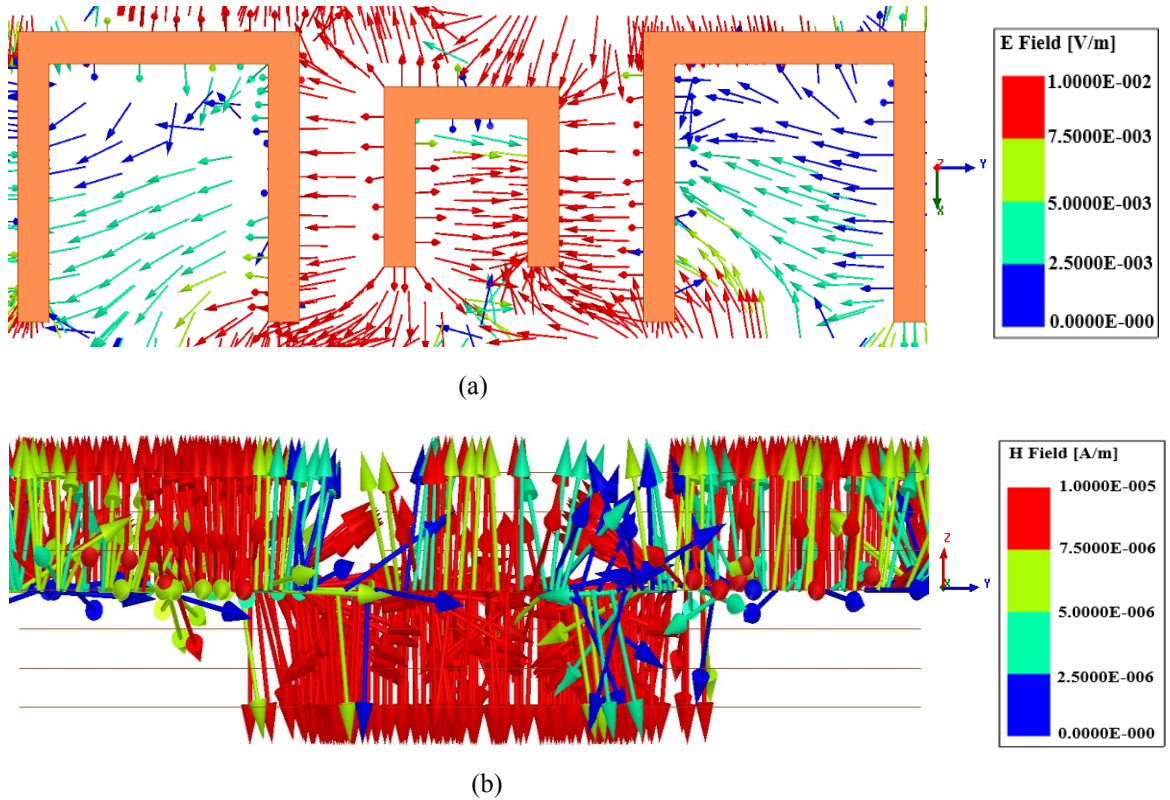


Figure 4.1 Field distributions of mode 1 of the EBG channel based-foam. (a) E-field in horizontal (xy) cross section. (b) H-field in vertical (yz) cross section.

Fig. 4.2 shows the proposed structure for transition from the waveguide to coaxially-connected external components. It is inspired by [78] and consists of three sections: CPW input, phase delay and slot line. The CPW line has two parallel slot lines with 180° phase difference between E-field distributions within the slots (dominant mode of CPW). The 90° bend open stub works as a phase shifter supplying 180° phase shift to delay the phase of one of the CPW constituent slot line fields. Basically, the transition enables the in-phase

excitation of the fields at the end of the delay slot line. The structure was optimized through adjustment of the following parameters: coplanar slot width W_g , coplanar central conductor width W_c , slot line width W_s and length L for the back-to-back configuration. The dimensions of the CPW line were chosen to have 50Ω characteristic impedance over the operating frequency band and the width of the slot line was optimized to obtain the best performance for the EBG channel guide.

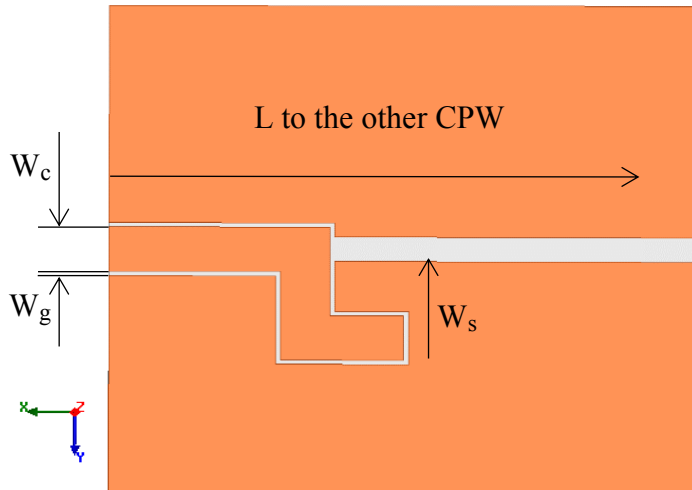


Figure 4.2 Geometry of the CPW-to-Slot line transition.

4.2.2 Fabricated Prototypes

The aforementioned transition was first etched on a 1 mil thick Kapton substrate with a copper thickness of 9 microns and relative permittivity of 3.5. Measured back-to-back arrangement did not perform well due to difficulties in fabrication. To overcome this problem a new transition was designed on 60 mils RT/Duroid® RO3035 substrate, copper thickness of 9 microns and relative permittivity of 3.6. The transition was defined by the following parameters: gap width $W_g = 0.1$ mm, strip width $W_c = 1$ mm, slot width $W_s = 0.55$ mm. For the back-to-back test configuration, consisting of CPW-transition-slot line-transition-CPW, the length of the structure was set at 43.8 mm. Simulated and measured results are shown in Fig. 4.3 for the back-to-back configuration with $L = 43.8$ mm and 63.8 mm. The measured return loss is better than 12 dB across the band, while the insertion loss has a mean value of 1.9 dB above 15 GHz; the transition was performing as expected and there was less than 1 dB difference in comparison with simulated insertion loss. the ripple effects observed in S1 are indicative of the characteristic impedance of the slot-line section

not being exactly 50 Ohms. The discrepancy of S21 at the lower frequency range (below 15 GHz) was caused by leakage/radiation losses from the CPW discontinuities.

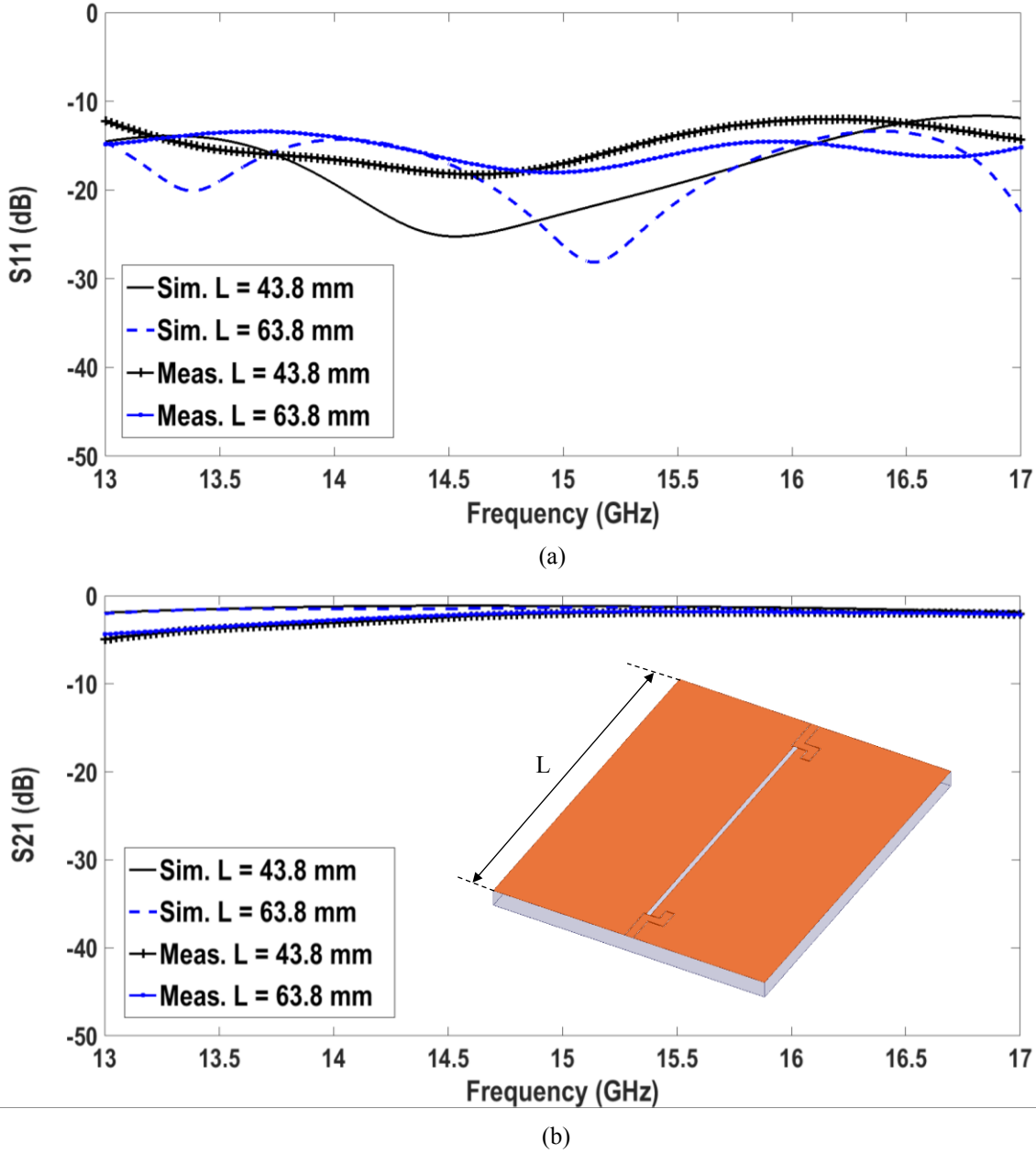


Figure 4.3 Simulated and measured S-parameters of the back-to-back CPW-to-slot line transition of lengths $L = 43.8$ mm and 63.8 mm. (a) S11 and (b) S21. Transition is shown in the inset of (b).

The prototyping of the EBG waveguide is considered next. The channel guide of seven layers with defects and six rows on each side of the channel as shown in Fig. 4.4, is used to implement the planar circuit. In the structure, the feeding CPW-slot-line transitions are

placed at the fourth (excitation) layer of the guide. The overall dimensions of the proposed design i.e., $L \times W \times H$ are 43.8 mm x 65 mm x 6.18 mm. The length of the channel is 19.8 mm (4 periods). The layered rings and the transitions at the entrance (In) and exit (Out) of the channel guide are supported by foam material.

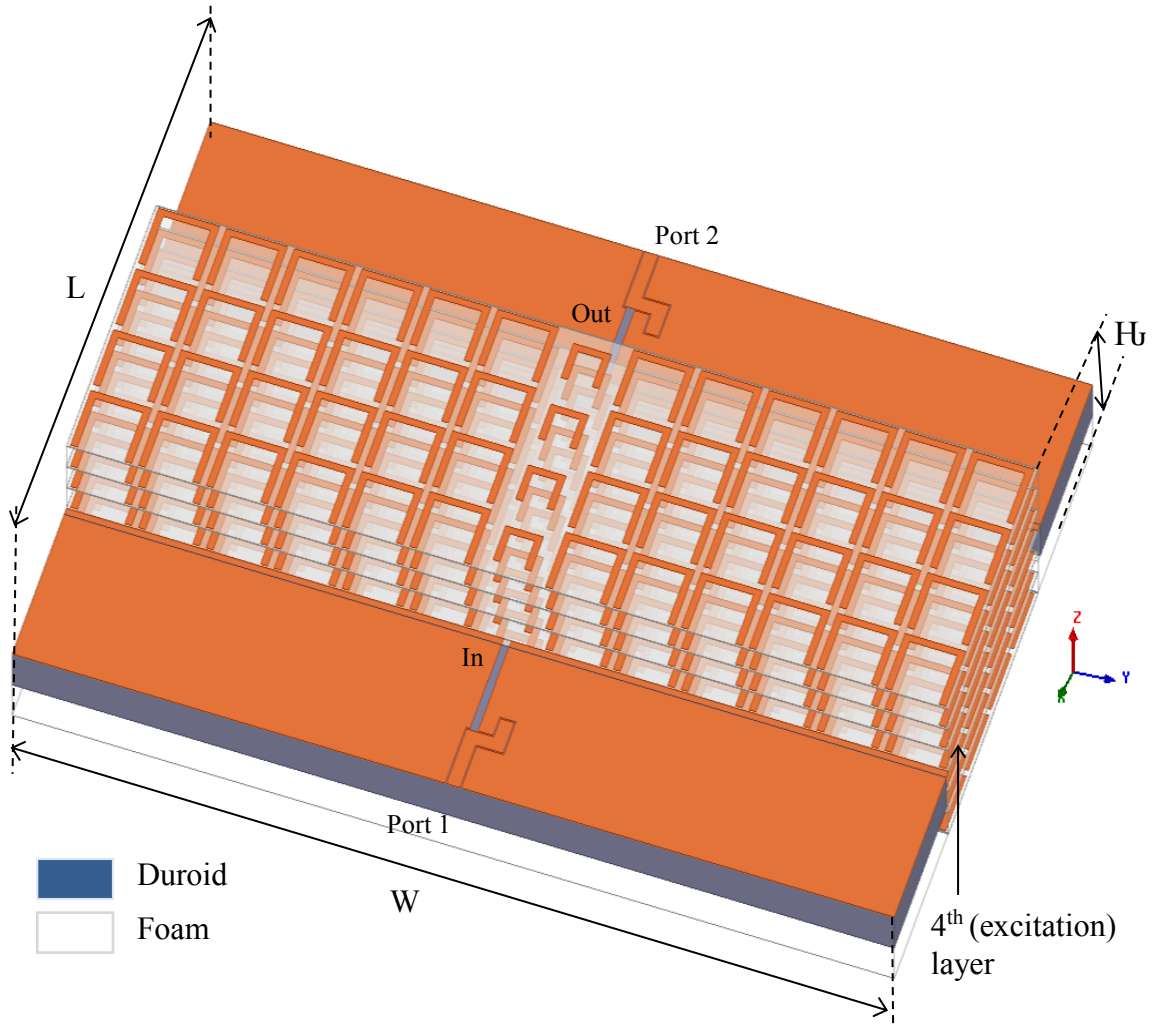


Figure 4.4 CPW-to-Slot line fed EBG waveguide based-foam. The guide has seven layers with defects and six rows on each side of the channel. The channel length is 19.8 mm (4 periods). Total dimensions of the guide are L (43.8 mm) x W (65 mm) x H (6.18 mm).

Seven waveguides in Fig. 4.5 were experimentally studied. Two types of waveguide that originated from the structure depicted in Fig. 4.4 are reduced stacked defect rings (RDR) waveguide for which the number of defect rings is decreased vertically from seven to four and reduced lateral rows of stacked rings (RRR), where three rows have been removed from each side of the channel. Fig. 4.5 shows a photograph of several fabricated EBG waveguide

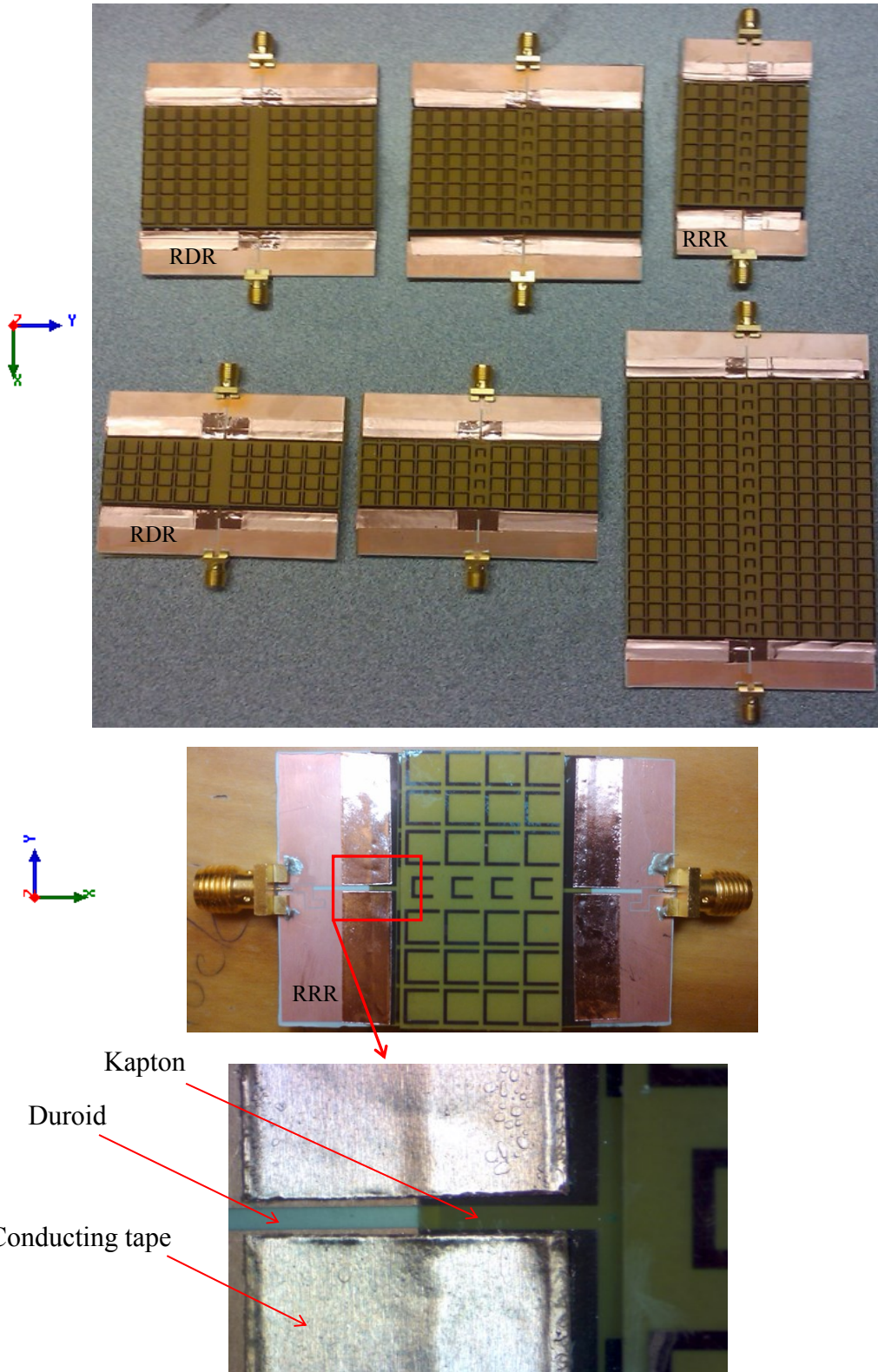


Figure 4.5 Photo of the fabricated EBG waveguide prototypes with transitions. The enlarged view shows the connection between the slot line of the transition on Duroid and the existing slot line on the Kapton sheet. Conducting tapes are used to make the connection.

prototypes and new transitions, connected in a back-to-back configuration and their SMA connectors. Conducting tapes were used in development to make an electrical connection between the slot line of the new transitions and the existing slot line on the Kapton sheet. This non-ideal fabrication may indeed cause additional losses.

4.2.3 Simulated and Measured Results

The simulated and measured performances of the seven waveguides of Fig. 4.5 are now examined. Fig. 4.6 shows simulated and measured S-parameters of the waveguide depicted in Fig. 4.4 for three different lengths of 43.8 mm, 63.8 mm and 103.8 mm, which correspond to channel lengths of 4 periods, 8 periods and 16 periods, respectively. The simulated S-parameters show 1 GHz transmission bandwidth from 15.2 GHz to 16.2 GHz, for which the mean value of insertion loss is around 1.8 dB (i.e., excluding the contribution of the two CPW-to-slot line transitions) and the return loss is better than 14 dB. An improved return loss performance is observed for longer channels. This indicates that the guided mode is influenced by the periodic structure along the guided direction.

Simulation results of waveguide length of 103.8 mm are not available due to the restriction of computational resources (CPU and memory). Measured insertion loss mean values are 3.75 dB for the 4 and 8 periods and 4.62 dB for the long 16 periods in the 15 GHz-16 GHz, excluding the contribution of transitions. Therefore, the losses are 0.28 dB/period (0.056 dB/mm) for 16 periods long EBG guide. This value is close to (0.058 dB/mm at 10 GHz) in what was measured in [79] for a coplanar line.

The simulated and measured S-parameters of the RDR waveguide of the channel lengths 4 and 8 periods are given in Fig. 4.7 that demonstrate 15.2 GHz-16.2 GHz transmission characteristic (simulated return loss greater than 15 dB, insertion loss has a mean value of 2.4 dB, excluding transition losses). The insertion loss has been increased by reducing the number of vertical defects. This is due to the lack of vertical confinement in the layered channel. This agrees with Fig. 3.24 which shows that the mode is pushed away from the band gap toward the light line. i.e., is not highly confined in the channel.

Measured insertion loss mean values are 3.3 dB for the short 4 periods and 3 dB for the long 8 periods in the 15 GHz-16 GHz, excluding the contribution of transitions. The losses

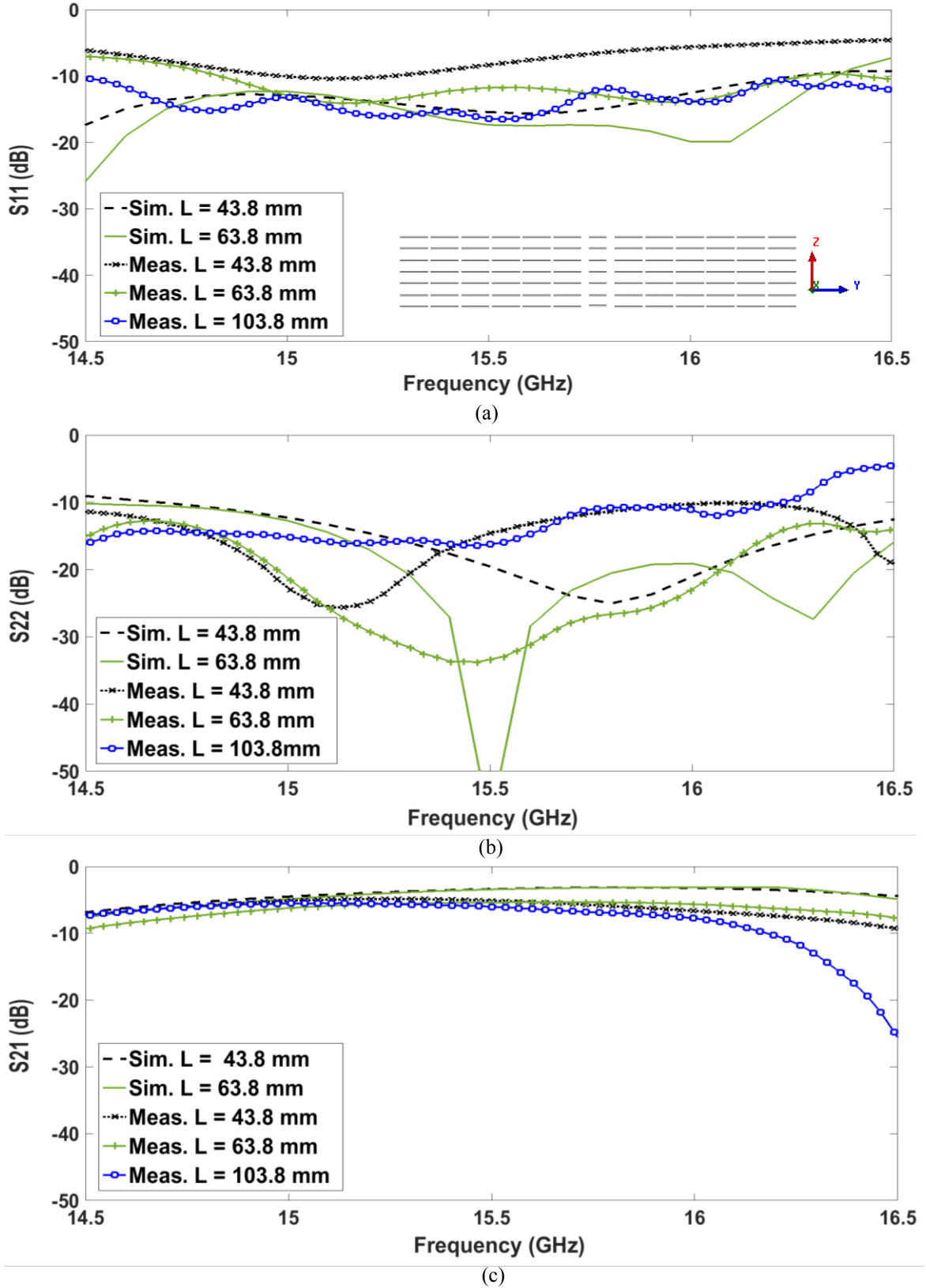


Figure 4.6 Simulated and measured: (a) S_{11} , (b) S_{22} and (c) S_{21} of EBG guide in Fig. 4.4 of lengths $L = 43.8$ mm, 63.8 mm and 103.8 mm. Cross section of the guide is shown in the inset of (a).

are 0.37 dB/period (0.075 dB/mm) for 8 periods long EBG guide. This value is close to the theoretical value.

In both guides, the simulated insertion loss is higher below 15 GHz that agrees well with eigen-mode simulations that showed inferior field confinement in the guiding channel. The same conclusion can be drawn from the dispersion diagram shown in Fig. 3.24, where the in-gap mode is very close to the light line that makes it more susceptible to radiation.

The performance of the RRR waveguide for channel lengths of 4 and 8 periods is shown in Fig. 4.8, which demonstrates transmission bandwidth of 14.4 GHz-15.4 GHz, with a slightly higher simulated insertion loss of 3.1 dB. Measured insertion loss is 4.8 dB. Therefore, the losses are 0.6 dB/period (0.12 dB/mm) for the 8 periods guide. This indicates that the electromagnetic energy is not highly concentrated in the guiding region that is caused by insufficient EBG crystal on both sides of the channel. This agrees with Fig. 3.24 (i.e., for the case of seven layers with six rows on the sides the channel, as changing the number rows does not impact the dispersion) that shows that the mode 1 is very close to the light line in the frequency range 14.4 GHz-15.4 GHz. As is well known, the guided mode bounces back and forth between the crystal walls as it is propagating along the channel. Its fields decay exponentially into the crystal.

The transmission bandwidths of the three EBG waveguides are within frequency range of the computed dispersion diagrams. Although, eigen-mode simulations show similar dispersion characteristic of the waveguides, driven mode simulations present slightly different results, where the performance of the RRR waveguide is shifted to lower frequencies with an increase of the insertion loss. This is due to the fact that the number of rows on the two sides of the channel affect the guided wave in the EBG channel. This behavior results from the destructive Bragg interference (no reflection) that arise from the insufficient surrounding crystal regions.

Note also that increasing the length of an EBG-OSR channel does not significantly impact the insertion loss of the waveguide.

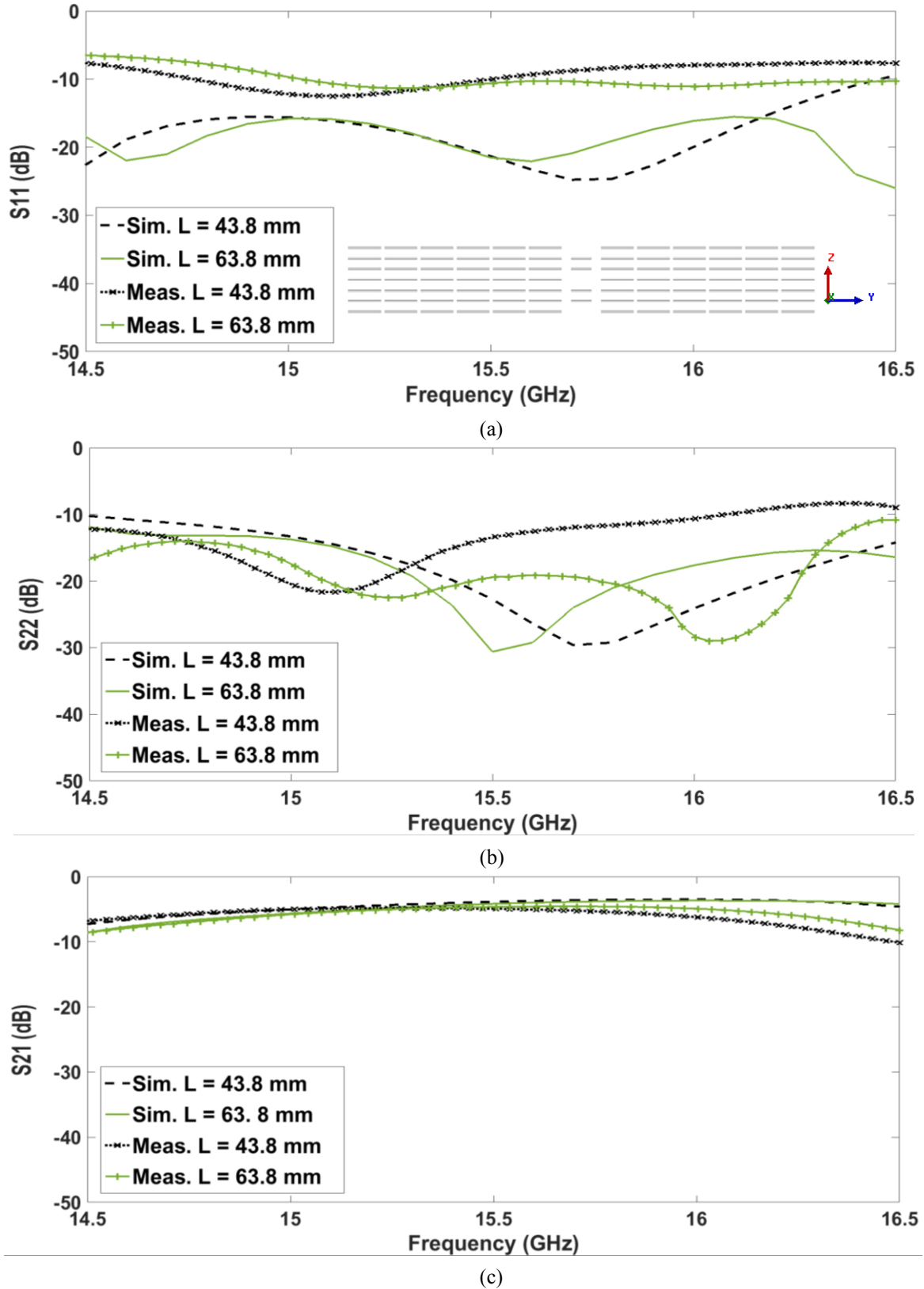


Figure 4.7 Simulated and measured: (a) S_{11} , (b) S_{22} and (c) S_{21} of EBG RDR guide of lengths $L = 43.8 \text{ mm}$ and 63.8 mm . Cross section of the guide is shown in the inset of (a).

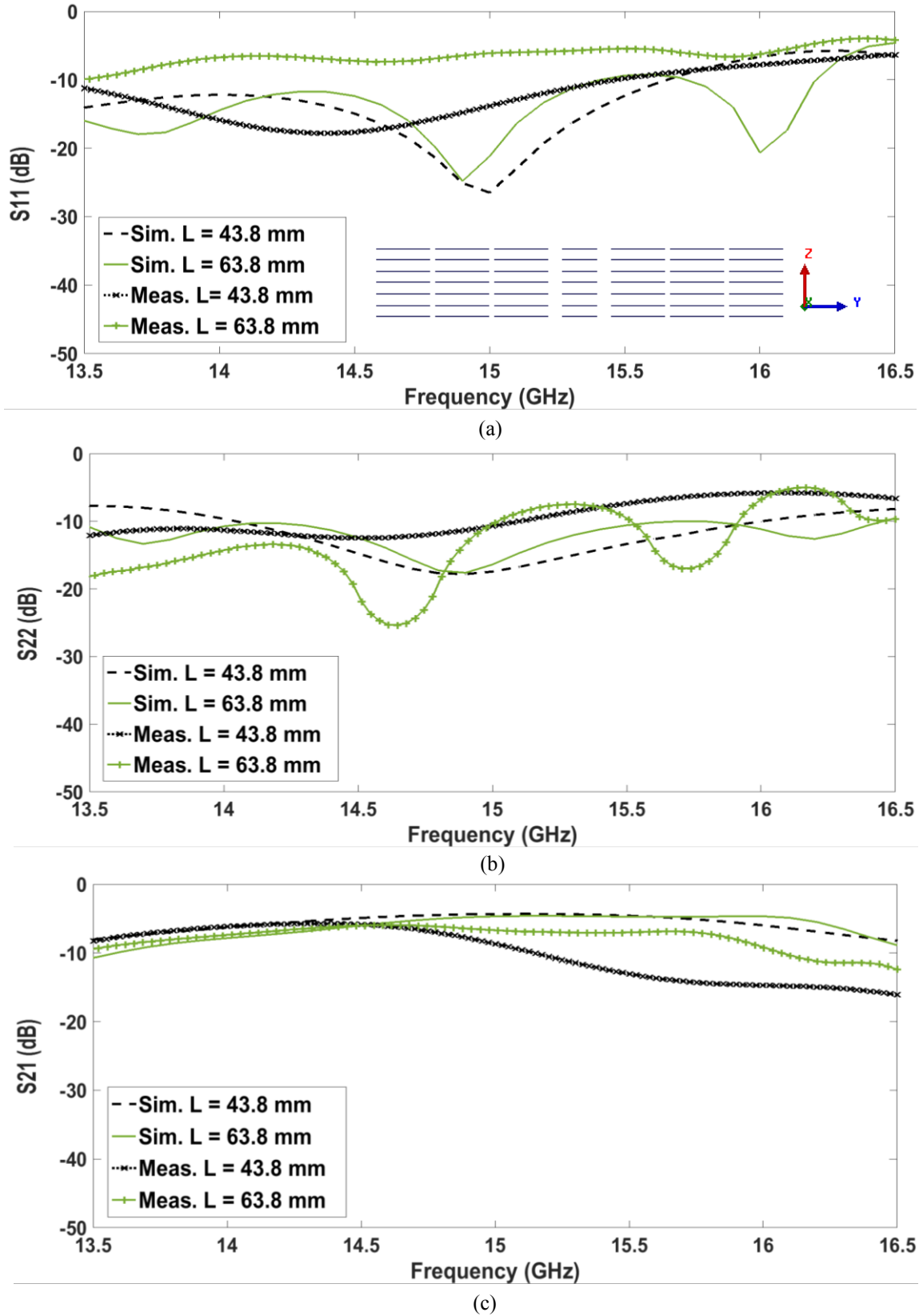


Figure 4.8 Simulated and measured: (a) S_{11} , (b) S_{22} and (c) S_{21} of EBG RRR guide of lengths $L = 43.8 \text{ mm}$ and 63.8 mm . Cross section of the guide is shown in the inset of (a).

The losses in the EBG waveguides are mainly attributed to leakage from the transitions, surface waves and leakage along the interface transition/rings. The latter arises from inefficient power transmission from the slot line channel to the EBG channel and vice versa. The difference in guiding mechanisms between the two channels is responsible for non-perfect coupling. The EBG (Bloch) mode is affected by scattering inside the crystal and it contains forward- and backward- traveling fields contributions (Bloch-Fourier components) whereas the slot line mode contains only forward- propagating field components. The existence of field along the interface transition/rings at the right and left of the channel end is attributable to the excitation of surface modes [2;80]. These modes are the result of the termination of the periodic rings (i.e., broken periodicity) and couple with the guided mode. To support these arguments, Fig. 4.9 shows the electric field distributions at $f = 15.8$ GHz, in the waveguide of Fig. 4.4 of lengths 43.8 mm (4 periods) and 63.8 mm (8 periods). As can be seen in the both plots the mode is well confined to the channel with field leakage from the transition and EBG channel.

Note that the leakage strength inside the periodic structure in the longer channel (8 periods) is less intense than the one in the shorter channel (4 periods). This is due to the effect of distributed Bragg reflection (DBR) [72] that depends on the length of the periodic structure in the guiding direction. In Fig. 4.6, the reflection is lower for longer channel while the transmission is stable. This is due to the longer interaction between the propagating field and the crysral region (i.e., the propagating mode experiences strong reflections by the periodic structure). If the leakage were due to coupling to other EBG modes, the transmission would be much lower than the plotted value.

Due to the required computational time, simulation results of the EBG waveguides do not include conductor losses. Despite the symmetry of the simulated eigen mode, measured S11 and S22 are not equal that can be explained by difference in the interply of the electric field within the slot line and EBG guided channel field at port one and two. Measured results include the effects of the two CPW-to-slot line transitions. There is some disagreement between simulated and measurement results that is due to fabrication imperfections such as vertical misalignment of the layers (to be addressed in the next section), conductor losses and manual non-ideal connection of the Kapton and Duroid slot lines. The latter obviously induces unavoidable small air gaps which in turn generate some field radiation on the air

side. Furthermore, connection of the new transitions to the EBG channel forms a quasi-homogeneous structure; in a sense that the propagating wave sees media of different dielectric constants. This creates a discontinuity in the feed line and results in degradation in return loss performance. These limitations of the prototypes are attributable to the initial fabrication of the novel layered EBG structure which aimed at verification of the design concept. In this regard, the performance of this EBG waveguide is not directly comparable to conventional transmission lines.

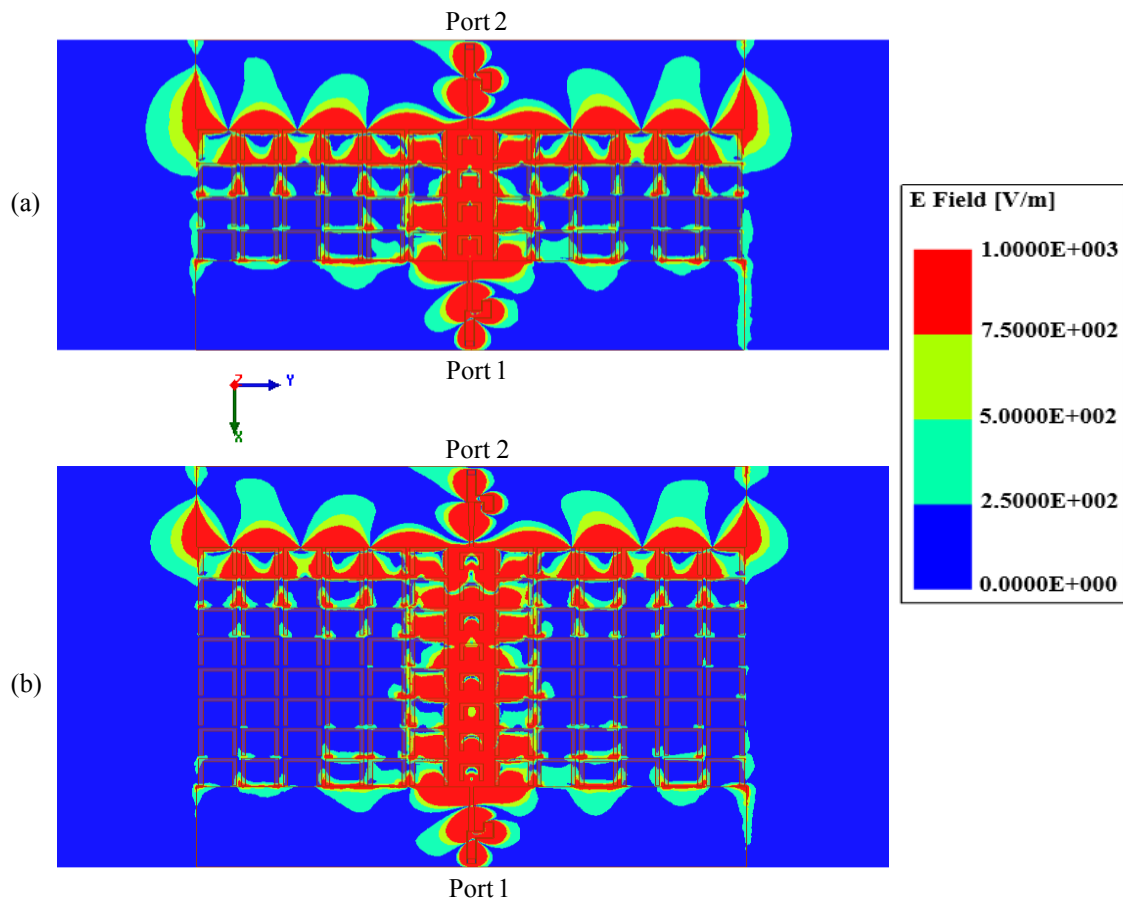


Figure 4.9 Electric field distribution at $f = 15.8$ GHz in the EBG waveguide channel of length: (a) Four periods (a). (b) Eight periods.

4.2.4 Sensitivity Analysis and Vertical Misalignment

The above results demonstrate the concept of waveguiding in a layered periodic metallic ring medium. However, visual inspection (Fig. 4.5) of the layer to layer alignment of this design revealed an offset of the top 3 layers with respect to the feed layer (layer 4), and the

same offset for the bottom 3 layers with respect to layer 4 needs to be improved. Here, this vertical misalignment of the layered rings is assessed by the position offset of the layers. Fig. 4.10 shows the simulation results of the RDR waveguide when the top 3 and bottom 3 layers being positioned 0.5 mm and 1 mm off horizontally (along positive x-axis, Fig. 4.4) from the center (4th) layer. The simulated results of the original case (i.e. without offset) are also shown for comparison. As can be seen from the graphs corresponding to the RDR waveguide (Fig. 4.7 and Fig. 4.10), the misalignment shifts the operating band and degrades the performance of the waveguide exactly in the manner that was observed in the measured S-parameters. Therefore, the disagreement between simulations and measurements of the presented waveguide configurations are attributed mainly to misalignment, on the order of 1 mm in this case. To illustrate more clearly, Fig. 4.11 compares the simulated (for 1 mm offset) and the measured results of the waveguide. S11 and S22 are now in close agreement, while the remaining difference between the simulated and measured S22 troughs (15.2 GHz and 15.5 GHz) confirms that other minor factors are at play, such as the connector mounting and conductive tape transitions cited above. Indeed, the vertical misalignment of the layers could be alleviated by using other fabrication technologies such as photoimageable thick-film and LTCC.

This sensitivity of the EBG structure to misalignment can be utilized as a strain sensor [81] applications. For instance, if an object is under stress along the x-axis, the EBG-based sensor will deform following the object. i.e., displacement distance of the layers along the x-axis. This change will result in a shift in the resonance frequency.

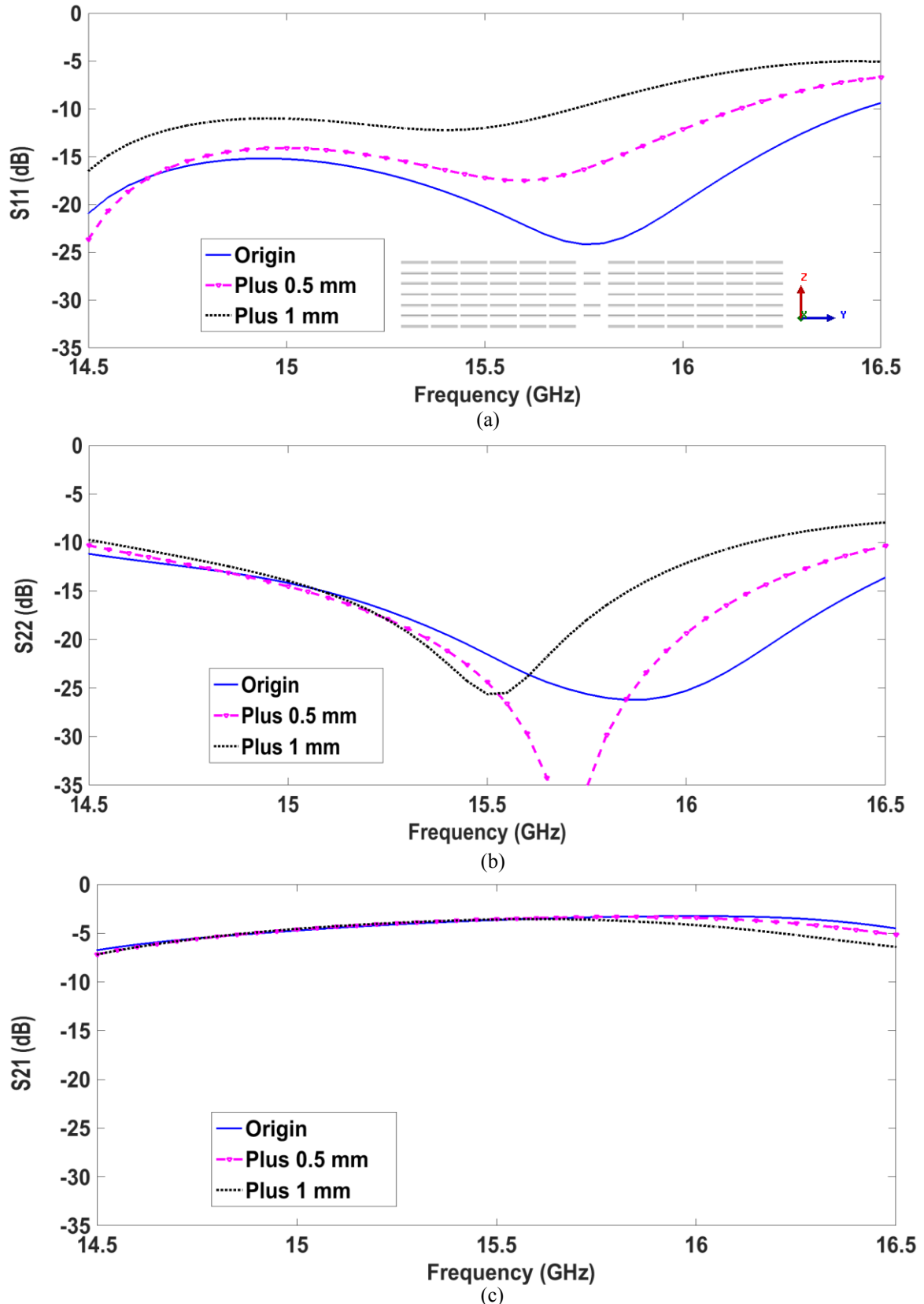


Figure 4.10 Simulated results of the RDR waveguide of length $L = 43.8$ mm: (a) S_{11} , (b) S_{22} and (c) S_{21} . Layers above and below the fourth layer are positioned 0.5 mm and 1 mm offset horizontally (along positive x-axis). Cross section of the guide is shown in the inset of (a).

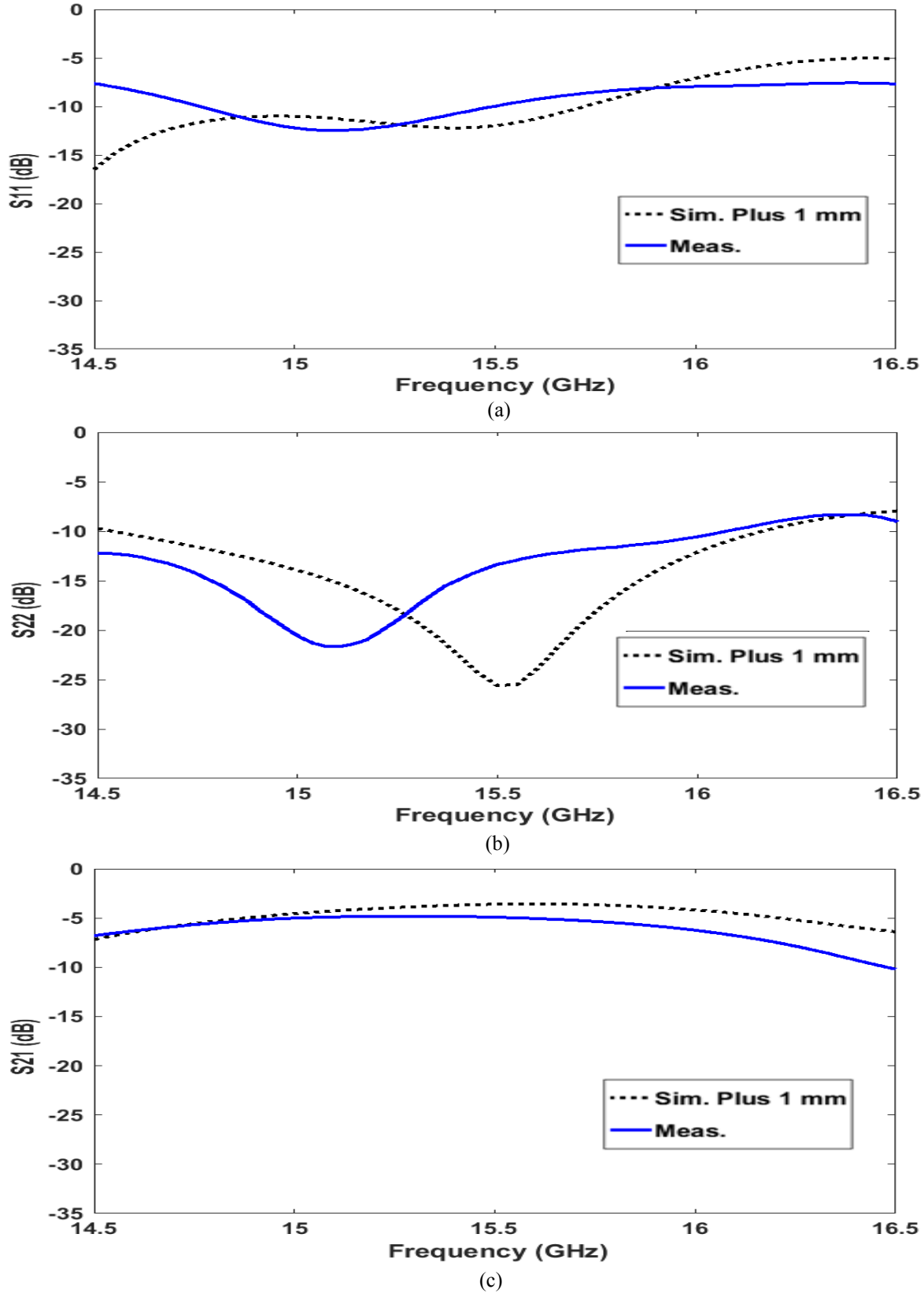


Figure 4.11 Simulated Offset 1 mm and measured results of the RDR waveguide: (a) S11 (a), (b) S22 and (c) S21.

4.3 EBG Waveguide Dielectric Supported

In section 4.2 guiding was demonstrated at Ku-band using a layered one-dimensional (1D) channel waveguide in an EBG slab, that utilizes foam material as spacer. However, a number of difficulties were encountered that stem from fragile nature of foam layers and also their planarity which rendered the measurement process very cumbersome. Therefore, feed transition was implemented on Duroid material to overcome the challenges with the foam. To overcome these challenges, the proposed waveguide configuration is immersed into dielectric substrate (instead of foam). The EBG in the periphery of the defect consists of seven layers of rings while several options, depending on the number of rings along the z-axis, were used for the defect at the center of the EBG lattice an example of which is depicted in Fig. 3.30 (a). This waveguide structure is more amenable to conventional measurement setups as compared to the EBG guide with foam spacer between layers. The dispersion properties of this type of waveguide and its experimental characterization are presented in this section. Some material of this section can be found in [82].

4.3.1 Feed Transition

Similar to the waveguide based on foam material, mode 1 presents polarization identical to the polarization of the fundamental mode of a slot line. Thus, a coplanar to slot line transition is used to excite mode 1 of the waveguide. The transition structure is shown in Fig. 4.2 with the following parameters : gap width $W_g = 0.1$ mm, strip width $W_c = 1.25$ mm, slot width $W_s = 0.7$ mm. Back-to-back configurations of lengths $L = 49$ mm and 69 mm were designed and fabricated on standard 60 mils RT/Duroid 6002 substrate of $\epsilon_r = 2.94$ with copper thickness of 18 microns. The close agreement of the simulated and measured results that are shown in Fig. 4.12, validates the design procedure. The insertion loss has a mean value of 1.7 dB in the 10-11.5 GHz and is comparable to simulated value and measured return loss is better than 14 dB. The discrepancy that is observed below 10 GHz can be attributed to leakage losses and the connection between SMA connectors and the feed point of the CPW.

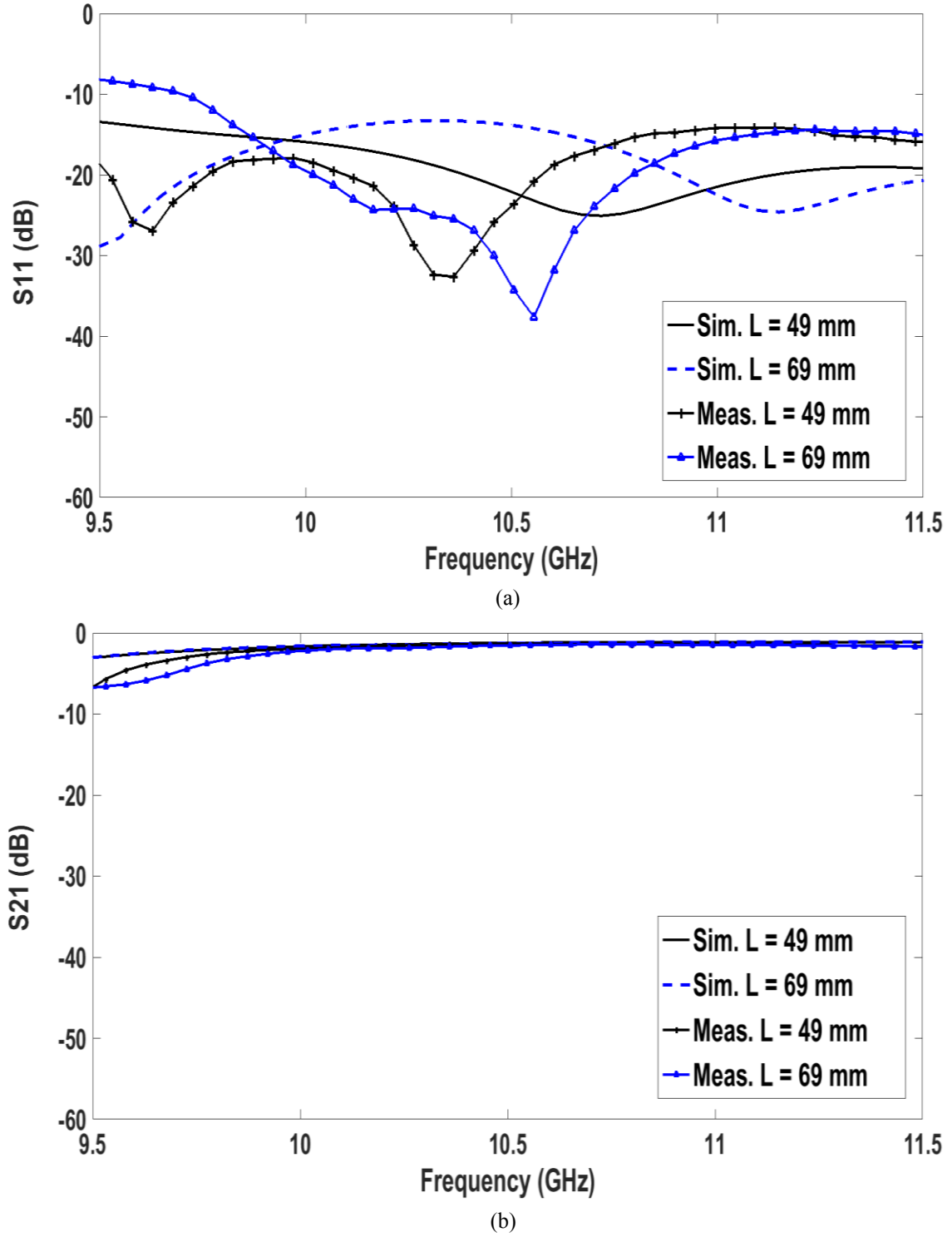


Figure 4.12 Simulated and measured S-parameters of the back-to-back CPW-to-slot line transition of lengths $L = 49$ mm and 69 mm. (a) S₁₁. (b) S₂₁.

4.3.2 Excitation of the EBG Waveguide

Fig. 4.13 depicts the planar structure of a typical CPW-slot-line fed EBG channel. The feeding transitions and the defect (i.e., fourth) layer of the guide are placed on the same side of the substrate. Layered rings are placed on Duroid 6002 (of thickness 0.25 mm with single side metal). The overall dimensions of the waveguide are $L \times W \times H_b = 49 \text{ mm} \times 35 \text{ mm} \times 3 \text{ mm}$ and channel length is 4 periods.

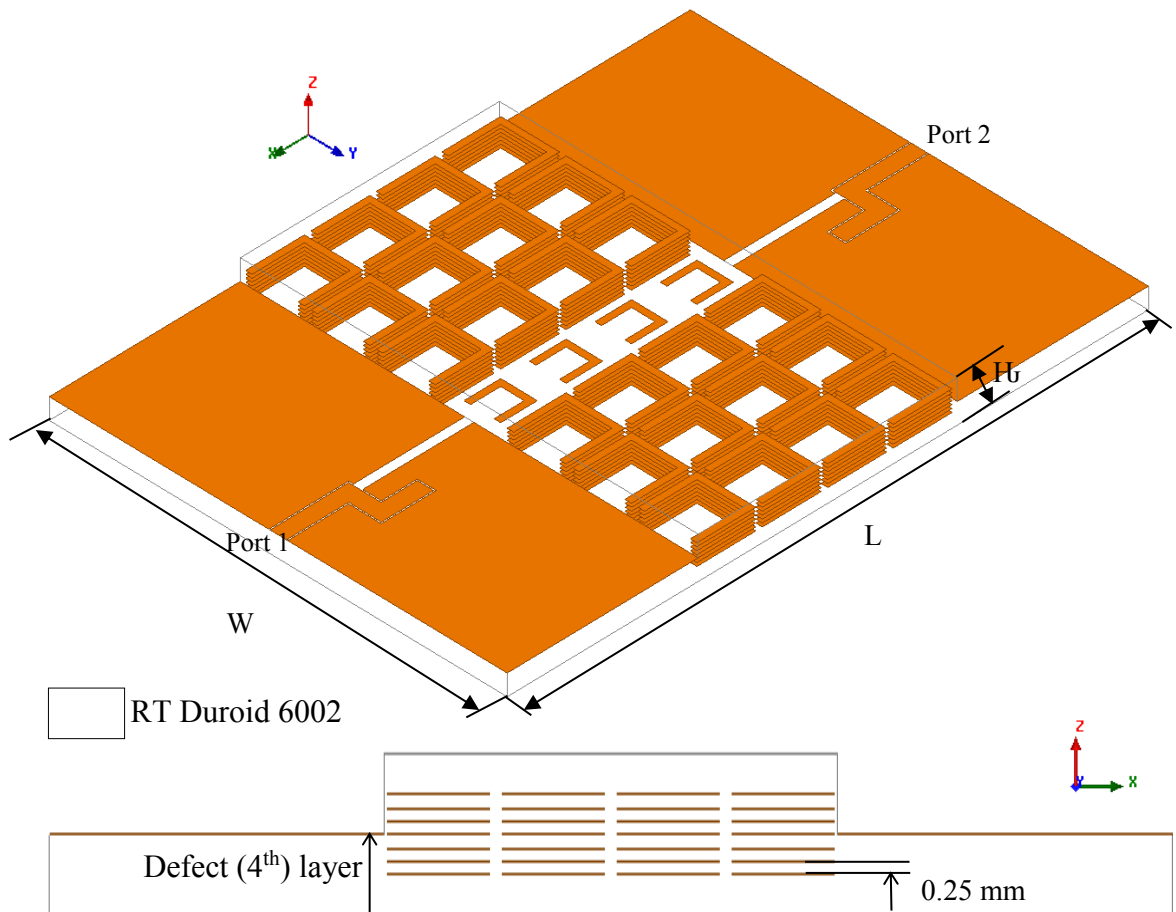


Figure 4.13 EBG waveguide in dielectric fed by CPW-to-slot line transitions. The waveguide has 3 rows on the sides of the channel. The size of the waveguide is $L \times W \times H_b = 49 \text{ mm} \times 35 \text{ mm} \times 3 \text{ mm}$.

Three configurations of the waveguide model with several lengths were designed and fabricated. The waveguide configurations are referred to as: waveguide with one, three, and six rows (periods) of layered rings on the sides of the guiding channel. Fig. 4.14 illustrates the waveguide configurations.

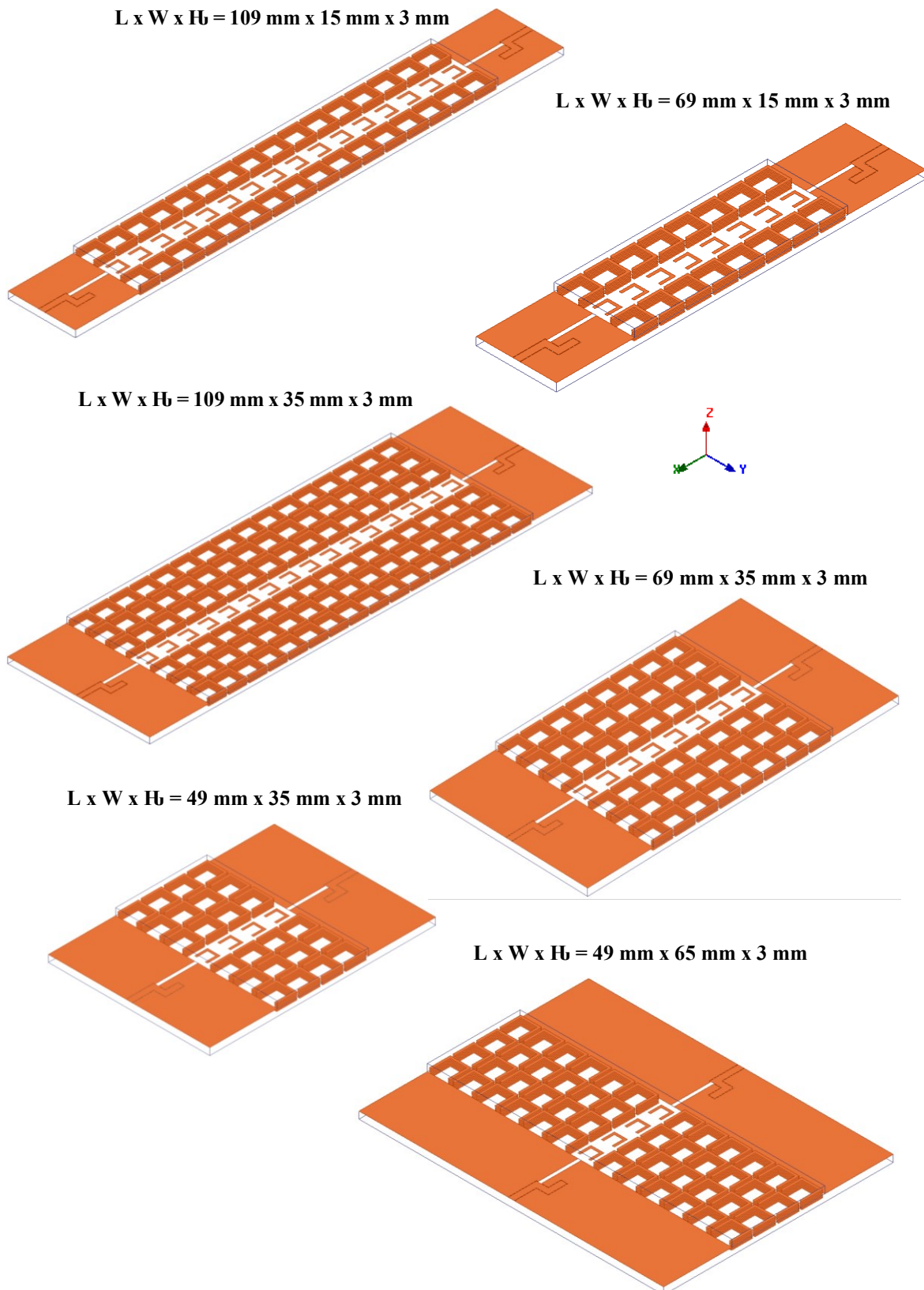


Figure 4.14 EBG waveguide configurations.

Fig. 4.15 shows a photograph of the fabricated waveguide configurations and transitions fed by SMA connectors. Rogers 2929 Bonding thin adhesive film with a dielectric constant close to that of Rogers 60 mils substrate was used to assemble the layers.

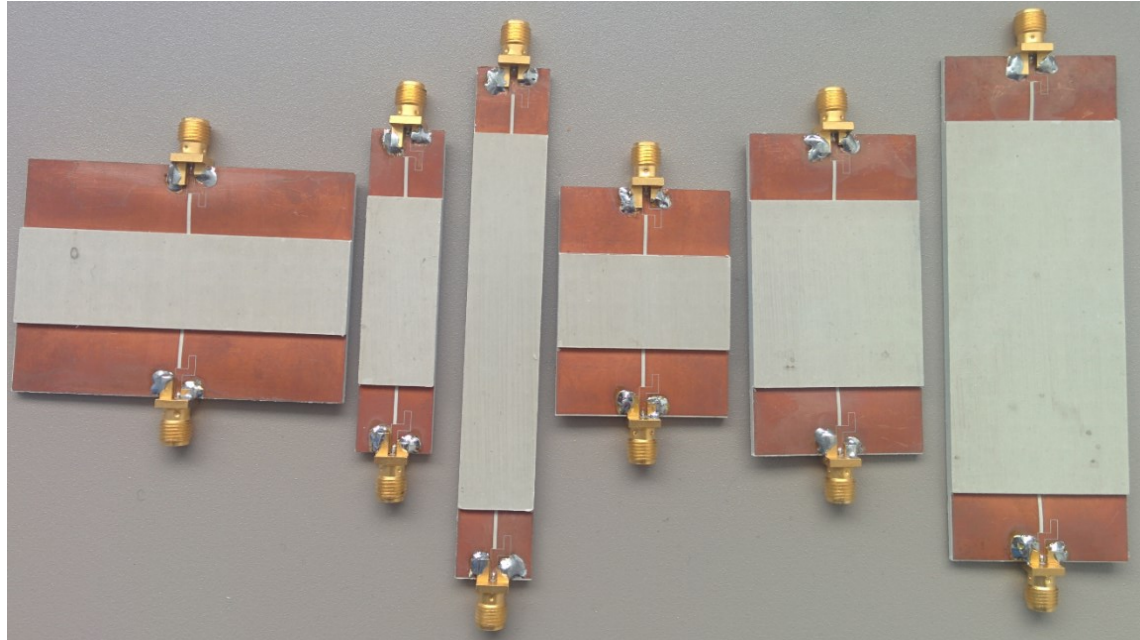


Figure 4.15 Photo of the fabricated EBG waveguides embedded in a dielectric.

4.3.3 Simulated and Measured Results

The EBG waveguide depicted in Fig. 4.13 was designed and fabricated for three different lengths of 49 mm, 69 mm and 109 mm (Fig. 4.14) that correspond to channel length of 4, 8 and 16 periods, respectively. Fig. 4.16 shows the simulated and measured return and insertion losses of these three waveguides. Measured return loss is better than 11 dB and is comparable to predictions in the 9.5 - 11 GHz range. Measured insertion loss has a mean value of 5.2 dB, 4.3 dB and 3.7 dB for the 16 periods, 8 periods and 4 periods' guides respectively, in the 10-11 GHz as compared to the simulated mean value that is 2 dB.

The simulated and measured S-parameters of the waveguide with one row on each side of the channel and channel length of 8 and 16 periods are shown in Fig. 4.17. Measured return loss is greater than 12 dB, while the insertion loss has a mean value of 4.2 dB and 3.7 dB for the 16 and 8 periods' guides respectively, in the 10-11 GHz. The simulated value is 1.8 dB in the whole frequency range.

The performance of the waveguide with six rows on each side of the channel and channel length of 4 periods is shown in Fig. 4.18. The measured return loss is around 10 dB and is comparable to simulations. Measured insertion loss has a value of 6.6 dB, while simulated value is 2.3 dB in the 10-11.5 GHz.

Measured results include the contributions of the transitions. There is a certain deviation between measured and simulated insertion losses of the waveguide prototype. This deviation can be attributed to manufacturing tolerances, conductor losses and soldering of the connectors and CPW feed line. Eigen-mode simulations of section 3.7 showed that the number of rows on the sides of the channel has a marginal impact on the dispersion of the guided mode. However, measurement results of the realized prototypes demonstrate otherwise. Indeed, the insertion loss has been increased by increasing the number of rows on the sides of the channel for the same length of the channel. The loss is more pronounced for wider guide (which is contrary to the behavior of waveguide foam-supported). This is due to the larger coupling of the guiding mode into the surface waves at the end of the channel. In other words, local surfaces modes are more pronounced in thicker neighboring EBG crystal [72] as can be seen in Fig. 4.19 (b-d). Guides of three and six rows and channel length of 4 periods show 3.7 dB and 6.6 dB loss, respectively. However, guides of one and three rows and channel length of 16 periods offer insertion losses of 4.2 dB and 5.2 dB, respectively.

It is important to note that the loss due to increased channel length is smaller than that of increased side rows. This is due to the effect of DBR along the guiding direction and longer interaction region between the propagating mode and the surrounding crystal. The effect of the DBR does not greatly vary with the length of the waveguide. This argument reveals why increasing the length of the channel has insignificant impacted on the loss of the waveguide. Therefore, the decrement of the transmitted power due to the excitation of the surface modes is greater than that due to the DBR effect.

The longer EBG guide with one row on each side of the channel offers the smallest insertion loss. This can be explained as the leakage from the channel bounces (returns) back to the channel and contributes to the propagating field along the channel. Furthermore, local surface waves are weaker as shown in Fig. 4.19(a).

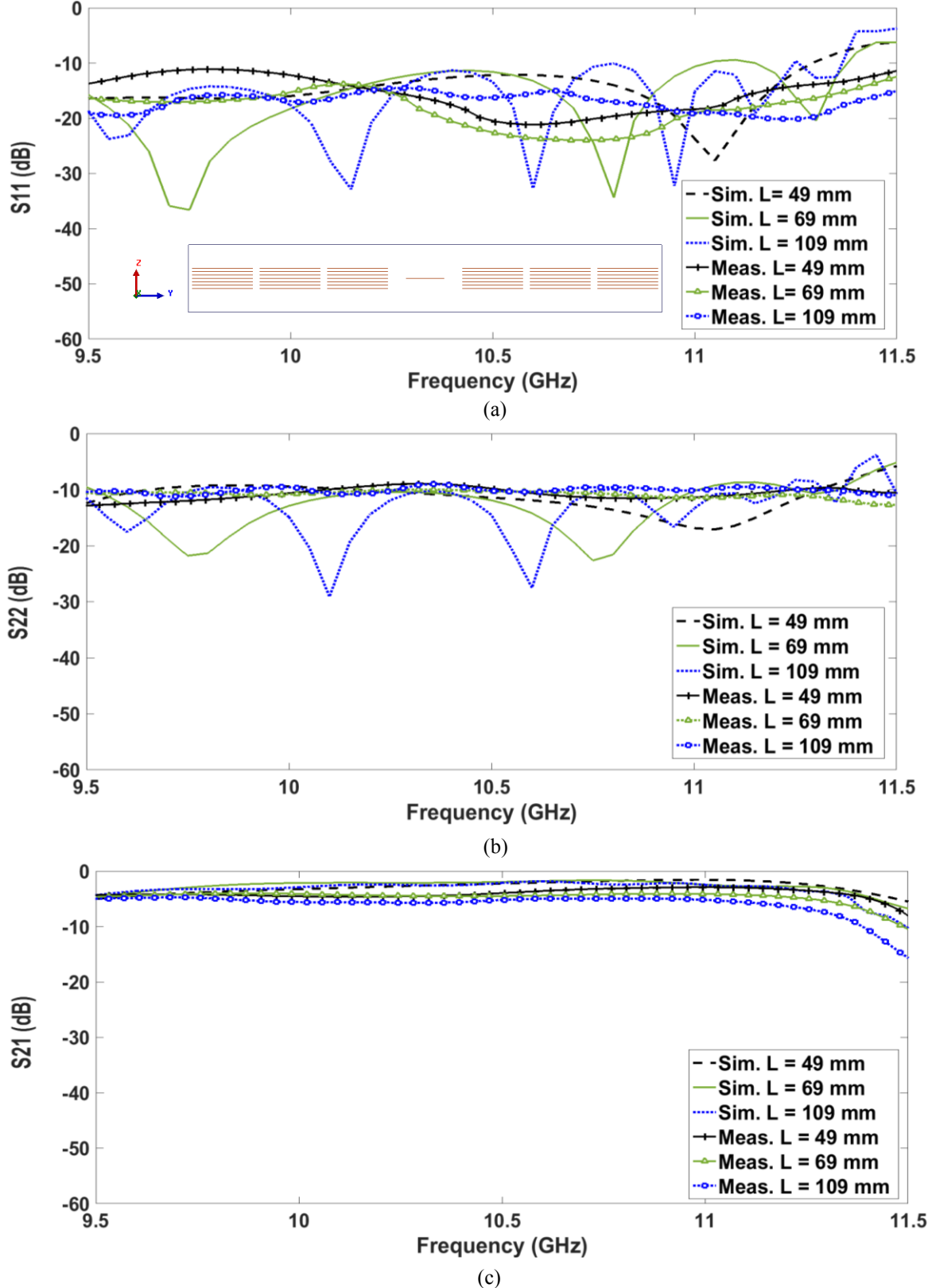


Figure 4.16 Simulated and measured: (a) S_{11} , (b) S_{22} and (c) S_{21} of EBG guide with three rows and lengths L of 49 mm, 69 mm and 109 mm. Cross section of the guide is shown in the inset of (a).

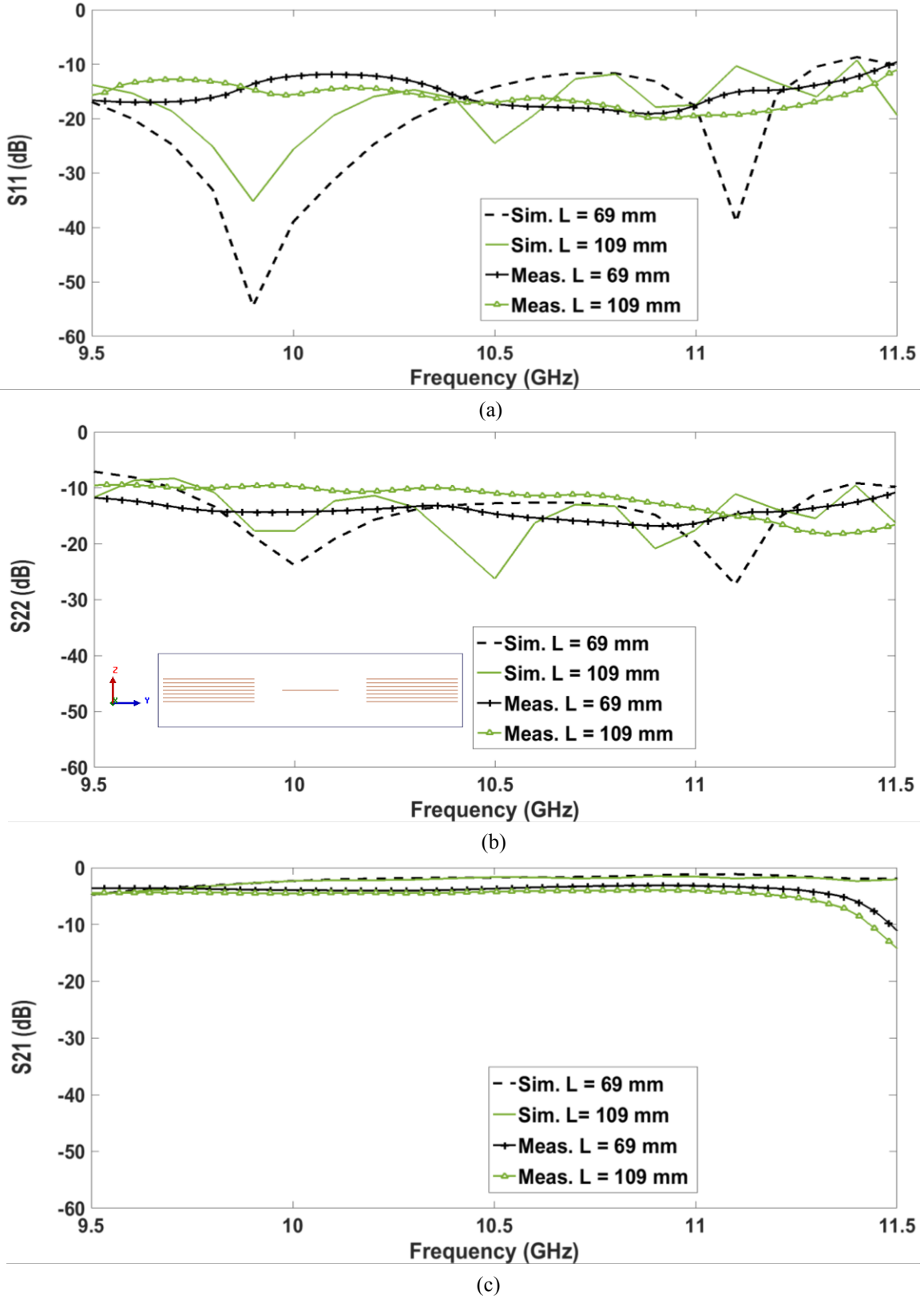


Figure 4.17 Simulated and measured: (a) S11, (b) S22 and (c) S21 of EBG guide with one row and lengths of 69 mm and 109 mm. Cross section of the guide is shown in the inset of (b).

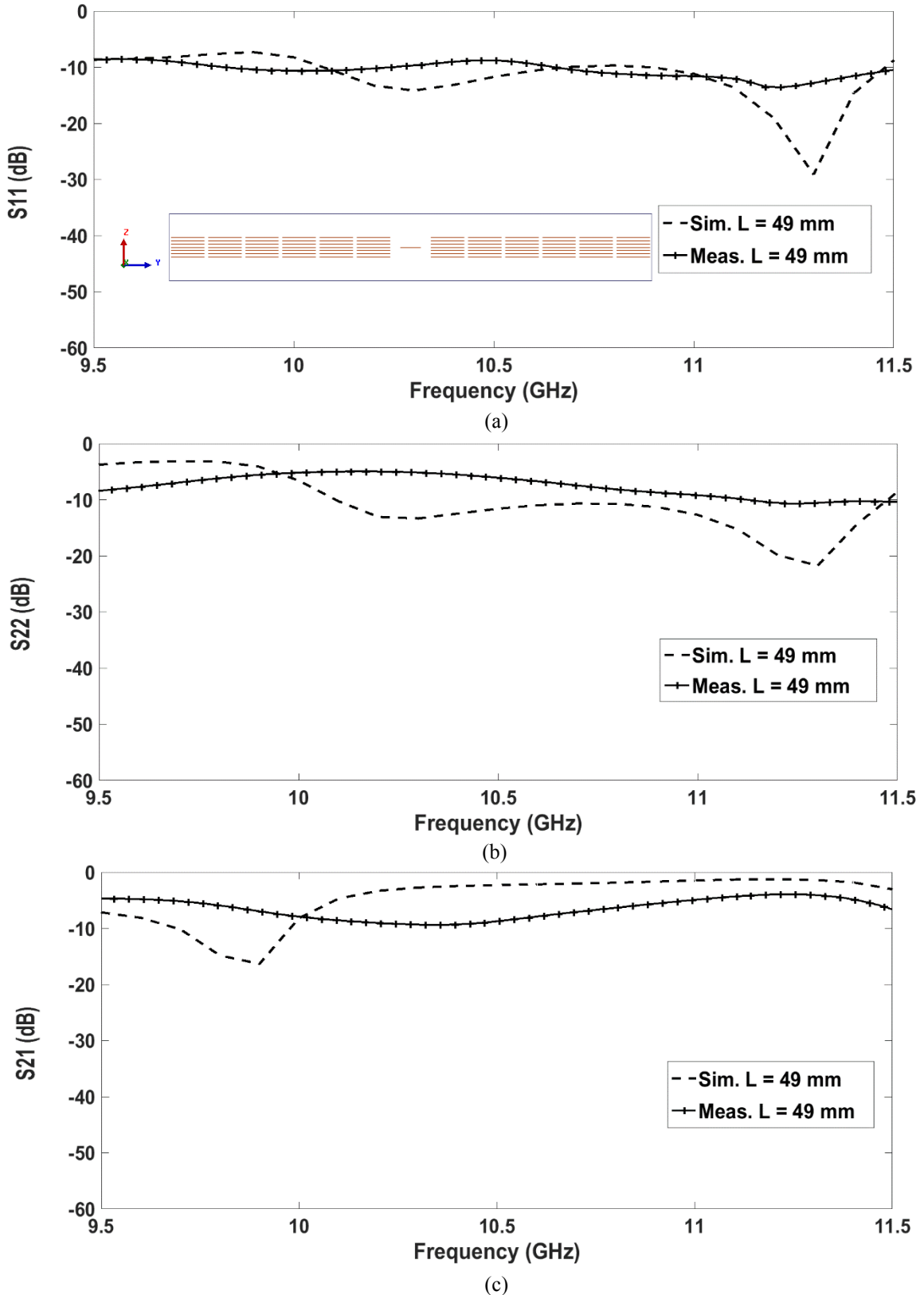


Figure 4.18 Simulated and measured: (a) S_{11} , (b) S_{22} and (c) S_{21} of EBG guide with six rows and length of 49 mm. Cross section of the guide is shown in the inset of (a).

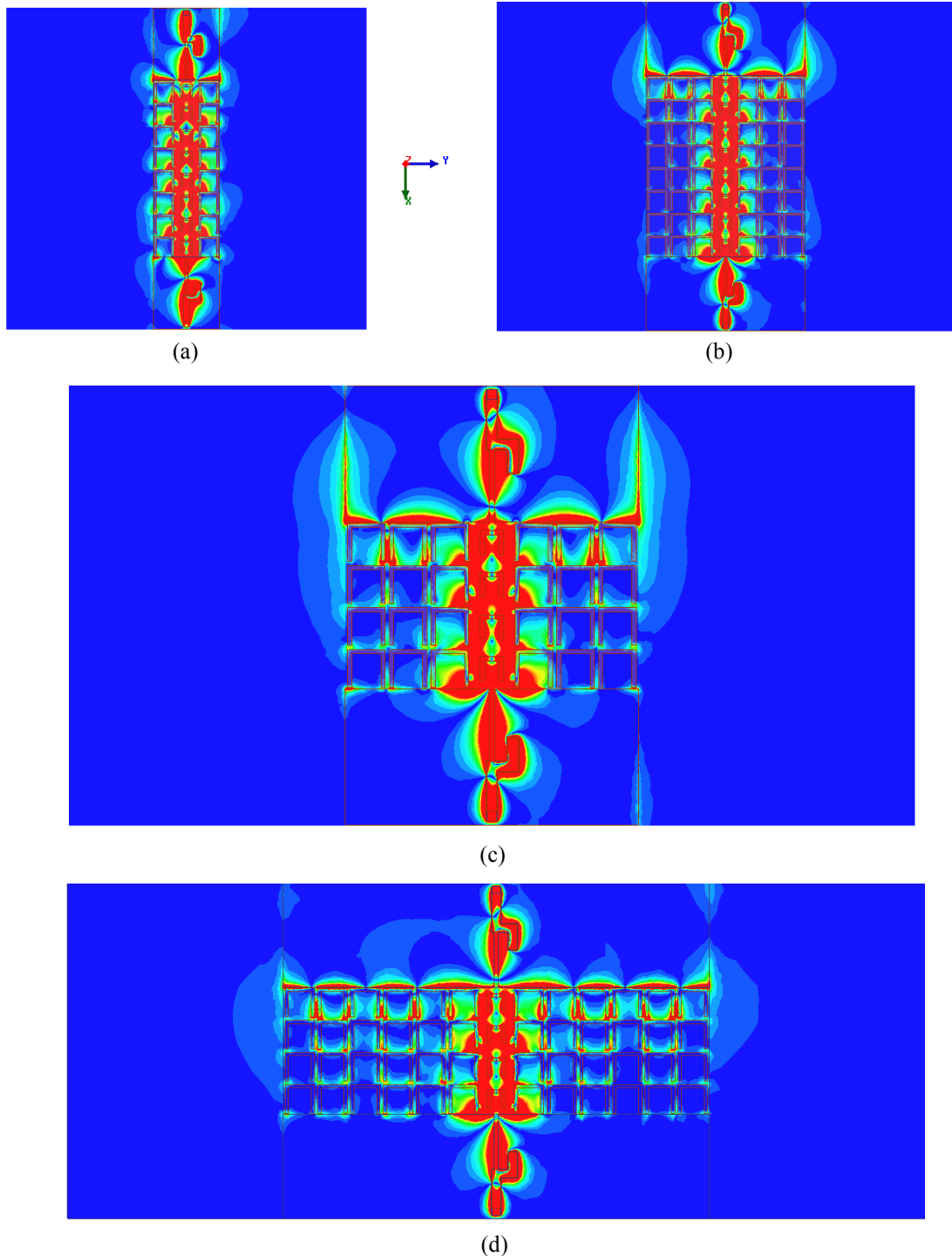


Figure 4.19 Electric field distribution at $f = 10.5$ GHz in the EBG waveguide. (a) Channel length of eight periods with one row and (b) with three rows. (c) Channel length of four periods with three rows and (d) and six rows.

4.3.4 Detailed Waveguide Characterization Through De-embedding

In order to characterize only the EBG waveguide channel, it is necessary to remove the effect of the feeding line that is composed of CPW-slot-line transitions. This is generally accomplished by applying a de-embedding technique to the overall measurement [83]. The de-embedding method that is used here was proposed in [84]. The method is based on bisection of a single two-ports THRU structure. It utilizes transmission matrix to split mathematically a symmetric THRU into mirrored halves which may then be mathematically removed from both ports of a two ports measured structure, leaving only the desired device under test (DUT). This method provides an alternative to open-short de-embedding techniques that is restricted by lumped element assumptions [85-87].

4.3.4.1 Model for De-embedding

The method developed here employs the structures shown in Fig. 4.20 which is composed of the DUT; EBG channel placed between symmetric halves of the THRU (back-to-back CPW-slot-line transition) (Fig. 4.20 (b)). There are six basic steps in the de-embedding process of the DUT cascaded with half THRU structure models.

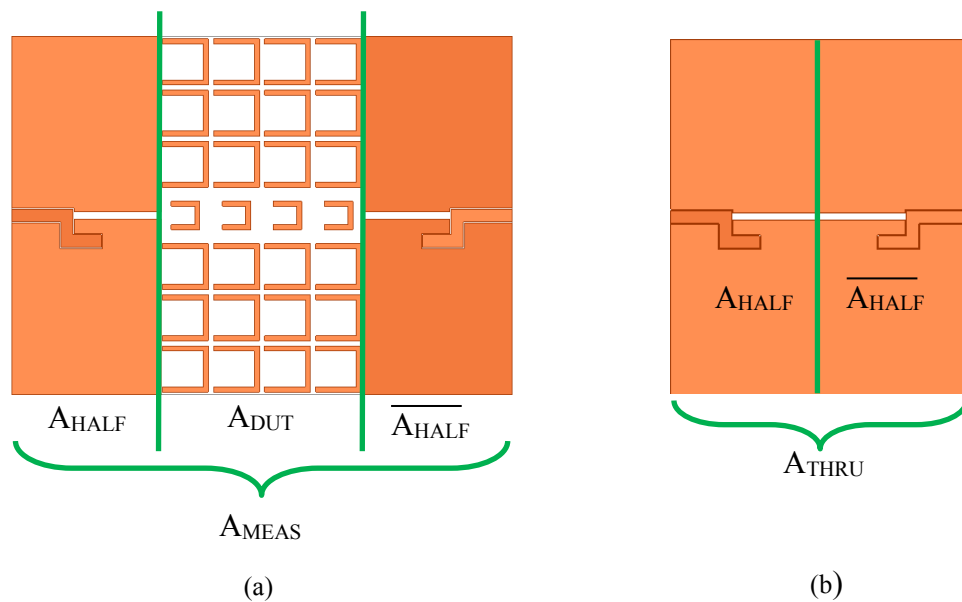


Figure 4.20 De-embedding technique using transmission matrix bisect de-embedding. (a) Measured structure having the DUT. (b) THRU structure.

Step 1: Bisect the THRU into mirror image halves. This is accomplished by solving the following ABCD matrix:

$$A_{HALF} \cdot \overline{A_{HALF}} = A_{THRU} \quad (4.1)$$

where the overbar shows symmetric conjugation defined as follows :

$$\overline{\begin{bmatrix} a & b \\ c & d \end{bmatrix}} \equiv \frac{1}{ad - dc} \begin{bmatrix} d & b \\ c & a \end{bmatrix}$$

Half THRU structure is modeled using simulation tool (HFSS) to obtain data in terms of S-parameters. Based on [88], the simulated model of half structure can be used to de-embed the DUT.

Step 2: Obtain measured S-parameters of the DUT with the transitions; Circuit 4.20 (a) as measured at the coaxial measurement planes. The S-parameters are represented as complex numbers.

Step 3: Convert the simulated (step 1) and measured S-parameters in (steps 2) to ABCD parameters using the following equation (4.2).

$$\begin{bmatrix} A & B \\ C & D \end{bmatrix} = \begin{bmatrix} \frac{(1+S_{11})(1-S_{22})+S_{12}S_{21}}{2S_{21}} & Z_0 \frac{(1+S_{11})(1+S_{22})-S_{12}S_{21}}{2S_{21}} \\ \frac{1}{Z_0} \frac{(1-S_{11})(1-S_{22})-S_{12}S_{21}}{2S_{21}} & \frac{(1-S_{11})(1+S_{22})+S_{12}S_{21}}{2S_{21}} \end{bmatrix} \quad (4.2)$$

Step 4: Perform the matrix calculation to convert bisected half structure model of the ABCD parameters matrices into their inverse matrices.

Step 5: Using the ABCD parameters model of each half structure model and the DUT, apply the de-embedding equation (4.3).

$$A_{DUT} = [A_{HALF}]^{-1} \cdot [A_{MEAS}] \cdot [\overline{A_{HALF}}]^{-1} \quad (4.3)$$

Step 6: Convert the final ABCD parameters matrix, i.e. A_{DUT} , back to S-parameters matrix using the following equation (4.4). This matrix represents the S-parameters of the device under test (S_{DUT}) and the transitions effects have been removed.

$$S = \begin{bmatrix} S_{11} & S_{12} \\ S_{21} & S_{22} \end{bmatrix} = \begin{bmatrix} \frac{A + \frac{B}{Z_0} - CZ_0 - D}{A + \frac{B}{Z_0} + CZ_0 + D} & \frac{2(AD - BC)}{A + \frac{B}{Z_0} + CZ_0 + D} \\ \frac{2}{A + \frac{B}{Z_0} + CZ_0 + D} & \frac{-A + \frac{B}{Z_0} - CZ_0 + D}{A + \frac{B}{Z_0} + CZ_0 + D} \end{bmatrix} \quad (4.4)$$

4.3.4.2 Results and Discussion

In this section, the de-embedding method above is applied to measurement of the prototype structures of Fig. 4.15. The results of the simulated and calculated (eq. 4.1) THRU structure ($L = 29.2$ mm), along with measured back-to-back short transition ($L = 49$ mm) are plotted in Fig. 4.21. From the figures, good agreement can be observed between simulated and calculated THRUs that satisfy Eq. 4.1. Measured back-to-back transition exhibits some deviation at lower frequencies as mentioned above.

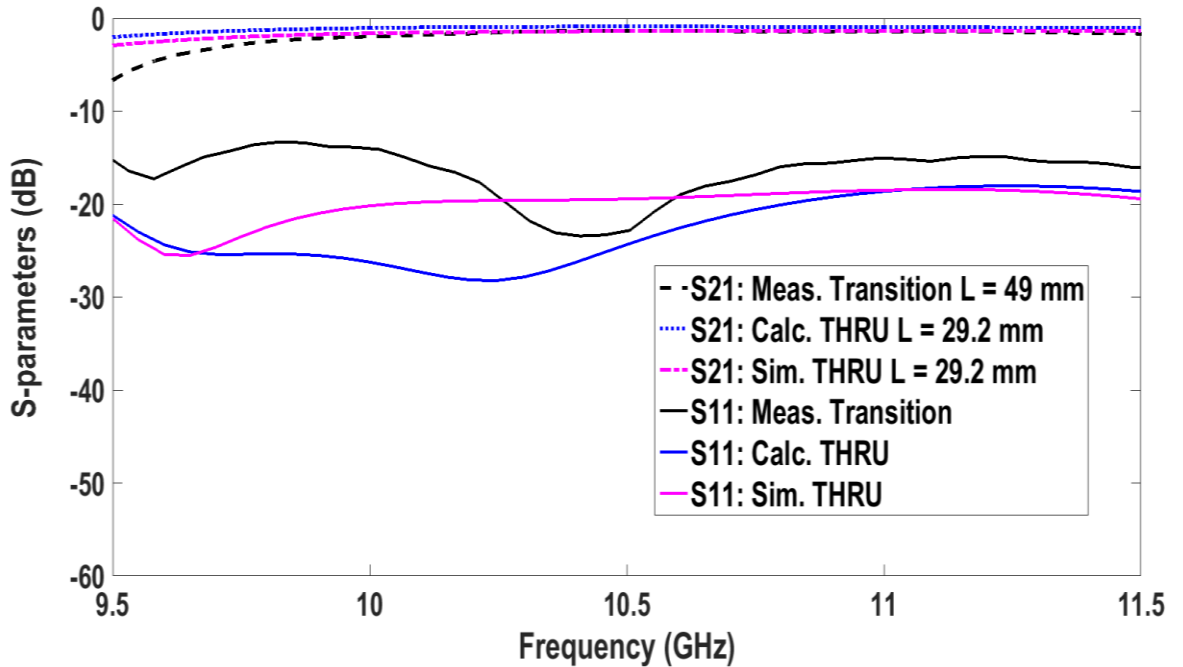


Figure 4.21 S-parameters of the calculated, simulated THRU structure of length $L = 29.2$ mm and measured back-to-back transition of length $L = 49$ mm.

The results of experimental performance before and after de-embedding are depicted in Figs. 4.22, 4.23 and 4.24 for the EBG waveguide with three rows and channel lengths of 4, 8 and 16 periods, respectively. Figs. 4.25 and 4.26 show the results for the guide with one row on the sides of the channel and channel lengths of 8 and 16 periods, respectively. Finally, Fig. 4.27 shows similar results for the guide with six rows and channel length of 4 periods. The simulated results (Raw) of the device under test (DUT) are plotted for comparison with the de-embedded results. From these figures, it can be seen that the de-embedded results are better than the measured ones and follow closely the simulated performance for the majority of the fabricated samples. The deviations between simulated

and de-embedded results can be attributed to the manufacturing impefections and conductor losses. The following table summarizes the performance of the fabricated de-embedded EBG waveguides prototypes in the frequency range (9.5-11) GHz.

Table 4.1: Performances of the fabricated de-embedded EBG waveguides in dielectric

Number of Rows	Channel length (periods)	Return loss	Min. In-band insertion loss
1	8	> 11 dB	1.7 dB
	16	> 11 dB	2.8 dB
3	4	> 11 dB	2.6 dB
	8	> 11 dB	2.8 dB
	16	> 11 dB	3.2 dB
6	4	10 dB	3.1 dB

From the table it can be seen that as the number of rows on the two side of the channel increases, the insertion loss of the EBG waveguide increases moderately. This is contrary to what was observed in the study of the foam-supported channel. The reason are that significant radiation losses of the foam structure decreases, while dielectric and surfaces waves losses of dielectric structure increases. The mean loss of the 16 periods long waveguide with one row is 0.2 dB/period (0.04 dB/mm). This value is less than (0.28 dB/period) in what was calculated for the foam-supported, 16 periods long EBG guide with six rows on the sides of the channel. Therfore, the losses in the EBG-OSR come mainly from radiation and surface wave losses.

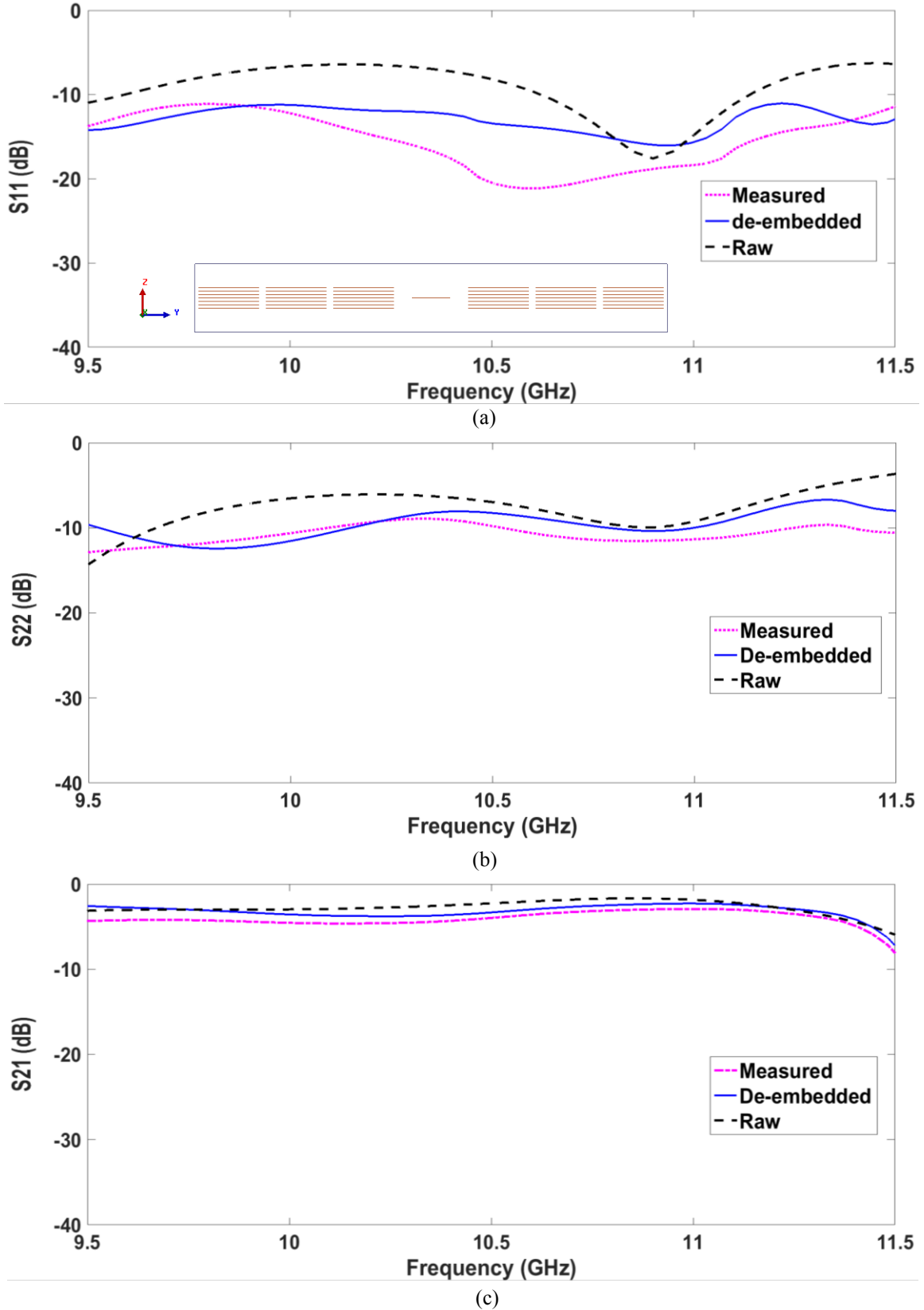


Figure 4.22 Characteristic S-parameters before and after de-embedding of EBG guide with three rows and length L of 49 mm. Raw is simulated result of DUT. (a) S₁₁, (b) S₂₂ and (c) S₂₁.

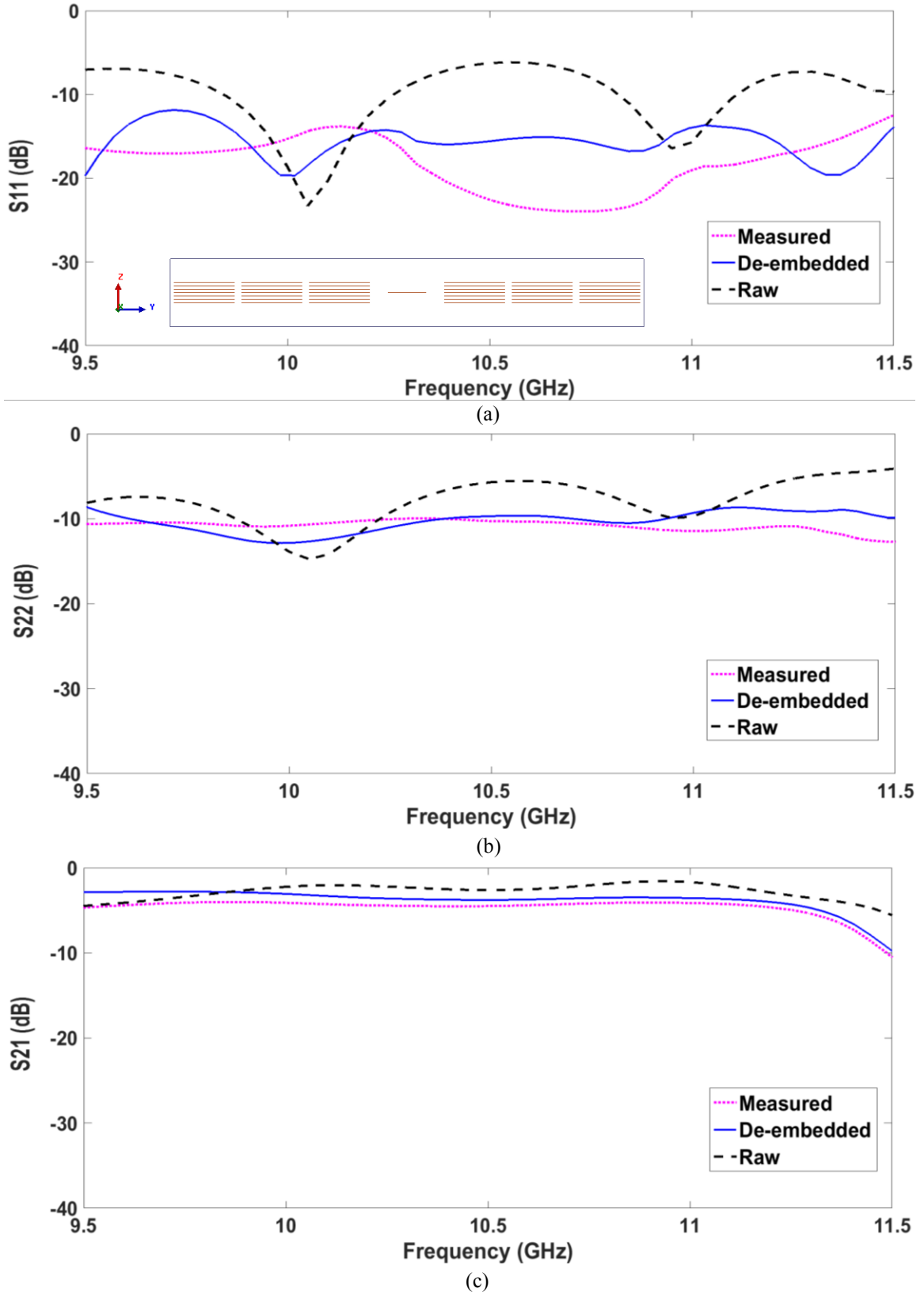


Figure 4.23 Characteristic S-parameters before and after de-embedding of EBG guide with three rows and length L of 69 mm. Raw is simulated result of DUT. (a) S11, (b) S22 and (c) S21.

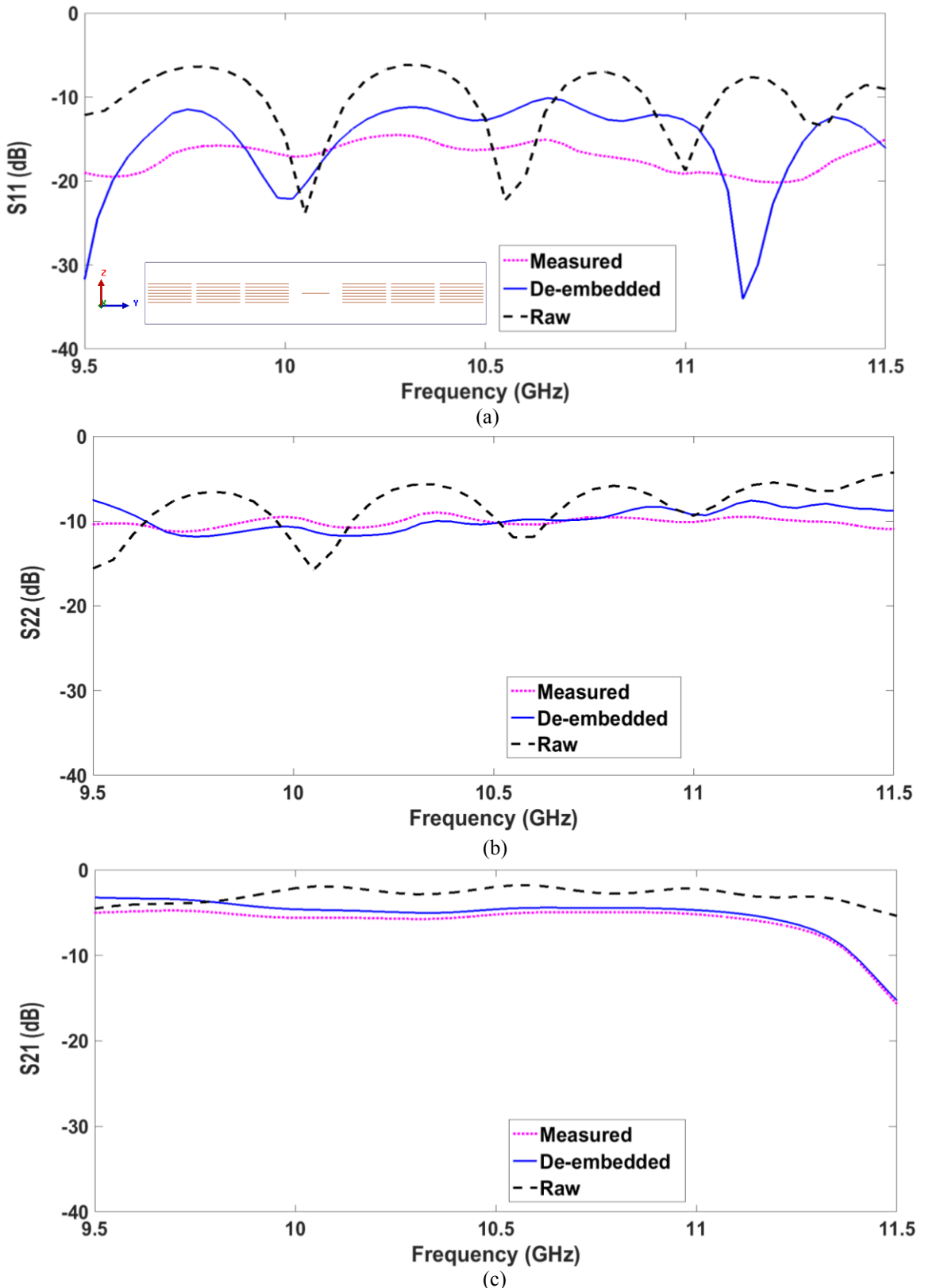


Figure 4.24 Characteristic S-parameters before and after de-embedding of EBG guide with three rows and length L of 109 mm. Raw is simulated result of DUT. (a) S₁₁, (b) S₂₂ and (c) S₂₁.

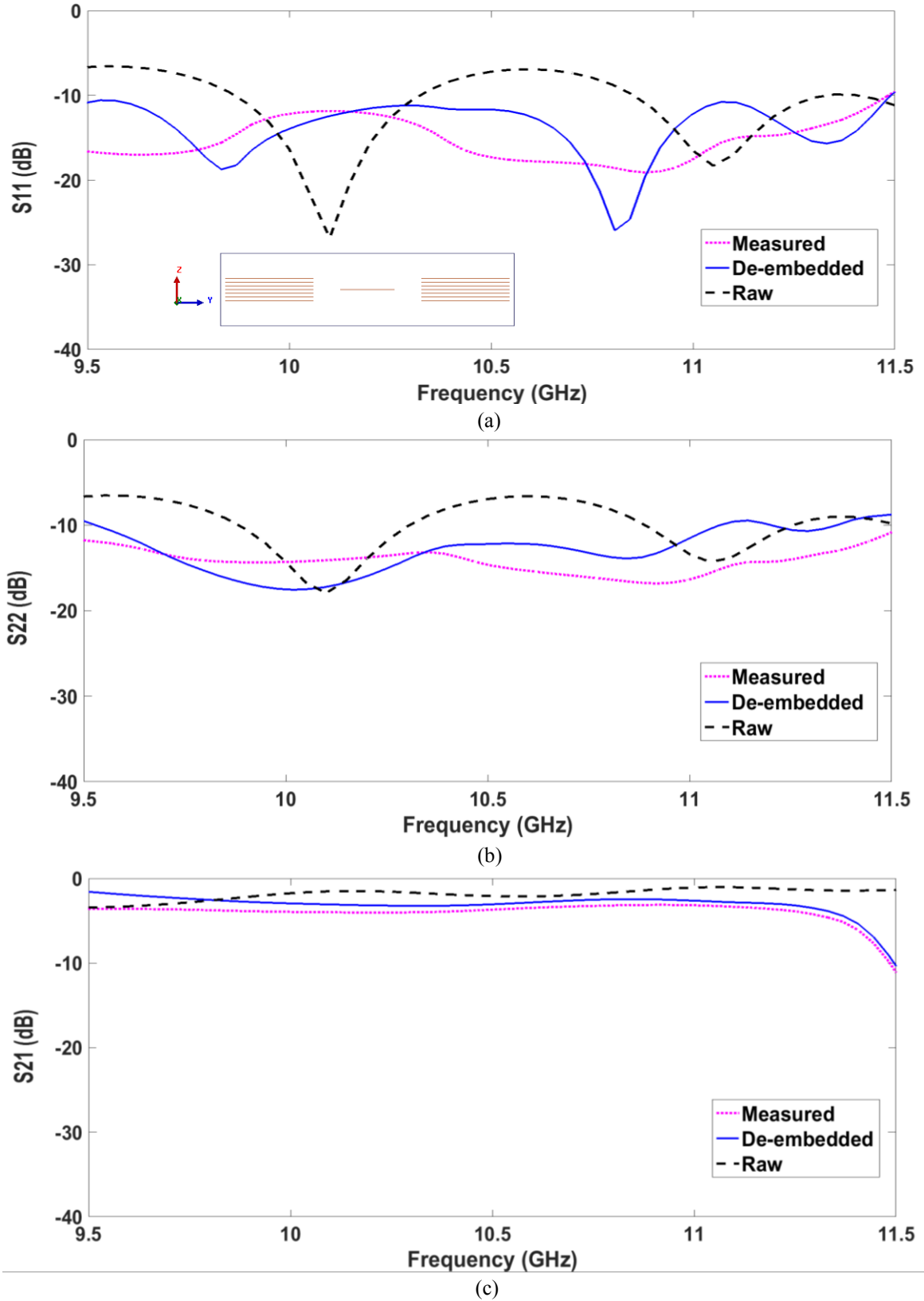


Figure 4.25 Characteristic S-parameters before and after de-embedding of EBG guide with one row and length L of 69 mm. Raw is simulated result of DUT. (a) S11, (b) S22 and (c) S21.

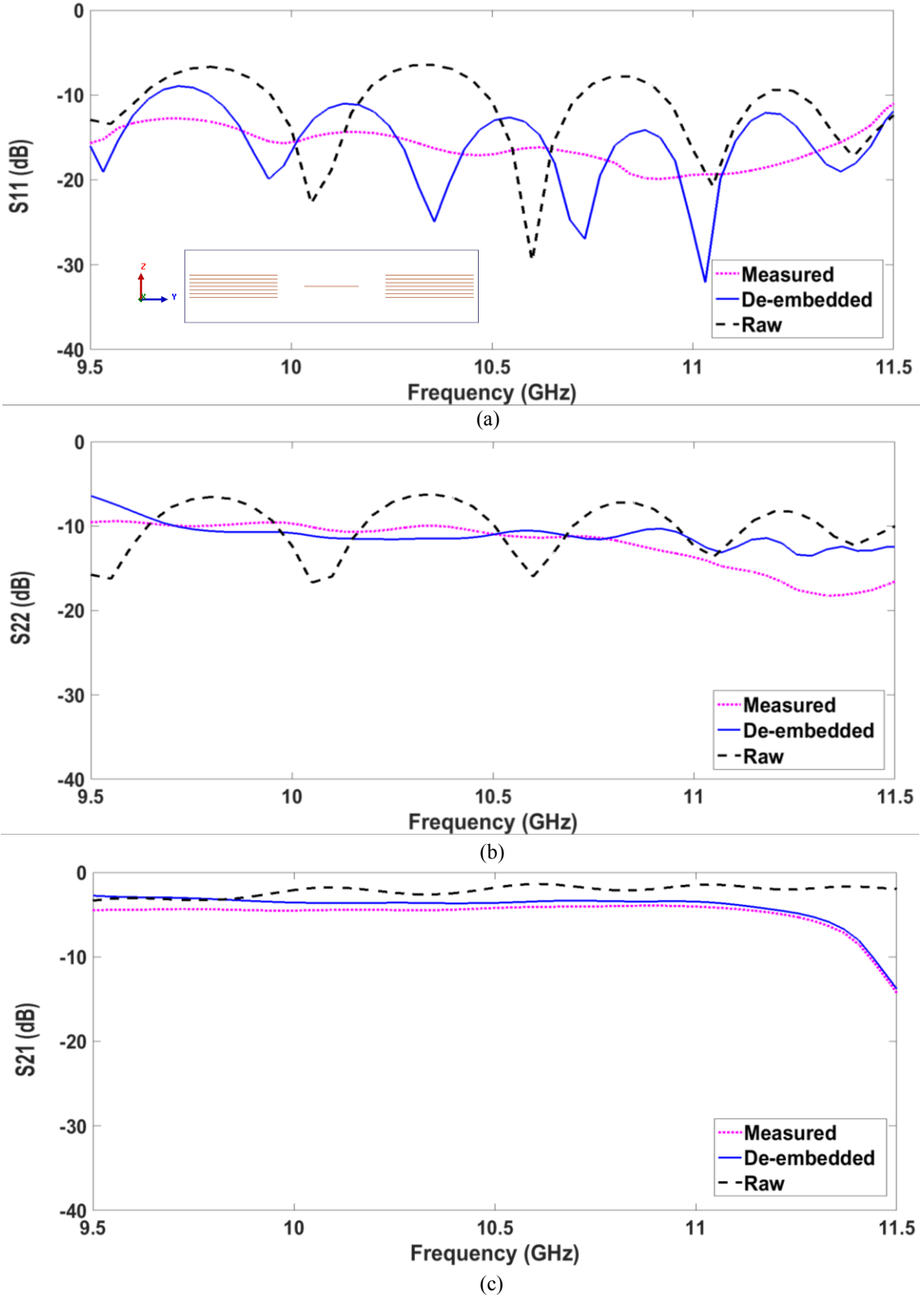


Figure 4.26 Characteristic S-parameters before and after de-embedding of EBG guide with one row and length L of 109 mm. Raw is simulated result of DUT. (a) S₁₁, (b) S₂₂ and (c) S₂₁.

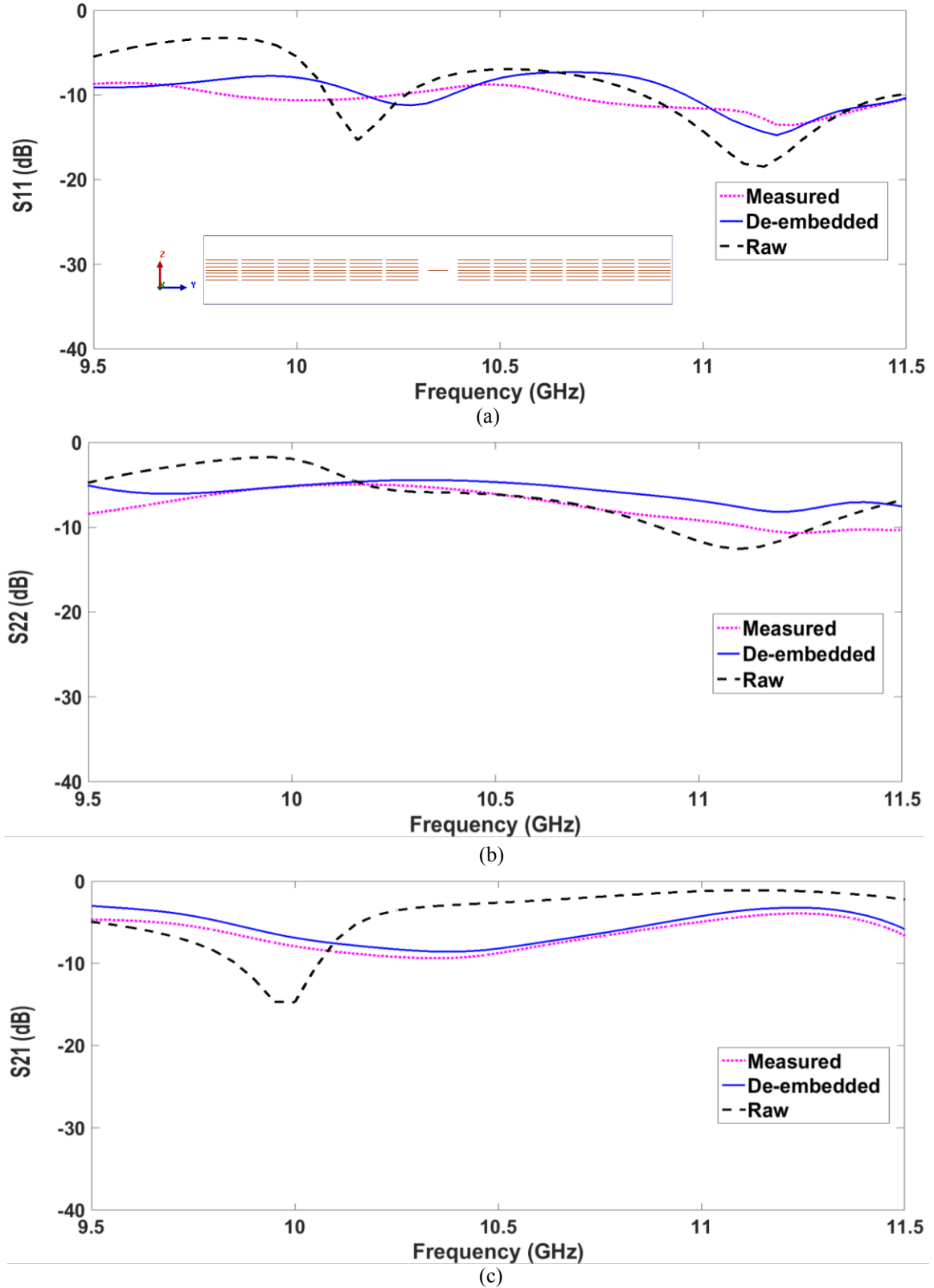


Figure 4.27 Characteristic S-parameters before and after de-embedding of EBG guide with six rows and length L of 49 mm. Raw is simulated result of DUT. (a) S11, (b) S22 and (c) S21.

4.3.5 Performance Comparison With Other Transmission lines

This section presents a performance comparison between the EBG waveguide in dielectric, presented in this chapter and classical transmission lines namely, microstrip (MIS), coplanar waveguide (CPW), rectangular waveguide (RW), substrate integrated waveguide (SIW) and ridge gap waveguide (RGWG). The comparison is based on loss, complexity of fabrication, compactness and compatibility with multi-chip modules MCM and suitability for multifunctional couplers and other circuits. An EBG waveguide was designed at V-band (S-parameters are not included in thesis). The tabulated loss at 60 GHz was computed by taking the difference of simulated losses at 60 GHz and 10 GHz added to the measured value at 10 GHz. The loss at 60 GHz frequency in the V-band EBG guide is slightly higher than the loss in the other transmission lines.

Table 4.2: Performances of the EBG waveguide and other transmission lines.

Line type	Loss at 10 GHz (dB/cm)	Loss at 60 GHz (dB/cm)	Complexity of Fabrication	Compactness & compatibility with MCM	Suitability for multi-functional couplers and other circuits
MIS [89]	0.07	0.23	Low	Very compact, compatible ⁴	Low
CPW [89]	0.15	0.43	Medium ¹	Compact ⁵ , compatible ⁶	Low
RW [90]	0.00108	0.015	Low	Bulky, not compatible	Low
SIW	0.12 [91]	0.24 [92]	Medium ²	Compact, compatible ²	Medium
RGW [93]	0.018	0.1	Medium ³	Less compact, compatible	Medium
EBG (this work)	0.15	0.58	Low	Less compact, compatible	High

¹ requires ground straps, ² requires metal vias and is not amenable for integrating active elements, ³ requires metal posts, ⁴ requires metal vias for grounding, ⁵ requires wide ground planes, ⁶ requires metal vias.

Insertion loss is the key parameter in the evaluation of the performance of microwave and millimetre-wave guiding structures but phase linearity cannot be ignored in the design. The group delay is a measure of the linearity of the phase of the waveguide. A linear phase characteristic implies a constant group velocity and is also distortionless in terms of the transmitted signal. The group delay of the designed V-band EBG guide is plotted in Fig. 4.28 that is less than 0.13 ns over the entire pass band and is 0.016 ns over 58 GHz-60 GHz. Relative constant value of group delay throughout the passband indicates suitability of the proposed EBG waveguide for RF communication applications.

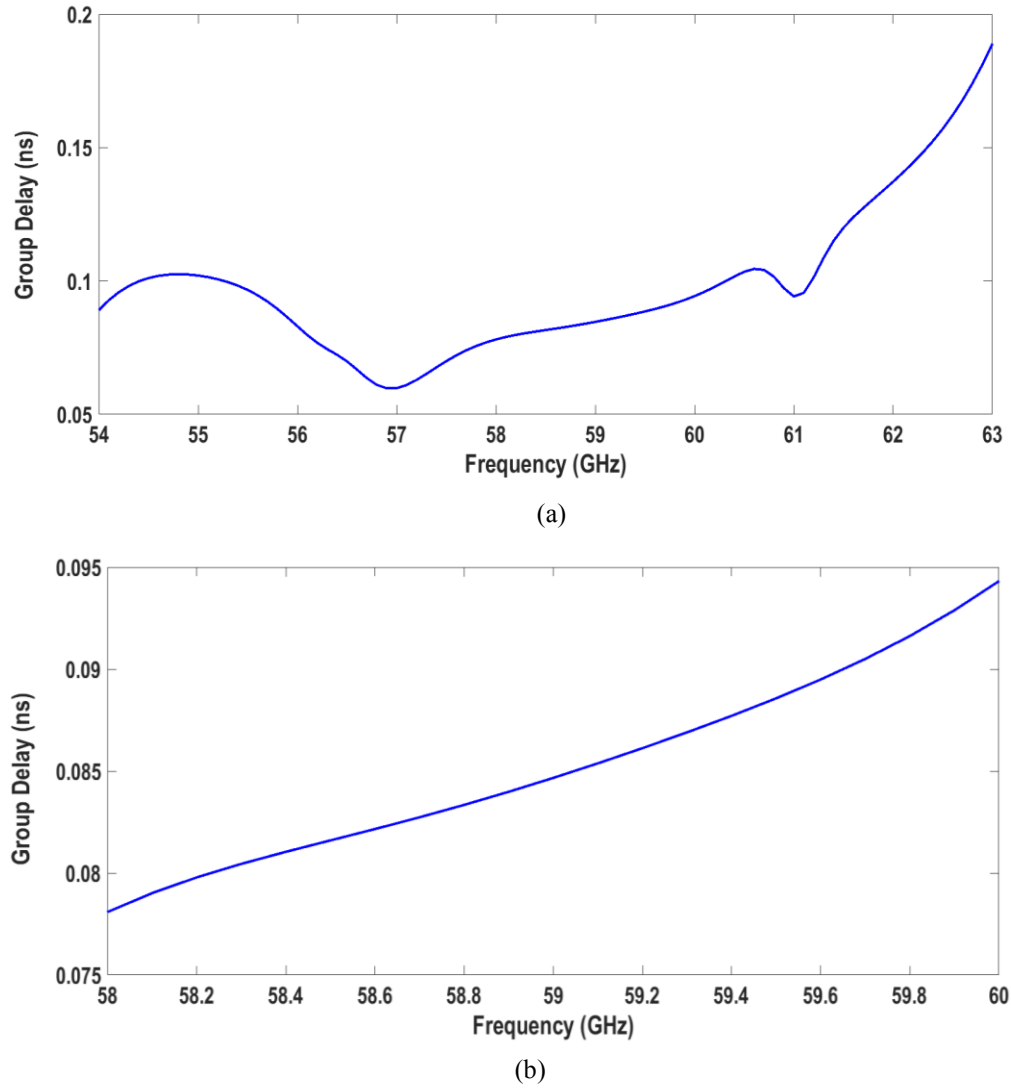


Figure 4.28 Simulated group delay of the EBG guide in the V-band. (a) 54GHz-63 GHz band and (b) 58GHz-60GHz band.

4.4 Conclusion

In this chapter, novel EBG line-defect waveguide capable of guiding transmission in two media air and dielectric is presented. The structure was fed by a coplanar-slot-line transition. A set of prototypes were designed and fabricated.

Acceptable agreement was found between simulations and measurements in Ku-band of the foam-supported guide despite the lack of precision fabrication. Losses were 0.28 dB/period in the channel with 16 periods long and six rows on the sides of the channel. However, the main limitation of this guide is that the foam does not have a perfect smooth

surface which makes RF-on-wafer probe measurements cumbersome and time consuming. Therefore, the dielectric-supported guide was introduced to overcome this shortcoming. Good agreement was observed between theoretical and experimental results in X-band for the EBG guide with dielectric spacer for which insertion loss in the range of 0.2 dB/period was measured. The insertion loss increases by increasing the number of layered rings on the sides of the guiding channel that was contrary to behavior observed in the case of foam-supported EBG guide. In both EBG channel types, the insertion loss does not change significantly by increasing the length of the channel.

CHAPTER 5. EBG COUPLED LINE-DEFECT WAVEGUIDE DIRECTIONAL COUPLER

5.1 Introduction

Directional coupler is widely used in microwave and millimeter-wave systems, for generating desired power splitting with certain specifications such as bandwidth and coupling level. One important application is in antenna feeding circuit, to obtain a specified power division. Directional coupler is a four-port network, which can be implemented in a variety of forms such as: waveguide directional couplers, hybrid junction, branch-line and rat-race directional couplers.

Rectangular waveguide directional coupler was extensively investigated [94-96], and a numbers of circuits have been developed to achieve given specifications for coupling and isolation between ports within the operating band. However, the device is bulky and expensive to manufacture and is difficult to integrate it with other planar circuits. Microstrip coupled-lines coupler offers planarity and low fabrication cost while it is difficult to achieve tight coupling such as 3-dB due to the required impractical very small spacing between lines [97]. Moreover, it suffers from the poor directivity that results from the unequal even- and odd- mode phase velocities in the inhomogeneous medium [98-99]. The directivity performance becomes worse as the coupling is decreased or as the dielectric permittivity is increased. Alternative solutions to improve the coupling include Lange structures [100], and composite right/left-handed transmission lines [101]. Recently, substrate integrated waveguide (SIW) technology has been utilized in the design and fabrication of planar single [102] and multilayer [103-104] directional couplers. All these approaches provide enhanced desired coupling and directivity, but they complicate the design process or make the fabrication cumbersome due to the use of bonding wires, via holes, high dielectric substrates, etc. This chapter investigates the possibility of realizing coupling using the proposed EBG line-defect waveguide.

EBG line-defect waveguide directional coupler with arbitrary tight coupling is presented in this chapter along with exploitation of eigen-mode analysis to understand the operation of forward-wave and/or backward-wave quasi-0-dB and 3-dB couplers. Design guideline

is verified and validated through full wave driven-mode simulations in HFSS. The proposed coupler is deemed to be an interesting alternative to conventional couplers, as it is capable of arbitrary coupling in the forward-wave and/or backward-wave directions. In addition, it is reconfigurable while being an inexpensive uni-planar structure.

This chapter is organized as follows: In section 5.2 the architecture of the coupler is described and the fundamental principle underlying its operation is explained using a modal analysis. Implementation of the coupler is presented in section 5.3 while the subsequent section focuses on simulation results of forward/backward-wave quasi-0-dB and 3-dB couplers. The closing section of this chapter is concluding remarks.

5.2 Architecture and Design of the EBG Line-defect Waveguide Directional Coupler

Fig. 5.1 depicts the investigated EBG line-defect waveguide directional coupler structure. The waveguides are oriented along Γ -X direction of the square lattice of three stacked U-rings in a dielectric slab with $\epsilon_r = 2.94$. The layered rings are spaced by $H = 0.5$ mm and the thickness of the slab is $d = 5$ mm which is a slight modification of the previously designed structure (in Section 3.6.3). Frequency band gap is in the range of 7.8-10.15 GHz. The waveguides are made by reducing the size of one row of stacked rings from $d_l = 4.5$ mm to $d_w = 2.8$ mm. Defect rings are on single (vertically centered) layer to ensure single-mode propagation. Fig. 5.2 illustrates the dispersion curves of the corresponding waveguide. As shown in this figure, mode 1 is an in-gap guided mode, as it is within the band gap. Mode 2 is very close to the light line and the field distribution showed that it is not confined in the channel which testifies to its leaky unbounded nature.

To create the EBG coupler, a number of rows with defected (coupling) region of stacked coupling rings is left between two identical line-defect waveguides. In this study, the number of the rows and the dimension of the coupling rings are $n_r = 2$, $n_c = 3$ and $d_c = 3$ mm respectively. In order to calculate the dispersion relation of the structure, the computational super-cell highlighted in Fig. 5.1 (b) is used, with periodic boundary conditions on its x-sides and perfect magnetic conductors on its z and y-sides. The dispersion diagram of the coupler is shown in Fig. 5.3. It can be observed that two guided

modes lie in the bandgap. These guided modes are known as super-modes of the coupler [105-106]. In other words, the single waveguide mode splits into two directional coupler modes. These super-modes have even and odd symmetry with respect to the coupler symmetry plane, which is perpendicular to the y-axis and runs in the middle of the structure. Note that the even mode is placed lower than the odd mode in terms of frequency which resembles the modes of dielectric-rod-type directional coupler [105].

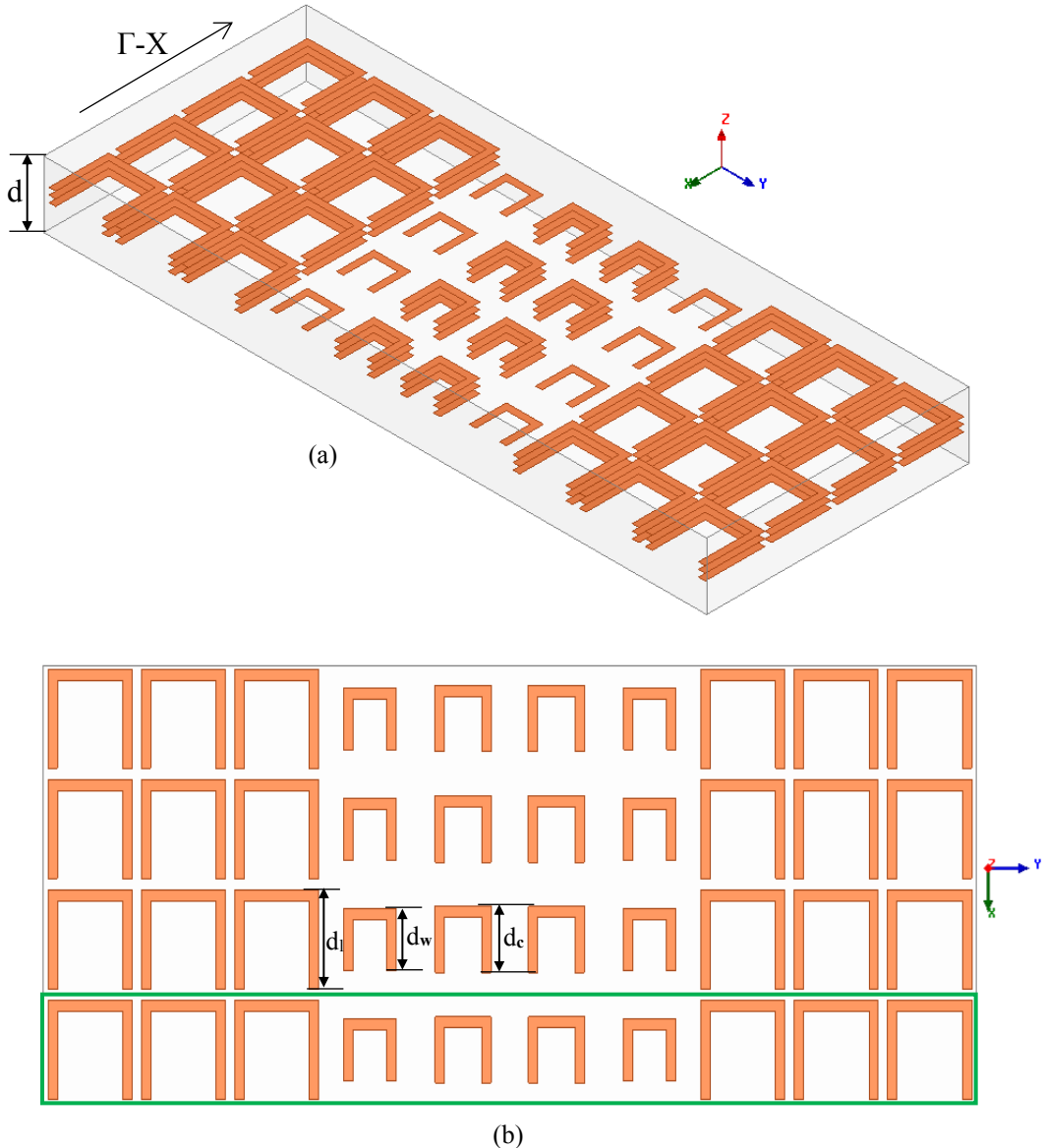


Figure 5.1 Schematic diagram of the proposed line-defect EBG slab waveguide coupler. (a) xyz plane: d is the thickness of the slab. (b) xy plane: the sizes of the lattice ring, waveguide ring and coupling ring are d_l , d_w and d_c respectively. The highlighted rectangle is the supercell used to calculate the dispersion relation.

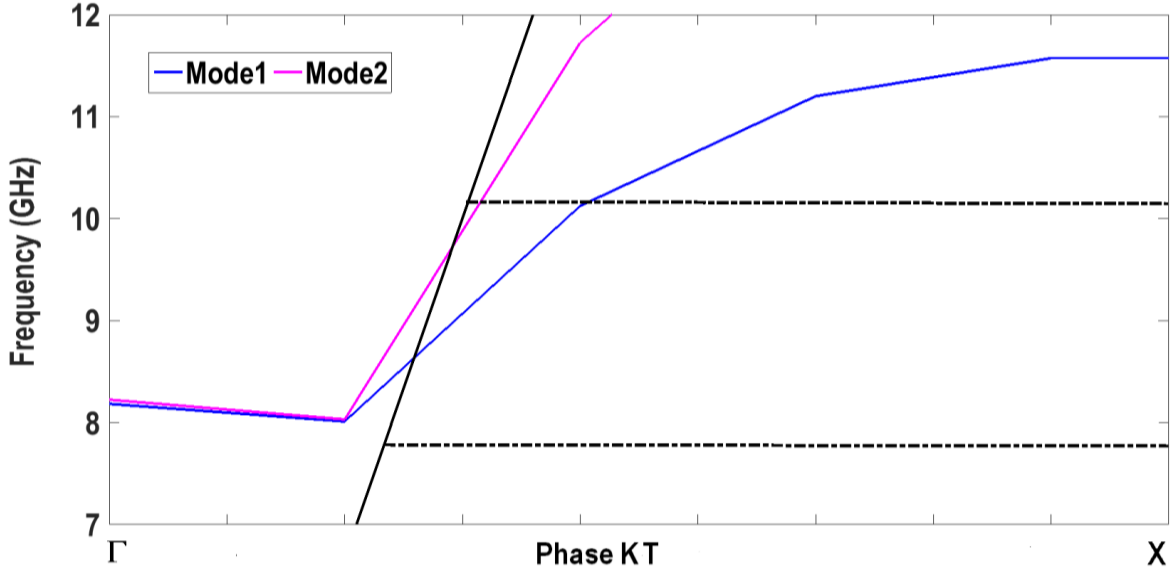


Figure 5.2 Dispersion of modes of single EBG line-defect waveguide.

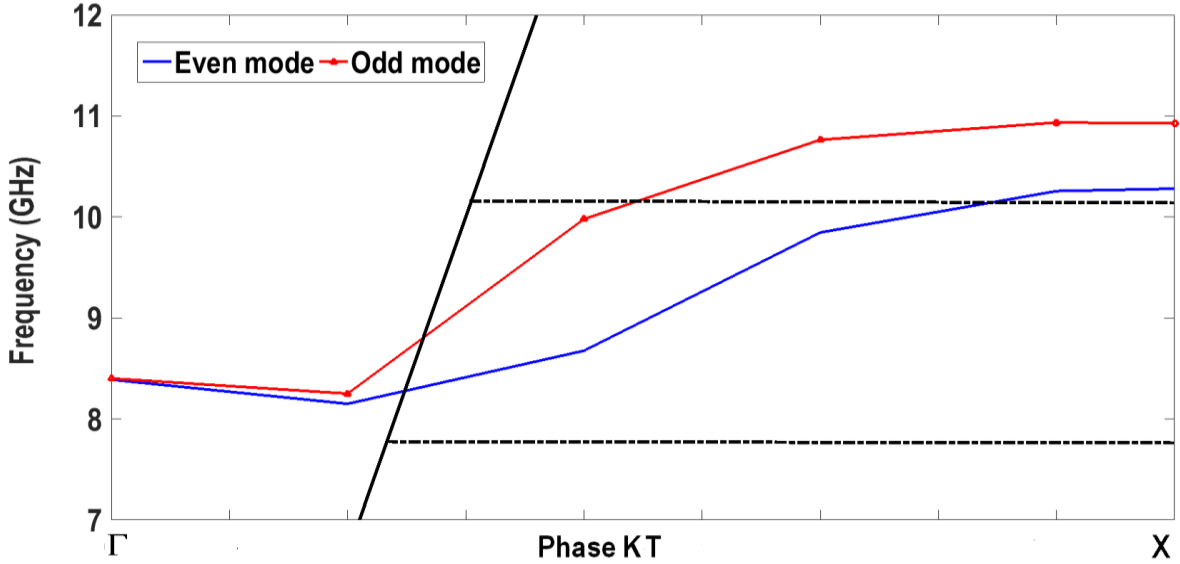


Figure 5.3 Dispersion of supermodes of the proposed EBG waveguide coupler.

The field patterns for the eigen-modes in the coupling region are shown in Fig. 5.4. The fields are calculated at the frequency of 9 GHz and it can be seen that the even (odd) mode is maximum (minimum) on the symmetry plane.

Wave propagating in each of the waveguides is a superposition of the even and odd supermodes of the directional coupler [106]. These super-modes have different Bloch

propagation constant k_e and k_o , henceforth propagating at different phase velocities. Complete transmission of RF power from one guide to the other occurs after propagating a length, known as the minimum coupler length L_c [107].

$$L_c = \frac{\pi}{|k_e - k_o|} = \frac{\pi}{\Delta k} = \frac{\pi}{2\kappa} \quad (5.1)$$

with $\kappa = \frac{\Delta k}{2}$ is the coupling coefficient.

This coupler is known as forward-wave (or co-directional) directional coupler [97] because the coupled wave on the secondary guide travels in the same direction as the primary guide. Forward-wave directional coupler can be realized using non-TEM mode transmission lines [97], and yet the proposed EBG coupler supports non-TEM (TE) modes.

When the mismatch between the propagation constants of both modes is large, the coupling length becomes small. The coupling length can be calculated from the dispersion graph by choosing a specific frequency and finding the corresponding values of the Bloch phase shifts, for the even and the odd eigenmodes.

As an example, for the proposed coupler and for a frequency $f = 10.1$ GHz, from Fig. 5.3 the propagation constants are $k_e T = 0.8\pi$ and $k_o T = 0.47\pi$, where T is the lattice constant. The calculated coupling length from Eq. (5.1) is $L_c = 3T$.

From the graph, it can be noticed that Δk decreases as the frequency decreases. Therefore, the coupling length becomes longer at the lower edge of the operating band. However, Δk enlarges as the frequency increases. Thus the coupling is frequency dependent.

Fig. 5.5 displays the dispersion relation of the modes of the coupler for different d_c values. From the graph, it can be observed that the even and odd modes shift to higher frequencies as the size of the coupling rings reduces. Moreover, the spacing between the even and odd modes reduces, indicating higher coupling length and lower coupling coefficient.

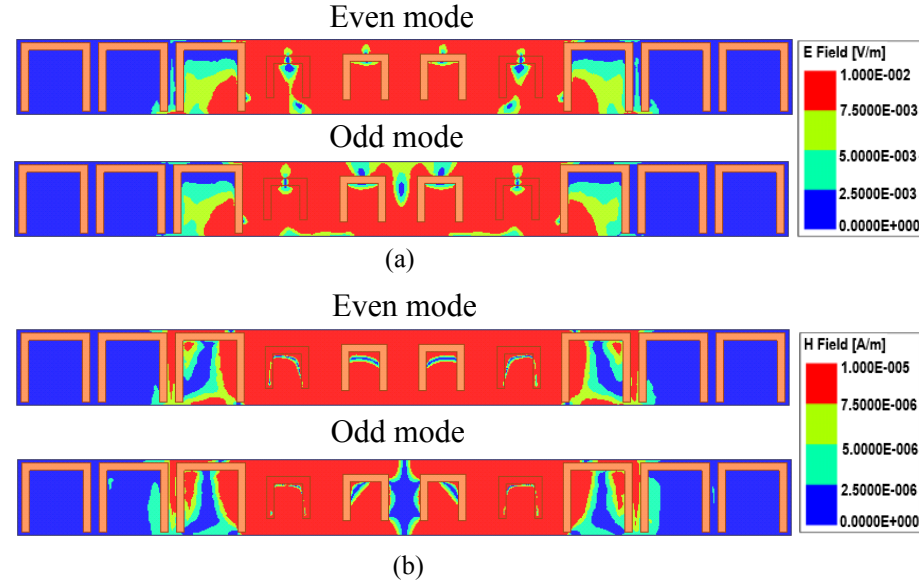


Figure 5.4 (a) Electric and (b) magnetic field profiles for the super-modes.

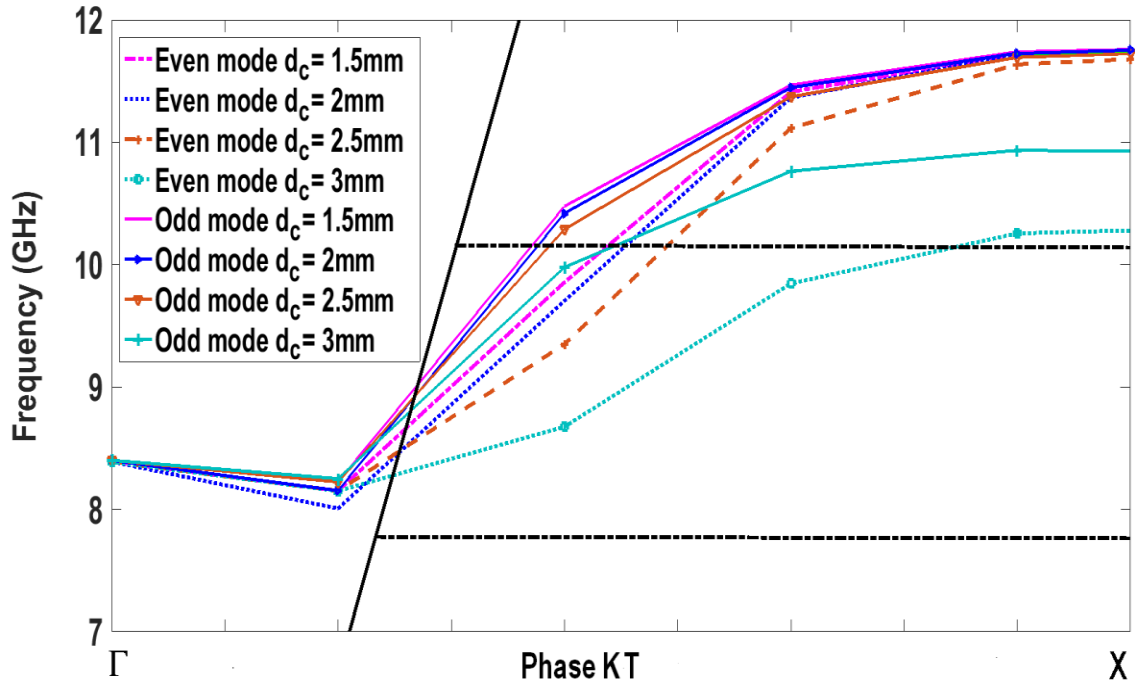


Figure 5.5 Dispersion relation of the proposed EBG coupler for different d_c values.

5.3 Implementation

Fig. 5.6 (a) shows the configuration of the proposed EBG directional coupler. It consists of two line-defect waveguides, sharing two rows of layered rings that have a defect region of three unit cells to realize coupling between the two channels. The layered rings in the defect region are spaced by s as shown in Fig. 5.6 (b). The coupling is mainly controlled by the parameter s . The dimension of the coupling rings is $d_c = 3 \text{ mm}$.

That port numbering schemes has been defined in the same figure port 1, 2, 3 and 4 being input, through, isolation, and coupling ports, respectively. Since the field distributions in a line-defect waveguide are like those in a slot line, CPW-to-slot line transition is used to launch the waveguide mode. The geometrical parameters of the transition are as presented in Chapter 4 (Section 4.3.1).

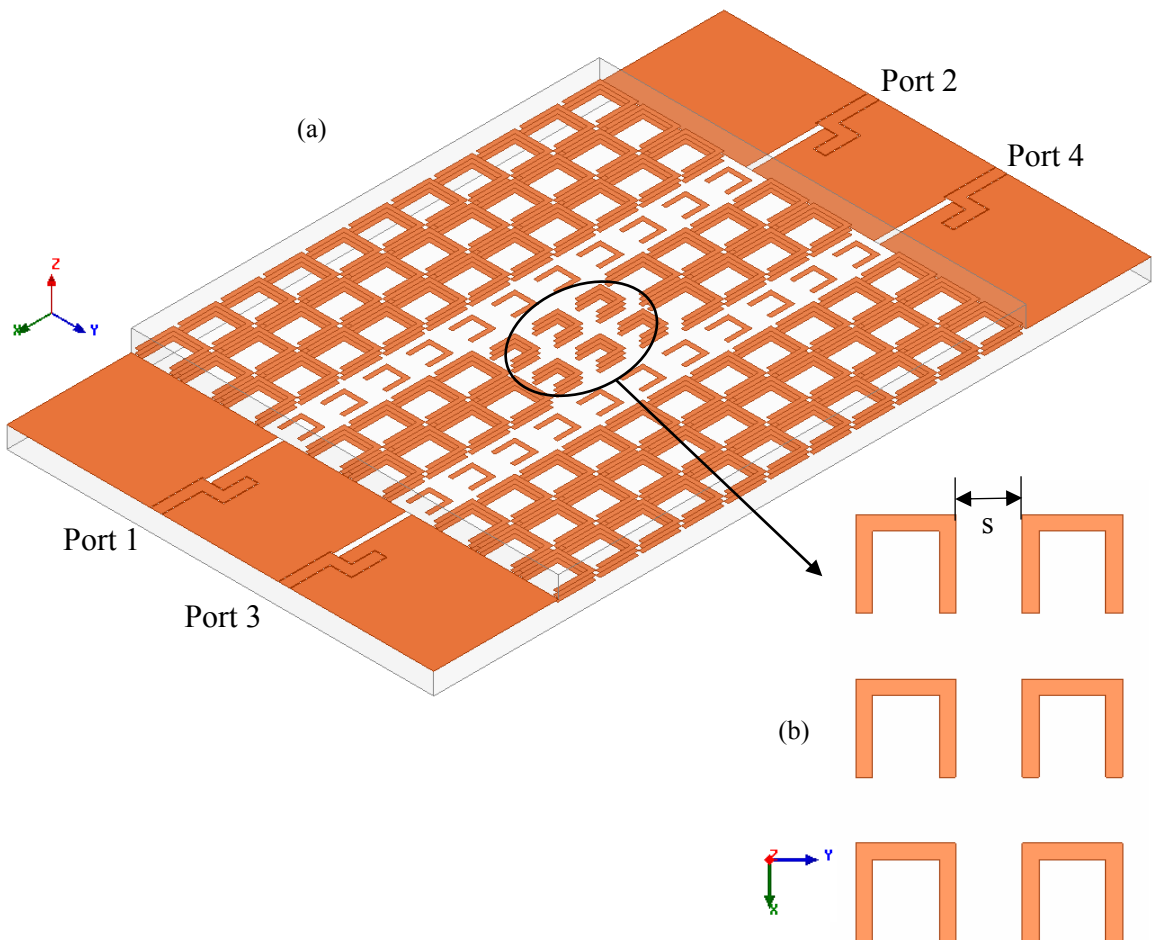


Figure 5.6 (a) Structure of the proposed EBG coupler. (b) Coupling region, where layered rings are spaced by $s = 2 \text{ mm}$ along y-direction.

5.4 Results and Discussion

5.4.1 Quasi-0-dB Forward-Wave Coupler

The proposed coupler is capable of achieving wide range of coupling values by adjusting the spacing s between coupling rings. Fig. 5.7 shows the simulated S-parameters of the coupler for $s = 2.2 \text{ mm}$. Strong coupling can be observed, which validates the above eigen-mode theory. The insertion loss for coupling (S41) varies between 3.4 and 4 dB in (10.5-10.75) GHz. The return loss S11 and isolation S21 and S31 are better than 14 dB. Those results suggest a 2.3% bandwidth of this quasi-0-dB coupler. The E-field distribution at 10.7 GHz is reported in Fig. 5.8. It shows complete forward power coupling from the input channel to the coupled channel. This confirms that the structure is a forward-wave directional coupler. In fact, this phenomenon of full wave coupling can also be demonstrated with other spacing values s between the coupling rings.

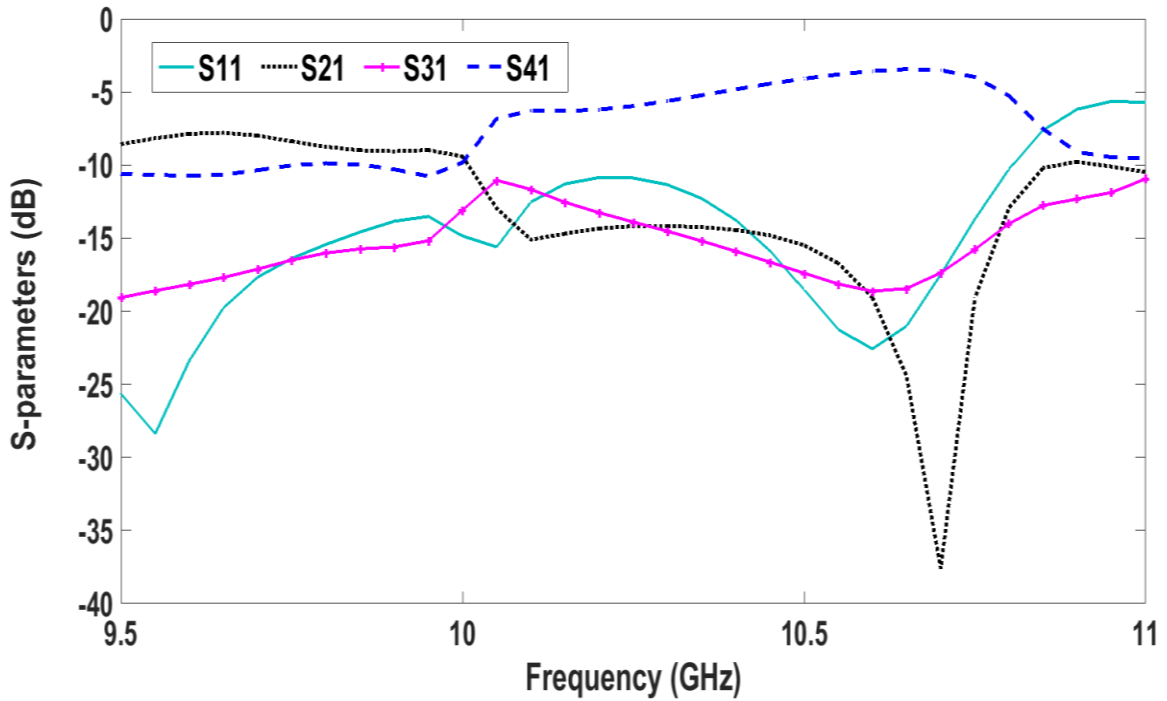


Figure 5.7 S-parameters of the quasi-0-dB EBG forward-wave coupler.

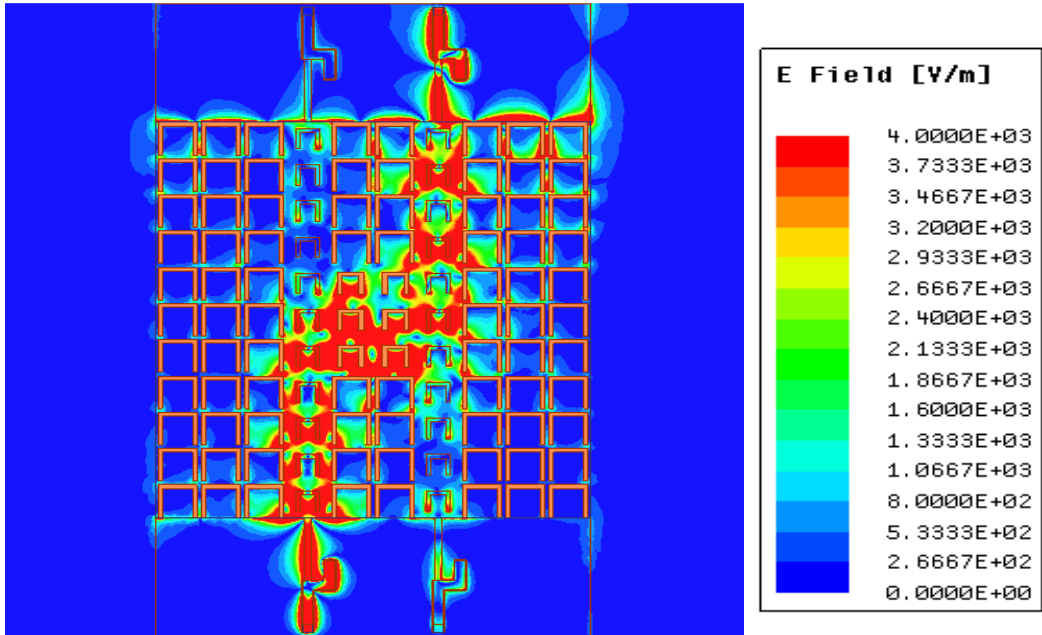


Figure 5.8 E-field distribution at 10.7 GHz for the quasi-0-dB EBG forward-wave coupler.

5.4.2 Quadrature Forward-wave Coupler

By decreasing the distance s to 0.8 mm in the configuration of Fig. 5.7, a 3-dB coupler is achieved. Its performance is depicted in Figs. (5.9-5.11) showing the response of S-parameters. The amplitudes of S_{21} and S_{41} are 6 ± 0.5 dB, therefore the amplitude balance varies between -0.15 and 0.8 dB. The return loss S_{11} and the isolation S_{31} are greater than 15 dB in the frequency range 10.4 GHz-10.9 GHz.

Figs. (5.12-5.13) show the phase difference between port 2 and port 4 of the proposed coupler. The quadrature phase balance is $90^\circ + 5^\circ$ from 10.55 to 10.8 GHz. Those results suggest that the bandwidth of the 3-dB directional coupler for equal power splitting is 2.3%. The E-field distribution at $f = 10.75$ GHz is shown in Fig. 5.14.

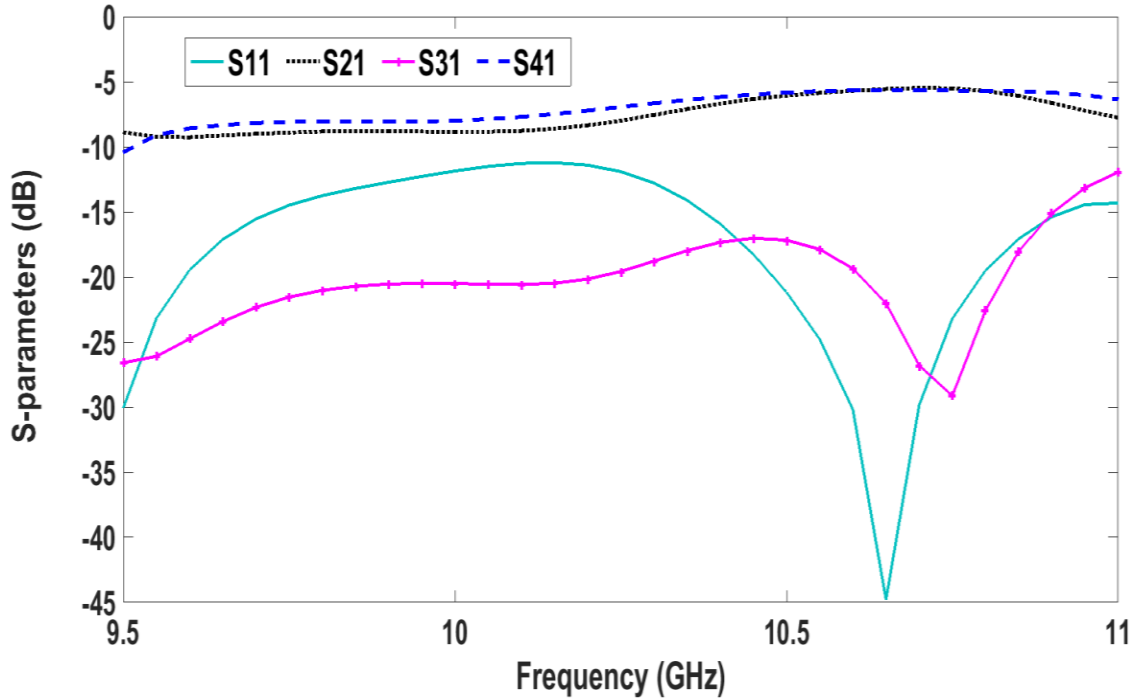


Figure 5.9 S-parameters of the quadrature forward-wave EBG coupler.

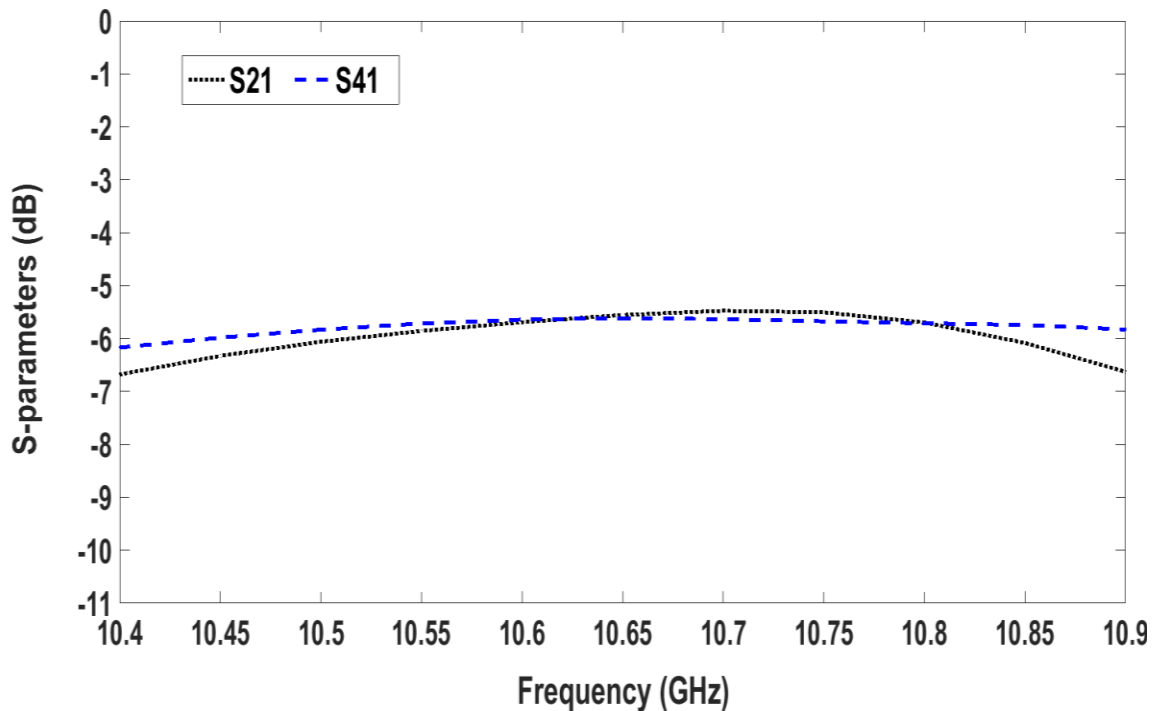


Figure 5.10 S21 and S41 of the quadrature EBG coupler.

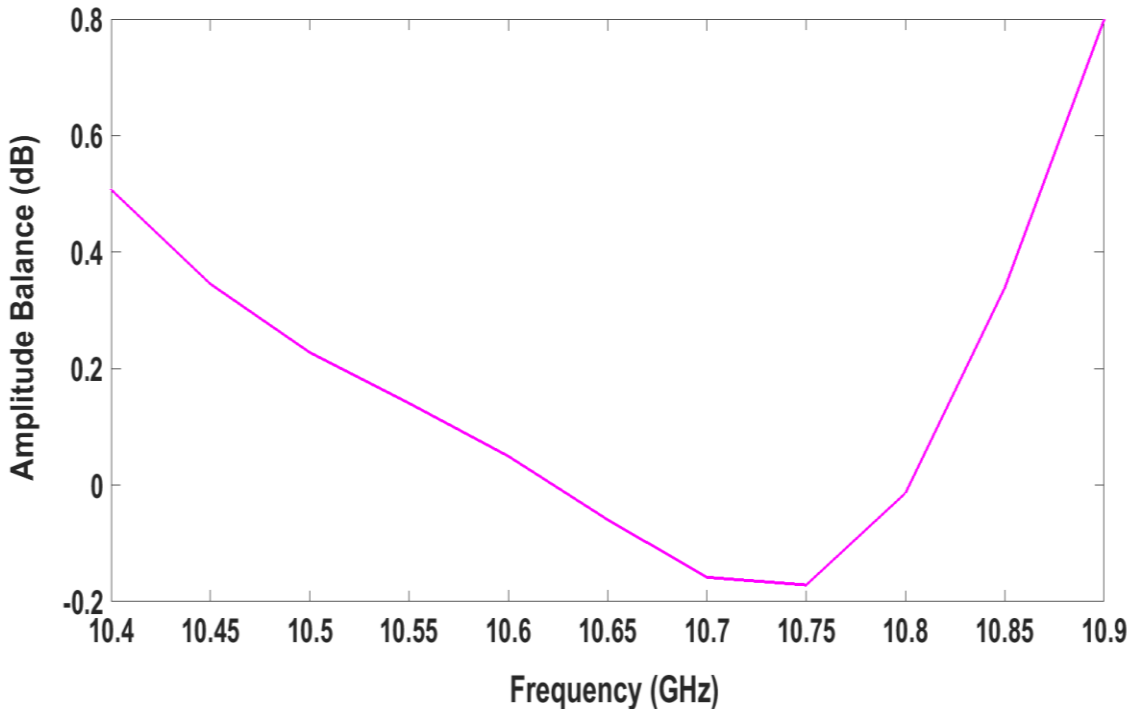


Figure 5.11 Amplitude difference between S21 and S41.

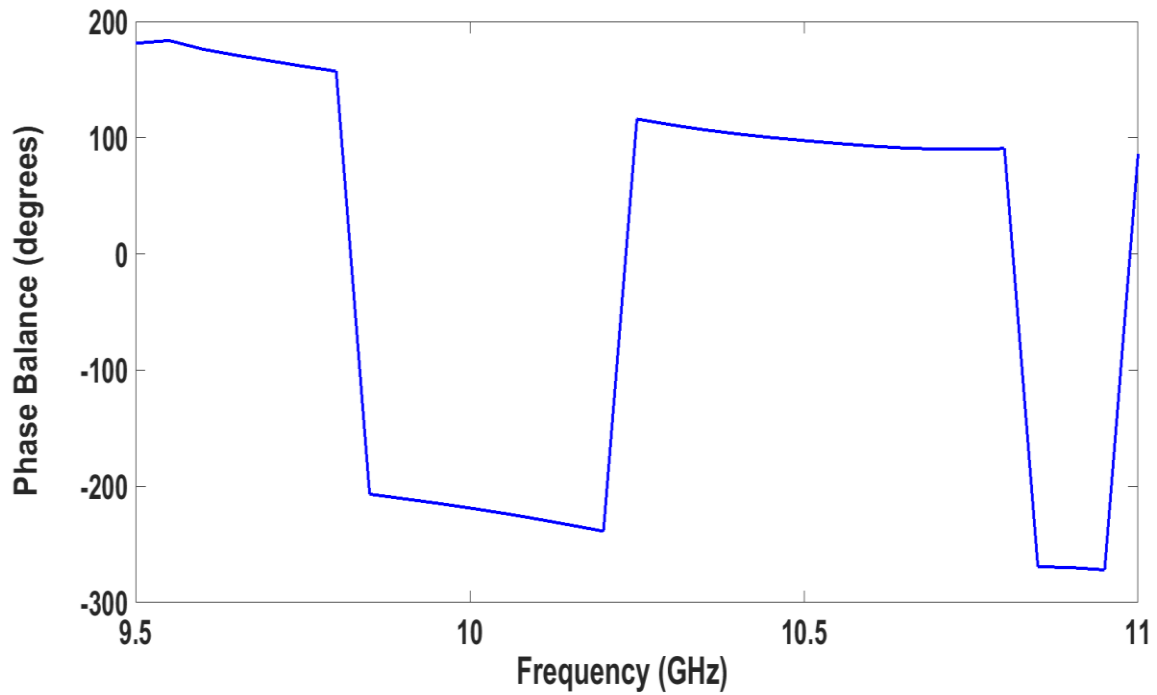


Figure 5.12 Phase difference between S21 and S41.

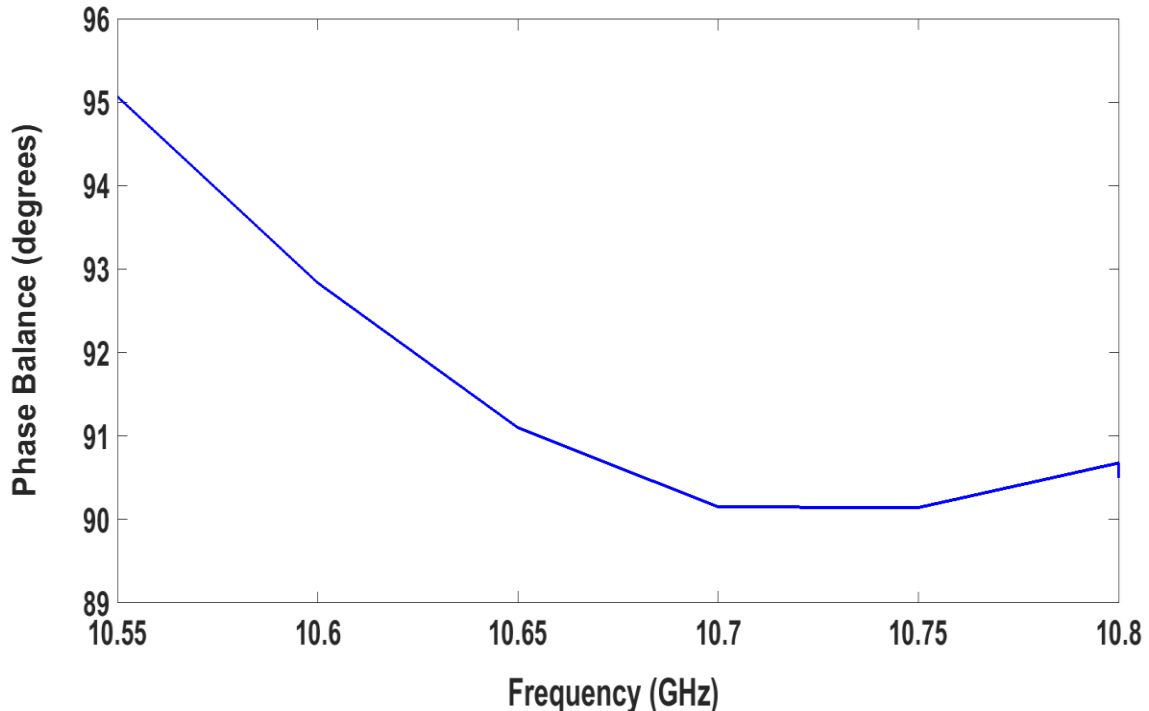


Figure 5.13 Phase difference between S21 and S41 in the coupling bandwidth 10.55-10.8 GHz.

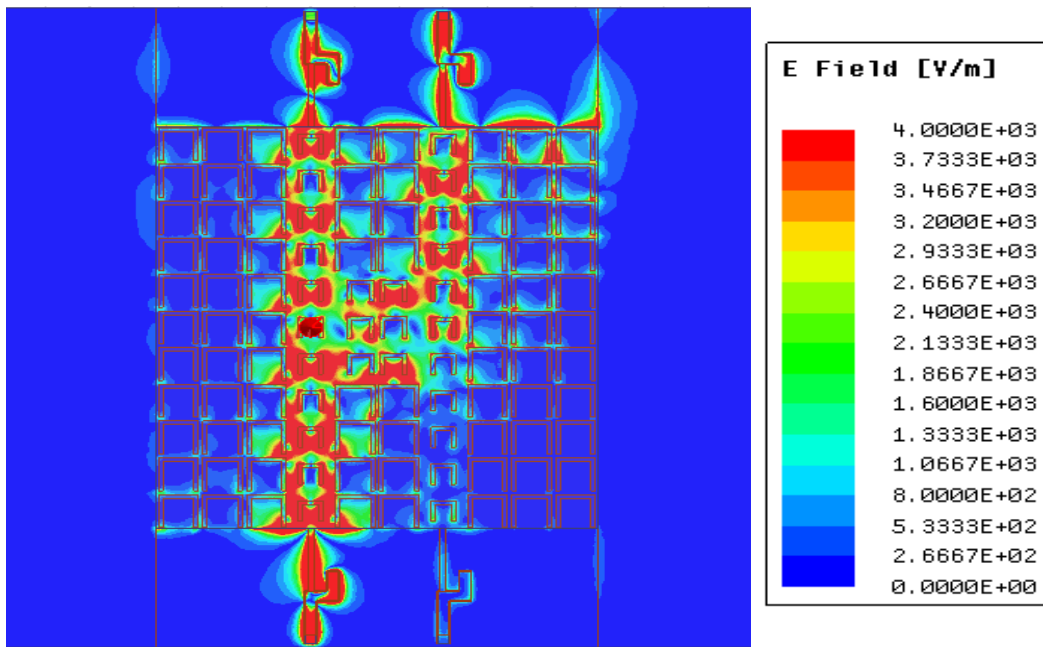


Figure 5.14 E-field distribution at 10.7 GHz for the quadrature EBG coupler.

5.4.3 Through Coupling

Fig. 5.15 shows S-parameters of the quadrature coupler of Fig. 5.9 when the coupling rings are rotated 90°. A through transmission, i.e., decoupling is in the whole frequency range 9.5-11 GHz. A careful examination of the electric and current fields in the channel and the region of rotated rings showed that the fields have different polarizations. The incident electric fields in the channel are directed along the symmetry axis of the rotated rings. These fields induce polarization currents in the rotated rings, that do not couple to the polarization currents (propagating state) in the channel.

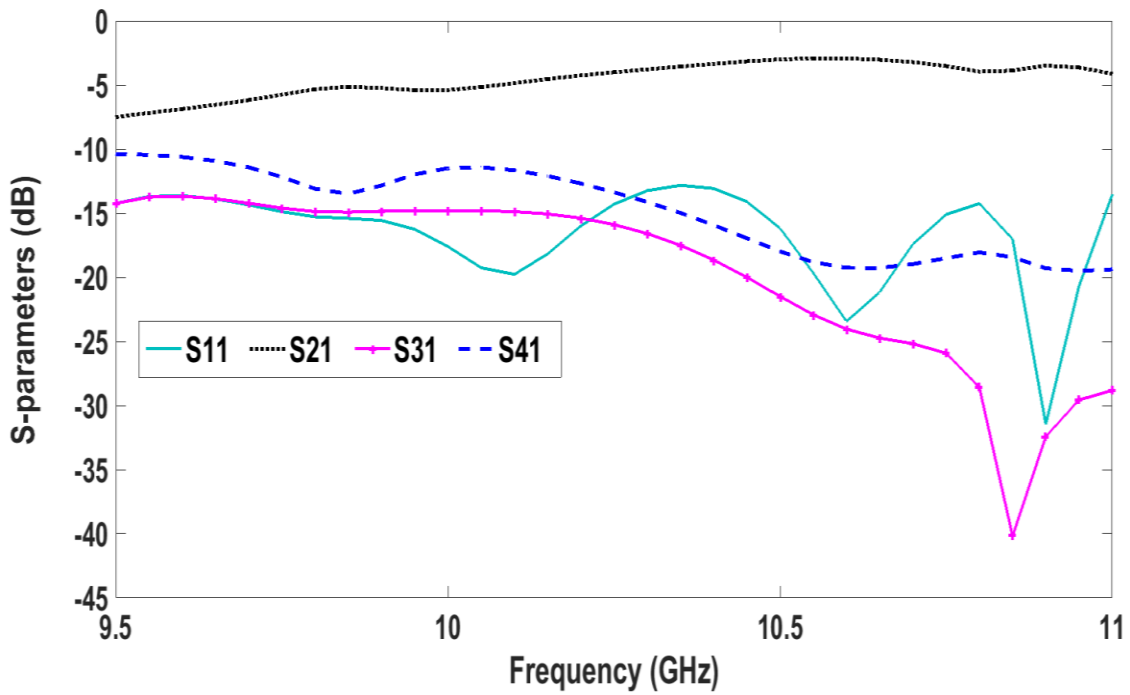


Figure 5.15 S-parameters of the through propagation.

Fig. 5.16 illustrates the E-field distribution at frequency 10.7 GHz. Indeed. This through propagation occurs for any spacing between rotated 90° coupling rings such as the case of quasi-0-dB coupler. Beside that, it can be implemented using single rotated row, i.e., the first one. Therefore, this property can be used to make the coupler reconfigurable.

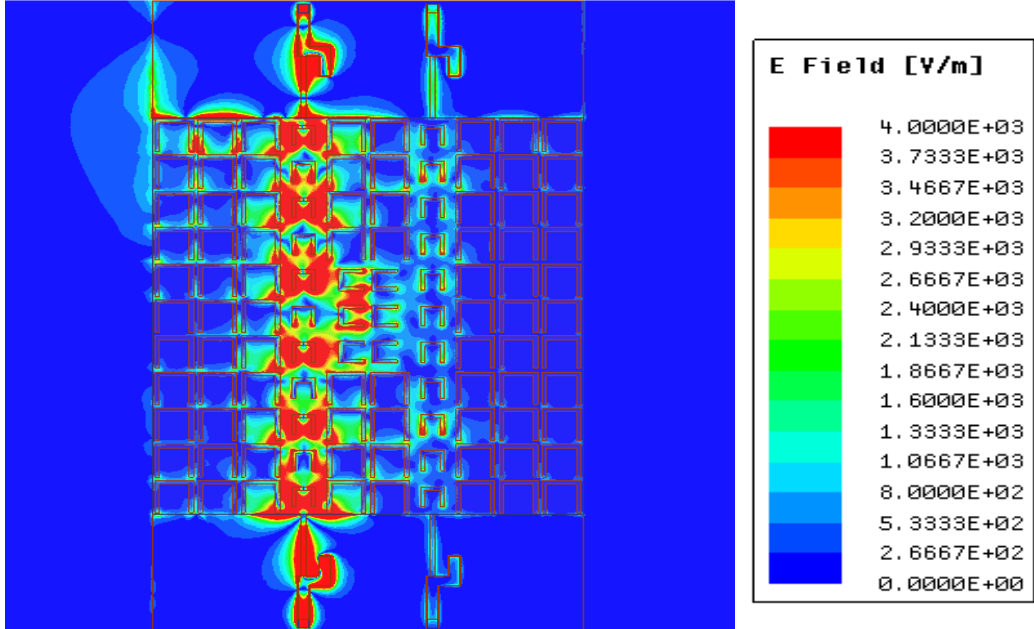


Figure 5.16 E-field distribution at 10.7 GHz of the through propagation.

5.4.4 Quasi-0-dB Forward/Backward Wave Coupler

Quasi-0-dB forward-wave coupler was demonstrated in Sec. 5.4.1, whereas a through coupling was shown in Sec. 5.4.3. In fact, through coupling was achieved by changing the orientation of the rings in the coupling region. Changing the orientation of the rings in the direct and coupled channels results in coupling the power to other ports (directions). where the rotated channel rings create strong scattering to launch backward- and forward-propagating mode. Figs. 5.17 (a-b) are the structures of the above quasi-0-dB coupler with rings in the channels rotated by 90° and 180° respectively. Figs. 5.18 and 5.19 show the results of the two implementations. From both graphs, it should be noted that in addition to the quasi-0-dB forward-wave coupling, there is a backward-wave coupling (ports 3) and through coupling (port 2) from 11.2 to 11.55 GHz when the rings are rotated 90° (Fig. 5.18), and a backward-wave coupling (port 3) from 11.05 to 11.3 GHz when the rings are rotated by 180° (Fig. 5.19).

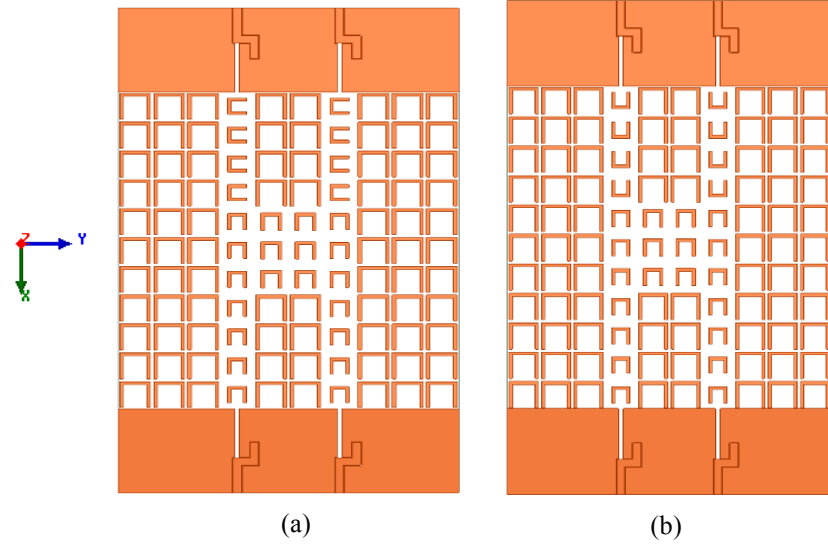


Figure 5.17 Structure of the quasi-0-dB EBG coupler with rotated channel rings'. (a) Rings are rotated by 90°. (b) Rings are rotated by 180°.

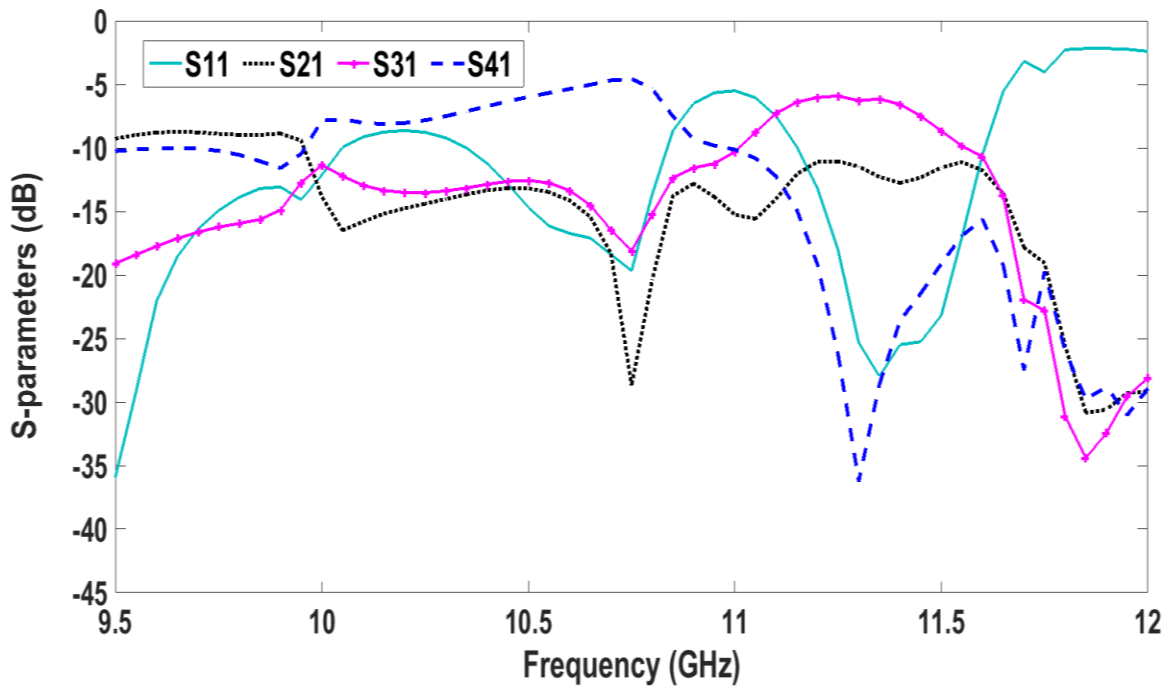


Figure 5.18 S-parameters of the quasi-0-dB coupler, with channel rings' rotated 90°.

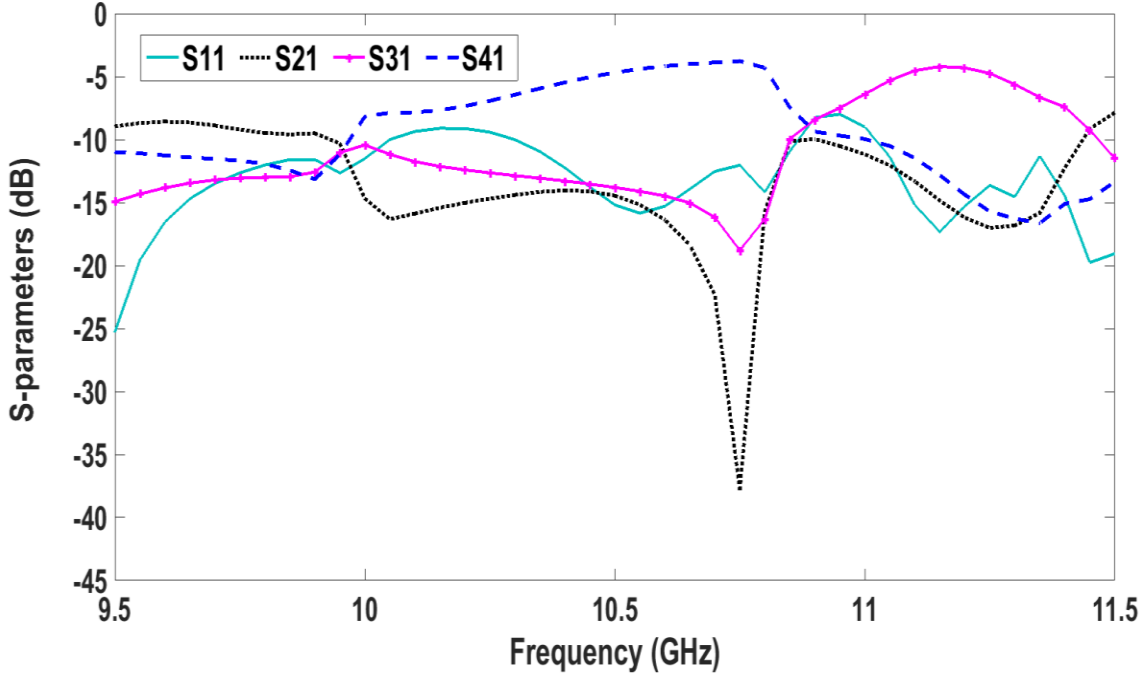


Figure 5.19 S-parameters of the quasi-0-dB coupler, with channel rings' rotated 180°.

5.4.5 3-dB Forward-/Backward-Wave Coupler

Adding an extra row of layered rings between the two line-defects waveguide structures shown in Fig. 5.6 is another possibility that was studied. The implementation is shown in Fig. 5.20, where the rings in the coupling region are spaced with $s = 2.5 \text{ mm}$. Fig. 5.21 shows the performance of this design. A 3-dB coupler is achieved in the frequency range 10.4-10.7 GHz. The amplitudes of S31 and S41 are $7.6 \pm 0.4 \text{ dB}$ achieving equal power split between port 3 and 4. This unique coupler couples the incident wave in the backward direction (port 3), and forward coupling direction (port 4). The amplitude balance varies between -0.84 and 0.51 dB, this is shown in Fig. 5.22. The return loss S11 and the isolation S41 are greater than 15 dB. The phase difference between ports 3 and 4 varies between 27.6° and 48.3°. The result is shown in Fig. 5.23. The E-field at $f = 10.65 \text{ GHz}$ is shown in Fig. 5.24.

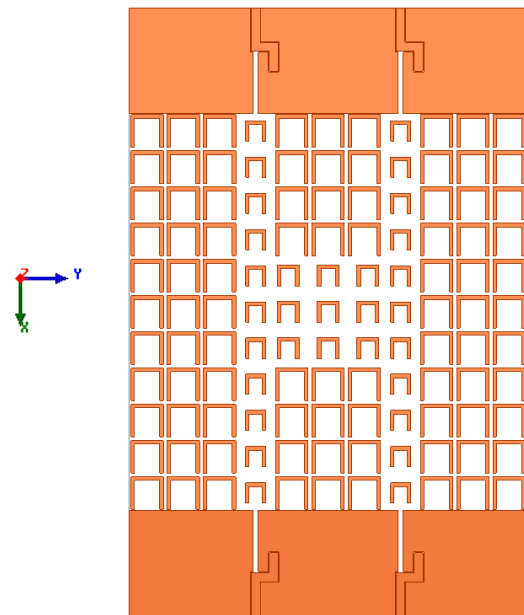


Figure 5.20 Structure of 3-dB forward-/backward- wave EBG coupler.

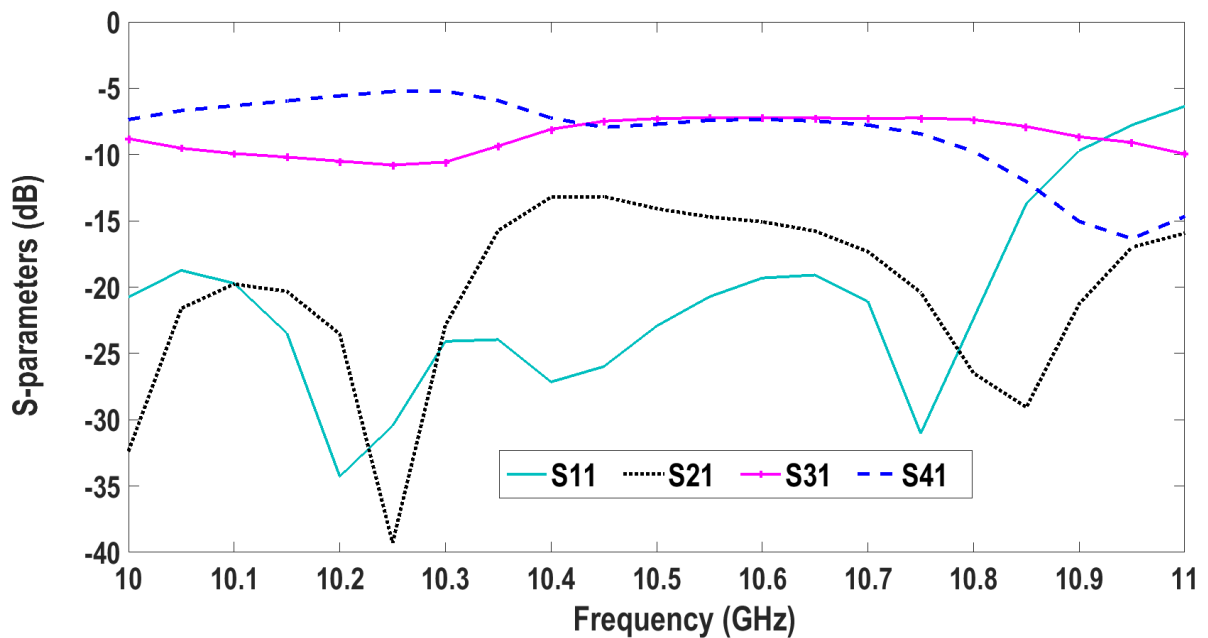


Figure 5.21 S-parameters of the 3-dB forward-/backward- wave EBG coupler.

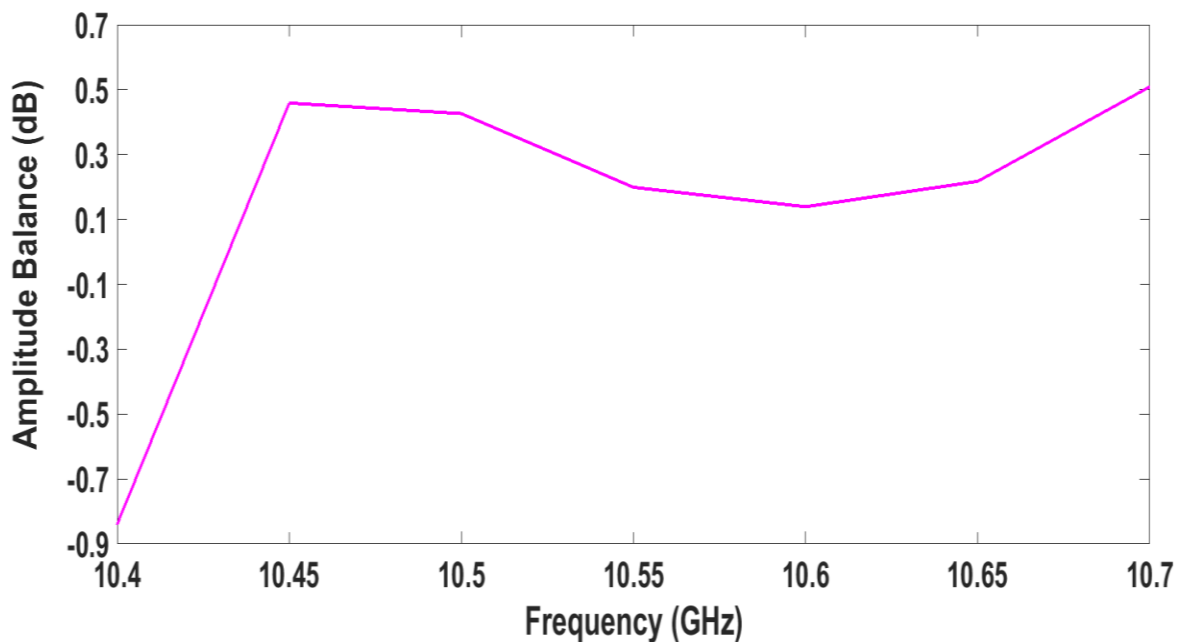


Figure 5.22 Amplitude difference between S31 and S41.

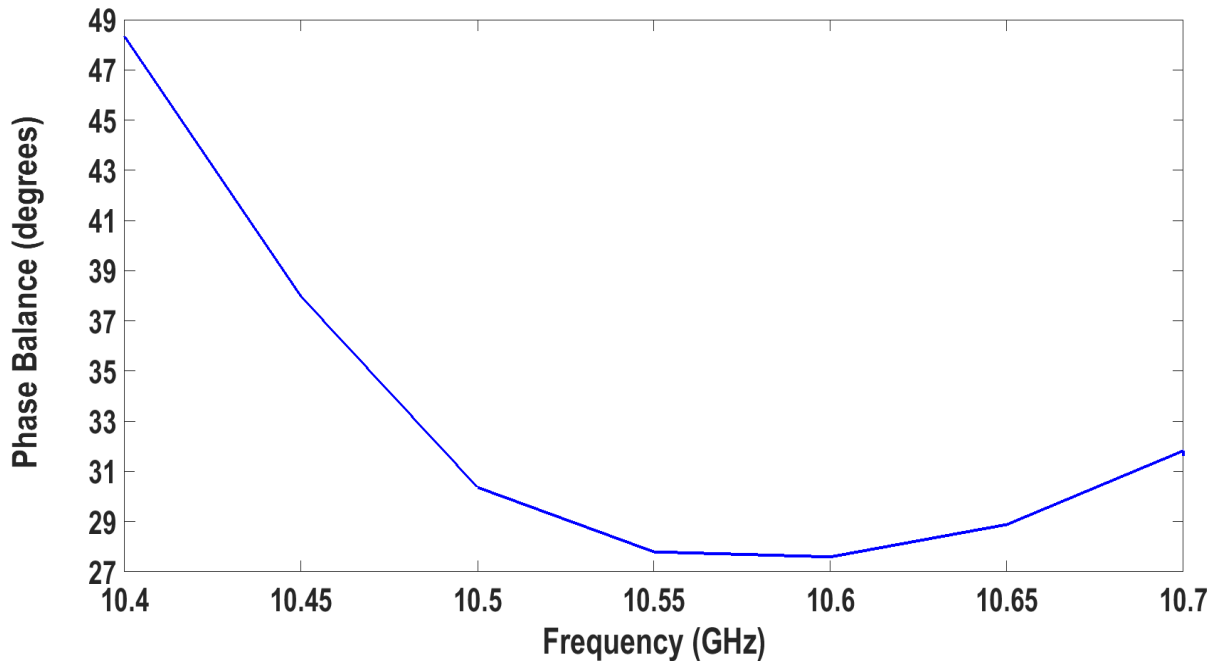


Figure 5.23 Phase difference between S31 and S41.

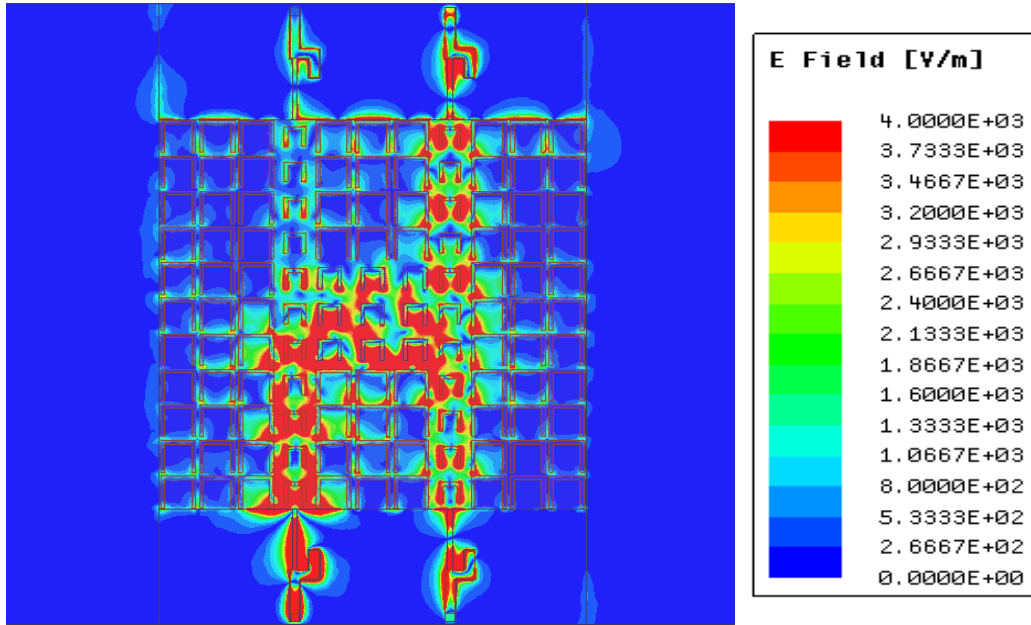


Figure 5.24 E-field distribution at 10.65 GHz of the 3-dB forward-/backward- wave EBG coupler.

5.5 Conclusion

In this chapter, a novel EBG coupler capable of producing arbitrary coupling was presented. The structure was studied using eigen mode analysis which gives insight into dispersion characteristics of the structure. The underlying principle of the coupler was validated by a coplanar-slotline feeding of the structure that was outlined and presented in the previous chapter. Quasi-0-dB couplers and 3-dB couplers have been demonstrating good phase balance and isolation. Unique features of this coupler are wave propagation in the forward- and/or backward- directions and it can be reconfigurable by simply rotating its coupling elements.

CHAPTER 6. CONCLUSIONS, CONTRIBUTIONS AND RECOMMENDATION FOR FUTURE WORK

6.1 Summary

This thesis focused on the following objectives:

- a) Studying the dispersion characteristics of EBG-OSR structures.
- b) Developing EBG-OSR waveguides.
- c) Applying EBG waveguides to microwave circuits such as multifunctional couplers.

Chapter three covered in detail the proposed novel EBG-OSR structure. EBGs with air and dielectric host material were considered. Parametric studies were performed to demonstrate dependence of dispersion characteristics on the structural parameters of the EBG structure. Then, a study of OSR EBG slabs was presented. The thorough study of guiding mechanisms by embedding a 1D defect in the regular OSR lattice was undertaken subsequently. Various techniques were presented for the design of OSR-based EBG slab waveguides. The performance of the U-ring structure at microwave frequencies was considered next.

Chapter four focused on the implementation and experimental characterization of slab waveguides in air (foam) and dielectric material, based on the design of slab structures presented in chapter three. A set of waveguides were designed for operation in the 13-16 GHz bands. Specifically, compact and simple CPW feeding structures were designed and integrated into the waveguides. Challenges of physical realization were identified and methods to overcome them were proposed and verified experimentally by new waveguides that operate in the 8-12 GHz band. The experimental results of all fabricated prototypes demonstrated reasonable agreement with simulation results.

Chapter five presented the design of novel directional couplers based on EBG waveguide by setting linear defects in close proximity and introducing an isolated coupling region. By changing either the distance between the rings or orientation of the rings in the coupling region, one can achieve a very interesting and unique coupling mechanisms that have not been reported previously in the conventional implementations of couplers. Forward-wave

and/or backward-wave quasi-0-dB and 3-dB couplers with the ability of being reconfigurable have been demonstrated.

The developed line-defect waveguides are quite narrow band and lossy. The mean loss is 40 dB/m in (10-11) GHz, which originates from surface waves excitation and radiation. More work is needed to further improve these aspects.

6.2 Contributions

This thesis aims to contribute to the research of EBG structures.

The main contributions from this research include:

- Study of novel EBG-OSRs fundamental behaviors (i.e., dispersion characteristics, eigen field distributions, band gaps, guiding mechanisms) with design guides. Some material was presented in [57-58] and the rest of the study will be submitted for publication.
- Design, fabrication, measurement and validation of novel EBG-OSRs slab waveguide in foam and dielectric media including feed transition optimization. Some material is in [76][83] and the rest will be submitted as full length journal papers.
- Study and demonstration of novel couplers applications based on EBG-OSRs waveguides. This will be submitted as full length journal paper.

6.3 Future Work

The OSR-EBG concept is at its early stages and diverse capabilities of this class of EBG need further exploration and development. Since the structure is compatible with planar circuits, innovative devices and circuits can be developed for mm-wave and sub-mm-wave applications.

- 1) The parametric analysis was performed by changing one variable at a time and keeping others constant to gain basic understanding of the trends. A multi-variable analysis, i.e., Monte Carlo analysis is needed for complete exploration of the multidimensional parameter space.

- 2) Multilayer fabrication process, i.e., photoimageable thick-film technology could be used for increased precision and reduced misalignment between vertical layers. The process is cost-effective and has been used successfully to develop high performance components and circuits of up to 180 GHz.
- 3) The Line-defect EBG waveguide can be applied to design EBG phase shifter.
- 4) The EBG 90° hybrids (couplers) and phase shifters can be used to develop an NxN EBG Butler matrix.
- 5) The EBG butler matrix can be used to feed multi-beam antenna array.
- 6) The line-defect EBG waveguide can be applied to design slot array antenna array and distribution feed network to transmit the power to the radiating elements.
- 7) The OSR-EBG structure could be used to develop filters, sensors and antennas.
- 8) The principle of reconfigurable EBG-coupler was introduced in Chapter 5. The next step is to implement true reconfigurability using RF-switches. The latter would form the green and black segments as shown in Fig. 6.1 to perform the ON-OFF states. A study of coupling-decoupling mechanism needs to be conducted, taking into account parasitics and biasing effects.

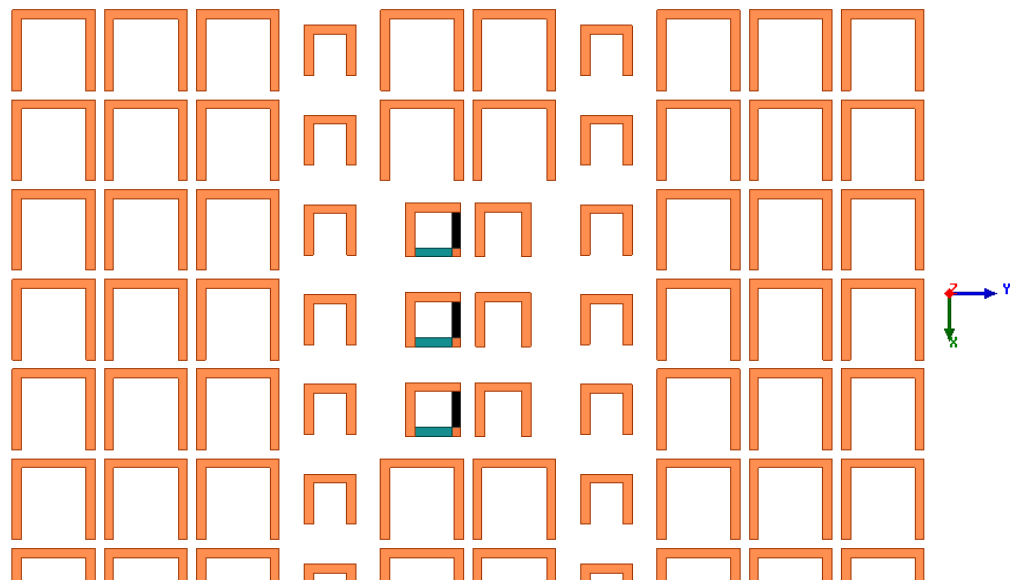


Figure 6.1 Reconfigurable coupler, to be implemented using the ON-OFF green and black segments.

BIBLIOGRAPHY

- [1] J. Maddox, "Photonic Band-Gaps Bite the Dust," *Nature* 348, 481, 1990.
- [2] J. D. Joannopoulos, R. D. Meade, and J. N. Winn, *Photonic Crystals; Molding the Flow of Light*. Princeton, NJ: Princeton Univ. Press, 1995.
- [3] E. Yablonovitch, "Photonic Band-Gap Structures," *Journal Optical Society of America*, vol. 10, no. 2, pp. 283 – 295, Feb. 1993.
- [4] F. R. Yang, K. P. Ma, Y. Qian, and T. Itoh, "A uniplanar compact photonic-band gap (UC-PBG) structure and its applications for microwave circuits," *IEEE Trans. Microw. Theory Tech.*, Vol. 47, No. 8, pp. 1509–1514, Aug. 1999.
- [5] B. Lin, Q. Zheng and N. Yuan, "A novel planar PBG structure for size reduction," *IEEE Microw. Wireless Comp. Lett.*, Vol.16, No. 5, pp. 269-271, May 2006.
- [6] G. S. Smith, M. P. Kesler, and J. G. Maloney, "Dipole antennas used with all-dielectric, woodpile photonic-bandgap reflectors: gain, field patterns, and input impedance," *Microwave and Optical Technology Letters*, Vol. 21, No. 3, 191–196, May 1999.
- [7] Y. Qian, V. Radisic, and T. Itoh, "Simulation and experiment of photonic bandgap structures for microstrip circuits," *Proceedings of Asia Pacific Microw. Conf. (APMC)*, Hong Kong, China, pp. 585–588, 1997.
- [8] D. Sievenpiper, L. Zhang, R.F.J. Broas, N.G. Alexopolus, and E. Yablonovitch, "High-impedance Electromagnetic Surfaces with a Forbidden Frequency Band," *IEEE Trans. Microwave Theory Tech.*, vol. 47, no. 11, pp. 2059 – 2074, Nov. 1999.
- [9] T. H. Loh, "High Impedance Surface Electromagnetic Band Gap Metamaterials: Design approach and applications for antenna engineering", Invited paper, published in ARMMS 21st – 22nd Nov. 2011.
- [10] R. Cocciali, F. Yang, K. Ma, and T. Itoh, "Aperture-Coupled Patch Antenna on UC-PBG Substrate," *IEEE Transactions on Microwave Theory and Techniques*, vol. 47, no. 11, pp. 2123-2130, 1999.
- [11] L. Azcona, B. Alderman, P. G. Huggard, R. Gonzalo, B. Martinez, I. Ederra, C. Del Rio, B. M. C. de Hon, M. van Bearden, L. Marchand and P. de Maagt, "EBG technology for imaging arrays at the sub-MM range: designs, materials and precision micromachining techniques," in *Metamaterials for Microwave and (Sub) Millimetre Wave Applications: Photonic Bandgap and Double Negative Designs, Components and Experiments*, 2003. IEE Seminar on , vol., no., pp.1/1-1/10, 24 Nov. 2003.

- [12] B. Martinez, I. Ederra, R. Gonzalo, B. Alderman, L. Azcona, P. G. Huggard, Bas de Hon, A. Hussain, S. R. Andrews, L. Marchand, and P. de Maagt "Manufacturing Tolerance Analysis, Fabrication, and Characterization of 3-D Submillimeter-Wave Electromagnetic-Bandgap Crystals," in *Microwave Theory and Techniques, IEEE Transactions on*, vol. 55, no.4, pp.672-681, April 2007.
- [13] R. Gonzalo, B. Martinez, C. M. Mann, H. Pellemans, P. H. Bolivar, and P. de Maagt "A low-cost fabrication technique for symmetrical and asymmetrical layer-by-layer photonic crystals at submillimeter-wave frequencies," *IEEE Trans. Microwave Theory Tech.* 50, 2384-2392, 2002.
- [14] A. Chelnokov, S. Rowson, J. Lourtioz, L. Duvillaret, and J. Coutaz, "Terahertz characterisation of mechanically machined 3D photoniccrystal," *Electronics Letters* 33(23), 1981–1983 (1997).
- [15] E. Öbay, E. Michel, G. Tuttle, R. Biswas, K. M. Ho, J. Bostak, and D. M. Bloom, "Terahertz spectroscopy of three-dimensional photonic bandgap crystals," *Opt. Lett.* 10, 1155–1157, 1994.
- [16] F. Laermer and A. Urban, "Challenges, developments and applications of silicon deep reactive ion etching," *Microelectron. Eng.* 67-68, 349–355,2003.
- [17] N. Jukam and M. Sherwin, "Two-dimensional terahertz photonic crystals fabricated by deep reactive ion etching in Si," *Applied Physics Letters* 83, 21 (2003).
- [18] G. Kiriakidis and N. Katsarakis, "Fabrication of 2-D and 3-D photonic band-gap crystals in the GHz and THz regions," *Mater. Phys. Mech.* 1, 20-26, 2000.
- [19] G. Feiertag, W. Ehrfeld, H. Freimuth, H. Kolle, H. Lehr, M. Schmidt, M. Sigalas, C. Soukoulis, G. Kiriakidis, T. Pedersen et al., "Fabrication of photonic crystals by deep x-ray lithography," *Applied Physics Letters* 71, 1441 (1997).
- [20] C. Walker, G. Narayanan, H. Knoepfle, J. Capara, J. Glenn, A. Hungerford, T. Bloomstein, S. Palmacci, M. Stern, and J. Curtin, "Laser Micromachining of Silicon: A New Technique for Fabricating High Quality Terahertz Waveguide Components," in [Proc. Eighth International Symposium on Space Terahertz Technology], 358–376 (1997).
- [21] J. Shaker, and M.R. Chaharmir, "Characteristics of photonic bandgap structure comprised of open square rings," *Electronics Letters* , vol.46, no.21, pp.1454-1455, October 2010.
- [22] E. Yablonovitch, "Inhibited spontaneous emission in solid state physics and electronics". *Physical Review Letters*, vol. 58, p. 2059, 1987.
- [23] S. John, "Strong Localization of Photons in Certain Disordered Dielectric Superlattices," *Physical Review Letters*, Vol. 58, No. 23, 8 June 1987.

- [24] E. R. Brown, C. D. Parker, and E. Yablonovitch, "Radiation properties of a planar antenna on a photonic-crystal substrate," *J. Optical Soc. America B*, Vol. 10, No. 2, pp. 404–407, Feb. 1993.
- [25] H. Boutayeb and M. Nedil, "High Gain Slot Array with Fabry-Perot Cavity Feeding Circuit," *International Journal of Antennas and Propagation*, vol. 2016, Article ID 9674742, 5 pages, 2016.
- [26] T. A. Denidni, Y. Coulibaly and H. Boutayeb, "Hybrid Dielectric Resonator Antenna With Circular Mushroom-Like Structure for Gain Improvement," in *IEEE Transactions on Antennas and Propagation*, vol. 57, no. 4, pp. 1043-1049, April 2009.
- [27] S. G. Johnson, P. R. Villeneuve, S. Fan, and J. D. Joannopoulos , "Linear waveguides in photonic-crystal slabs," *Physical Review B*, vol. 62, pp. 8212–8222, 2000.
- [28] I. Ederra, I. Khromova, R. Gonzalo, N. Delhote, D. Baillargeat, A. Murk, B. Alderman, and P. de Maagt, "Electromagnetic-Bandgap Waveguide for the Millimeter Range," *Microwave Theory and Techniques, IEEE Transactions on* , vol.58, no.7, pp.1734,1741, July 2010.
- [29] S. Fan, P. Villeneuve, J. Joannopoulos, and H. Haus, "Channel drop filters in photonic crystals," *Opt. Express* 3, 4-11 (1998).
- [30] V. Radisic, Y. Qian, R. Cocciali, and T. Itoh, "A novel 2-D photonic band-gap structure for microstrip lines," *IEEE Microwave Guided Wave Lett.*, vol. 8, pp. 69–71, Feb. 1998.
- [31] R. Cocciali, W. R. Deal, and T. Itoh, "Radiation characteristics of a patch antenna on a thin PBG substrate," presented at the IEEE AP-S Int. Symp., Atlanta, GA, June 21–26, 1998.
- [32] Q. Xue, K. M. Shum and C. H. Chan, "Novel 1-D microstrip PBG cells," in *IEEE Microwave and Guided Wave Letters*, vol. 10, no. 10, pp. 403-405, Oct 2000.
- [33] E. Yablonovitch, T. J. Gmitter, and K. M. Leung, "Photonic band structure: The face centered-cubic case employing nonspherical atoms," *Phys. Rev. Lett.*, Vol. 67, pp. 2295–2298, Oct. 1991.
- [34] E. Ozbay. E. Michel, G. Tuttle, R. Biswas, M.M. Sigalas and K.M. Ho "Micromachined millimeter-wave photonic band-gap crystals," *Applied Physics Letters* . vol. 64. pp. 2059-2061, 1994.
- [35] M. C. Wanke, O. Lehmann, K. Muller, Q. Wen and M. Stuke "Laser rapid prototyping of photonic band gap microstructures," in *Science* vol. 275,, 1997. pp. 1284-1286.

- [36] S. Y. Lin, J. G. Fleming, D. L. Hetherington, B. K. Smith, R. Biswas, K. M. Ho, M. M. Sigalas, W. Zubrzycki, S. R. Kurtz, and J. Buret, "A three-dimensional photonic crystal operating at infrared wavelengths," *Nature*, Vol. 394, pp. 251 – 254, July 1998.
- [37] J. G. Fleming and S. Y. Lin, "Three-dimensional photonic crystal with a stop band from 1.35 to 1.95 micrometers," *Opt. Lett.*, Vol. 24, pp. 49 – 51, Jan. 1999.
- [38] N. Yamamoto, S. Noda and A. Chutinan, "Development of one period of a three-dimensional photonic crystal in the 5-0 micrometers wavelength region by wafer fusion and laser beam diffraction pattern observation techniques," *Jpn. J. Appl. Phys.*, Vol. 37, pp. L1052 – L1054, September 1998.
- [39] S. Noda, N. Yamamoto, H. Kobayashi, M. Okano, and K. Tomoda, "Optical properties of three-dimensional photonic crystals based on III-V semiconductors at infrared to near-infrared wavelengths," *Appl. Phys. Lett.*, Vol. 75, pp. 905-907, Aug. 1999.
- [40] S. Noda, K. Tomoda, N. Yamamoto, and A. Chutinan, "Full three-dimensional photonic crystals at near-infrared wavelengths," *Science*, Vol. 289, pp. 604 – 606, July 2000.
- [41] J. S. McCalmont, M.M. Sigalas, G. Tuttle, K.M. Ho and C.M. Soukoulis "A layer-by-layer metallic photonic band-gap structure." *Applied Physics Letters*. vol. 68, pp. 2759-2761, 1996.
- [42] H. Shigesawa, M. Tsuji, and A. A. Oliner, "Conductor-backed slot line and coplanar waveguide: Dangers and full-wave analyzes," in *IEEE MTT-S Int. Microwave Symp. Dig.*, New York, May 25–27, 1988, pp. 199–202.
- [43] K. P. Ma, K. Hirose, F. R. Yang, Y. Qian and T. Itoh, "Realisation of magnetic conducting surface using novel photonic bandgap structure," in *Electronics Letters*, vol. 34, no. 21, pp. 2041-2042, 15 Oct 1998.
- [44] F. R. Yang, K. P. Ma, Y. Qian, and T. Itoh, "A novel TEM waveguide using uniplanar compact photonic-bandgap (UC-PBG) structure," *IEEE Trans. Microw. Theory Tech.*, Vol. 47, No. 11, pp. 2092–2098, Nov. 1999.
- [45] J. B. Pendry and D. R. Smith, "Reversing Light With Negative Refraction," *Physics Today*, vol. 57, pp. 37-43, 2004.
- [46] Ke Wu, D. Deslandes and Y. Cassivi, "The substrate integrated circuits - a new concept for high-frequency electronics and optoelectronics," *Telecommunications in Modern Satellite, Cable and Broadcasting Service, 2003. TELSIKS 2003. 6th International Conference on*, 2003, pp. P-III-P-X vol.1.

- [47] A. Mekis, J. C. Chen, I. Kurland, S. Fan, P. R. Villeneuve and J. D. Joannopoulos, "High Transmission Through Sharp Bends in Photonic Crystal Waveguides," Phys. Rev. Lett., vol. 77, no 18, pp. 3787-3790, 1996.
- [48] L. H. Frandsen, P. I. Borel, Y. X. Zhuang, A. Harpøth, M. Thorhauge, and M. Kristensen, "Ultralow-loss 3-dB photonic crystal waveguide splitter," Optics Letters, Vol. 29, No. 14, 1623-1625, 2004.
- [49] M.K. Moghaddam, M.M. Mirsalehi and A.R. Attari, "Slow light transmission in a photonic crystal power splitter with parallel outputs", Photonics and Nanostructures - Fundamentals and Applications, Volume 12, Issue 1, February 2014, Pages 75-82.
- [50] Y. Tanaka, H. Nakamura, Y. Sugimoto, N. Ikeda, K. Asakawa and K. Inoue, "Coupling properties in a 2-D photonic crystal slab directional coupler with a triangular lattice of air holes," in IEEE Journal of Quantum Electronics, vol. 41, no. 1, pp. 76-84, Jan. 2005.
- [51] M.K. Moghaddam, A.R. Attari, and M.M. Mirsalehi, "Improved photonic crystal directional coupler with short length, Photonics and Nanostructures - Fundamentals and Applications", Volume 8, Issue 1, January 2010, Pages 47-53.
- [52] M. Thorhauge, L.H. Frandsen, and P.I. Borel, " Efficient photonic crystal directional couplers", Optics Letters, Vol. 28, No. 17, 2003.
- [53] F. Cuesta, A. Martínez, J. García, F. Ramos, P. Sanchis, J. Blasco and J. Martí, "All-optical switching structure based on a photonic crystal directional coupler" Opt. Express 12 161, 2004
- [54] A. Sharkawy, S. Shi, D. Prather, and R. Soref, "Electro-optical switching using coupled photonic crystal waveguides," Opt. Express 10, 1048-1059, 2002
- [55] Y. S. E. Abdo, M. R. Chaharmir, J. Shaker, and Y. M. M. Antar, "Detailed study of millimeter wave EBG guide: broadbanding techniques, modal structure, and crosstalk behavior," Progress In Electromagnetics Research B, Vol. 50, 141-156, 2013
- [56] C. Biancotto and P. Record, "Triangular Lattice Dielectric EBG Antenna," in *IEEE Antennas and Wireless Propagation Letters*, vol. 9, no. , pp. 95-98, 2010.
- [57] H. Ouassal, J. Shaker, L. Roy and R. Chaharmir, "A Novel Multi-Layer Electromagnetic Band Gap Structure (EBG) Comprised of 3-D Lattice of Square Rings," 2015 IEEE MTT-S International Conference on Numerical Electromagnetic and Multiphysics Modeling and Optimization (NEMO), Ottawa, ON, 2015, pp. 1-4.
- [58] H. Ouassal, L. Roy, J. Shaker and R. Chaharmir, "Guided modes of a line-defect EBG slab waveguide in a 3-D square lattice of metallic open square rings," Millimeter Waves (GSMM), 2015 Global Symposium On, Montreal, QC, 2015, pp. 1-3.

- [59] S. Enoch, G. Tayeb and D. Maystre, "Dispersion diagrams of Bloch modes applied to the design of directive sources," Progress In Electromagnetic Research, PIER 41, p. 61-81, 2003
- [60] ANSYS HFSS 17.2TM
- [61] J. Zhou, T. Koschny and C. Soukoulis, "Magnetic and electric excitations in split ring resonators," Opt. Express 15, 17881-17890, 2007.
- [62] C. Rockstuhl, T. Zentgraf, E. Pshenay-Severin, J. Petschulat, A. Chipouline, J. Kuhl, T. Pertsch, H. Giessen, and F. Lederer, "The origin of magnetic polarizability in metamaterials at optical frequencies - an electrodynamic approach," Opt. Express 15, 8871-8883, 2007.
- [63] C. Rockstuhl, F. Lederer, C. Etrich, T. Zentgraf, J. Kuhl, and H. Giessen, "On the reinterpretation of resonances in split-ring-resonators at normal incidence," Opt. Express 14, 8827-8836, 2006.
- [64] C. Rockstuhl, F. Lederer, T. Zentgraf, I. Loa, K. Syassen, J. Kuhl and C. Etrich, "Resonances of Split-Ring Resonator Metamaterials in the Near Infrared," Applied Physics B: Lasers and Optics, 84, 219-227, 2006.
- [65] N. Katsarakis, T. Koschny, M. Kafesaki, E.N. Economou and C.M. Soukoulis, "Electric coupling to the magnetic resonance of split ring resonators," Applied Physics Letters , vol.84, no.15, pp.2943,2945, Apr 2004.
- [66] S. Linden, C. Enkrich, M. Wegener, J. Zhou, T. Koschny, and C. M. Soukoulis, "Magnetic Response of Metamaterials at 100 Terahertz," Science 306, 1351-1353, 2004.
- [67] T. D. Corrigan, P. W. Kolb, A. B. Sushkov, H. D. Drew, D. C. Schmadel, and R. J. Phaneuf, "Optical plasmonic resonances in split-ring resonator structures: an improved LC model," Opt. Express **16**, 19850-19864 (2008)
- [68] K.R. Carver and J.W. Mink, "Microstrip antenna technology," Antennas and Propagation, IEEE Transactions on , vol.29, no.1, pp.2,24, Jan 1981.
- [69] M. N. Armenise, C. E. Campanella, C. Ciminelli, and E. Scivittaro, "Modelling of photonic crystals: A comparison among various analysis methods," in Proc. Int. Conf. Transparent Opt. Netw., vol. 2. Athens, Greece, pp. 1-4, 2008
- [70] S. G. Johnson, S. H. Fan, P. R. Villeneuve, J. D. Joannopoulos, and L. A. Kolodziejski, "Guided modes in photonic crystal slabs," Phys. Rev. B, vol. 60, pp. 5751-5758, Aug. 15, 1999.

- [71] H. Jin, D.S. Citrin, W. Huaming, G. Dingshan, Z. Zhiping and C. Shaoping, "Slab-Thickness Dependence of Photonic Bandgap in Photonic-Crystal Slabs," Selected Topics in Quantum Electronics, IEEE Journal of , vol.18, no.6, pp.1636,1642, Nov.-Dec. 2012.
- [72] A. Adibi, Yong Xu, R. K. Lee, A. Yariv and A. Scherer, "Properties of the slab modes in photonic crystal optical waveguides," in *Journal of Lightwave Technology*, vol. 18, no. 11, pp. 1554-1564, Nov. 2000.
- [73] K. Yamada, H. Morita, A. Shinya and M. Notomi, " Improved line-defect structures for photonic-crystal waveguides with high group velocity," Optics Communications, Volume 198, Issues 4–6, 1 November 2001, Pages 395-402.
- [74] K. Kiyota, T. Kise, N. Yokouchi, T. Ide and T. Baba, "Various low group velocity effects in photonic crystal line defect waveguides and their demonstration by laser oscillation". *Applied physics letters*, 88(20), 201904, 2006.
- [75] Y. Tanaka, Y. Sugimoto, N. Ikeda, H. Nakamura, K. Asakawa, K. Inoue, and S. G. Johnson, "Group velocity dependence of propagation losses in single-line-defect photonic crystal waveguides on GaAs membranes," *Electron. Lett.*, vol. 40, pp. 174–176, 2004.
- [76] H. Ouassal, J. Shaker, L. Roy, R. Chaharmir and K. Hettak, "A Novel Multi-layer Electromagnetic Band Gap(EBG)Structure Comprised of Square Rings as a Microwave Guiding Structure" Submitted to the *IEEE Transactions on Components, Packaging and Manufacturing Technology (TCMPT)* for second revision.
- [77] S. B. Cohn, "Slot line on a dielectric substrate," *IEEE Trans. Microw. Theory Techn.*, vol. MTT-17, no. 10, pp. 768–778, Oct. 1969.
- [78] T. G. Lim, H. N. Ang, I. D. Robertson and B. L. Weiss, " Ka-band CPW-to-slotline transition in photoimageable thick film technology for tapered slot antenna applications", *Microw. Opt. Technol. Lett.*, vol. 48, no. 10, pp 2032–2034, Oct. 2006.
- [79] C. L. Holloway and E. F. Kuester, "A quasi-closed form expression for the conductor loss of CPW lines, with an investigation of edge shape effects," in *IEEE Transactions on Microwave Theory and Techniques*, vol. 43, no. 12, pp. 2695-2701, Dec 1995.
- [80] R. Hwang, "Surface waves and volume waves in a photonic crystal slab," *Opt. Express* 15, 7913-7921 (2007).
- [81] J. Li, W. Withayachumnankul, S. Chang and D. Abbott, "Metamaterial-based strain sensors," *Intelligent Sensors, Sensor Networks and Information Processing (ISSNIP)*, 2011 Seventh International Conference on, Adelaide, SA, 2011, pp. 30-32.

- [82] H. Ouassal, J. Shaker, K. Hettak, R. Chaharmir and L. Roy, "Compact EBG guides using substrate layered rings," *2016 17th International Symposium on Antenna Technology and Applied Electromagnetics (ANTEM)*, Montreal, QC, Canada, 2016, pp. 1-3..
- [83] R. F. Bauer and P. Penfield, "De-Embedding and Unterminating," in *IEEE Transactions on Microwave Theory and Techniques*, vol. 22, no. 3, pp. 282-288, Mar 1974.
- [84] E. S. Daniel, N. E. Harff, V. Sokolov, S. M. Schreiber, and B. K. Gilbert.“Network analyzer measurement de-embedding utilizing a distributed transmission matrix bisection of a single THRU structure,”63rd ARFTG Conf. , pp. 61–68, Jun. 2004
- [85] L. F. Tiemeijer and R. J. Havens, "A calibrated lumped element de-embedding technique for on-wafer RF characterization of high-quality inductors and high-speed transistors," *Electron Devices, IEEE Transactions on*, vol. 50, pp. 822-829,2003.
- [86] M.C.A.M. Koolen, J.A.M. Geelen, and M.P.J. G. Versleijen, “An improved de-embedding technique for on-wafer high-frequency characterization,” Proc. IEEE, Bipolar/BiCMOS Circuits and Tech. Meeting, pp.188-191, Sept. 1991.
- [87] H. Cho and D. E. Burk, "A three-step method for the de-embedding of high-frequency S-parameter measurements," *Electron Devices, IEEE Transactions on*, vol. 38, pp. 137 1 - 1375, 1991.
- [88] A. Munir, V. Fusco and O. Malyuskin, "Parallel plate waveguide simulator design, characterisation and DUT de-embedding," *2008 IEEE Antennas and Propagation Society International Symposium*, San Diego, CA, 2008, pp. 1-4.
- [89] E. J. Denlinger, "Losses of Microstrip Lines," in *IEEE Transactions on Microwave Theory and Techniques*, vol. 28, no. 6, pp. 513-522, Jun 1980.
- [90] <http://www.microwaves101.com/encyclopedia/waveguide-loss>.
- [91] M. Bozzi, S. A. Winkler and K. Wu, "Broadband and compact ridge substrate-integrated waveguides," in *IET Microwaves, Antennas & Propagation*, vol. 4, no. 11, pp. 1965-1973, November 2010.
- [92] F. Parment, A. Ghiotto, T. P. Vuong, J. M. Duchamp and K. Wu, "Air-Filled Substrate Integrated Waveguide for Low-Loss and High Power-Handling Millimeter-Wave Substrate Integrated Circuits," in *IEEE Transactions on Microwave Theory and Techniques*, vol. 63, no. 4, pp. 1228-1238, April 2015.
- [93] P. S. Kildal, "Gap waveguides and PMC packaging: Octave bandwidth mm- and submm-wave applications of soft & hard surfaces, EBGs and AMCs," *2013 Asia-Pacific Microwave Conference Proceedings (APMC)*, Seoul, 2013, pp. 34-36.

- [94] K. Binbin, Li. En, and Z. Zhang , "A Ku Band High Power Rectangular Waveguide Directional Coupler's Design," Engineering and Technology (S-CET), 2012 Spring Congress on , vol., no., pp. 1-4, 27-30 May 2012.
- [95] I. Ohta, Y. Yumita, K. Toda, and M. Kishihara, "Cruciform directional couplers in H-plane rectangular waveguide," Microwave Conference Proceedings, 2005. APMC 2005. Asia-Pacific Conference Proceedings , Vol. 2, no., pp. 4 pp., 4-7 Dec. 2005.
- [96] M. Kishihara, K. Yamane, I. Ohta, "Design of Cruciform Directional Couplers in E-Plane Rectangular Waveguide," Microwave Symposium Digest, 2006. IEEE MTT-S International, vol., no., pp. 1722-1725, 11-16 June 2006.
- [97] R. Mongia, I. Bahl and P. Bhartia, RF and Microwave Coupled-Line Circuits. Nonvocd, MA: Anech House, 1999.
- [98] S. L. March, "Phase Velocity Compensation in Parallel-Coupled Microstrip," *Microwave Symposium Digest, 1982 IEEE MTT-S International*, Dallas, TX, USA, 1982, pp. 410-412.
- [99] T. G. Bryant and J. A. Weiss, "Parameters of microstrip transmission lines and of coupled pairs of microstrip lines" , IEEE Trans. Microwave Theory Tech., vol. MTT-16, no. 12, pp. 1021-1027, December 1968.
- [100] J. Lange, "Interdigital stripline quadrature hybrid," IEEE Trans. Microwave Theory Tech., vol. MTT-17, pp. 1150–1151, Dec. 1969.
- [101] C. Caloz, A. Sanada, and T. Itoh, "A novel composite right-/left-handed coupled-line directional coupler with arbitrary coupling level and broad bandwidth," IEEE Trans. Microwave Theory Tech., vol. 52, no. 3, pp. 980-992, March 2004.
- [102] T. Djerafi and K. Wu, "Super-Compact Substrate Integrated Waveguide Cruciform Directional Coupler," in *IEEE Microwave and Wireless Components Letters*, vol. 17, no. 11, pp. 757-759, Nov. 2007.
- [103] P. Chen, G. Hua, D. T. Chen, Y. C. Wei, and W. Hong, "A double layer crossed over Substrate Integrated Waveguide wide band directional coupler," in Proc. Asia-Pacific Microw. Conf., Dec. 2008, pp. 1-4.
- [104] Z. Pourgholamhossein, R. Safian, and H. Pourghassem, "Wideband double layer substrate integrated waveguide directional coupler," in Proc. Int. Symp. Telecommun., Dec. 2010, pp. 328–331.
- [105] S. Boscolo, M. Midrio and C. G. Someda, "Coupling and decoupling of electromagnetic waves in parallel 2D photonic crystal waveguides," in *IEEE Journal of Quantum Electronics*, vol. 38, no. 1, pp. 47-53, Jan 2002.

[106] J. Zimmermann, M. Kamp, A. Forchel, R. März, Photonic crystal waveguide directional couplers as wavelength selective optical filters, *Optics Communications*, Volume 230, Issues 4–6, 1 February 2004, Pages 387-392.

[107] D. M. Pustai, A. Sharkawy, S. Y. Shi, G. Jin, J. Murakowski, and D. W. Prather, "Characterization and analysis of photonic crystal coupled waveguides," *Journal of Microlithography Microfabrication and Microsystems* 2. 292-299, (2003).